Towards Improved Understanding of Mass Transport in Polymer Electrolyte Membrane Water Electrolysers

Maximilian Maier

Submitted in part fulfilment of the requirements for the degree of Doctor of Philosophy at
University College London (UCL)

Electrochemical Innovation Lab
Department of Chemical Engineering
University College London

2021

Declaration

I, Maximilian Maier confirm that the work presented in this thesis is my own. Where information has been derived from other sources, I confirm that this has been indicated in the thesis.

[redacted]

Signature

29/09/2021
……………………………………..

Date

Acknowledgements

I would like to express my deep and genuine gratitude towards my supervisor, Prof. Dan Brett. Only his persuasiveness convinced me to actually move to London, and his passion for science has kept me going throughout my PhD. I thank him for countless hours of discussions, correcting my work, motivating me, and never doubting my decisions (at least not openly). He has never held me back in my endeavours and put more resources at my disposal than I could have ever reasonably used throughout the past years. It's mostly due to him that I thoroughly enjoyed my PhD and it was a time of great experiences.

I would also like to thank my second supervisor, Prof. Paul Shearing, for always being available for help and advice, as well as keeping a watchful eye on my work whenever I needed it. His comments during my transfer viva have helped me a lot in shaping this work.

My third supervisor, Dr. Gareth Hinds, was a great source of inspiration and always gave me quick and brilliant feedback, indispensable for correcting my course of action and turning my work into publishable results. Just as my other supervisors, I owe him deeply felt gratitude for being patient with me and my work, and unrelentingly improving it along the way.

Lastly, I would like to thank all my friends and colleagues in the EIL for countless hours of fun and good discussions. Some people I have grown particularly fond of over the past years, but I will refrain from naming them as I know they would make fun of me for doing so.

Abstract

The advent of a global societal and governmental movement to curb climate change has put low-carbon technologies at the centre stage of public interest and scientific efforts. In the wake of rising concerns around the carbon footprint of personal mobility and the energy sector, the concept of a ‘Hydrogen Economy’ has experienced yet another rapid spur of popularity. Polymer electrolyte membrane water electrolysers (PEMWEs) are a promising candidate for large-scale hydrogen production, and improvements in the technology have led to increasingly high operational current densities exceeding 2 A cm^{-2}, which requires adequate mass transport strategies to ensure sufficient supply of reactant and removal of products.

Optimization and diagnosis of mass transport processes in PEMWEs has long been neglected despite its significance, but the amount of scientific literature has recently increased sharply. This thesis uses existing diagnostic tools to gather new insights into the processes within PEMWE flow channels and liquid-gas diffusion layers, aims at providing new low-cost diagnostic tools to accelerate the investigation of mass transport processes, and consequently deduces novel approaches to the design of PEMWEs components, cells, and stacks.

Neutron and X-ray imaging are used to demonstrate the effect of liquid-gas diffusion layer microstructure on the water-gas distribution in a PEMWE, revealing significant inhomogeneity across the active area. Due to cost and accessibility issues around radiation imaging, acoustic methods are explored as alternative diagnostic tools. Acoustic emission is successfully demonstrated as an *operando* technique to monitor two-phase flow in the flow channels, detecting the transition from bubbly to slug flow. Bubbly flow is observed at the onset of electrochemical activity and low current densities, with a high number of small bubbles, while at higher current densities these small bubbles coalesce and form larger slug bubbles. Lastly, acoustic time-of-flight imaging is used to monitor the water-gas distribution in the liquid-gas diffusion layer and the flow channels, with results being consistent with expectations and previous results obtained via neutron imaging.

Impact Statement

Hydrogen technology is increasingly seen as crucial for the fight against climate change and a more sustainable energy and transport system. In the concept of a ‘Hydrogen Economy’, hydrogen serves as a universal energy carrier (vector), able to store large amounts of intermittent renewable energy and hence stabilise the electricity grid, is used in the gas grid to reduce carbon emissions, and enables low-carbon mobility for all modes of transport, including cars, trucks, trains, and ships. Among hydrogen production methods, polymer electrolyte membrane water electrolysers (PEMWEs) have attracted particular attention due to their advantages over other electrolysis technologies, which include a low resistance, high attainable current densities, and a compact build. PEMWEs were conceived in the 1970s, and even though considerable progress has been made, the technology and its components have not significantly changed since their inception. In particular, mass transport processes have long been overlooked, but are set to increase in importance due to improvements in PEMWE technology that are leading to increasingly high current densities.

This thesis seeks to address the lack of understanding and available diagnostic tools relevant to two of the most critical PEMWE components for mass transport: the flow-fields and the liquid-gas diffusion layer (LGDL). While the flow-fields have to provide sufficient ingress and egress of water and gas, the LGDL’s role is to transport water from the flow-field to the catalyst sites and product oxygen gas in concurrent flow towards the flow-field, while also providing electrical and thermal conductivity. Therefore, this work used existing diagnostic tools, such as neutron imaging and optical imaging, to gain insight into mass transport processes in the flow-fields and LGDL, but also introduced a suite of novel acoustic diagnostic tools for the investigation of mass transport processes in PEMWEs.

The results presented in this work will significantly contribute to the understanding of mass transport processes in PEMWEs and, through establishing new diagnostic possibilities, accelerate the speed of scientific discovery in relation to mass transport processes. Further, the results presented here challenge the existing understanding of PEMWE design and assembly, and contribute to a more integrated approach towards component design.

The diagnostic tools applied to PEMWEs are also of considerable commercial interest. Integrating acoustic diagnostic methods into large-scale PEMWE plants could enable optimized operation and real-time adjustment of local inefficiencies, such as bubble blockage or insufficient water supply. Further, the two acoustic diagnostic tools investigated in this work could successfully be employed for a range of applications in the chemical industry, leveraging their demonstrated suitability to monitor multi-phase systems in real-time, at low-cost, and in a non-destructive manner.

The results presented in this thesis have been disseminated in four first-author peer-reviewed publications in internationally renowned journals, and conferences including the 235th ECS Meeting in Dallas (USA) and the 22nd World Hydrogen Economic Forum (WHEC) in Rio de Janeiro (Brazil). Academic collaborators included researchers from the National Physics Laboratory (UK), the Helmholtz Zentrum Berlin (Germany), and the School of Chemistry at the University of New South Wales (Australia).

Table of Contents

Table of Contents

List of Tables

List of Figures

List of Abbreviations and Nomenclature

Abbreviations

AC	Alternating Current
AE	Acoustic Emission
AToF	Acoustic Time-of-Flight
AWE	Alkaline Water Electrolysis
CAD	Computer-Aided Design
CCD	Charge-Coupled Device
CCM	Catalyst Coated Membrane
CHT	Circular Hough Transform
CL	Catalyst Layer
CONRAD	Cold Neutron Tomography and Radiography
CT	Computed Tomography
DC	Direct Current
EBM	Electron Beam Melting
EIS	Electrochemical Impedance Spectroscopy
FFT	Fast Fourier Transform
GDL	Gas Diffusion Layer
HER	Hydrogen Evolution Reaction
LGDL	Liquid-Gas Diffusion Layer
MPL	Micro-Porous Layer
OER	Oxygen Evolution Reaction
PEM	Polymer Electrolyte Membrane
PEMFC	Polymer Electrolyte Membrane Fuel Cell
PEMWE	Polymer Electrolyte Membrane Water Electrolyser
PNM	Pore Network Model
PSD	Pore Size Distribution
PTFE	Polytetrafluoroethylene (Teflon)
PTL	Porous Transport Layer
P&ID	Piping and Instrumentation Diagram
SEM	Scanning Electron Microscope
SLM	Selective Laser Melting
SLS	Selective Laser Sintering
ToF	Time-of-Flight
URFC	Unitized Reversible Fuel Cell
XCT	X-Ray Computed Tomography

Nomenclature

A	Peak Amplitude (-)
A	Active Area (cm^2)
$A(n)$	Surface Area of a Cluster (m^2)
a	Thermodynamic Activity (-)
a	Cross-Sectional Area of a Flow Channel (m^2)
a_V	Surface Area per Unit Volume (m^2 m^{-3} or m^{-1})
c	Concentration (mol m^{-3})
D	Hit Duration (µs)
D	Bubble Size (mm)
d	LGDL Thickness (mm)
E	Elastic Modulus (N mm^{-2} or Pa)
E	External Electric Field (V m^{-1})
E	Hit Energy (aJ)
e	Induced Electric Field (V m^{-1})
F	Faraday Constant (96485.3 C mol^{-1})
f	Frequency (Hz or s^{-1})
G	Gibb's Free Energy (J)
G	Mass Flux (kg s^{-1} m^{-2})
g	Piezoelectric Voltage Constant (V m N^{-1})
H	Hit Rate (s^{-1})
I	Current (A)
I	Intensity (-)
i	Current Density (A cm^{-2})
i_0	Exchange Current Density (A cm^{-2})
j	Flow Velocity (m s^{-1})
K	Permeability (m^2)
k	Wave Number (m^{-1})
k_B	Boltzmann Constant ($1.4 \cdot 10^{-23}$ J K^{-1})
M	Water Flow through LGDL (kg s^{-1})
M	Molar Mass (kg mol^{-1})
N	Number of Bubbles (-)
N_A	Avogadro Constant ($6.0 \cdot 10^{23}$ mol^{-1})
n_C	Critical Cluster Size (-)
n_{chan}	Number of Flow Channels (-)
n_{drag}	Electro-Osmotic Drag Coefficient (-)
p	Pressure (Pa)
p	Projection (m^{-1})

$\boldsymbol{p_\infty}$	Pressure far away from the Bubble (Pa)
$\boldsymbol{R}$	Reflection Coefficient (-)
$\boldsymbol{R}$	Gas Constant (J mol^{-1} K^{-1})
$\boldsymbol{R}$	Electrical Resistance (Ω)
$\boldsymbol{R_0}$	Oscillation-Free Bubble Radius (m)
$\boldsymbol{r}$	Radius (m)
$\boldsymbol{r_C}$	Radius of Bubble Cloud (m)
$\boldsymbol{S}$	External Mechanical Stress (N m^{-1})
$\boldsymbol{S}$	Supersaturation (-)
$\boldsymbol{s_L}$	Liquid Phase Factor (m^2 mol$^{2/3}$)
$\boldsymbol{s}$	Spatial Coordinate (-)
$\boldsymbol{T}$	Temperature (K)
$\boldsymbol{T}$	Transmission Coefficient (-)
$\boldsymbol{t}$	Sample Thickness (m)
$\boldsymbol{t}$	Time (s)
$\boldsymbol{u}$	Spatial Coordinate (-)
$\boldsymbol{V}$	Voltage (V)
$\boldsymbol{v}$	Molecular Volume (m^3 mol^{-1})
$\boldsymbol{v_S}$	Speed of Sound (m s^{-1})
$\boldsymbol{W}$	Through-Plane Water Thickness (mm)
$\boldsymbol{x}$	Gas Fraction (-)
$\boldsymbol{x}$	Spatial Coordinate (-)
$\boldsymbol{y}$	Spatial Coordinate (-)
$\boldsymbol{Z}$	Acoustic Impedance (-)
$\boldsymbol{Z_{img}}$	Imaginary Electric Impedance (Ω cm^2)
$\boldsymbol{Z_R}$	Real Electric Impedance (Ω cm^2)

$\boldsymbol{\alpha}$	Attenuation Coefficient (m^{-1})
$\boldsymbol{\alpha}$	Charge Transfer Coefficient (-)
$\boldsymbol{\gamma}$	Polytropic Coefficient (-)
$\boldsymbol{\delta}$	Piezoelectric Strain Constant (N V^{-1} m^{-1})
$\boldsymbol{\varepsilon}$	Porosity (-)
$\boldsymbol{\zeta}$	Water Ratio (-)
$\boldsymbol{\eta}$	Viscosity (Pa s)
$\boldsymbol{\vartheta}$	Rotation Angle (rad)
$\boldsymbol{\mu}$	Chemical Potential (J)
$\boldsymbol{\mu}$	Linear Attenuation Coefficient (m^{-1})
$\boldsymbol{\xi}$	Particle Displacement (m)

ρ	Density (kg m^{-3})
σ	Absorption Cross-Section (m^2)
σ	Mechanical Strain (N m^{-2})
σ	Surface Tension (N m^{-1})
τ	Residence Time (s)
τ	Tortuosity (-)
ω	Angular Frequency (Hz or s^{-1})
$\mathfrak{R}$	Radon Transform (-)

1 Introduction

1.1 Background

The world faces the unprecedented challenge of decarbonising its transport, energy, farming, and industrial sectors. The fight against climate change is a central policy issue in most developed countries, most notably through the pledge to reduce global warming to 2 °C, stated in the Paris climate targets [1] which were recently supported by the new US administration [2]. However, global carbon emissions are increasing above the predicted and required rate, jeopardizing the progress of decarbonisation [1,3]. To keep global warming within acceptable limits and reduce air pollution, systematic change has to occur on multiple fronts: ending the use of internal combustion engines for light and heavy vehicles, reducing the use of natural gas in the energy sector, and drastically reducing the use of fossil fuels based energy production.

This vision heavily relies on deploying renewable energy technologies, such as wind, solar, nuclear, and tidal power. As most renewable energy technologies are intrinsically intermittent, stabilisation will be necessary to build a grid dominated by renewables. However, no single technology has proven dominant or clearly favourable over others and the uptake of energy storage technologies is subject to a complex interplay between policy and market issues, actual and expected costs, as well as risk perception and proliferation of these technologies in adjacent sectors such as transport or domestic energy management. In consequence, the future market for energy storage technologies for grid stabilization is likely to be strongly granular, with various solutions adopted on a national or regional level [4–6]. This requires a flexible and highly adaptable technology for energy storage, able to be integrated effectively into the local energy system.

The ‘Hydrogen Economy’ concept was developed in response to the world's rising energy consumption and concerns about pollution in the early 1970s [7]; with heightened awareness around climate change, the idea has gained increasing traction and has been discussed extensively [7–10]. The Hydrogen Economy is based on the use of hydrogen as a universal energy carrier (vector) and fuel. Transporting energy in the form of hydrogen through pipelines is more cost-efficient than the transport of electricity through wires [7] and hydrogen is highly flexible and can be used in fuel cells to produce electricity or directly as a fuel in combustion engines [10]. Furthermore, among several potential solutions, such as Li-ion batteries and redox flow batteries, hydrogen technology is a well-suited technology to provide the necessary stabilisation means required for a grid dominated by intermittent renewables. However, the consideration whether to deploy battery or hydrogen storage for grid stabilisation is highly dependent on a range of factors, among which electricity prices are one of the key considerations. Due to the lower efficiency of hydrogen generation and energy production from hydrogen at a later point compared to battery energy storage, the overall suitability and cost of the two storage technologies need to be considered carefully. In the case of electricity overproduction, hydrogen can be produced and stored. However, the energetic requirements of hydrogen compression need to be factored into the overall consideration whether to use hydrogen-based grid stabilisation technology. When, at a later point, electricity production is not sufficient, the previously produced hydrogen can be converted into power using fuel cell technology. As a result, peaks and troughs in renewable electricity production are mitigated and the grid stabilised [11,12]. As electricity production from renewable sources is enforced by policy and growing exponentially worldwide (Figure 1 (a)), the need for an efficient and robust grid-scale storage system is increasing in tandem.

The main drawback of this vision is the fact that hydrogen is rarely found naturally in its molecular H_2 form, but in other molecules such as water, crude oil or natural gas. This makes hydrogen production technologies the backbone of the Hydrogen Economy and a crucial bottle-neck for its realisation. The most commonly used methods of hydrogen production are reforming of hydrocarbons, the use of biomass in some form, and water splitting [13,14]. Reforming and biomass gasification emit carbon dioxide as a by-product, which necessitates carbon capture and storage technology [13]. Hence, water electrolysis using electricity from renewable energy sources is an attractive alternative as its only local by-product is oxygen. Life cycle assessment analysing the whole supply chain yields a global warming potential for PEMWE hydrogen production of more than 30 $\frac{\mathrm{kg\,CO_2}}{\mathrm{kg\,H_2}}$ for the use of grid energy, and between 1 $\frac{\mathrm{kg\,CO_2}}{\mathrm{kg\,H_2}}$ and 3 $\frac{\mathrm{kg\,CO_2}}{\mathrm{kg\,H_2}}$ for a range of renewable energy sources [15], which compares to 4 $\frac{\mathrm{kg\,CO_2}}{\mathrm{kg\,H_2}}$ for biomass conversion and around 9 $\frac{\mathrm{kg\,CO_2}}{\mathrm{kg\,H_2}}$ for fossil fuel reforming [16].

The most widely applied water-splitting technology is alkaline water electrolysis (AWE), which is a commercially mature technology and enables multimegawatt hydrogen production, with further advantages including a simple design and low-cost electrolyte (KOH) [17]. However, AWE suffers from drawbacks such as relatively low current densities, typically below 0.6 A cm^{-2} [11], and a higher gas crossover between anode and cathode [18].

In response to these disadvantages, polymer electrolyte membrane (PEM) water electrolysers have been developed, which use a polymer membrane instead of a liquid electrolyte to allow for the transport of hydrogen ions. PEM water electrolysers (PEMWEs) can achieve high current densities of up to 10 A cm^{-2} [19], but are mostly used up to around 3 A cm^{-2} [11]. This, and the use of a membrane instead of a simple separator material as in AWEs, allows for a very compact design and a significantly reduced gas crossover compared to alkaline electrolysis. Despite these conceptual advantages, PEMWEs have only recently been commercialised; however, significant advances in deployment have been made in recent years, with plants being rated up to 6 MW [20], 10 MW [21], and a planned 100 MW plant [21]. Nevertheless, PEMWEs have yet to be developed to the same scale of hydrogen production as alkaline electrolysis [11] and capital expenditure for PEMWEs is still high; however, it is expected to reach cost parity with AWEs by 2030 [22] (see Figure 1 (b)).

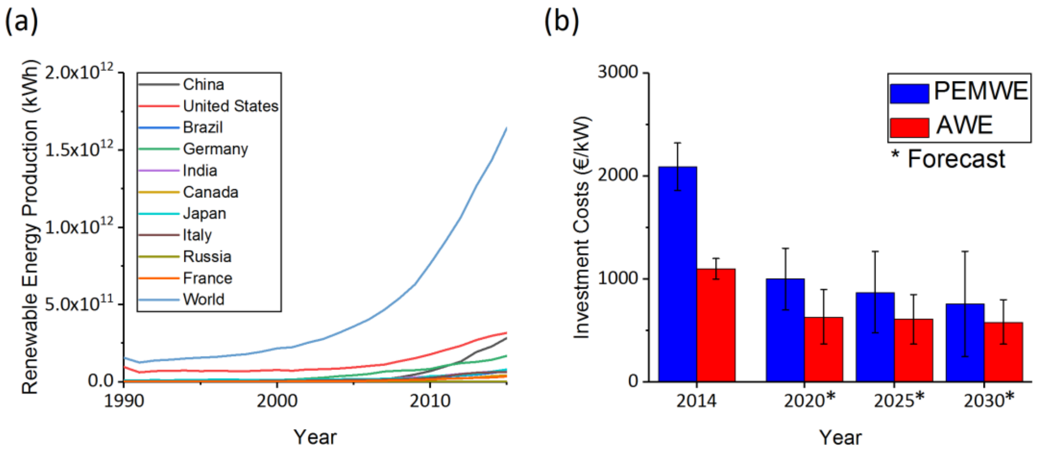

Figure 1: (a) The world's renewable energy production is steadily increasing and has strongly accelerated in the past decade [23]. *(b) The investment costs (capital expenditure without installation costs) for PEMWE plants are forecast to steadily decrease in the coming decade and reach levels typical for current alkaline water electrolysis (AWE) plants* [24].

1.2 PEM Water Electrolysers

PEMWEs were first introduced by General Electric in 1973 [25]. One of the main advantages of PEMWEs (Figure 2 (a)) is the low ohmic resistance of the thin solid electrolyte, which allows for very high current densities. In comparison, AWEs (Figure 2 (b)), which are widely commercialised, rely on a liquid electrolyte resulting in a much higher ohmic resistance.

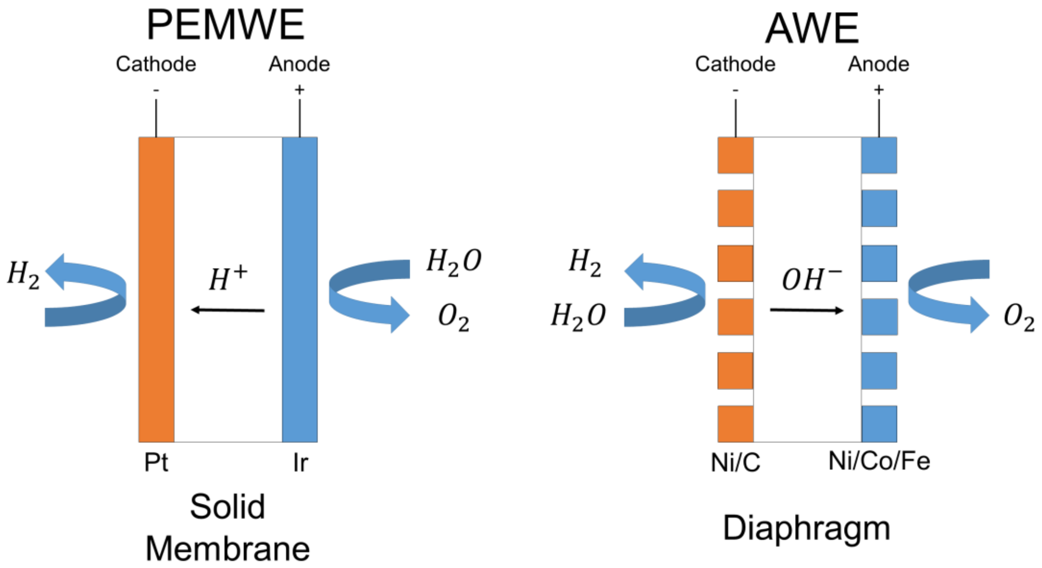

Figure 2: (a) PEMWEs rely on a solid polymer membrane through which protons are transported from the anode to the cathode, while for (b) alkaline water electrolysers (AWEs) a liquid electrolyte is used and hydroxyl ions move from cathode to anode (adapted from [18]*).*

Another positive aspect of PEMWEs is the increased operational safety due to the very low gas crossover through the solid electrolyte. The negligible crossover of hydrogen is also a prerequisite for pressurised water electrolysis, which is possible using a PEMWE due to the very compact design without a liquid electrolyte [26–28]. This allows for the direct production of pressurized hydrogen without further compression, although it has been debated if pressurized electrolysis is the most energy-efficient option [27]. The energy required for compression can be reduced by differential water electrolysis; operating the anode at ambient pressure, while only the cathode is pressurized, which has been found to be more energy efficient than post-compression of hydrogen for operating pressures up to 40 bar. Operating pressures above 40 bar lead to deteriorating Faradaic efficiency due to increased hydrogen crossover [29,30].

The main disadvantage related to PEM water electrolysis are the very high stack costs due to expensive catalyst, liquid-gas diffusion layer and flow-field materials. On the PEMWE anode a very corrosive environment, with $pH \approx 2$ and high potentials above 2 V, is found [18], which not many materials can withstand. Among these titanium is the most commonly used at the anode for liquid-gas diffusion layer and flow-fields. Even though titanium has a much higher corrosion resistance compared to less frequently used materials like graphite and stainless steel, it is far more expensive and still causes a PEMWE performance degradation over time as an oxide layer is forming [31]. This can potentially be overcome by coating with nickel [32], gold, or silver [31], but long term studies on the stability of these configurations are missing.

Due to the high stack costs for PEMWEs, AWEs are still the industrially dominant electrolysis technology. However, due to the principal advantages of PEMWEs over AWEs and the projected cost reductions (see Section 1.1), PEMWEs are likely to play a significant role for industrial hydrogen production and grid stabilisation. In order to achieve the technological improvements necessary to drive the uptake of PEMWEs for these real-world applications, systematic testing of small, lab-scale, single-cell systems is the preferred mode of research. It allows for rapid testing of new materials and design approaches at moderate costs and reduced complexity compared to large stacks or systems.

Resulting from the current state-of-the-art and future requirements for PEMWE technology, a number of key challenges for further development can be identified:

- Reduction of catalyst loading, e.g. through novel engineering approaches [33] or careful analysis of the required catalyst amount [34].
- Substitution of noble metal catalysts with low-cost earth-abundant materials, e.g. nickel- or cobalt-based electrocatalysts [35].
- Discovery of novel membrane materials, such as fluorine-free hydrocarbons, to lower cost and reduce operational voltage to 1.8 V at 3.5 A cm^{-2} [36].
- Improvement of lifetime beyond 20000 h and reduction of degradation rate below 14 µV h^{-1} [18].
- Reduction or replacement of titanium as the primary material for current collectors and flow-plates.

- Reduction of the concentration overpotential at high current densities (beyond 2 A cm^{-2}).

1.3 Mass Transport Limitations in PEMWEs

A number of effects contribute to the PEMWE operational voltage, which should be as low as possible to minimise energy consumption. Among these contributions, the concentration (or mass transport) overpotential is the least known, well-defined, and understood. Even though the exact definition of the concentration overpotential varies slightly [37–39], it can be described as the portion of the overall PEMWE voltage which is caused by mass transport processes and the subsequent lack of reactants or product removal.

The analysis and diagnosis of the concentration overpotential is usually focussed on the anode, as the mass transport processes here are more complex than at the cathode. Water has to be transported through the liquid-gas diffusion layer (LGDL) towards the catalyst layer, where oxygen is produced and subsequently has to be removed from the LGDL into the flow channels. This concurrent flow of water and oxygen occurs in the pores of the LGDL, which are limited in size and number, with tortuous pathways, and often only connected by narrow throats. As the current density increases, the amount of water and oxygen to be transported scales accordingly, and it becomes increasingly challenging to ensure sufficient mass transport through the LGDL. Hence, the mass transport contribution to the overall PEMWE overpotential increases with current density.

However, other processes are believed to contribute to the concentration overpotential. The two-phase flow in the anode flow-field is widely believed to affect the PEMWE performance due to blockage effects or shearing of gas bubbles from the LGDL surface [40–45]. Further, cathode processes can contribute to the concentration overpotential; however, as water is not usually circulated through the cathode in commercial plants and the gas diffusion layer is much thinner than the LGDL at the anode, these effects are likely to be less significant.

1.4 Research Motivation

The goal of this thesis is to provide new insight and a suite of low-cost diagnostic tools for mass transport processes in PEMWEs, particularly enabling improved rates of water and gas transport at the anode of a PEMWE; hence improving efficiency at high current densities. The significance of mass transport processes to PEMWE operational voltage will be outlined in Section 2.3 and the relevant mass transport mechanisms and PEMWE components will be discussed in the Sections 3.2 and 3.3.

As the issues around climate change and the establishing of renewables as the default option for energy production become ever more pressing, PEMWEs are likely to be widely used for hydrogen production and grid stabilisation. This renewed interest in PEMWEs has caused the technology to mature and the attainable current density to increase. At high current densities, the mass transport overpotential increasingly contributes to the overall PEMWE voltage and power requirement, reducing the overall efficiency of hydrogen production.

As outlined above, the causes and mechanisms of the mass transport overpotential are not well understood, with significant questions remaining around the exact causes leading to an increase in overpotential and potential improvements to PEMWE design mitigating mass transport limitations.

This work aims at gaining insight into the mass transport processes in the anode LGDL and flow-fields and developing a set of novel diagnostic tools. Due to the high and selective attenuation of neutrons in water, neutron imaging will be used for measurements of the LGDL through-plane water thickness and analysed with a focus on mass transport processes. The neutron imaging data will be combined with X-ray micro-tomography of LGDL materials to gain an improved understanding of mass transport in the LGDL. These radiation-based imaging methods will form a benchmark for the low-cost acoustic diagnostic tools used in this work. Two different acoustic techniques, acoustic emission and acoustic time-of-flight imaging, will be used to investigate mass transport in the PEMWE flow channels and LGDL and the results validated against established techniques and calculations. These acoustic diagnostic techniques have not been previously applied to PEMWEs, and with one exception not to AWEs either [46]. By combining insights from this suite of techniques it is expected to develop an understanding of the effects in LGDL and flow channels contributing to the mass transport overpotential. Further, this work is expected to establish the aforementioned low-cost diagnostic techniques in the PEMWE field; hence, accelerating future work on mass transport limitations in PEMWEs and contributing to the development of new materials and novel engineering approaches to improve PEMWE performance. The relative advantages and disadvantages of the diagnostic techniques used in this work are summarized in Table 1. Lastly, the techniques described here may be applied to related electrochemical energy storage and conversion devices, such as redox flow batteries and PEM fuel cells, or unrelated fields (e.g. chemical plant monitoring).

Table 1: Comparison of the diagnostic techniques used in this work in terms of equipment cost, availability, achievable spatial and temporal resolution, and ease of using the equipment for experiments. Techniques are scored relative to each other (+++: scored best, ++: scored second best, +: scored third best) and in some cases absolute values are assigned to categories. However, it should be noted that all values are based on this work and are estimations.

	Radiation-based Imaging	Acoustic Emission	Acoustic Time-of-Flight Imaging
Cost	+	+++ (~ £5000)	++ (~£20000)
Availability	+	+++	++
Spatial Resolution	+++ (20 µm)	+	++ (0.94 mm)
Ease of Use	+	+++	++

1.5 Thesis Overview

This introduction will be followed by a short discussion of the fundamental aspects of PEMWE assembly and sources of voltage loss in a PEMWE, which are necessary to facilitate understanding of this work. PEMWE electrocatalysts and membrane materials are not within the scope of this thesis, but a short summary will be given on state-of-the-art materials.

Subsequently, the scientific literature on the PEMWE components most relevant to this work, the liquid-gas diffusion layer (LGDL) and the flow-fields, will be reviewed, and existing materials and designs will be discussed. A particular focus will be placed on mass transport aspects. The literature review will end with a discussion of the existing body of literature on PEMWE diagnostic tools – the most common techniques as well as the novel tools introduced in this work.

A detailed discussion of the experimental methodology employed in this work will begin with details on the operation and assembly of PEMWE cells. This will be followed by the scientific foundations of X-ray and neutron imaging, the elementary methodology of image analysis and tomographic reconstruction, and the underlying mechanisms of acoustic processes.

The main results section is separated into three main chapters: results on the influence of LGDL microstructure on the water-gas distribution in the LGDL obtained with neutron imaging, followed by diagnosis of the flow regime in the flow channels using acoustic emission, the use of acoustic time-of-flight imaging to monitor the flow regime in the flow channels, as well as the water-gas distribution in the LGDL. Each chapter will end with a conclusion, outlining the significance of the results and their implications on the optimisation of PEMWE design.

This thesis will be concluded by a summary of the presented work and a number of potential directions for future work, based on the results obtained. This includes novel engineering approaches mitigating the drawbacks of existing LGDLs, and the use of acoustic techniques in conjunction with radiation-based imaging techniques (e.g. neutron imaging).

2 *Fundamentals of PEMWE Operation*

2.1 Overview

This chapter will briefly review the fundamental knowledge necessary for understanding the following sections. The assembly of PEMWE cells from individual components will be introduced, followed by a discussion of voltage losses in a PEMWE, with a focus on the mass transport overpotential. Lastly, the electrocatalysts used at anode and cathode and the membrane material will be discussed briefly.

2.2 PEMWE Cell Assembly

Figure 3 shows the assembly of a typical PEMWE with the catalyst coated membrane (CCM), the liquid-gas diffusion layer (LGDL) at the anode, the gas diffusion layer (GDL) at the cathode, flow-fields, and end-plates. The end-plates are usually relatively thick (2 cm or more), which minimizes bowing of the end-plates and avoids breaking of brittle end-plate materials, such as acrylic. The flow-plates typically have a current collector tab, which allows for easy mounting of the power supply terminals. Gaskets (not displayed) are usually employed to keep LGDL, GDL, and CCM in place and to prevent leakage. The use of a CCM is the most commonly used approach, but it is possible to apply the catalysts to the surface of the LGDL/GDL and combine these with an uncoated ionomer membrane. This yields an equivalent sequence of functional layers and has been shown to produce comparable performance [47,48].

The single-cell PEMWE shown here is typically used for research work and is well-suited to demonstrate the basic processes and function of a PEMWE. However, for commercial applications PEMWE stacks are used, that combine multiple single cells into one unit [49], but are subject to the same processes discussed in this work.

The nomenclature used in this work for LGDL and GDL was chosen as it best describes the movement of water and gas in the respective components. However, a variety of terms are used across the scientific literature, with the anode LGDL often described as the porous transport layer (PTL) or, in analogy to PEM fuel cells, as the gas diffusion layer (GDL).

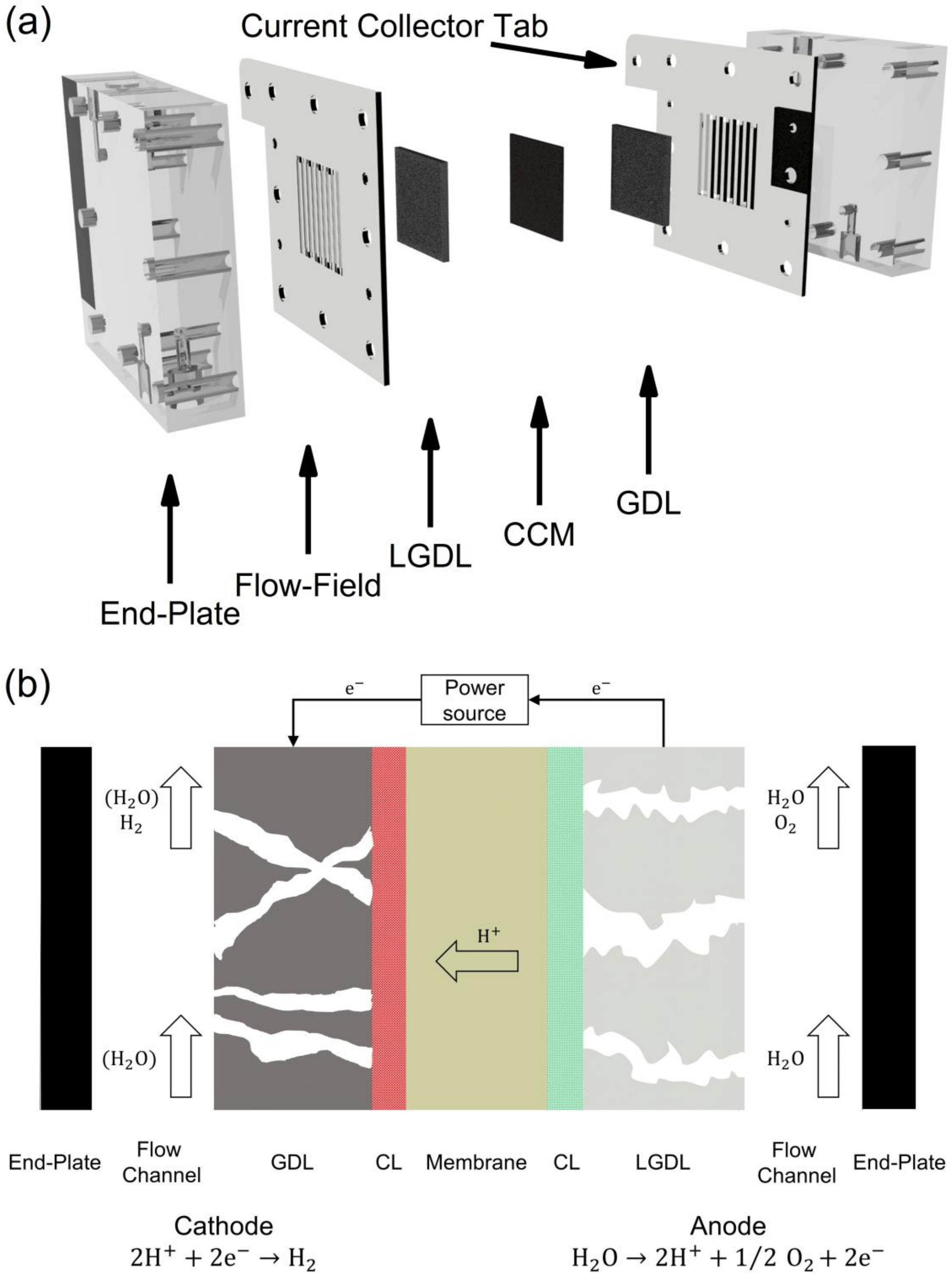

Figure 3: (a) The assembly of a single-cell PEMWE with end-plates, flow-fields, liquid-gas diffusion layer (LGDL), gas diffusion layer (GDL), and catalyst coated membrane (CCM). (b) Water reacts at the catalyst layer (CL) on the anode side. Oxygen is transported back to the flow channels through the LGDL, while protons migrate through the membrane and electrons through the outer circuit to the cathode side. These react at the cathode CL to form hydrogen. Water circulation at the cathode is not strictly necessary, but is often used to facilitate hydration (indicated by brackets).

Water enters the PEMWE through the end-plate on the anode side and is transported across the active area along the channels of the flow-field. The water then crosses through the porous LGDL towards the anode catalyst layer (CL), where it is oxidised to form protons, electrons and molecular oxygen. The protons are transported through the membrane to the cathode CL, where hydrogen is formed. However, the oxygen has to be transported from the anode CL, through the LGDL, back to the flow channels where it is carried out of the PEMWE cell with the unreacted water. While crossing the LGDL, the oxygen gas is in counter-current flow to the water traveling from the flow-field to the catalyst layer. Even though it is not strictly necessary for the operation of a PEMWE, water is often circulated through the cathode side as well to ensure sufficient hydration of the membrane, which reduces its ohmic resistance and facilitates proton transport through the membrane. The use of a solid electrolyte allows for a compact build with a minimum amount of liquid in the PEMWE cell. Nevertheless, the costs of a PEMWE stack still amount to a significant proportion of the overall system, with indicative reports quoting 37 % of the total costs of a plant [50]. Innovation in stack design and manufacture is reducing costs and improving durability and efficiency. For example, Chisholm et al. [31] 3D printed and silver-coated PEMWE flow plates from polypropylene. These flow plates were ~4 times lighter and 5 times cheaper than conventional plates from titanium and showed a voltage degradation rate of only 0.14 mV h^{-1} over 100 hours at 0.25 A cm^{-2}. Another approach to use additive manufacturing for PEMWE parts was taken by Yang et al. [51], who used selective laser melting to create a multifunctional plate incorporating LGDL, gasket, flow-plate and end-plate.

2.3 Sources of Voltage Loss in a PEMWE

The decomposition of water is driven by heat and electrical energy. The minimum electrical energy required for the decomposition of water is the reversible voltage $\mathrm{V}_{rev} = 1.23\ V$, while the thermoneutral voltage $\mathrm{V}_{tn} = 1.48\ V$ is required if no external heat is supplied [27].

V_{rev} is the minimum thermodynamic potential necessary to drive the water-splitting reaction at standard conditions. However, several other voltage contributions have to be accounted for, which constitute the operational voltage V [37,38,52].

$$\mathrm{V} = \mathrm{V}_{oc} + \mathrm{V}_{act} + \mathrm{V}_{ohm} + \mathrm{V}_{con} \qquad \text{(Equation 2-1)}$$

Here, V_{oc} is the open-circuit voltage, which depends on the reversible voltage V_{rev} and the activities a of reactants and products [38,52,53]:

$$\mathrm{V}_{oc} = \mathrm{V}_{\mathrm{rev}} + \frac{RT}{2F}\ln\left(\frac{a_{H2}\sqrt{a_{O2}}}{a_{H2O}}\right). \qquad \text{(Equation 2-2)}$$

T denotes the temperature, R is the universal gas constant, and F is the Faraday constant. The activity of liquid water is 1.

V_{act} is the activation overpotential, which is associated with the activation energy of the water electrolysis reactions and can be described by the Butler-Volmer equation. The equation given here is most commonly used in the literature [18,37,38,53–56]; however, the use of the Butler-Volmer equation for multi-electron reactions as occurring in PEMWEs has been questioned [57].

$$\mathrm{V}_{act} = \mathrm{V}_{act,an} + V_{act,cat} \qquad \text{(Equation 2-3)}$$

$$\mathrm{V}_{act} = \frac{RT}{\alpha_{an}F}\sinh^{-1}\left(\frac{i}{2i_{0,an}}\right) + \frac{RT}{\alpha_{cat}F}\sinh^{-1}\left(\frac{i}{2i_{0,cat}}\right) \qquad \text{(Equation 2-4)}$$

Anode and cathode contributions are denoted by an and cat, respectively. Typical values for the charge transfer coefficients are $\alpha_{an} = 2$ and $\alpha_{cat} = 0.5$ [18]. The exchange current density is denoted by i_0. The current density i is the current I normalized by the geometric active area A of the PEMWE.

The exchange current density is calculated from the activation energy E_A at the respective electrode and a reference value $i_{0,ref}$ which is obtained from literature or fitting experimental polarisation data [58]:

$$i_0 = i_{0,ref} exp\left(-\frac{E_A}{R}\left(\frac{1}{T} - \frac{1}{T_{ref}}\right)\right) \qquad \text{(Equation 2-5)}$$

The activation overpotential represents the kinetic characteristics of the electrode processes, and as such can be significantly influenced by electrode and catalyst microstructure and morphology. A more detailed discussion of electrode kinetics and the use of the Butler-Volmer equation for water electrolysis can be found elsewhere [57].

The ohmic overpotential V_{ohm} is caused by the ohmic resistance R of the different parts of the PEMWE, which consists of flow-plates, fp, liquid-gas diffusion layers, $lgdl$ and the catalyst coated membrane, ccm [38,39,52]:

$$V_{ohm} = RI = \left(R_{fp} + R_{lgdl} + R_{ccm}\right)I \ . \qquad \text{(Equation 2-6)}$$

The ohmic resistances above contain a portion that is attributed to the contact resistance between the respective part and the adjacent PEMWE component. This contact resistance can contribute significantly to the overall PEMWE overpotential [51] and is typically calculated from electrochemical impedance spectroscopy results [59]. Further, if the ohmic overpotential of a PEMWE stack is calculated, the ohmic resistance of the bipolar plates has to be accounted for.

The concentration overpotential V_{con} is caused by limitations in the supply of reactant or the blockage of active catalyst sites by an excess of product. This occurs in particular at high current densities when high flow rates of water are required, and large amounts of oxygen and hydrogen are produced. From the inlet, water is transported through the flow channels and has to cross the porous LGDL to reach the active catalyst sites on the surface of the membrane. Simultaneously, the product gas is produced at the CCM and needs to move through the LGDL in counter-current flow to the water. As the mass flow through the LGDL is increasingly inhibited by the increasing amount of water and gas, additional energy is required to overcome this resistance. To provide this excess energy, an increased voltage has to be supplied to the PEMWE, which is the concentration overpotential.

The concentration overpotential is modelled as a logarithmic increase for product (O_2, H_2) concentrations at the membrane me exceeding the concentrations at a reference state 0. This definition was introduced for PEMWEs by Marangio et al. [37] and has been followed by the vast majority of publications [38,39,52,53,55,60,61].

$$V_{con} = V_{con,an} + V_{con,cat} \qquad \text{(Equation 2-7)}$$

$$V_{con} = \frac{RT}{4F}\ln\left(\frac{c_{O2,me}}{c_{O2,me,0}}\right) + \frac{RT}{2F}\ln\left(\frac{c_{H2,me}}{c_{H2,me,0}}\right) \qquad \text{(Equation 2-8)}$$

The concentration c of the species at the membrane me depends not only on the gas generation rate, but also the rate of mass transport through the LGDL and flow channels. The polarisation curve of a PEMWE, which is the sum of the contributions described above, is shown in Figure 4 (a) for different temperatures, while a theoretical *i-V* curve with a rapid voltage runaway due to the concentration overpotential is displayed in Figure 4 (b). The polarisation curve is typically divided into three regimes dominated by different effects: activation energy, ohmic resistance, and mass transport. The first regime is observed at the onset of electrochemical activity and low current densities during which the PEMWE voltage is dominated by the requirement to provide the activation energy of the chemical reactions. At higher current densities, the relationship between current density and voltage is linear and the overall PEMWE voltage is mainly constituted by the ohmic response of the PEMWE. If the current density is increased further, mass transport processes are increasingly dominating the overall PEMWE voltage and a deviation from the linear, ohmic response is observed.

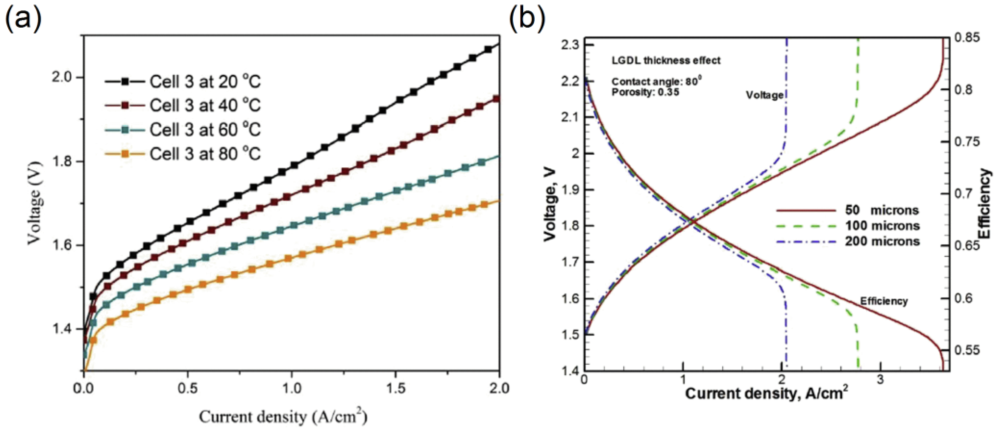

Figure 4: (a) Polarisation curve of a PEMWE at different temperatures [62] *(Reprinted from 'J Power Sources, 396, Yang et al., Bipolar plate development with additive manufacturing and protective coating for durable and high-efficiency hydrogen production, 590–8, 2018', with permission from Elsevier). (b) Theoretical polarisation curve, predicting rapid voltage increase due to the concentration overvoltage* [52] *(Reprinted from 'Int J Hydrogen Energy, 42, Han et al., Modeling of two-phase transport in proton exchange membrane electrolyzer cells for hydrogen energy, 4478–89, 2017', with permission from Elsevier).*

2.4 PEMWE Catalysts and Membrane

2.4.1 Electrocatalysts

This section will briefly discuss the most commonly used electrocatalysts used for PEMWEs, as well as some recently proposed alternatives. An in-depth discussion or review of PEMWE electrocatalysts is not within the scope of this thesis.

At the anode, water reacts in the oxygen evolution reaction (OER) to form oxygen and protons (see Figure 3). Iridium oxide is the most commonly used electrocatalyst for this reaction, with high activity and good corrosion resistance. Ruthenium oxide has an even higher activity towards the OER but suffers from significant corrosion, which makes the sole use of it an unviable option. Therefore, iridium/ruthenium oxides are often used at the PEMWE anode, combining high activity and corrosion resistance [18]. There is vast literature on potential alternative OER catalyst configurations and morphologies, aiming at reducing catalyst loading and increasing surface area [63].

After being produced in the OER, protons migrate to the cathode where they react in the hydrogen evolution reaction (HER). The development of HER electrocatalysts has mainly been driven through advances in PEM fuel cells, with platinum black or platinum supported on carbon black being the state-of-the-art electrocatalysts.

The need for platinum and iridium is a major drawback of PEMWEs. Not only are these elements scarce and expensive, with the CCM accounting for 36 % of the total PEMWE stack cost [50], but especially iridium is mined in a small number of locations, making security of supply a concern. Furthermore, iridium is being used for LEDs (for TVs and monitors), and widespread uptake of PEMWEs would therefore probably lead to increasing catalyst prices [18].

2.4.2 Membrane and Ionomer

Anode and cathode catalyst are typically coated onto a proton-conducting membrane to form the CCM, with Nafion being the state-of-the-art membrane material. It is a perfluorosulfonated copolymer with a tetrafluoroethylene backbone and perfluoroalkyl ether side chains, which are terminated in sulfonic acid groups (Figure 5), and is commonly deployed in thicknesses of 0.007 inch (~0.18 mm, Nafion 117) or 0.005 inch (~0.13 mm, Nafion 115) [64].

Nafion is also commonly mixed into the catalyst layers as an ionomer, which enhances proton conductivity from the catalyst layer to the membrane and provides a support structure for the catalysts, hence acting as a binder. The ionomer loading typically ranges between 20 wt% and 30 wt% of the catalyst [18].

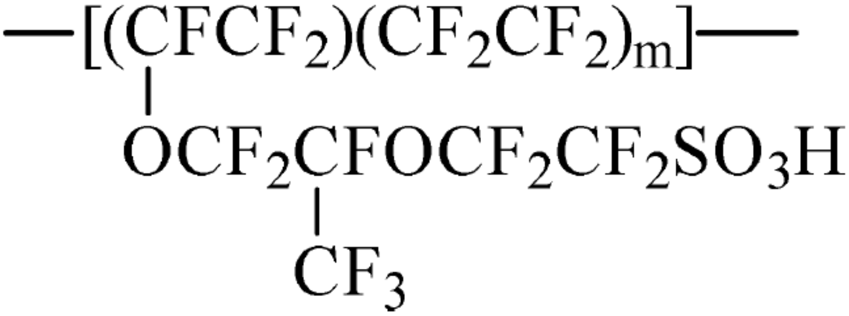

Figure 5: Chemical structure of Nafion, consisting of a tetrafluoroethylene backbone and side chains carrying a sulfonic acid group [64]*. (Reprinted with permission from Mauritz KA, Moore RB. Chem Rev. 104:4535–85. Copyright (2004) American Chemical Society.)*

3 Literature Review

3.1 Overview

This chapter will review and discuss the scientific literature relevant to mass transport in PEMWEs. The review will begin with an outline of the mass flux in PEMWE flow-fields, the different flow regimes found, and the design of flow-field geometries. This will be followed by a discussion of typical LGDL materials; their structure, properties, as well as use in PEMWEs. The review will end with a summary of the diagnostic techniques used to investigate mass transport aspects in PEMWEs. The work in this chapter has been submitted to the *International Journal of Hydrogen Energy*.

3.2 Mass Transport in the Flow Channels

Flow-fields provide a geometrical structure which allows for the ingress of water and the egress of product gas from the PEMWE. While water supply is only necessary on the anode side, flow-fields are also often used on the cathode side to facilitate the removal of hydrogen and excess water. The following discussion focuses on the processes on the anode side; however, many aspects apply to the cathode as well.

3.2.1 Flow Regime

Depending on the amount of oxygen produced, the flow regime can vary from single-phase flow (no oxygen production) to several different forms of two-phase flow. As current density increases a range of flow regimes can be observed, with varying descriptions used in the literature. It is not uncommon to find identical flow regimes being described by different terms or identical terms describing slightly different flow regimes. In this chapter, the classification of flow regimes according to Mishima et al. [65] is used throughout.

Figure 6 describes the development of flow regimes with increasing gas-to-water ratio. With the onset of electrochemical activity and related gas production, the flow regime changes from single-phase water flow to bubbly flow. As more gas is produced, bubbles coalesce to form plugs then slugs, filling the entire diameter of the tube or channel. In churn flow, slug bubbles are deformed and no longer display a spherical shape. The liquid between gas slugs is increasingly filled with small gas bubbles. As flow transitions into annular, the remaining water forms a film along the channel wall, while the rest of the channel is almost exclusively filled with gas. A further increased gas flow disperses the liquid film along the wall. Hence, the whole channel is filled with a gas-liquid dispersion; this is classified as annular-mist flow [65].

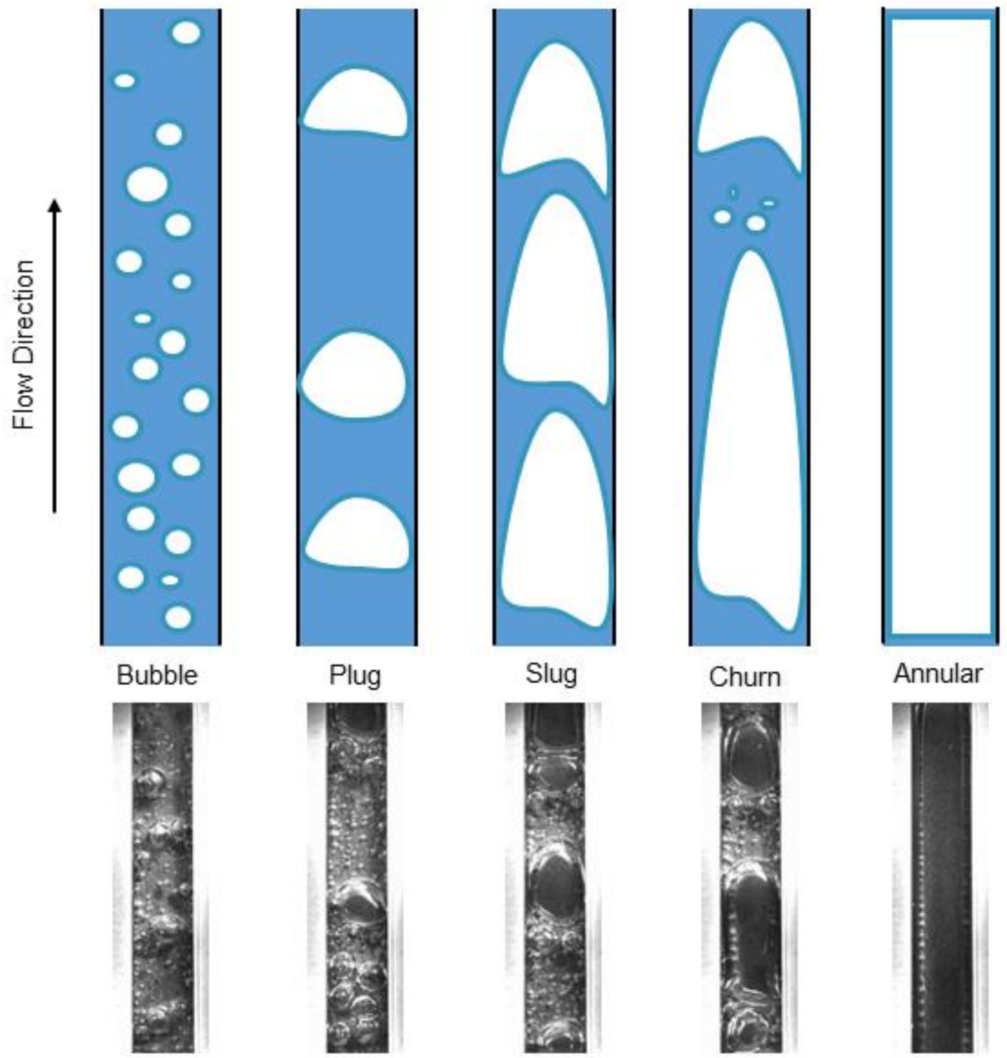

Figure 6: With increasing current density, more gas is produced and has to be removed through the flow channels. The flow regime progresses from bubble to plug, slug, churn and annular regime.

3.2.2 Mass Flux

To link the electrochemical activity of a PEMWE to the flow regime in its flow channels, a flow map can be developed. This requires knowledge of the rate of water consumption and oxygen gas generation; the necessary equations are presented in the following normalised to the cross-sectional area of individual flow channels. Water is consumed by the oxygen evolution reaction (OER) on the anode side at a given rate by [40]:

$$G_{cons} = \frac{iAM_{H2O}}{2Fn_{chan}a}. \qquad \text{(Equation 3-1)}$$

Here, i is the current density, A is the active area of the electrolyser, M_{H2O} is the molecular mass of water, F is the Faraday constant, n_{chan} is the number of flow channels and a is the cross-sectional area of a flow channel.

At the same time, water is removed from the anode side of the PEMWE due to electro-osmotic drag. This is caused by protons moving from anode to cathode through the polymer membrane. The rate of water removal by this process is defined by [40]:

$$G_{drag} = n_{drag} \frac{iAM_{H2O}}{Fn_{chan}a}. \qquad \text{(Equation 3-2)}$$

The number of water molecules transported through the membrane per proton is defined by the temperature-dependent electro-osmotic drag coefficient n_{drag}. Commonly, an empirical approximation by Onda et al. is used in PEMWE literature [66]:

$$n_{drag} = 0.0134\,T + 0.03\,. \qquad \text{(Equation 3-3)}$$

The rate of oxygen production is calculated as [40]:

$$G_{O2} = \frac{iAM_{O2}}{4Fn_{chan}a}, \qquad \text{(Equation 3-4)}$$

where M_{O2} is the molecular mass of oxygen.

The gravimetric gas fraction x can be calculated from the above mass fluxes and the total rate of water circulation into the anode side of the PEMWE G_{circ}. It is the ratio of gas generation rate (G_{O2}) to the total mass flux in the channel, which is the sum of the water mass flux ($G_{circ} - G_{cons} - G_{drag}$) and gas generation rate [40].

$$x = \frac{G_{O2}}{G_{circ} - G_{cons} - G_{drag} + G_{O2}} \qquad \text{(Equation 3-5)}$$

It should be noted that x is dependent on the location along the flow channel. To calculate x for a position before the outlet, the active area A has to be reduced accordingly so that only the fraction of the active area is used which is located upstream of the location to be investigated.

Another metric to characterise the flow in the PEMWE is the water ratio ζ, which is defined as the ratio of the rate of water circulation to the rate of water removal by the combination of the OER and electro-osmotic drag [40,42].

$$\zeta = \frac{G_{circ}}{G_{cons} + G_{drag}} \qquad \text{(Equation 3-6)}$$

Theoretically, a value of ζ=1 is sufficient for electrolysis. However, in practice, a higher value is required to ensure sufficient water supply and cooling. Minimum, safe values for the water ratio found in the literature range from ζ=3 [42] to ζ=5 [40]. A comparison of water flux and gas generation and the gas fraction at the outlet as a function of current density is shown in Figure 7 (a) and for the water ratio in Figure 7 (b).

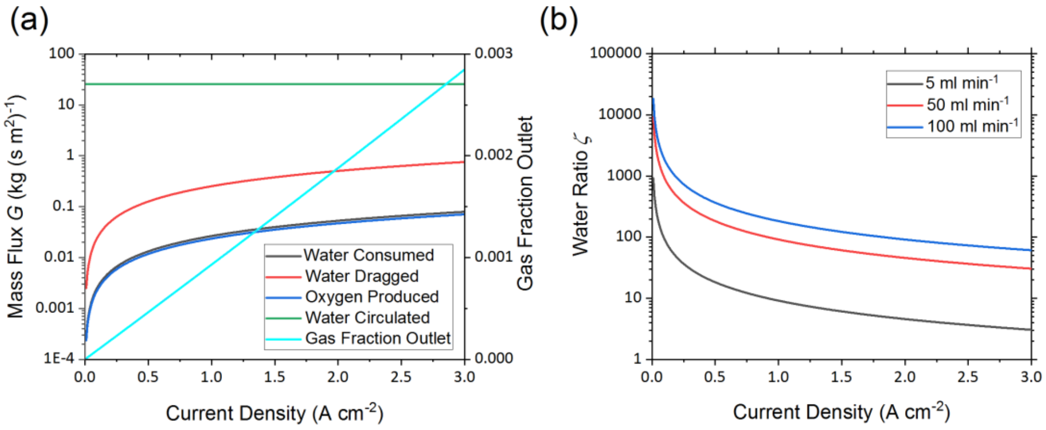

Figure 7: (a) Comparison of the mass fluxes of water with the oxygen generation in the range from 0 A cm^{-2} to 3 A cm^{-2} at a water circulation rate of 50 ml min^{-1} and a temperature of 90 °C, in a parallel flow-field with 9 channels (Width: 1.76 mm, Depth: 2.00 mm). The gravimetric gas fraction at the outlet increases linearly with current density. (b) Water ratio as a function of current density at the same conditions, for water circulation rates of 5 ml min^{-1}, 50 ml min^{-1}, and 100 ml min^{-1}.

The flow velocity of liquid j_l and gas j_g can be calculated as a function of the gas fraction [40].

$$j_l = \frac{G(1-x)}{\rho_{H2O}} = \frac{(G_l+G_g)(1-x)}{\rho_{H2O}} \qquad \text{(Equation 3-7)}$$

$$j_g = \frac{Gx}{\rho_{O2}} \qquad \text{(Equation 3-8)}$$

$$G = G_l + G_g = G_{circ} - G_{cons} - G_{drag} + G_{O2} \qquad \text{(Equation 3-9)}$$

Here, the total flow through the flow channels G consists of the total liquid flow G_l and gas flow G_g. The flow velocities of gas and liquid can be used to compare the state of operation of a PEMWE with known flow maps to define the flow regime in the flow channels. For comparison of operational states a flow map, which was observed in a system as similar as possible (materials and geometry) to the flow channels of the PEMWE, has to be chosen. Two flow maps commonly used for research relating to PEMWEs are shown in Figure 8. However, it should be noted that these flow maps were produced from experiments observing two-phase flow with gas being injected into the water flow upstream from the observation point. Therefore, a key difference to the two-phase flow in a PEMWE is the additional gas production along the length of the flow channels which changes the water-gas ratio.

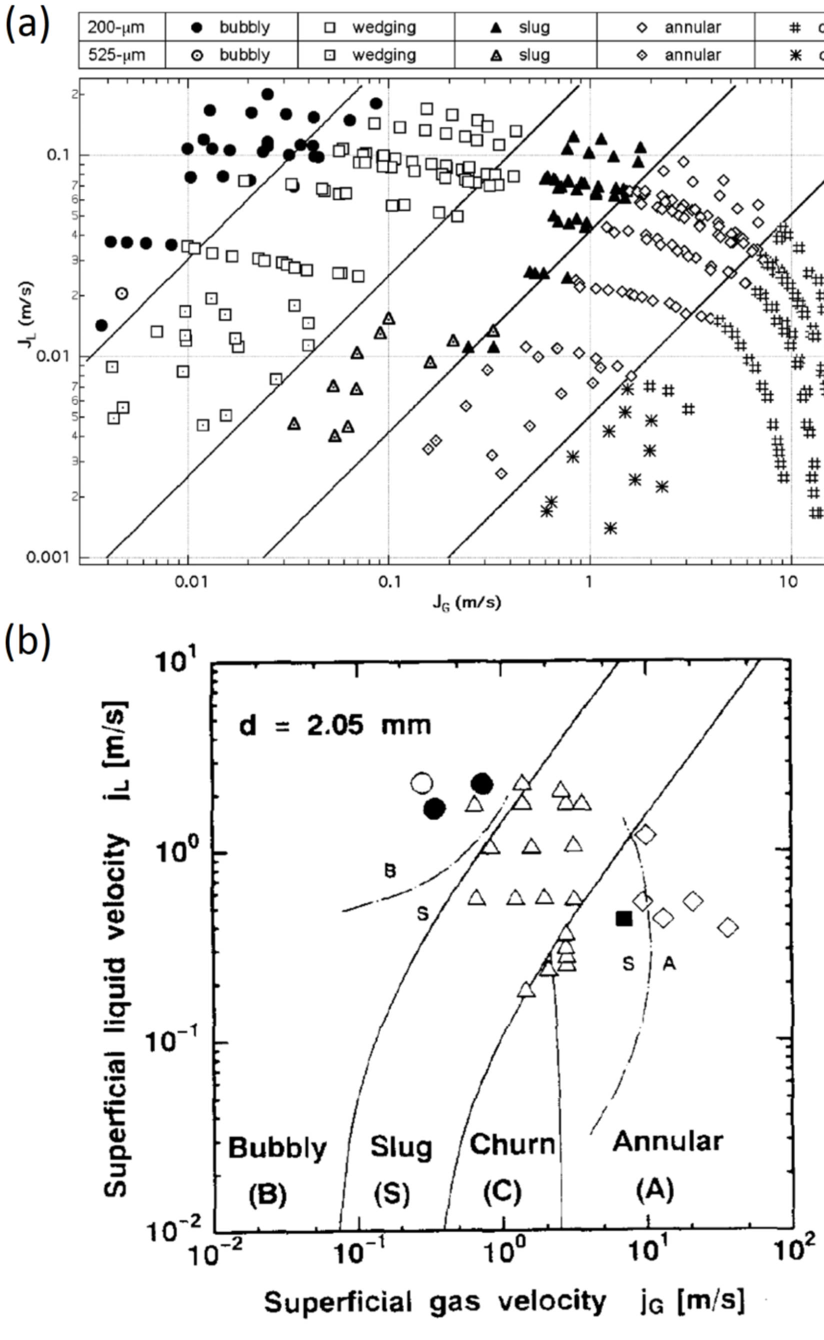

Figure 8: The flow maps of (a) Cubaud et al. [67] *(Reprinted from 'Cubaud et al., Transport of bubbles in square microchannels. Phys Fluids 2004;16:4575–85.', with the permission of AIP Publishing.) and (b) Mishima et al.* [65] *(Reprinted from 'Int J Multiph Flow, 22, Mishima et al., Some characteristics of air-water two-phase flow in small diameter vertical tubes, 703–12', with permission from Elsevier), defining the occurrence of various flow regimes as a function of the velocity of the liquid and gas phase in the flow channels. The shape and location of the regime borders vary depending on the exact shape and size of the channels of the experimental systems used to create the flow map.*

3.2.3 Flow-Field Design and Diagnostics

The design of the flow-field affects pressure drop, gas and water flow velocities, gas removal, and the flow regime. Most commonly described in the literature are parallel, single-serpentine, and multiple-serpentine flow-fields. Each design varies in the amount of water and gas that is transported through an individual channel (Figure 9). Other flow-field geometries, such as interdigitated [68–70] or pin-type [51,71] flow-fields, exist but are not very commonly used. Further, other alternatives are possible, such as the use of metal meshes as flow-fields, which are used in proprietary commercial PEMWE systems.

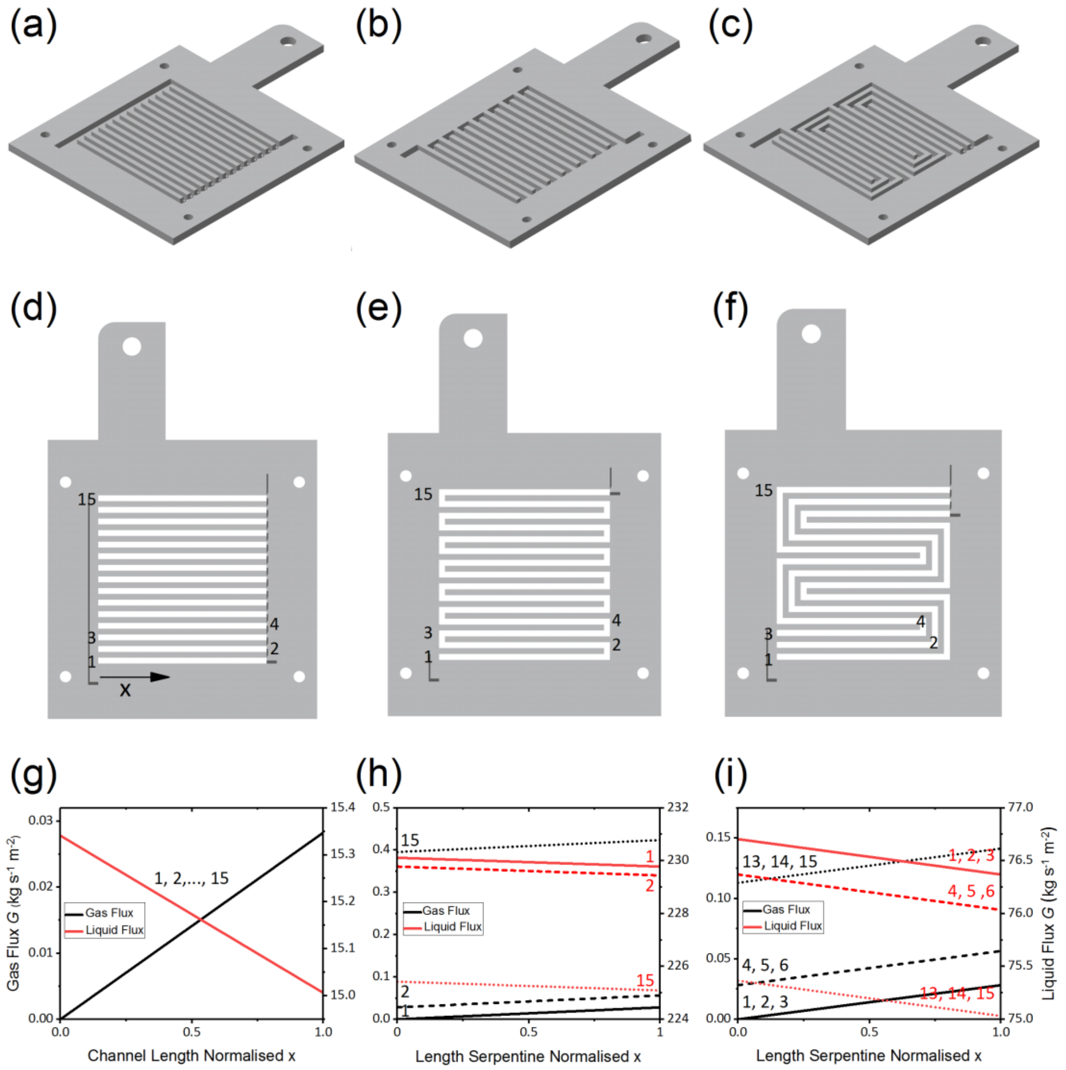

Figure 9: Perspective (a-c) and top-down (d-f) view of a parallel (a,d,g), single-serpentine (b,e,h), and triple-serpentine (c,f,i) flow-field. The gas and liquid amount in each channel along its length (g-i) varies depending on the flow-field geometry. The channel number is indicated in (d-f) and used accordingly in (g-i). The axis titles on the left and right of (g-i) apply to all three figures.

In parallel flow-fields (Figure 9 (a),(d),(g)), the flow is separated into a number of separate channels, which are connected by a dividing and a combining manifold. Ideally, the amount of water and gas passing through an individual channel is the corresponding fraction of the total amount of water and gas with respect to the total number of channels, however, a non-uniform distribution of flow occurs [72]. For a single-serpentine flow-field (Figure 9 (b),(e),(h)), all of the water and gas has to pass through one channel, thus causing much higher flow velocities than in a parallel flow-field. Hence, the pressure drop in a single-serpentine flow-field is significantly higher than for a parallel flow-field [40].

There is conflicting information on the performance of these flow-fields. Ito et al. [40] showed improved performance of a PEMWE (active area: 5.2 × 5.2 cm) with a parallel flow-field up to 1 A cm^{-2}. They assigned this difference in performance to an increased concentration overpotential in the single-serpentine flow-field. However, it is unlikely that this effect is notable at current densities as low as 1 A cm^{-2}. Majasan et al. [73] also found improved performance for the parallel flow-field for current densities of up to 3 A cm^{-2}, whereas, Li et al. [74] showed superior performance of a single-serpentine flow-field. In this study, the parallel flow-field was also shown to have the highest ohmic resistance, which partly explains the decreased performance. This raises the question if the dominant factors influencing the electrochemical performance of different flow-fields are flow effects or simply the ohmic resistance of the flow-plate. In the latter case, further work is necessary to optimise flow-field geometry by minimising ohmic resistance (channel-to-land ratio) while ensuring a sufficiently low pressure drop.

Multiple-serpentine flow-fields (Figure 9 (c),(f),(i)) share characteristics of the parallel as well as the single-serpentine flow-field. Their electrochemical performance and pressure drop were found to be intermediate to those of parallel and single-serpentine flow-fields [40].

All flow-fields shown in Figure 9 are of the Z-type, with the inlet and outlet being located at diagonally opposed sides of the active area (bottom left and top right). Alternatively, flow-fields can be designed in a U-shape, which would require the inlet and outlet being located at the same side of the active area (e.g. bottom left and top left). The location of inlet and outlet has been shown to have a significant impact on the distribution of water flow between individual channels of a flow-field [72,75,76].

There is very little published research examining possibilities to optimise flow-fields beyond the differentiation of parallel, single and multiple-serpentine designs. Majasan et al. showed that the performance of a PEMWE is affected by the depth of the flow channels and demonstrated a varying degree of mass transport limitation with flow channel depth at different current densities. A non-monotonic trend was found, implying the possibility of optimising the flow-field design [77].

A multitude of approaches have been deployed to image and diagnose the processes in the flow channels of PEMWEs. Most publications use either optical, X-ray or neutron imaging to visualize bubble and water flow. Optical imaging is comparatively low-cost and easy to implement, which makes it a preferred tool for flow-field diagnosis [33,43,44,78–82]. X-ray and neutron imaging, on the other hand, are expensive, require large-scale facilities, and often the PEMWE cell needs to be adapted or miniaturized to facilitate measurement. However, these techniques offer quantitative capabilities and the possibility of analysing the processes in the flow-field, LGDL and catalyst layer simultaneously, which explains the attraction of X-ray [83,84] and neutron imaging [85–90] techniques for the study of PEMWEs. X-ray imaging usually offers a higher flux and therefore shorter acquisition times, while the preferential attenuation of neutrons in hydrogen and water makes neutron imaging an especially valuable diagnostic tool by enhancing the contrast of these molecules compared to other materials [91].

3.2.4 Influence of the Flow Regime on Performance

There are essentially two opposing model concepts on how the flow regime can affect the overall performance of a PEMWE. The first idea assumes that the formation of gas slugs in the flow channel hinders the supply of water to the LGDL, and consequentially to the catalyst sites. This would then decrease overall performance by amplifying the concentration overpotential [41]. The second concept assumes that the bubbles in the flow channel cause turbulence which leads other bubbles in the vicinity to detach from the LGDL surface. This effect gets stronger when the size of bubbles in the flow channel increases. Hence, bubbles are effectively removed from the LGDL surface, which accelerates gas removal from the catalyst sites and through the LGDL. This would cause a decrease in concentration overpotential [44].

Ito et al. [40] measured the performance of a PEMWE, comparing three different flow-field designs: parallel, single-serpentine, and dual-serpentine. As shown in Section 3.2.3, the water flow speed, water-to-gas ratio, and flow regime vary widely between these designs even at identical operating conditions. In particular, flow-fields with fewer flow channels (serpentine) favour the development of flow regimes with a low water-to-gas ratio (slug, annular), while flow-fields with multiple channels (parallel) favour flow regimes with a higher water-to-gas ratio, such as bubbly flow. As the authors observed a decrease in performance from the parallel to single-serpentine and then dual-serpentine flow-field, they concluded that performance deteriorates for flow regimes with a lower water-to-gas ratio than bubbly flow [40].

In later work, Ito et al. [41] examined the occurrence and pressure drop of different flow regimes and the link between the mean pore diameter of the LGDL and the development of the flow regime. Their theoretical considerations and experimental data imply that an LGDL with bigger pores results in a larger bubble detachment diameter and hence plug and slug flow are reached at lower current densities compared to an LGDL with smaller pores. This leads to vast areas of the liquid-gas diffusion layer being covered by gas bubbles, which they postulated had a negative effect on performance. In subsequent work, the authors [92] measured the cell resistance and overall performance using titanium felts of different pore size as LGDLs. An increase in cell resistance with increasing pore size was found, which is attributed to an increase in bubble detachment radius.

Sun et al. [42] performed current mapping and localised electrochemical impedance spectroscopy (EIS) on a PEMWE under water starvation and showed that in the case of water starvation, performance decreases under slug and churn flow compared to the bubble regime. Similar observations of the decrease of local current density towards the end of the channel (where slug and churn flow preferably occur) under water starvation have been made by Immerz et al. [93,94]. However, both authors compared subsequent locations along the flow in a PEMWE and not a whole cell under different regimes. Therefore, it is uncertain if these results can show the influence of the flow regime properly, as flow regime and water starvation effects occur at the same time.

Using EIS and high-speed imaging, Dedigama et al. [43] came to a contrary conclusion; their results showed an improvement in mass transport which is associated with the transition from bubble to slug flow. Further, Dedigama et al. [44] mapped the current density at different locations along a single-channel PEMWE and found an increase in performance towards the top end of the channel and showed that slug flow is the dominant flow regime at this location. This supported the earlier finding that performance is enhanced in slug flow. However, it has been proposed that this might be caused by an increase in temperature along the flow channel [95]. Further, the increase in mass transfer inhibition observed at higher water flow rates (in bubble flow) can be seen as a consequence of the increased kinetic energy of water flow in the flow channel, which hinders the detachment of gas bubbles from the LGDL surface into the flow channel [45]. In that case, the performance effect would be unrelated to the flow regime in the flow channels.

There is a lack of consensus and understanding of the exact relationship between PEMWE performance and the flow regime. Further, to date, no coherent model of the processes underlying potential performance changes due to a specific flow regime has been developed and backed by conclusive experimental data.

3.2.5 Two-Phase Modelling

Modelling of the two-phase flow offers the opportunity to predict the effects of changes to geometry or physical parameters in a low-cost and rapid way. Only a few publications have provided comprehensive 3D models incorporating two-phase flow, specifically aiming at PEMWEs [68,70,96,97]. Lafmejani et al. [70] published a 3D volume-of-fluid model and qualitatively confirmed their results with optical imaging of the flow in an interdigitated flow-field. Olesen et al. [68,69] presented a full-scale, mathematical 3D model of a PEMWE, incorporating compressible two-phase flow as well as heat and charge transfer in the catalyst layer, micro-porous layer, LGDL and the flow channels. The authors used this model to predict the state of operation of a PEMWE for current densities up to 5 A cm^{-2}. For these elevated currents they found heterogeneity in the current density distribution of up to 1.5 A cm^{-2} and in the temperature distribution of up to 20 K. Further, they showed that changing the design of an interdigitated flow-field design can lead to significant variations in local temperature, which can accelerate catalyst degradation, while the overall cell performance with these flow-fields did not differ.

The work described above mathematically incorporated the two-phase flow in the LGDL without explicitly describing the movement of gas and water. Resolving the exact transport pathways of gas bubbles through the LGDL allows to study the effects of LGDL microstructure on mass transport, but it is challenging to link this to the overall PEMWE performance [98].

Other approaches to PEMWE flow modelling are limited to one-phase flow [56,72,99]. Nie et al. [72] simulated one-phase flow through a parallel flow-field with a Z-pattern. In this type of flow-field, the water inlet is positioned diagonally opposite the water outlet and it is commonly used in PEMWEs. The authors showed that for this type of flow-field the water flow velocity is very unevenly distributed between the single flow channels. The Z-shape favours flow through the flow channels closest to the outlet which causes the water flow velocity to be up to five times higher than in the middle channels. Further, the authors found a corresponding non-uniform pressure distribution, with the pressure roughly decreasing diagonally from inlet to outlet.

Toghyani et al. used single-phase flow modelling to address the optimization of standard flow-fields and the development of novel flow-field designs. The authors showed that serpentine flow-fields with a varying number of flow channels caused an improved electrochemical performance and lower temperatures compared with a parallel flow-field [56]. They also explored the use of metal foam as a flow-field material and concluded that the electrochemical performance of a PEMWE could be improved by this [100], and modelled the flow through a novel, spiral flow-field geometry [101].

3.3 Mass Transport in the Liquid-Gas Diffusion Layer

Fluid flow through a porous medium, such as the LGDL, is a highly complex process that is affected by the microstructure of the porous medium, interfacial interactions between fluid and walls, interactions between different fluids, and bulk properties of the fluids. This makes it challenging to analytically describe multi-fluid flow in porous media and numerous equations have been developed, each describing specific situations and introducing additional parameters to achieve improved precision. However, the most fundamental equation for fluid flow in porous media is Darcy's law, which links the fluid velocity j to its pressure gradient across a control volume $\frac{\partial p}{\partial x}$ [102]. It is commonly used in computational work on PEMWEs [52,69,70,103,104].

$$j = -\frac{K}{\eta}\frac{\partial p}{\partial x} \qquad \text{(Equation 3-10)}$$

Darcy's law takes into account the permeability of the porous media for the fluid K and the viscosity of the fluid η. The permeability can be calculated from various equations, as well as empirical correlations [69,70], but the Kozeny-Carman equation is the best-known approach. It links the macroscopic permeability with the microscopic parameters of the porous medium porosity ε, tortuosity τ, and the surface area per unit volume a_V, but various modifications and extensions have been discussed [102].

$$\sqrt{\frac{K}{\varepsilon}} = \left(a_V\sqrt{2\tau}\right)^{-1}\left(\frac{\varepsilon}{1-\varepsilon}\right) \qquad \text{(Equation 3-11)}$$

3.3.1 Liquid-Gas Diffusion Layer Materials

The liquid-gas diffusion layer serves a multitude of purposes; it is expected to provide good thermal and electrical conductivity, low interfacial losses and mechanical strength and support for the flexible CCM, especially under differential pressure operation. Furthermore, the LGDL needs to withstand the corrosive environment on the anode side during long-term operation. This requirement makes titanium the most commonly used material for the LGDL on the anode side. However, recent work by Becker et al. [105] has shown that, away from the catalyst layer/LGDL interface, the corrosion potential at the surface of the anode LGDL is decoupled from that of the catalyst layer due to the low conductivity of the water phase. This opens up the possibility to use cheaper LGDL materials such as carbon and carbon-coated stainless steel, which are also easier to manufacture into porous structures than titanium.

Another crucial purpose of the liquid-gas diffusion layer is to facilitate the two-phase counter-current flux of gas towards the flow channels and water towards the CCM. Hence, the microstructure of the LGDL needs to be optimized with respect to the trade-off between mass and electron transport, with mechanical stability, thermal conductivity and good interfacial contact as further constraints [18,78,106]. Especially the interface between LGDL and catalyst layer appears to have a strong influence on charge and mass transfer resistance [107–109].

Porous titanium sintered or fibrous materials have been most commonly used as LGDLs. In some cases, titanium meshes have been used as the LGDL, while recently the use of thin, perforated plates has been proposed as a beneficial alternative to more established materials. Another potential material that has been adopted as porous transport medium in PEM fuel cells (PEMFCs) are metal foams. SEM images and X-ray tomograms of these materials are shown in Figure 10, visualizing the surface and microstructure of the LGDL materials.

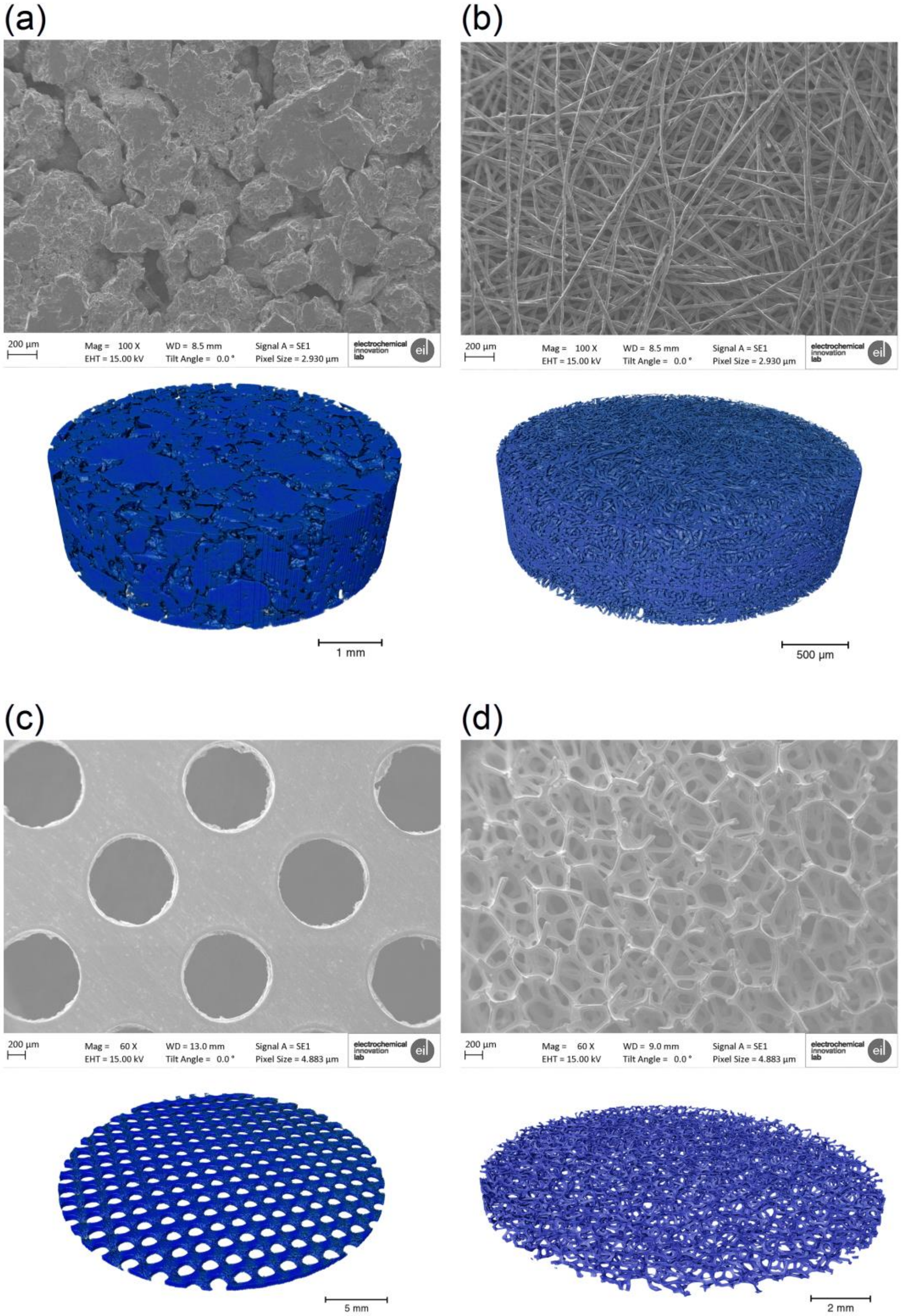

Figure 10: SEM images and X-ray tomograms of various materials that can be used as an LGDL in PEMWEs. (a) Sintered powder and (b) fibrous materials are commonly employed, while (c) perforated plates are very useful for optical access to the catalyst surface, and (d) metal foams have shown promise in unitized reversible fuel cells.

Porous titanium sinters (Figure 10 (a)) have been widely used as an LGDL, e.g. in the

PEMWE stacks developed for the GenHyPEM project [110–113]. Grigoriev et al. [114] have published a study that theoretically and experimentally examines the influence of different sinter properties on PEMWE performance. They concluded that 50 µm to 75 µm is the optimal titanium powder particle size, resulting in an LGDL pore mean diameter of 12 µm to 13 µm after sintering, which has recently been confirmed [115]. Other conclusions are that pore size and electrical resistance have a big influence on the performance of the LGDL, while porosity and gas permeability appear to be insignificant. However, this applies only to the sintered powder LGDLs investigated in this work, with porosity between 30 % and 50 % [114].

In recent years, titanium fibrous materials (Figure 10 (b)) have emerged as a potential alternative to sintered LGDL materials. These felts have very high porosities of more than 70 %, which is significantly higher than for a typical sinter. Ito et al. have tested the performance of a PEMWE using various felts, varying pore sizes and porosities. They showed that performance increases with decreasing pore size for pores above 10 µm, which is assigned to the mass transfer inhibitions related to larger gas bubbles. Furthermore, the results indicate that within the range of examined materials the porosity does not seem to affect the performance [41,92].

Another recent development is the use of perforated plates or foils (Figure 10 (c)) as LGDLs. The manufacturing of perforated titanium foils by mask-patterned wet etching methods and their potential application as LGDL was first described by Mo et al. [116]. A titanium foil is covered with photoresist and the pattern of pores is then developed using a photomask manufactured by soft lithography. Subsequently, the pores are etched into the foil with hydrofluoric acid. After removing the remaining photoresist, a pristine LGDL with regular, straight pores and easily tuneable features is obtained [106]. These thin, novel LGDLs have been shown to exhibit significantly superior performance compared to titanium felt, which is caused by the increased interfacial contact between LGDL, flow-field, and CCM, as well as the reduced thickness of the perforated foil compared to conventional LGDLs [117]. In a later study, Kang et al. [118] manufactured gold-coated, perforated titanium foils and demonstrated a reduced operating voltage at high current densities and stability of the gold coating for 100 hours.

A rarely applied alternative for LGDLs are titanium meshes, as demonstrated by Li et al. [119]. Steen et al. [120] tested various meshes, but even the mesh with optimum parameters performed significantly worse than titanium felt. Titanium meshes can also be used as low-cost flow-field, an alternative especially used for proprietary commercial systems.

For the future development of LGDLs in PEMWEs, metal foams (Figure 10 (d)) appear to be very promising. Baumann et al. [121] sprayed catalyst ink directly onto titanium foam and used this as a combined LGDL and electrode in a PEMWE. This demonstrated the feasibility of deploying metal foams in PEMWEs; however, a systematic study evaluating the role of metal foam as LGDL was not carried out. Titanium foam has also been used as the LGDL in a unitized reversible fuel cell (URFC), which can operate in either fuel cell or electrolysis mode, and good performance in electrolysis mode was demonstrated [122]. Arisetty et al. [123] used nickel foam as combined LGDL and flow-field in a direct methanol fuel cell and showed that this configuration can outperform a classical flow-field/LGDL combination. The idea of combining LGDL and flow-field by using nickel foam was later also applied in PEMFCs and was shown to yield superior performance compared to the use of separate LGDL and flow-field [124]. To this point, only a computational study on the use of metal foam as flow-field in a PEMWE exists (see Section 3.2.5) [100], highlighting the need for further research.

3.3.2 Micro-Porous Layers and Surface Modifications

Based on proven procedures for PEM fuel cells, modifying the surface of particles or fibres in the LGDL or introducing an additional layer to the LGDL has been widely proposed to reduce the mass transport overpotential and improve overall PEMWE performance. For PEM fuel cells, it has been shown that the introduction of a micro-porous or micro-protective layer (MPL) on the side of the GDL neighbouring the catalyst layer benefits performance by regulating water management and gas transport at the interface. This layer consists of carbon black or PTFE and forms a layer with smaller pores than the rest of the LGDL [125–129].

3.3.2.1 Micro-Porous Layers

Unfortunately, carbon or PTFE MPLs are not stable in the corrosive environment at the LGDL/catalyst layer interface at the anode of a PEMWE, therefore, other materials have been applied, trying to mimic the effect of the MPL in PEMFCs. Lettenmeier et al. [130] created an MPL by coating a titanium sinter with porous titanium via thermal spraying and demonstrated its superior performance, particularly at current densities exceeding 2 A cm^{-2}. Sung et al. [131] used a coating of IrO_2/Ta_2O_5 to produce a reactive MPL to convert active oxygen species to oxygen, but did not compare the performance of their system with a reference. Coating carbon paper with carbon black and subsequently with IrO_2 has been shown to yield an LGDL and MPL stable for 2000 hours, but no performance comparison to a conventional PEMWE system was made [132]. Kang et al. [79] used micro (~5 µm) and spherical nano (30 -50 nm) titanium particles to create an MPL on an LGDL with small, straight, regular pores via low-temperature air spraying. It was found that micro-particles yielded stronger performance improvement than nano-particles. A significant performance improvement (1.707 V to 1.687 V at 2 A cm^{-2}) was found for the micro MPL. High-speed imaging showed that the MPL increased the number of pores providing active catalyst sites. Schuler et al. [133] created sintered powder LGDL with MPLs of different pore sizes and porosities; they showed a performance improvement and a reduction of up to 60 mV with the use of an MPL compared to a conventional sintered powder LGDL.

The effect of coatings to provide an MPL has also been investigated in unitized reversible fuel cells (URFCs). Ito et al. [134] used a layer of PTFE coating on titanium felt as the LGDL in a URFC. They found that the influence of the modified LGDL depends on fibre size, but a positive effect was only shown for fuel cell mode, not for electrolysis operation. Hwang et al. confirmed many of these findings [135] and later created an MPL on titanium felt by applying titanium powder and showed improved performance in a URFC for fuel cell operation. No performance improvement was found in electrolysis mode; however, the system was only tested up to 1 A cm^{-2} [136].

Building on the idea of an MPL, the use of LGDLs with graded porosity, increasing towards the flow channels, has been shown to be beneficial in PEMFCs [137–139]. Lettenmeier et al. [140] produced a sinter-like structure with a graded pore size via vacuum plasma spraying. However, the authors could not show a significant performance improvement using this novel material as the LGDL in a PEMWE. In a similar approach, Kang et al. [141] created an LGDL structure with a gradual decrease in LGDL pore size. The authors introduced the concept of an in-plane transport enhancement layer, combining two LGDLs with straight, circular pores; one with large pores (~830 μm) neighbouring the flow channels, and a second one below it with significantly smaller pores (~100 μm). Results show a slight improvement in performance with the use of the enhancement layer. The authors attribute this to an improvement in access to pores, which would have otherwise been covered by the land areas of the flow plates.

3.3.2.2 Surface and Structural Modifications

For PEMFCs, chemical modification of the gas diffusion layer, e.g. by adding a hydrophobic agent such as PTFE, has been demonstrated to be feasible, stable, and beneficial to performance [142–145]. The chemical modification of the surface changes the contact angle of gas and water, favouring the transport of one or the other in specific areas or across the entire active area. The link between LGDL wettability (contact angle) and PEMWE performance is well established [52,119,146].

However, little work has focused on varying the wettability of LGDLs for PEMWEs. Li et al. [147] applied a hydrophobic monolayer of n-octadecyl tri-chlorosilane onto the surface of a titanium LGDL. They could not demonstrate any performance improvement compared to an untreated LGDL, but observed more frequent bubble detachment from the LGDL surface. Bystron et al. [148] etched titanium felts in hydrochloric acid, creating a titanium hydride sublayer. The authors showed significantly improved performance (voltage reduction of around 0.15 V at 0.5 A cm^{-2}) for more than 100 hours for felts treated in that manner. Kang et al. [149] measured the PEMWE performance of PTFE-treated Toray carbon paper and demonstrated a performance decrease with increasing hydrophobicity (PTFE content).

Recent work by Suermann et al. [150] demonstrated the treatment of a fibrous titanium LGDL with a femtosecond laser, inducing a high-surface structure, and showed a performance improvement linked to the reduced contact resistance.

An alternative approach to improve mass transport through the LGDL is to introduce a number of straight through-pores with significantly larger size than the natural pores of the material. Lee et al. perforated a commercial sintered powder LGDL with 400 µm pores, located in the channel regions of the PEMWE and in a distance of 2 mm from each other along the channel length. The authors showed improved performance of the perforated LGDL up to 9 A cm^{-2} and a reduction in the mass transport overpotential of up to 76.7 %, which is attributed to the reduced gas saturation at the interface between catalyst layer and LGDL.

3.3.3 Bubble Nucleation and Growth

Gas that is produced on the surface of the catalyst layer through electrochemical reaction forms bubbles which are then transported through the LGDL and into the flow channels. The nucleation of these bubbles is driven by the difference in chemical potential μ between gas (g) and liquid (l) phase at the conditions found in the liquid phase at nucleation [151].

$$\Delta\mu = \mu_l(p_l, T) - \mu_g(p_l, T) > 0 \qquad \text{(Equation 3-12)}$$

This driving force can be expressed in terms of temperature, pressure, the Boltzmann constant k_B and the pressure in the liquid phase p_l [146,151]:

$$\Delta\mu = k_B T \ln\frac{p_g}{p_l} = k_B T \ln S \ , \qquad \text{(Equation 3-13)}$$

with the supersaturation S. The pressure in the gas phase p_g is linked to the overall rate of electrochemical gas production, which can be calculated using Faraday’s law (see Section 3.2.2).

The Gibbs free energy ΔG of a cluster of n molecules is linked to this chemical potential difference, the surface tension of a planar cluster σ_∞ and the surface area of the cluster $A(n)$ [151].

$$\Delta G = -n\Delta\mu + \sigma_\infty A(n) \qquad \text{(Equation 3-14)}$$

ΔG has a maximum for the critical cluster size n_c. Clusters with less than n_c molecules require an increase in Gibbs free energy to grow and dissociate on average, while clusters with more than n_c molecules on average nucleate into bubbles [151].

$$n_c = \left[\frac{2}{3}\frac{\sigma_\infty s_l}{k_B T \ln S}\right]^3 \qquad \text{(Equation 3-15)}$$

The liquid phase factor is expressed as $s_l = (36\pi)^{1/3} v_l^{2/3}$, with the molecular volume of the liquid phase v_l.

Increasing current density leads to a rise in gas production, which increases the supersaturation; this reduces the critical cluster size and favours the formation of new gas bubbles. However, the classical nucleation theory only describes bubble nucleation on a regular surface under specific assumptions [151]. To our knowledge, there is no published work on the nucleation of bubbles on the irregular surface of the catalyst layer under real-world conditions.

Nouri-Khorasani et al. [146] developed a model of bubble nucleation and growth and its effect on the electrolysis overpotential. They identified four phases from nucleation of a bubble to its detachment from the LGDL surface. After sufficient supersaturation causes nucleation, the bubble undergoes spherical growth within the walls of the surrounding pore which is assumed to be a straight, vertical, cylindrical channel. Once the bubble diameter is equal to the pore diameter, the bubble continues to grow cylindrically. Bubble detachment occurs either due to the nucleation of a new bubble or as a result of changes in the balance of drag, buoyancy, pressure, inertia and surface tension gradient forces. After detachment, the bubble travels through the pore to the interface of LGDL and flow channel. It then undergoes further spherical growth until it either coalesces with an adjacent bubble or detaches from the LGDL surface due to the drag forces exerted by the convective flow of water through the flow channel.

Li et al. [152] used optical high-speed imaging to observe the processes described theoretically by Nouri-Khorasani. They used a novel, thin LGDL with straight, cylindrical pores and observed spherical bubble growth along the wall of pores. This confirmed earlier findings that bubble nucleation occurs only along the triple-phase boundary (see Section 3.4) [78,82]. Due to this limitation, and the relatively large pore diameter in this work (100 μm), cylindrical growth and detachment from the LGDL surface were not observed. The authors also found increasing bubble detachment diameters from the catalyst surface for higher current density and temperature.

The detachment of bubbles from the LGDL surface has been visualized by neutron and X-ray imaging. Hoeh et al. [83] found rapid, sudden detachment of bubbles followed by a slow growth up to the critical size. The location of detachment and bubble growth was observed to be constant, which implies the existence of preferential pathways through the LGDL. Leonard et al. [84] demonstrated the same periodicity of growth and detachment and further showed that detachment frequency and diameter increased with current density.

3.4 Mass Transport Diagnostic Techniques

There is a wide range of diagnostic techniques which have been or can be applied to PEMWEs (Figure 11), including the following:

- Electrochemical impedance spectroscopy (EIS) [59,153]
- Neutron imaging [85–88,90,154,155]
- X-ray imaging [83,84,156–159]
- Optical imaging [44,73,79–81]
- Porous transport layer (PTL)-on-a-chip [160,161]
- Acoustic methods

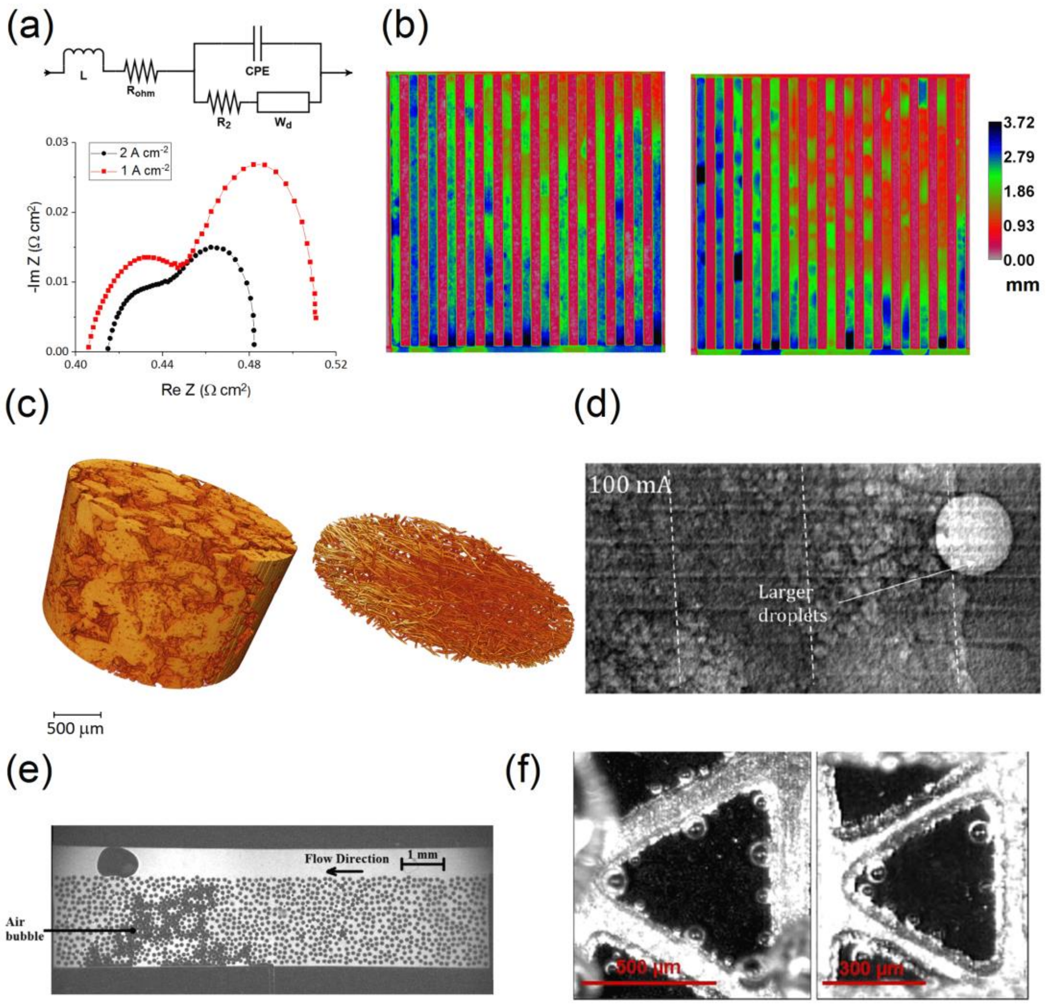

Figure 11: Examples of commonly used diagnostic techniques: (a) Nyquist diagram produced from electrochemical impedance spectroscopy and an equivalent circuit, (b) through-plane water thickness measurement via neutron radiography, (c) X-ray computed tomography of a sintered and a fibrous LGDL material, (d) X-ray synchrotron radiography of channel and land areas in a PEMWE [84] *(Reprinted from 'Electrochimica Acta, 276, Leonard et al., Operando X-ray tomography and sub-second radiography for characterizing transport in polymer electrolyte membrane electrolyzer, 424–33, 2018' with permission from Elsevier), (e) image obtained during a PTL-on-a-chip experiment* [160] *(Reprinted from 'J Power Sources, 258, Arbabi et al., Feasibility study of using microfluidic platforms for visualizing bubble flows in electrolyzer gas diffusion layers, 142–9, 2014' with permission from Elsevier), and (f) high-speed optical imaging of bubble nucleation along the triple-phase boundary of catalyst, LGDL, and water* [80] *(Reprinted with permission under a CC BY-NC licence (https://creativecommons.org/licenses/by-nc/4.0/legalcode) from 'Mo et al., Sci Adv 2016;2:e1600690–e1600690, https://advances.sciencemag.org/content/2/11/e1600690'. Copyright (2016) American Association for the Advancement of Science).*

3.4.1 EIS

Electrochemical impedance spectroscopy (Figure 11 (a)) is commonly used to identify different voltage contributions (ohmic, activation, mass transport) to the overall performance of PEMWEs. Data analysis can be either qualitative by comparing EIS spectra at various conditions or quantitative by fitting the spectra to an equivalent electrical circuit and extracting values for the resistance and impedance elements. The exact form of the equivalent circuit used and the number of elements in it varies widely [43,78,140,153,162–165] or is not reported at all. A more systematic approach to the analysis of EIS spectra, comparable to established work for fuel cells [166–169], has not yet been reported for PEMWEs.

Due to its versatility and comparable ease of application, the use of EIS is widespread. Examples include measuring the performance contribution of LGDLs [78], the effect of low platinum loadings on the cathode [34], localized performance [94], the effect of flow plate geometry [77], the role of LGDL microstructure [170], benchmark characterisation [113], the effect of water starvation [42] and intermittent operation [171], or the influence of flow effects on performance [43].

3.4.2 Neutron Imaging

The high sensitivity of neutrons towards hydrogen and water makes neutron imaging a powerful tool for the investigation of flow and mass transport phenomena in PEMWEs and PEM fuel cells [91] (Figure 11 (b)). *Operando* neutron imaging of a PEMWE was first demonstrated by Selamet et al. [85,86], while Hoeh et al. [87] used neutron imaging to measure the water-gas ratio under land and channel areas of a PEMWE.

Several examples demonstrate the level of insight into water saturation and movement in the LGDL that neutron imaging can offer. Seweryn et al. [89] found that the amount of water within the LGDL on the anode side is constant for current densities from 0.1 A cm^{-2} to 2.5 A cm^{-2}, which shows the ability of sintered titanium materials to hold up and transport large amounts of water and hence prevent water starvation. Panchenko et al. compared the water content of a sintered titanium LGDL with a felt material used as LGDL [88] and found that a significant portion of pore volume in a sintered LGDL did not contribute to mass transport [154]. Lee et al. [155] combined neutron radiography and electrochemical testing and found a decrease in mass transport overpotential at increased temperatures. This was assigned to a more uniform water-gas distribution in the flow channels, due to the reduced viscosity of water at high temperatures.

3.4.3 X-ray Imaging

Whilst X-rays lack the high sensitivity of neutrons towards water, the extremely high flux of synchrotron sources allows for very short exposure times (sub-second radiography). Synchrotron X-ray imaging (Figure 11 (d)) was first used by Hoeh et al. [83] for *operando* imaging of a PEMWE. The authors showed the periodicity of bubble formation and detachment at specific locations on the surface of the LGDL, supporting the theory of preferential pathways for mass transport. While the work of Hoeh et al. was limited to radiography, Leonard et al. [84] obtained three-dimensional tomography data sets during the operation of a PEMWE. This allowed the authors to study a multitude of processes on different length scales, ranging from catalyst thinning and redepositing to the formation of bubbles and their movement in the flow channels.

Besides synchrotron *operando* imaging of whole PEMWEs, the use of lab-scale X-ray sources for micro-computed tomography (X-ray CT) has been prolific in recent years. X-ray CT allows for the in-depth study of the microstructure of LGDL materials *ex-situ* and can achieve a spatial resolution in the range of a few micrometres (Figure 11 (c)). Several authors have combined X-ray CT with EIS and electrochemical characterisation to link LGDL microstructure and performance [77,140,153,172,173]. X-ray CT data can further be used to calculate various transport properties like thermal and electrical conductivity and permeability [156].

3.4.4 Optical Imaging

The investigation of flow phenomena via high-speed optical imaging is limited to the macroscopic spatial resolution occurring in optically accessible regions, such as the flow channels or open pores of perforated plates. However, it is a low-cost, easy to implement and therefore widespread diagnostic tool. It is often used in conjunction with electrochemical characterization techniques, such as i-V-curves or EIS (Figure 11 (f)).

Optical imaging has proven very valuable when observing bubble nucleation in the pores of perforated plates, allowing direct optical access to the interface between catalyst layer and LGDL [78,82,152,174]. It has been shown that bubble nucleation only occurs along the pore edge, not in its centre, as visible in Figure 11 (f) [80]. This is due to the fact that catalytic active sites on the CCM, the current conduction through the LGDL, and water exist in close proximity only on the pore edge, while electrons have to travel along the surface of the CCM to reach catalyst sites further towards the middle of the pore. To examine the role of in-plane resistivity further, a numerical model was developed and used to simulate the current distribution within one pore as well as the overall performance of a PEMWE with LGDLs of different pore sizes and porosities [175].

Based on the new insight from the optical imaging experiments, a novel concept for PEMWEs in which the catalyst is only applied along the edges of the LGDL pores on the membrane site has been proposed [80], which allows for a much higher catalyst utilization. In an attempt to examine the impact of catalyst reduction, Kang et al. [33] sputter-coated a thin LGDL with straight pores and a porosity of 50 % with platinum. They showed that this does not reduce performance compared to using a conventional CCM, while the catalyst utilization was improved by a factor of around 30. Further, Mo et al. [81] developed an LGDL with an additional metal rod through the diameter of a pore in a perforated plate. They used optical imaging to prove catalytic activity around the surface of the rod and the consequential improvement in catalyst utilization.

Dedigama et al. used optical imaging in combination with EIS and localized current density measurements, which allowed for a correlation of flow regime to local and overall performance. The authors found a performance improvement in slug flow, which they attributed to more efficient bubble removal from the surface of the LGDL [43,44] (see Section 3.2.4).

Lafmejani et al. simulated the environment on the anode side of a PEMWE by passing gas through different LGDL materials while flowing water over its surface. They used optical imaging to observe the locations of bubble formation, the development of the flow regime and flow patterns along the length of the LGDL [95,176,177].

3.4.5 PTL-on-a-chip

An interesting approach to analysing mass transport within a porous LGDL is the so-called porous transport layer (PTL)-on-a-Chip (Figure 11 (e)). The authors created a 2D representation of different LGDL materials and analysed the flow of water and gas through this layer using optical microscopy [160,161]. This allows for the visualization of exact pathways of gas through the material which are usually obstructed by the thickness of the LGDL. Using this technique, Lee et al. [161] found that the bubble growth within pores of the LGDL consists of two different steps. During pressurization the bubble is stationary and its size constant while its internal pressure is increasing. Once the pressure reaches a critical value, the penetration step follows and the bubble rapidly expands into a neighbouring pore. The dynamics of this process are controlled by the diameter of the throat between the pores. As a consequence, within the pathway of gas through the LGDL, a limiting throat size exists, which requires the highest internal pressure to penetrate. Once this limiting throat size is passed, breakthrough to the surface of the LGDL immediately occurs. These findings shed new light on a number of studies examining the influence of LGDL pore size on PEMWE performance [41,92,114]. It is expected that throat size correlates quite closely to pore size, so the influence of pore size on performance found in these studies is likely to be related to the throat size effect described above. Qualitative findings from PTL-on-a-chip experiments are well suited to inform further pore network and modelling studies [178].

3.4.6 Acoustic Methods

3.4.6.1 Acoustic Emission

Acoustic emission (AE) testing is a non-destructive, *in situ* technique that detects transient elastic sound waves produced by a sudden redistribution of stress in a material or mechanical process. It has been extensively applied in building and structural health monitoring [179,180] and uses a piezoelectric sensor to convert mechanical perturbations occurring in a system into a voltage signal. This allows the monitoring of sound waves emitted by an object.

AE has been used to study electrochemical processes such as the exfoliation of aluminium alloys [181] or detection of corrosion in stainless steel [182]. It is increasingly being applied to power systems. For example, Ohzuku et al. [183] monitored particle fracture in Li/MnO_2 battery cells and found that accelerated discharge leads to increasing fracture. Rhodes et al. [184] monitored particle fracture in Si-based anodes of Li-ion batteries and showed that the fracture of Si particles can be modelled using a thermal analogy model [185]. This technique has also been applied to Li/$NiSb_2$ batteries [186], solid electrolyte interface (SEI) formation and Li intercalation in Li-ion batteries [187], solid oxide fuel cell seal cracking [188,189], Nafion dehydration [190], and flooding [191] and localised operation [192] in polymer electrolyte membrane fuel cells.

There are several examples of using AE to diagnose two-phase systems. Pandit et al. [193] used a hydrophone immersed in an air-water system to calculate bubble size distribution. Yen et al. [194] extracted various criteria from the acoustic emission of an air-water system and trained a neural network to recognize different flow patterns. In other instances, AE has been applied to gas-solid beds [195], annular and stratified flow in gas-liquid pipelines [196] and measurement of the gas void fraction during slug flow [197]. Husin et al. [198] showed that the formation and collapse of single bubbles can be studied using acoustic emission and also reported a signal specific to the movement of slug bubbles. The only previous report of the application of AE to electrolysis comes from Crowther et al. [46], who studied the onset of gas evolution in alkaline electrolysis.

3.4.6.2 Acoustic Time-of-Flight Imaging

Acoustic time-of-flight (AToF) imaging has so far not been applied to PEMWEs or PEM fuel cells, but was first introduced to electrochemical energy storage and conversion devices by Sood et al. [199], who successfully used AToF transmission measurements to detect interface degradation in a cycled Li-ion pouch cell. Hsieh et al. [200], who conducted transmission and reflection AToF experiments on cylindrical and pouch Li-ion and alkaline battery cells, demonstrated that changes in the time-of-flight of the acoustic signal are linked to physical changes in the electrodes (density and modulus). They showed that these changes can be used to measure the state-of-charge of the battery, and validated their results against a computational model of sound propagation in a series of battery electrodes. This work was later advanced to show the ability of AToF to detect Zn gel dehydration and ZnO_2 formation in Zn/MnO_2 batteries [201], as well as to develop a supervised machine learning technique to predict battery state-of-charge from acoustic time-of-flight [202]. Bommier et al. [203] combined XRD of graphite electrodes, electrochemical measurements, and AToF measurements, finding a correlation between the amount of lithium plating and the time-of-flight shift, indicating the possibility of detecting lithium plating in lithium ion batteries *operando*. Robinson et al. [204,205] combined AToF mapping across the surface of a Li-ion pouch cell with X-ray computed tomography to further demonstrate its ability to elucidate internal battery structure and investigated anode and cathode structure in detail during charge and discharge.

A variation of the described AToF measurements was proposed by Ladpli et al. [206–208] for analysis of processes in lithium ion batteries. Instead of using a sensor emitting an ultrasonic pulse perpendicularly into the sample, the authors deployed a 'guided wave' technique, with piezoelectric transmitter and receiver both being located on the same surface (side) of a prismatic battery cell. The transmitted signal does not travel through the cell, but along its surface, with time-of-flight and signal attenuation being a function of the battery's physical properties. A clear correlation between state-of-charge, acoustic time-of-flight, and acoustic amplitude at the receiver was shown, which also was affected by the number of charge/discharge cycles, indicating the possibility of state-of-health prediction.

Recently, it has been shown that AToF can be used to measure the effective stiffness of battery electrodes and full pouch cells, demonstrating the ability to obtain absolute values for physical material properties from non-destructive, low-cost AToF measurements [209].

To the author's knowledge, AToF imaging has not yet been applied to PEMWEs; however, the demonstrated feasibility of investigating two-phase systems with AToF imaging [210–212] suggests that it could be a valuable tool for the analysis of mass transport processes in PEMWEs.

4 Methodology

4.1 PEMWE Testing

4.1.1 PEMWE Cell Assembly

As described in Section 2.2, a PEMWE typically consists of end-plates, titanium flow-fields, a titanium LGDL at the anode, a carbon paper GDL at the cathode, and a CCM combining the polymer electrolyte membrane and the catalyst layers. Gaskets to fit the LGDL, GDL, and CCM were cut with a carbon dioxide laser cutter (Laserscript LS3020, HPC Laser, UK; Wavelength: 10.6 µm) from woven PTFE (Tygaflor) with a thickness of 0.1 mm, with several gaskets being stacked to achieve the thickness of the LGDL. All PEMWE parts were designed in the CAD software Rhino (Robert McNeel & Associates, USA). The PEMWE cells used in this work were held together by bolts, fastened to a defined torque with a torque wrench to ensure comparability of experiments.

Throughout this work, a CCM with 3.0 mg cm^{-2} iridium/ruthenium oxide on the anode side and 0.6 mg cm^{-2} platinum on carbon on the cathode side (ITM Power, UK) was used. The CCM was washed with sulphuric acid for a minimum of 15 minutes before experiments to hydrate the membrane and remove salts left from the catalyst synthesis.

4.1.2 Material Selection

Due to the acidic polymer electrolyte membrane, a very acidic regime (pH~2) is found in PEMWEs [18] and high potentials occur at the anode as well as the cathode [213,214]. Hence, the environment in a PEMWE is highly corrosive, and long-term voltage stability can only be achieved by selecting corrosion-resistant materials for catalysts, LGDL, and flow or bipolar plates [18,215]. Titanium is the most common choice for flow or bipolar plates and LGDLs in PEMWEs and was used in this work unless specified otherwise.

The need for titanium for components at the anode is illustrated using Pourbaix diagrams (Figure 12), which show the corrosion behaviour of titanium (Figure 12 (a)) and iron-chromium-nickel (Figure 12 (b)) as a function of pH and potential. Under the conditions typical for the PEMWE anode (pH~2 and 2 V [18]) titanium undergoes anodic protection to form TiO_2, while iron-chromium-nickel (e.g. stainless steel) forms the soluble Fe^{3+}. Similarly, chromium and nickel form soluble ions under these conditions (not displayed) [216], illustrating that stainless steel is not stable at the anode of a PEMWE.

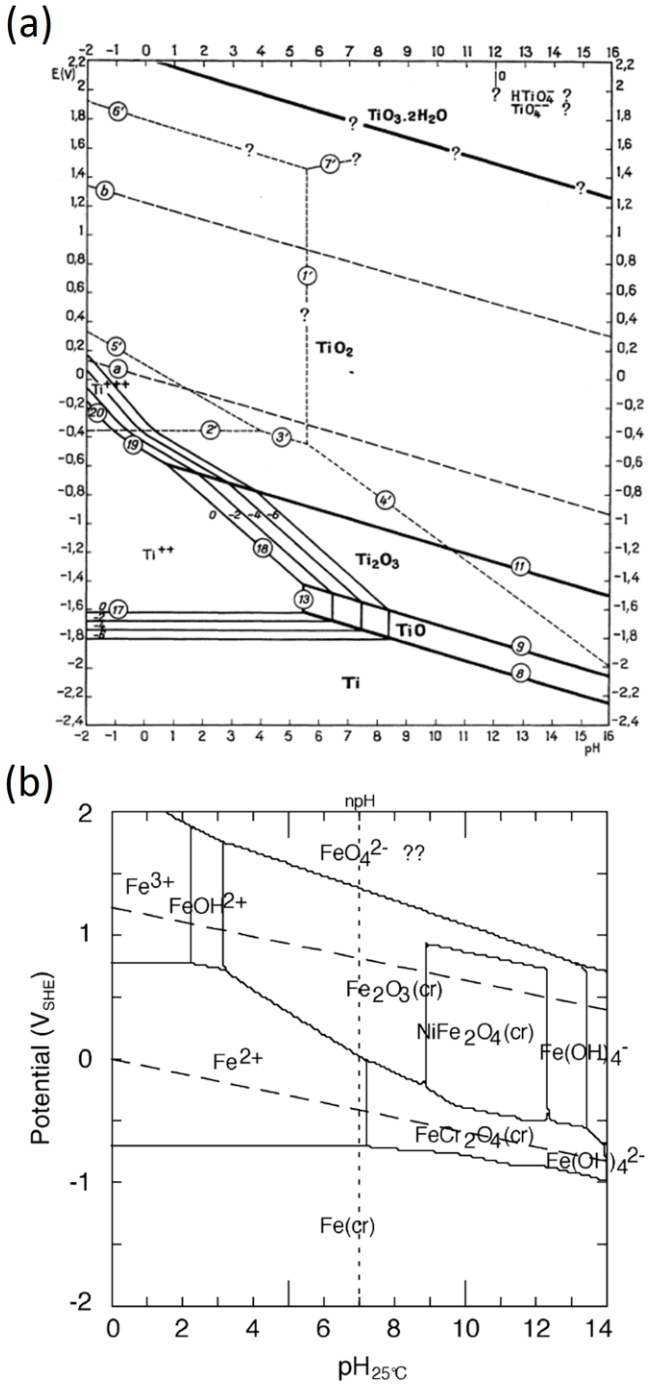

Figure 12: Pourbaix diagrams of (a) titanium (Republished with permission of NACE International – Corrosion Society, from [217] *'Atlas of electrochemical equilibria in aqueous solutions. Pourbaix M., 1974', permission conveyed through Copyright Clearance Center, Inc.) and (b) iron in iron-chromium-nickel at 25 °C (Republished with permission of National Association of Corrosion Engineers, from* [216] *'Pourbaix diagrams for the ternary system of iron-chromium-nickel, Beverskog et al., Corrosion, 55, 1077–87, 1999'; permission conveyed through Copyright Clearance Center, Inc,), illustrating the corrosion behaviour of both metals as a function of pH and potential.*

4.1.3 Balance-of-Plant

The operation of the PEMWE used in this work necessitated temperature control, a pump, and a water-gas separation system (Figure 13). However, commercial PEMWE systems or stacks require a substantially more elaborate balance-of-plant. A peristaltic pump (Watson Marlow 323D, UK) was used to pump deionised water through a water bath to reach the desired input temperature before entering the PEMWE. Unless otherwise stated, water was pumped through the anode as well as the cathode, with the inlet water flow being split equally between both electrodes. Even though water flow is only strictly necessary on the anode, additional water flow on the cathode ensures efficient membrane hydration. The water-gas mixture is pumped from the PEMWE into the separation unit, where oxygen is vented into the environment and hydrogen into an extraction system. The remaining water is recirculated from the separation units.

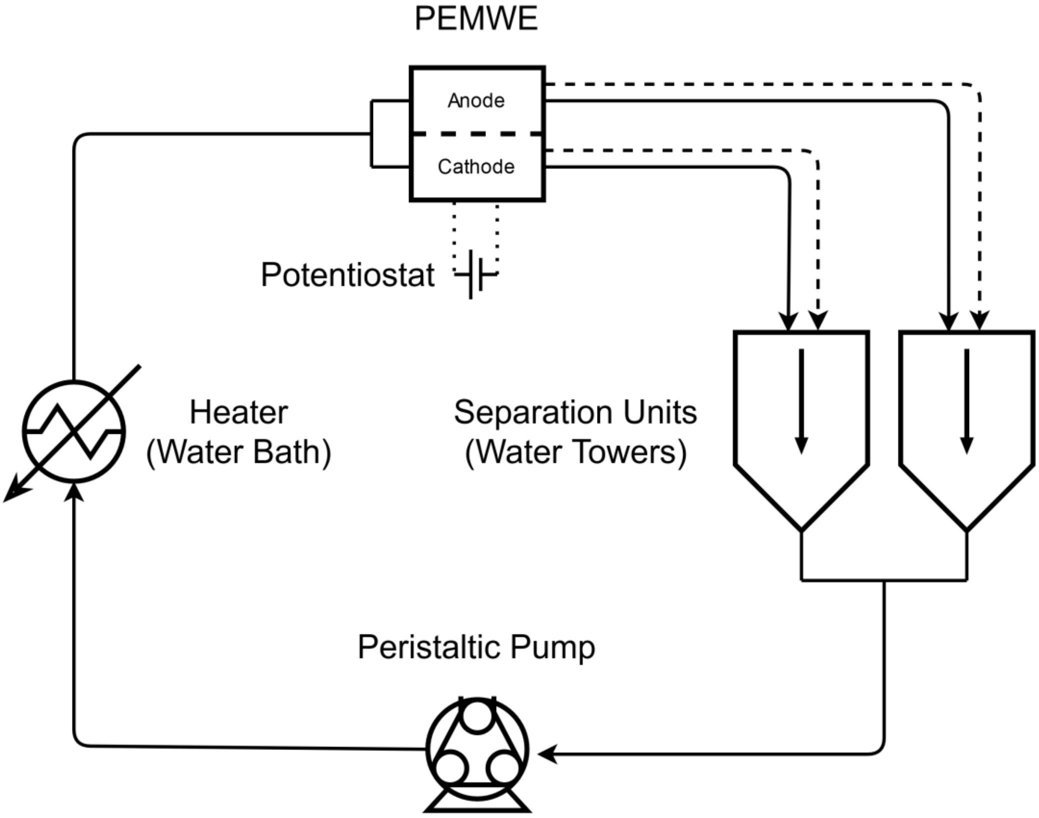

Figure 13: Process diagram of the balance-of-plant used for PEMWE testing. Solid lines denote liquid flows, while dashed lines indicate gas flows. The potentiostat is connected to anode and cathode simultaneously.

4.2 Optical Imaging

Optical high-speed imaging was used to visualise the two-phase flow in the flow channels of PEMWEs. For this purpose end-plates from transparent Perspex were used to allow for optical access to the flow channels [43,218]. A Photron FASTCAM SA1 was used for all experiments in this work, with a Tokina MACRO 100 F2.8 D lens used for high-resolution imaging (spatial resolution 50 µm) and a Sigma 1:2.8 DG HSM lens (spatial resolution 300 µm) for capturing the entire PEMWE cell.

4.2.1 Image Quantification

To achieve quantitative data on the number and size of bubbles in the flow channels from optical imaging, a MATLAB (MathWorks, USA) algorithm was developed. First, the images were thresholded into black and white representations using the *multithresh* and *imquantize* commands, with *multithresh* applying Otsu's method [219] to segment an image into two different domains and *imquantize* turning the segmented image into a discreet label field. After segmentation, a box filter with a kernel size of 5 was applied (*imboxfilt*) to remove outlier (bright or dark spots). A box filter averages the pixel values in a square with the length of the square being the kernel size. All values in the square of pixels are then compared to the average value and outliers are removed. After filtering all circular structures in the images were identified using *imfindcircles*, an algorithm applying a circular Hough transform (CHT) method [220]. The detailed mathematical formulation and implementation of Otsu's method and the CHT is beyond the scope of this thesis, but the use of these methods for image segmentation [221–223] and recognition of circular elements [224–226] is well established. In a last step, overlapping circles were removed to ensure individual bubbles were not identified multiple times (Figure 14). Two circles are considered to be overlapping if the distance between their centres D_{xy} is smaller than the sum of their radii $r_{1,xy}$ and $r_{2,xy}$. The index xy indicates that this criterion has to be valid in x as well as y direction for the circles to overlap.

$$D_{xy} < r_{1,xy} + r_{2,xy} \qquad \text{(Equation 4-1)}$$

The described algorithm is limited to circular bubbles, hence, for elliptically elongated bubbles only the length of the minor axis was correctly identified. A discussion of the accuracy of the algorithm in comparison to manually determined values for bubble number and size can be found in Section 6.4.1.

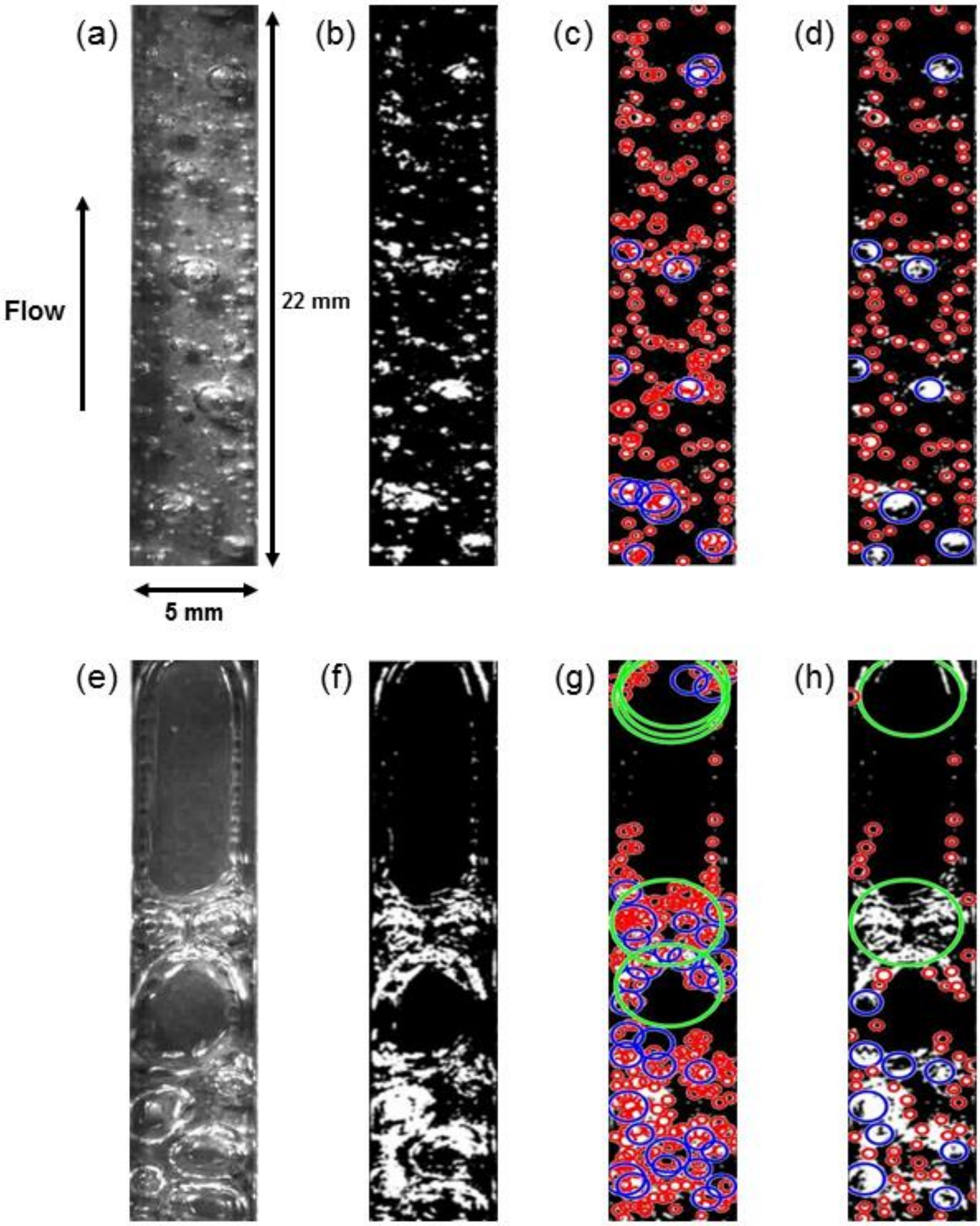

Figure 14: Illustration of the use of the algorithm for analysis of bubbly (a-d) and slug (e-h) flow for detection of bubble sizes and numbers. Raw images (a, e) are thresholded and filtered (b, f), circular structures are identified (c, g) and finally, overlapping circles are removed (d, h). Good bubble identification can be observed for bubbly flow, while the algorithms limitations are visible in slug flow. Only the minor axis of elliptical bubbles is measured and the overall detection accuracy was reduced.

4.3 Radiation-Based Imaging

Here, the scientific fundamentals of X-ray and neutron imaging, as well as the methodology of image acquisition and analysis for both will be outlined, and the section will be finished with a brief description of tomographic reconstruction, which is used to calculate three-dimensional data sets from a series of two-dimensional projection images.

Certain image analysis steps, such as the extraction of porosity, tortuosity, and pore size distribution from tomograms (Section 4.3.1.4), or the normalisation of radiographs with a reference image (Section 4.3.2.4), will be presented exclusively in the context of either X-ray or neutron imaging; however, this is to represent the techniques applied to specific data sets in this work, while the underlying techniques are more general and can be applied to any two- or three-dimensional image data.

4.3.1 X-ray Imaging

This section will introduce the production of X-ray radiation, its interaction with matter, and how this is used for the design of X-ray imaging systems. Typical post-processing steps for the reconstructed data sets are outlined, and the calculation of quantitative parameters such as porosity, tortuosity or pore size distribution from 3D data sets explained. Lastly, a lab-based system for the acquisition of X-ray computed tomograms (XCT) is presented.

4.3.1.1 Production of X-ray Radiation

X-ray photons originate either from the transition of an electron from an outer shell to a vacancy on the inner shell caused by the ejection of a core electron, or from the acceleration or deceleration of charged particles such as electrons [227]. The acceleration of electrons in a magnetic field is commonly used for achieving high flux X-ray radiation in synchrotrons, but will not be discussed further in this work.

The X-ray radiation in lab-based systems is produced by electrons being accelerated in a high voltage electric field and fired at a target. The subsequent emission of X-ray photons follows the two remaining mechanisms described above: discrete radiation at a number of element-specific wavelengths due to high energy electrons filling core electron vacancies, and a continuous radiation spectrum (Bremsstrahlung) caused by the deceleration of high-speed electrons by either the nuclei electric field or direct collision with a nuclei [228]. The resulting spectrum in an X-ray tube is a superposition of individual peaks and a continuous distribution of photons as a function of energy. This distribution is asymmetrical with a tail towards high energy photons and a maximum energy at the energy of the X-ray tube [227].

4.3.1.2 Interaction of X-ray Radiation with Matter

Upon interaction with a sample, X-ray photons are either transmitted, or absorbed via a number of different mechanisms, most notably the photoelectric effect and elastic and inelastic scattering. The production of an electron-positron pair and the emission of radioactive radiation (photonuclear effect) are not relevant within the typical energy range (between 5 keV and 150 keV) for X-ray spectroscopy [227]. The photoelectric effect, which dominates the photon interactions in the relevant energy range [228], is caused by the excitation of an electron by the incident X-ray photon. This electron is ejected, in turn causing excitation of the atom which is relaxed when an electron from an outer shell falls onto a lower energy level to fill the vacancy. Heavy atoms tend to emit the released energy in the form of X-ray radiation, while in light elements the energy is released via electrons (Auger effect) [227]. An overview of the interaction of X-ray radiation with a sample is shown in Figure 15.

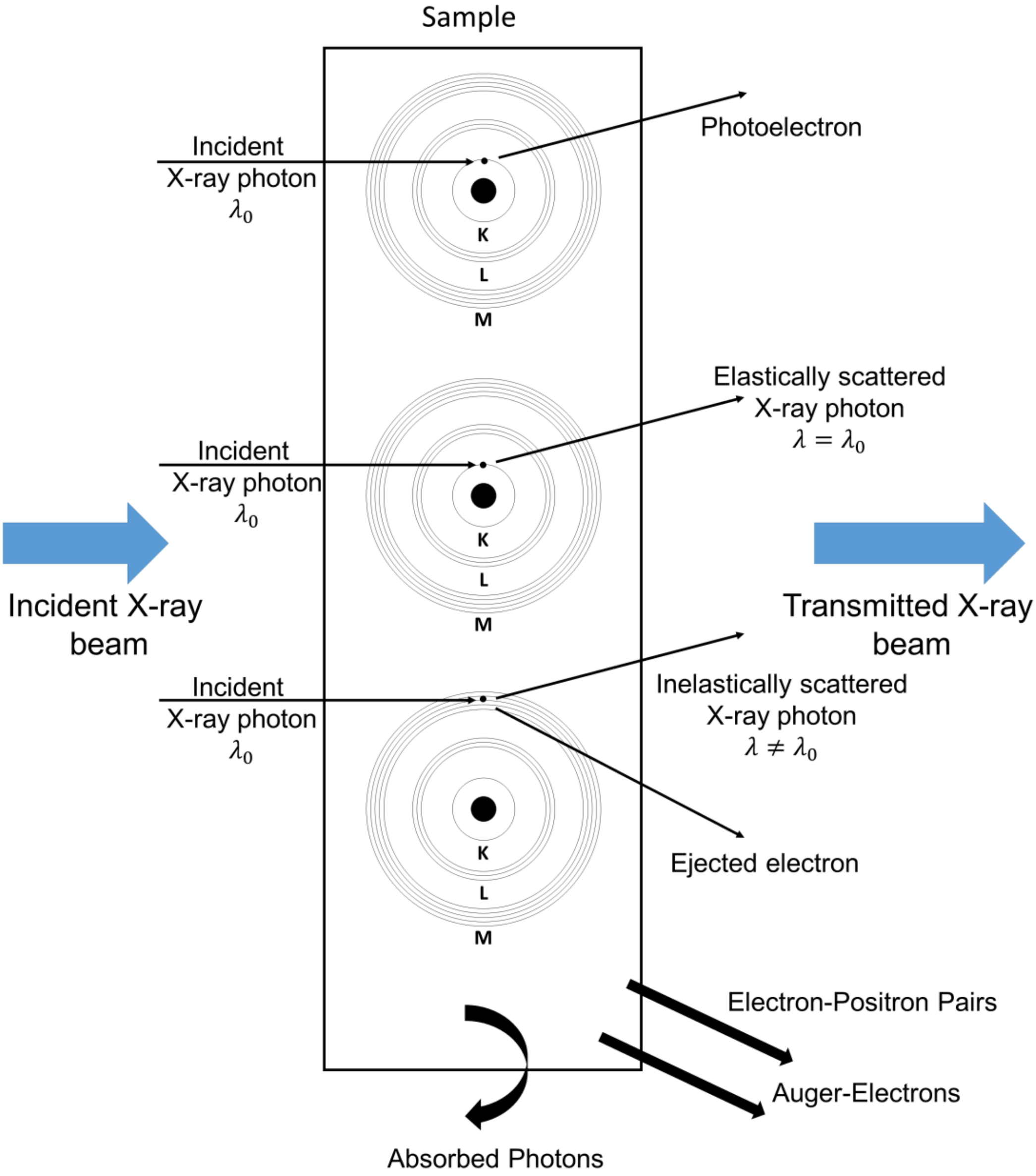

Figure 15: Overview of the interaction of an X-ray beam with a sample. The incident X-ray beam is attenuated due to a number of mechanisms, of which the photoelectric effect is dominant in the energy range relevant to X-ray spectroscopy. The transmitted portion of the X-ray beam is then detected [227].

To quantify the overall absorption of a sample, its absorption cross-section, σ_{tot}, which is the sum of the contributions from the photoelectric effect σ_{pe}, elastic scattering σ_{es}, and inelastic scattering σ_{is}, is used [227].

$$\sigma_{tot} = \sigma_{pe} + \sigma_{es} + \sigma_{is} \qquad \text{(Equation 4-2)}$$

To analyse X-ray spectroscopy data, a link between the cross-section, which is a microscopic property, and the macroscopic linear attenuation coefficient of a sample μ, is needed and is defined as a function of the material density ρ, Avogadro's constant N_A, and the molecular weight of the sample material M_A [229].

$$\frac{\mu}{\rho} = \sigma_{tot} \frac{N_A}{M_A} \qquad \text{(Equation 4-3)}$$

The linear attenuation coefficient is material specific and its measurement using X-ray spectroscopy can be used to identify separate phases in a sample. The linear attenuation coefficient is related to the photon transmission T, by the Beer-Lambert law which accounts for the thickness t, of the sample.

$$T = \frac{I}{I_0} = \exp(-\mu t) \qquad \text{(Equation 4-4)}$$

The intensity I, is the fraction of X-rays transmitted by the sample (ignoring scattering effects), while I_0 is the intensity of the incident beam directed at the sample. It is commonly measured by acquiring X-ray spectroscopic data with the sample removed from the field-of-view.

4.3.1.3 X-ray Spectroscopy Acquisition and Detection

The sample is placed between a detector and a source emitting an X-ray cone beam which is attenuated by the sample due to the mechanisms described in the previous chapter. The transmitted portion of the beam is then detected.

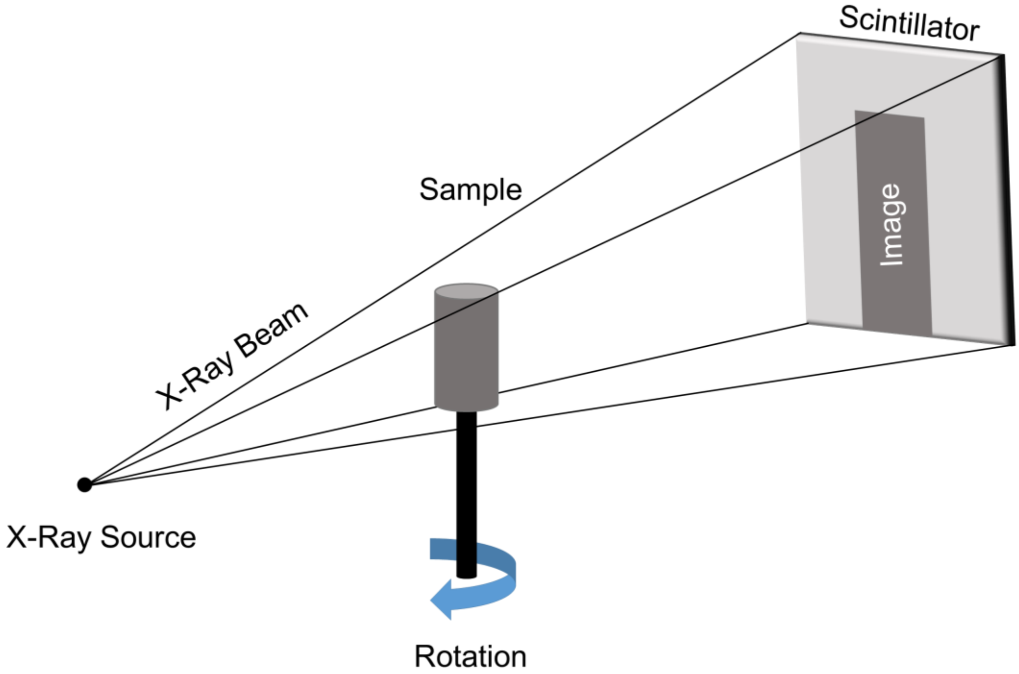

Figure 16: During acquisition of an X-ray tomography, the sample is rotated in an X-ray beam and the sample projection is captured on a scintillator screen. Here, acquisition with a cone beam is displayed, however, a parallel beam (typically at a synchrotron) can be used as well (adapted from [230]*).*

For tomographic acquisition, a number of single projections have to be taken to enable reconstruction into a 3D dataset (see Section 4.3.3), which is achieved by rotating the sample around its axis and acquiring two-dimensional projections at each discrete angular step (Figure 16). The minimum amount of required projections is defined by the Nyquist theorem, which states that the sampling distance should be no more than half of the desired spatial resolution [231]. In practice, a significantly lower amount of projections is usually sufficient [232]. Depending on the sample rate, detector, beam characteristics, and other parameters a spatial resolution is obtained for two- and three-dimensional data sets. The spatial resolution is often defined as twice the pixel/voxel size as at least two pixels are required to distinguish any change in the state of the sample. However, multiple pixels are often required to resolve a certain sample feature, e.g. distinguish two partially overlapping fibres. This leads to the definition of effective pixel size and resolution, which give the minimum size of resolvable features [227].

CCD detectors are commonly used to convert the transmitted X-ray radiation into a digital image. In a first step, a scintillator based on phosphor or a semiconductor converts the X-ray radiation into light. The light is magnified if required and coupled via lenses or fibre optics. In the last step, the optical signal is converted into an electrical one [233].

4.3.1.4 Image Quantification

To enable quantitative analysis and a more detailed comparison of different samples, key metrics like porosity, tortuosity, and pore size distribution (PSD) can be extracted from the reconstructed tomograms. In the first step, the data is segmented into different phases based on greyscale values. As different materials have different attenuation coefficients, the respective regions in the tomogram exhibit varying greyscale values. Hence, local minima in the histogram mark phase transitions that can serve as the basis for manual thresholding. In this case, all voxels to the left of the minimum are assigned to one phase (e.g. phase 0), while the voxels to the right are assigned to a second phase (e.g. phase 1), with errors and artefacts, such as beam hardening, ring artefacts, or partial volume effects, potentially introducing uncertainty to the location of the phase transition in the histogram. In many cases, this can be circumvented by applying filters before segmentation, or using machine-learning segmentation algorithms [232]. However, these methods are beyond the scope of this thesis. The product of image segmentation is a label field, assigning a phase-specific value to each voxel. Unless stated otherwise, all image quantification was performed in the software Avizo (Thermo Fisher Scientific, USA).

4.3.1.4.1 Porosity and Tortuosity

After segmentation, the porosity (or phase fraction) in a sample is easily determined from the contribution of a specific phase to the overall area in a slice through the label field. Typically, the fraction of a phase is averaged across all orthoslices to obtain the respective volume fraction. For example, the tomogram of an LGDL is segmented into two distinct phases: pores and solid phase/titanium. To determine the porosity of the LGDL, the fraction of pore of the overall area is determined for every orthoslice and averaged across all slices. Tortuosity was determined from XCT data using TauFactor [234], a Matlab application which compares the diffusive transport in a porous media with and without convolutions of the flow path.

4.3.1.4.2 Pore Network Model and PSD

Avizo provides a number of proprietary functions to extract the PSD from segmented XCT data. The *Separate Objects* method is applied to the pore phase, creating a label field of individually labelled pores. This label field is used as input for the *Generate Pore Network Model* module, which transforms the separated pores into a pore network model (PNM) consisting of a number of pores (spheres) connected by throats (cylinders). When generating the PNM, Avizo also calculates the permeability and tortuosity of the sample, as well as the flow rate of fluid per second through each throat. Applying a *Distribution Analysis* module to the pore network model produces the PSD. To limit the analysis to connected pores, hence excluding all pores without connection to the main pore network, an *Axis Connectivity* module may be applied to the segmented data [235].

4.3.1.5 X-ray micro-computed Tomography using the Zeiss Xradia Versa

The Zeiss Xradia Versa XRM-520T (Figure 17) is a lab-based X-ray micro-tomography system with a two-stage magnification design, capable of achieving a maximum spatial resolution of 0.7 µm. As shown in Section 5.4.1, the smalles pore sizes in LGDL materials are typically around 10 µm, making X-ray micro-tomography with the Zeiss Xradia Versa a suitable tool. Radiation is produced from a tungsten target (NT100, Nordson DAGE) and an X-ray tube operating in the voltage range from 30 kV to 160 kV and with a maximum power of 10 W. A range of filters are available to avoid beam hardening effects, which occur when using a polychromatic beam, as low energy X-ray photons are attenuated more strongly due to the photoelectric effect [227,232]. Beam hardening causes artificial variations in pixel intensity, typically a decreasing intensity profile from the edge to the centre of the sample. Images are acquired using a scintillator coupled with an optical magnification turret (0.4X, 4X, 20X, 40X) and a 2048×2048 pixels CCD detector. A scouting video camera is used to align the sample to the detector and source during setup [232,236].

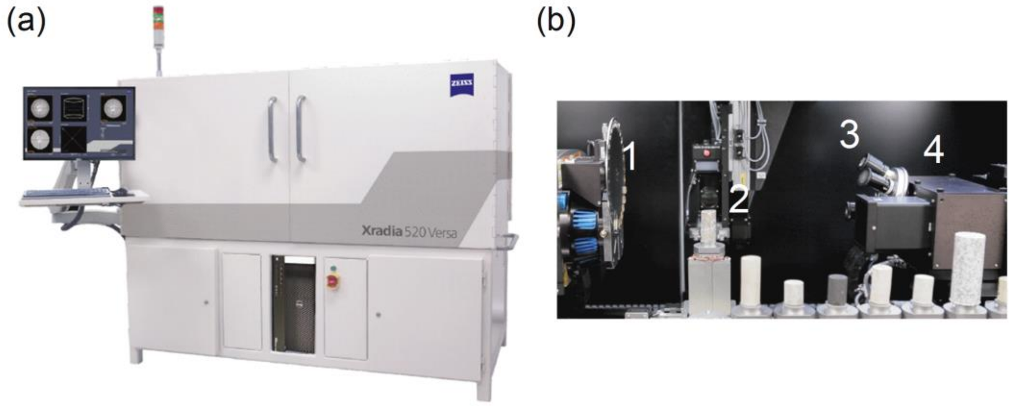

Figure 17: (a) The Zeiss Xradia Versa XRM-520T [236]*. (b) Inside the Versa chamber a sample (2) is rotated during tomographic acquisition. The projections are captured with a detection system (4), with the optical magnification being adaptable by selecting one lens from the magnification turret (3). To mitigate beam hardening effects, a range of X-ray filters can be used (1) (adapted from* [236]*).*

Zeiss provides the proprietary reconstruction software XMReconstructor for use with data acquired with the Xradia Versa. It generates tomograms from single-slice acquisitions, using a filtered back-projection algorithm. Centre shift and beam hardening corrections can also be applied.

4.3.2 Neutron Imaging

Similar to X-ray radiation, neutrons are used to acquire two-dimensional (radiography) or three-dimensional (tomography) imaging data. However, the production and preparation of a neutron beam and its interaction with matter is markedly different to the equivalent processes in X-ray imaging and will be outlined in the following. These differences in interaction cause neutrons to have a very high attenuation in some light elements, such as boron, lithium, and hydrogen, which makes neutron a complementary tool to X-ray imaging, and particularly well suited for the investigation of processes in Li-ion batteries, fuel cells, and PEMWEs. Further, the acquisition of neutron radiographs, their processing and visualization of the water thickness, and the setup of the CONRAD beamline at Helmholtz-Zentrum Berlin (HZB) will be outlined.

4.3.2.1 Production and Preparation of a Neutron Beam for Imaging

The very high flux of neutrons necessary for imaging is produced from nuclear fission reactors or spallation sources. The latter is based on bombarding a heavy element (e.g.

lead or tungsten) target with a pulsated proton beam, resulting in the production of a neutron beam. However, neutron imaging in this work was performed on a reactor-based beamline, and focus will be put on this technology in the following. Fission reactors consist of ^{235}U elements immersed in light or heavy water for thermalization of the neutrons produced by and driving the nuclear chain reaction. Neutrons can be extracted from the reactor via flight tubes and then transported towards imaging instruments using neutron guides – evacuated glass tubes with a reflective coating (e.g. nickel) keeping the neutrons within the guide. By using neutron guides with a large bending radius, high-energy neutrons and gamma radiation are forced out of the beam, ensuring a more homogenous beam [227].

In general, the cross-section of neutrons for many elements is increasing with the neutron wavelength. Hence, neutrons with a higher wavelength (cold neutrons) exhibit an increased sensitivity and allow for imaging with increased sensitivity and contrast. These are produced using tanks filled with hydrogen or deuterium, through which the neutron beam is transmitted [227]. The approximate wavelength spectra (in Å) of hot, thermal, and cold neutrons are found in Figure 18.

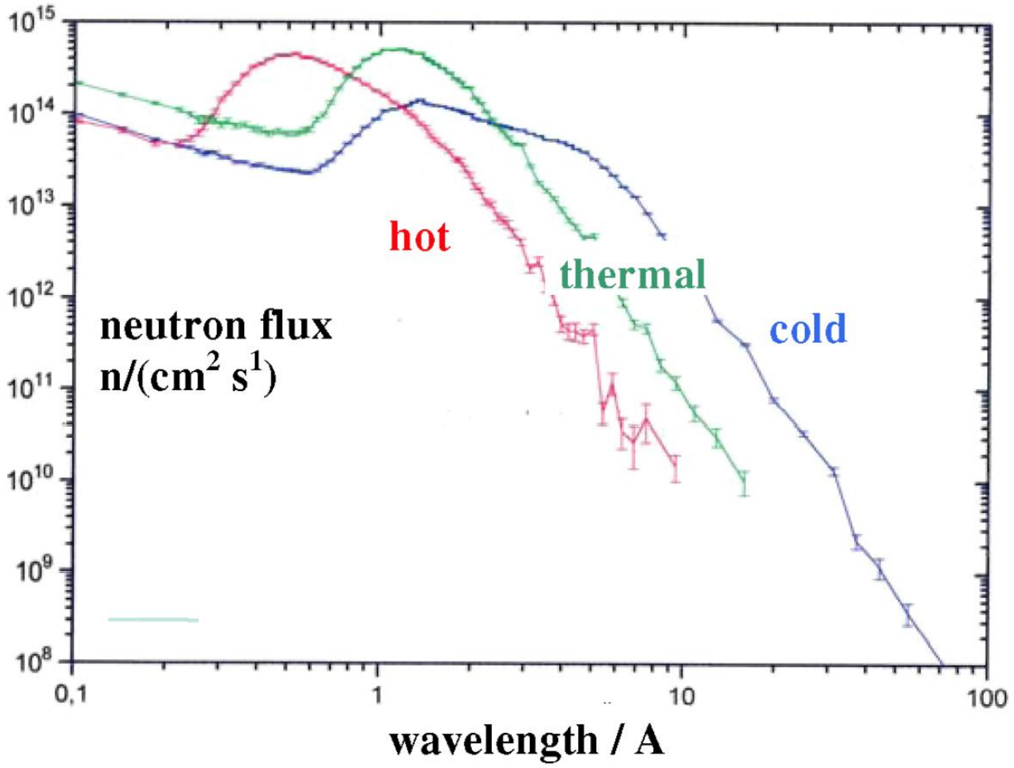

Figure 18: Neutron flux as a function of wavelength (in Å) for hot, thermal, and cold neutrons. (Reprinted from [237]*, with the permission of AIP Publishing.)*

After being transported from the reactor towards the imaging instrument, the beam usually undergoes further preparation steps to optimize for high-quality imaging. To reduce image blurring, the beam is usually collimated using a diaphragm. This reduces the beam size, approaching the ideal spot size more closely, and hence reducing penumbra effects and allowing for high-resolution imaging. However, collimation reduces the flux of neutrons, so choosing the collimator aperture is a compromise between resolution and acquisition time. Other preparation steps which can be applied if called for by the imaging application are monochromatization or polarization [227].

4.3.2.2 Interactions of Neutrons with Matter

Neutrons interact with matter due to forces acting between neutrons and nuclei, while the interaction of X-ray radiation is predominantly electromagnetic. Incidentally, the attenuation characteristics of neutrons are complementary to X-ray radiation for many elements of interest for electrochemical energy storage and conversion systems (Figure 19). While neutrons are highly attenuated in light elements, such as hydrogen, lithium, or boron, X-ray radiation is subject to a regular increase of attenuation with atomic number [227]. This makes neutron imaging a powerful tool for visualization and quantification of processes in electrochemical energy storage and conversion devices, such as PEMWEs [88,90], PEM fuel cells [238,239], and lithium-ion batteries [240]. Further, neutrons interact with the magnetic moment of nuclei, allowing for visualization of magnetic fields and domains [91]. However, this is beyond the scope of this thesis.

The main mechanisms of neutron attenuation are absorption and scattering. Absorption occurs when a neutron is captured by a nucleus, leading to nuclear decay and the consequent emission of fission products, such as α-particles, neutrons, or γ-radiation. Scattering of neutrons is caused by the interaction of the neutron with the potential force of a nucleus, which depends on the nucleus configuration in a complex manner and is not a continuous function of nucleus size [227].

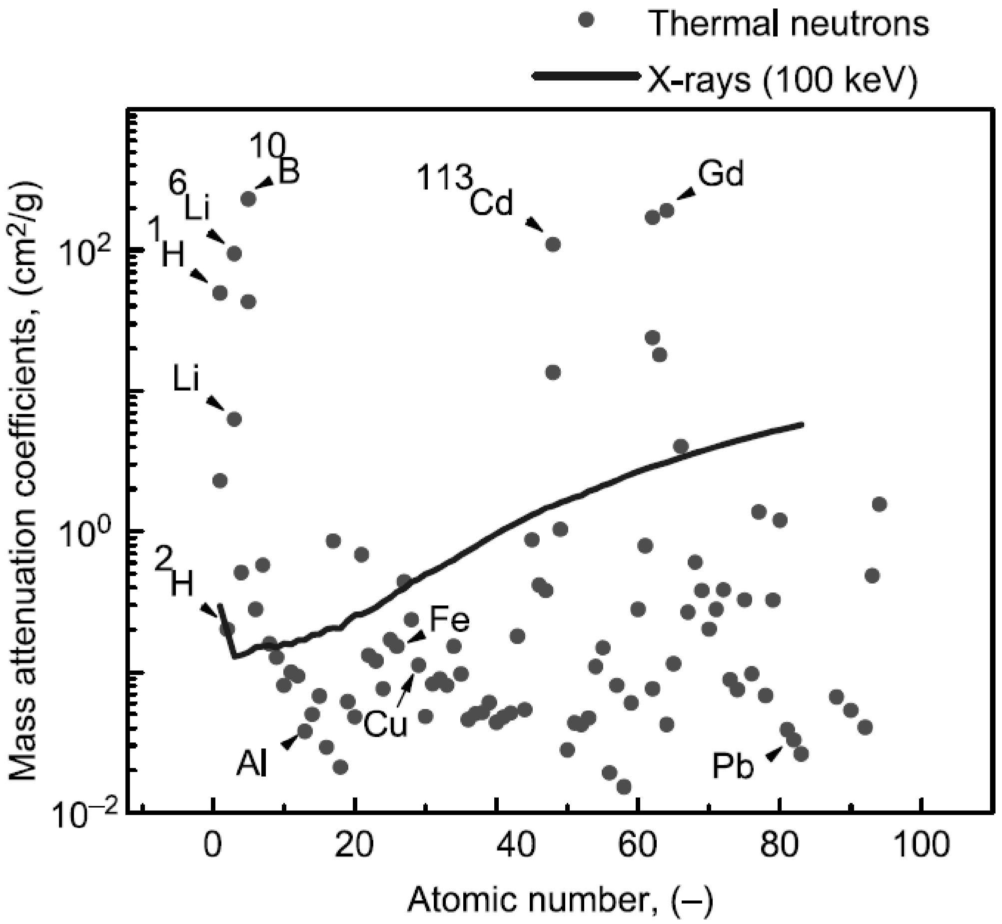

Figure 19: Attenuation coefficients as a function of the atomic number for thermal neutrons and X-rays. While the attenuation coefficient towards X-ray radiation is a continuous function of the atomic number, the neutron attenuation coefficient is non-continuous [241] *(Reprinted from Journal of Neutron Research. Vol 14. Kardjilov et al. Neutron tomography for archaeological investigations. 29–36. 2006, with permission from IOS Press. The publication is available at IOS Press through http://dx.doi.org/ 10.1080/10238160600673201).*

4.3.2.3 Neutron Imaging Acquisition and Detection

The acquisition systems for neutron imaging are conceptually similar to what has been described above for X-ray spectroscopy. The sample is located in the neutron beam between the detector and collimator. For tomographic acquisition, the sample is rotated around its axis and the individual frames are reconstructed into a three-dimensional data set (see Section 4.3.3). The incident neutron beam is attenuated by the sample due to the various mechanisms outlined above, while a fraction of neutrons is transmitted through the sample and onto the detector [227].

As for X-ray imaging, scintillators combined with CCD cameras are state-of-the-art for digitalized neutron image acquisition. However, due to the nature of neutrons' interaction with matter, very different scintillation materials are required. Commonly used scintillators are based on the nuclear decay of ^{6}Li, or ^{155}Gd and ^{157}Gd, after absorption of an incident neutron. Both elements are deployed in powder scintillator screens, either as Li/ZnS combination or as GdO_2S/Tb (Gadox). A more recent alternative to powder scintillators is based on a thin crystal layer, such as yttrium aluminium garnet (YAG), which offers higher resolution and photon yield [242].

4.3.2.4 Imaging Processing and Quantification

Neutron imaging can be used to acquire radiographic images (2D), but a number of radiographs taken during the rotation of the sample can be reconstructed into a tomographic (3D) data set. The method of acquiring and reconstructing tomographic data is equivalent to the processes used for X-ray imaging, outlined in Sections 4.3.3 and 4.3.1.3; however, as neutron imaging was solely used for 2D acquisition in this work the following will focus on the analysis of radiographic data.

The sample is placed in the collimated neutron beam, and the portion of the beam transmitted through the sample is detected. Typically, a large number of images are acquired and later median averaged to obtain a sufficient signal-to-noise ratio. This is also done with the sample removed from the beam and the resulting image (flat field) is subtracted from the sample acquisition to account for the specific acquisition sensitivity of the CCD camera. If parts of the sample remained unchanged throughout experiments, it is possible to eliminate their respective attenuation by acquiring radiographic data of only these parts and use it to normalize the sample radiographs. For PEMWEs, this procedure is realized by acquiring dry images of the cell before *operando* acquisition, hence without any liquid in the cell. The resulting data accounts for all parts of the PEMWE cell which remain unchanged during operation, such as end-plates, flow-fields, the titanium of the LGDL, and the CCM. When normalizing an *operando* PEMWE radiograph with this dry image, the resulting data excludes all cell parts imaged in the dry image and, hence, only accounts for the remaining components such as water and hydrogen gas. Details of the image analysis procedure are shown in Figure 20 and also described in previous work [90].

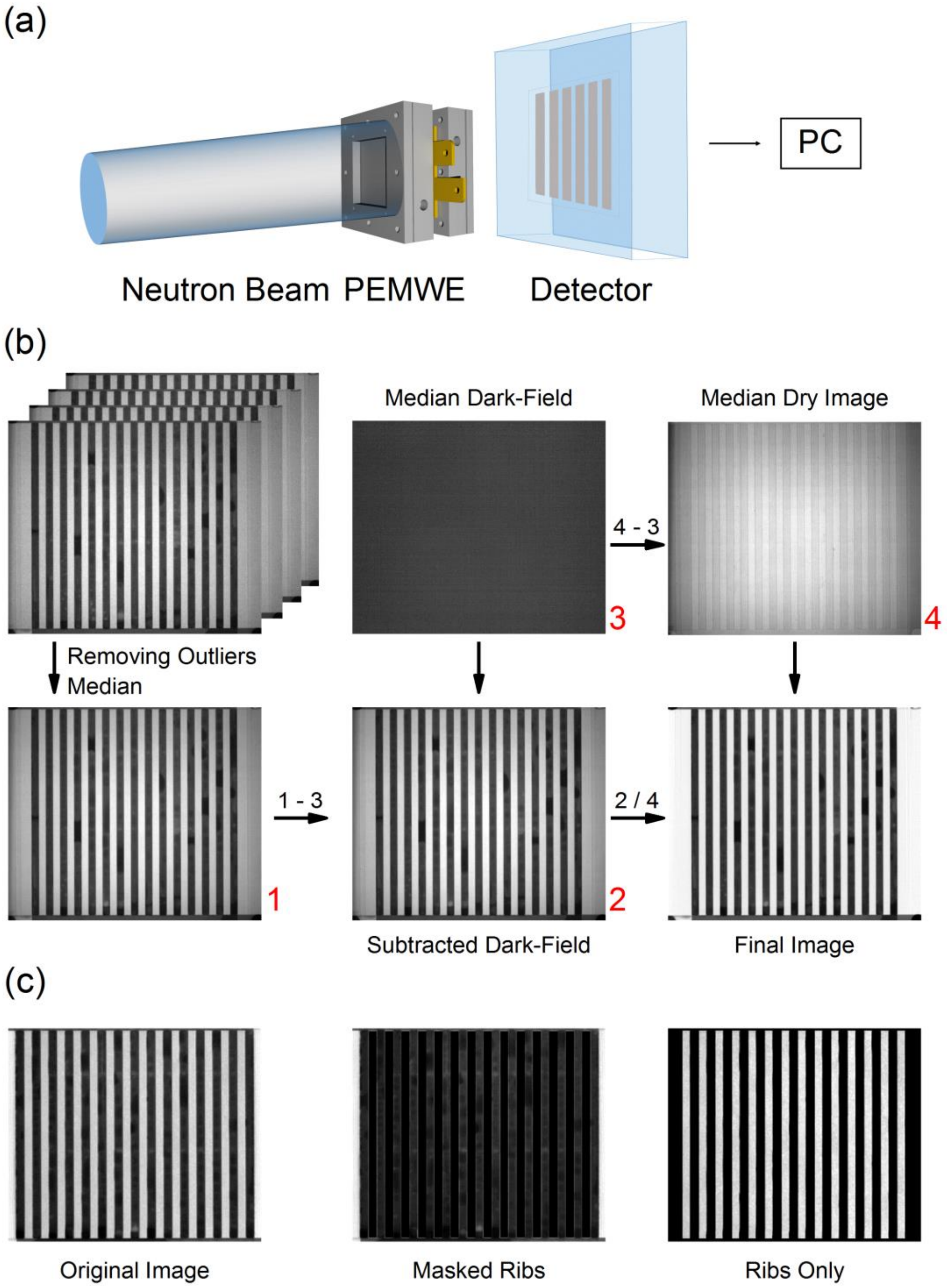

Figure 20: (a) The PEMWE is placed in a neutron beam. Due to the material-dependent attenuation of the neutrons, a radiographic image of the PEMWE is captured by the detector. (b) Each set of images is first filtered to remove outliers and averaged using a median. Then, the averaged dark-field is subtracted from the resulting image. This is then normalized with a dry image (also averaged) to obtain the final image. The greyscale values can be converted into the water thickness using the Beer-Lambert law. (c) The water thickness in the rib (land) areas is analysed separately by applying a mask, discarding the water thickness in the flow channels.

The attenuation of neutrons follows the Beer-Lambert law [227], so if image analysis yields radiographic data that only accounts for one component (e.g. water) the thickness of that component in the through-plane imaging direction can be calculated. This requires knowledge of the linear attenuation coefficient μ for the component, which is a function of the sample thickness and the distance between sample and detector. The Beer-Lambert law has been described in Section 4.3.1.2, and examples of its application to neutron imaging can be found in literature [85,88,90].

4.3.2.5 CONRAD Neutron Beamline

Neutron imaging results presented in this work were acquired at the CONRAD beamline at Helmholtz-Zentrum Berlin (HZB) [243,244], shown in Figure 21. CONRAD uses a beam of cold neutrons with a flux of $2.4 \times 10^{7}\ \mathrm{n\ cm^{-2} s^{-1}}$ and a CCD detector camera (Andor, 2048 × 2048 pixels) [243]. A spatial resolution of 20 µm at a field-of-view of 13 mm × 13 mm can be achieved [243], with rotational and translational stages allowing for sample positioning and tomographic acquisition. As outlined in Section 5.4.2, neutron imaging was used to visualize the entire PEMWE active area, with flow-field features being in the millimetre range, making neutron radiography at the CONRAD neutron beamline a suitable tool. A transparent crystal scintillator is used for neutron detection [242].

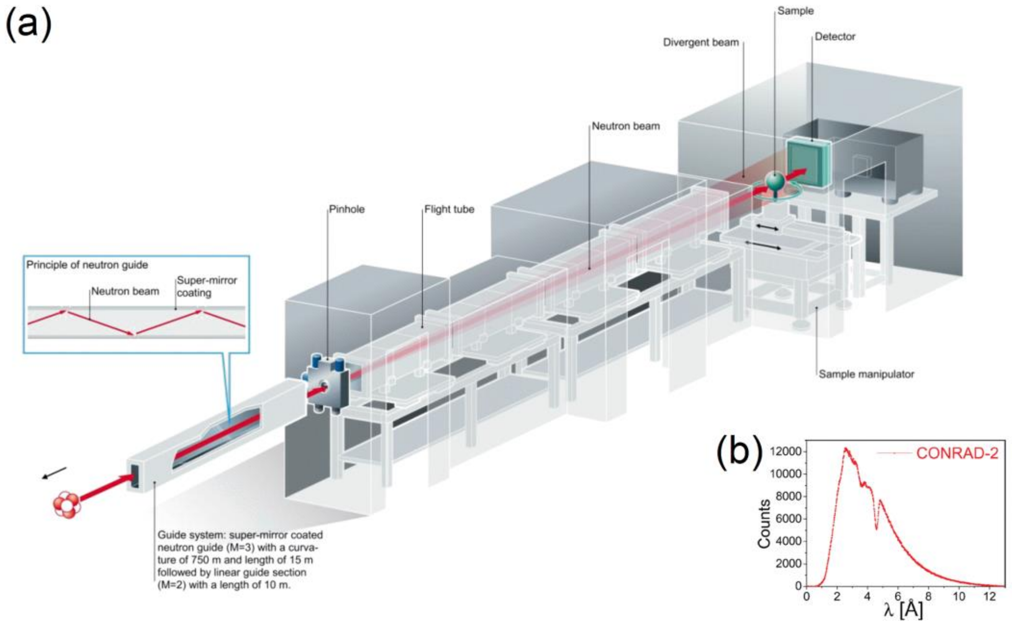

Figure 21: (a) The hutch setup at the CONRAD beamline HZB with collimated neutron beam, sample, and detector (Reprinted with permission under a CC BY 4.0 licence (https://creativecommons.org/licenses/by/4.0/legalcode) from [243] *'Kardjilov N et al., J Large-Scale Res Facil JLSRF, 2:2–7, https://jlsrf.org/index.php/lsf/article/view/108'. Copyright (2016) Journal of Large-Scale Research Facilities). (b) The neutron beam spectrum at CONRAD with a peak around 3 Å (Reproduced from* [244] *with permission of the International Union of Crystallography).*

4.3.3 Tomographic Reconstruction

Tomographic reconstruction is a process used to create a three-dimensional representation of a sample from a finite number of two-dimensional radiographs acquired at different angles. This requires the sample to be rotated around its central axis between the acquisitions of individual radiographs. Tomographic reconstruction is a mathematical procedure, which can be applied to X-ray as well as neutron imaging. However, this work is limited to the use of X-ray computed tomography, while neutron imaging was solely used for two-dimensional imaging.

Reconstructing a number of two-dimensional projections into a three-dimensional data set requires finding a function $f(x, y)$ which defines the values in each voxel of the sample. During acquisition, the integral along a horizontal line $x = x_0$ is measured in a specific detector pixel [227]:

$$\int_{-\infty}^{\infty} f(x_0, y)\, dy \qquad \text{(Equation 4-5)}$$

This can be visualised as an $N \times N$ array of elements with a homogenous attenuation coefficient μ for each element. The projection p is the summation of attenuation coefficients through the respective elements on the path of the beam through the sample (Figure 22). At least N^2 projection functions must be solved to determine the $N \times N$ array of attenuation coefficients [232].

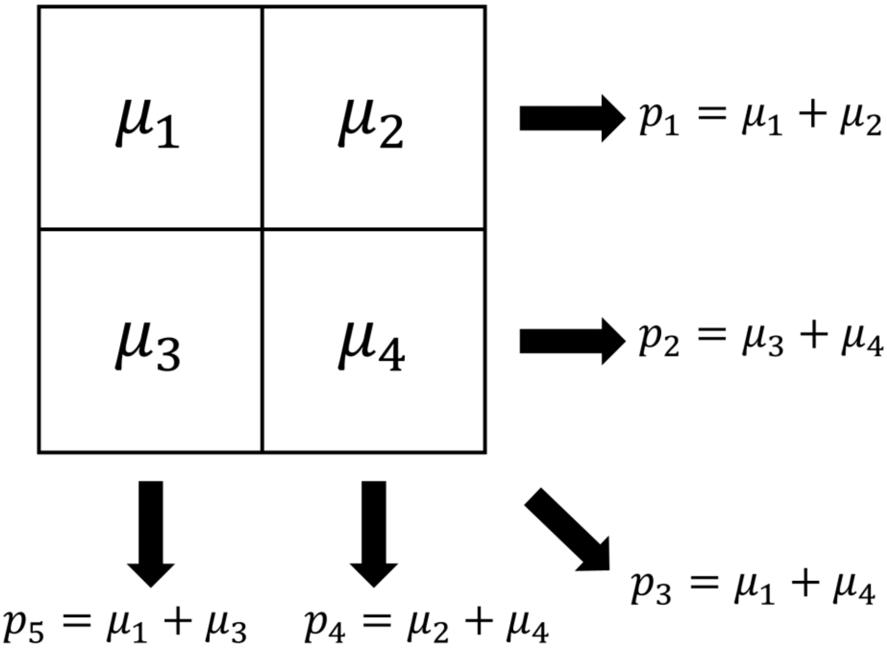

Figure 22: Visualisation of the tomographic reconstruction problem. The projection p*, which is measured by the detector, is the summation of the attenuation coefficients* μ *of the elements on the beam path* [232].

To account for the rotation of the sample around its axis by the angle ϑ, transformed coordinates (s, u) are introduced [227].

$$s = x\cos\vartheta + y\sin\vartheta \qquad \text{(Equation 4-6)}$$

$$u = -x\sin\vartheta + y\cos\vartheta \qquad \text{(Equation 4-7)}$$

The reconstructed function f can then be transformed between (s, u) and (x, y) by using the Radon transform $\Re$ [227].

$$|\Re f(s, \vartheta)| = \int_{-\infty}^{\infty} f(x, y)\, du \qquad \text{(Equation 4-8)}$$

Acquisition yields $|\Re f(s, v)|$, hence to determine f, the inversion of the Radon transform is required. All reconstruction algorithms are based on either the exact or approximate determination of the inverse Radon transform. However, the mathematical basis for obtaining this is beyond the scope of this work. The most commonly deployed solution for the problem described above is the filtered back-projection algorithm [227].

4.4 Acoustic Methods

Acoustic methods are low-cost, rapid, non-destructive, and *operando* diagnostic tools, using piezoelectric materials to generate and detect mechanical perturbations, which are then analysed with regards to the interaction or generation of these perturbations in the sample. Two different acoustic methods were used in this work: passive acoustic emission (AE) and actively probing acoustic time-of-flight (AToF). For a discussion of the application of acoustic methods to electrochemical devices, see Majasan et al. [245]. AE detects signals emitted by mechanical or chemical processes in the sample (e.g. cracking, phase transitions, bubble oscillations), while AToF sensors emit an ultrasound pulse and measure the portion of the signal which is reflected or transmitted by the sample.

Sound propagates as an acoustic wave of small, dynamic perturbations in a fluid or solid, which are subject to mass, momentum, and energy conservation [246]. The displacement of a particle ξ due to the acoustic wave can be described by the one-dimensional wave equation [247].

$$\frac{\delta^2\xi}{\partial t^2} = \left(\frac{\omega}{k}\right)^2 \frac{\delta^2\xi}{\partial x^2} = \left(\frac{\omega}{\frac{\omega}{v_s}-i\alpha}\right)^2 \frac{\delta^2\xi}{\partial x^2} \qquad \text{(Equation 4-9)}$$

Here, k is the wave number, $\omega\ (= 2\pi f)$ is the angular frequency, f is the frequency, v_s is the speed of sound, α is the acoustic attenuation coefficient, and $i = \sqrt{-1}$.

The speed of sound in a solid is a function of the elastic modulus E and the material density ρ [200,247]:

$$v_s = \sqrt{\frac{E}{\rho}} \qquad \text{(Equation 4-10)}$$

For sinusoidal waves, the solution of the above equation for the particle displacement is an exponential decay of the initial amplitude of displacement ξ_0 [247].

$$\xi = \xi_0\ e^{i(\omega t - kx)} \qquad \text{(Equation 4-11)}$$

The acoustic processes occurring in PEMWEs during operation or AToF probing are highly complex and cannot be easily be reduced to model systems. Hence, a mathematical description of acoustic processes in PEMWEs is beyond the scope of this thesis and the following chapters will be limited to phenomenological discussions.

4.4.1 Piezoelectric Materials

The ability of certain materials to produce an electric charge in response to mechanical stress is called piezoelectricity. It is a thermodynamically reversible process; hence, a mechanic strain is introduced into piezoelectric materials in an external electric field [248,249]. A range of materials exhibit piezoelectric properties, among the most common are single crystals, certain ceramics and electroactive polymers [248]. The microscopic mechanisms of piezoelectricity are highly complex and material-dependent, and are beyond the scope of this thesis. However, macroscopically the piezoelectric effect can be described as the relation between the induced electric field e and the external mechanical stress S, or between the external electrical field E and the induced strain σ, with the piezoelectric strain constant δ and the piezoelectric voltage constant g [248].

$$e = gS \qquad \text{(Equation 4-12)}$$

$$\sigma = \delta E \qquad \text{(Equation 4-13)}$$

Piezoelectric materials are crucial for the function of acoustic sensors and actuators. For AE, acoustic signals emitted by mechanical processes (e.g. bubble oscillations in a PEMWE) cause a voltage signal in the piezoelectric sensor, with its intensity and shape dependent on the nature of the original mechanical signal (sound). AToF measurements rely on a piezoelectric sensor to produce an ultrasound pulse from an input voltage signal, which is then used to probe a sample. The input ultrasound signal interacts with the sample, and a piezoelectric sensor is used to create a voltage signal from either the reflected or transmitted part of the ultrasound signal. The mechanisms by which mechanical perturbations are produced and altered in PEMWEs are discussed in the following chapter.

4.4.2 Sound and its Interaction with Matter

4.4.2.1 Sound Emission

Sound might be emitted from any source of mechanical stress in a sample, which makes acoustic methods a very versatile tool, but also greatly complicates the correlation between an acoustic signal and a specific source. Potential sources of acoustic signals include particle cracking [183,185], the formation of thin films [187,250], water or gas flow [191,192], the hydration of a polymer membrane [190], or the oscillation of gas bubbles in a liquid [218]. However, when applying an acoustic technique to a system for the first time, a thorough assessment of all physical and chemical processes is necessary to identify potential sources of an acoustic signal.

One sound-emitting process of particular relevance for this work is the oscillation of gas bubbles in a liquid. When a bubble is excited by a mechanical force (e.g. water convection in a PEMWE channel), it oscillates with a frequency that is specific to its oscillation-free bubble radius R_0 [251].

$$f = \frac{1}{2\pi}\sqrt{\frac{3\gamma p_\infty}{\rho_l R_0^2} - \frac{2\sigma}{\rho_l R_0^3}} \qquad \text{(Equation 4-14)}$$

Here, γ is the polytropic coefficient, p_∞ is the pressure at a point in the liquid far away from the bubble, ρ_l is the density of the surrounding liquid, and σ is the surface tension between liquid and gas. For systems similar to air-water the surface tension is negligible and one obtains [193].

$$f = \frac{1}{2\pi}\sqrt{\frac{3\gamma p_\infty}{\rho_l R_0^2}} \qquad \text{(Equation 4-15)}$$

This illustrates that the frequency of oscillation is inversely proportional to bubble size.

The magnitude of the amplitude of an acoustic event is determined by the pressure impulse emitted by the acoustic event. In the case of a multitude of bubbles oscillating at the same time the resulting pressure pulse p_{res} directly scales with the number of bubbles N and the pressure impulse p emitted by one bubble [193]:

$$p_{res}^2 = N\, p^2 \qquad \text{(Equation 4-16)}$$

This equation can be used to draw conclusions on the origin of an acoustic signal. If the number of bubbles varies, e.g. when the flow regime changes, the resulting pressure impulse is expected to change. When observing a constant pressure impulse, and hence a constant acoustic amplitude, the source of acoustic emission is likely to be single bubble events and not the simultaneous oscillation of a multitude of bubbles (see Section 6).

4.4.2.2 Sound Attenuation

In line with the fundamental description outlined above, an acoustic perturbation originating in the sample propagates in all directions. Its intensity continuously decreases as the distance from the acoustic source increases, highlighting the need to place the acoustic sensor as close to the acoustic source as possible. As the sound propagates through a medium, its initial peak amplitude A_0 is attenuated exponentially and reaches the amplitude A at a distance x [247]:

$$A = A_0 e^{-\alpha x} \qquad \text{(Equation 4-17)}$$

The main causes of acoustic attenuation in a medium are absorption, which predominantly converts acoustic energy into heat, and scattering [247]. However, the exact mechanisms are beyond the scope of this thesis.

Further, the acoustic intensity of a perturbation drops when propagating through a phase interface as a part of the energy is reflected. The ratio of reflection R and transmission T at an interface is a function of the acoustic impedances Z_1 and Z_2 of the two phases forming the interface [247].

$$R = \frac{Z_1 - Z_2}{Z_1 + Z_2} \qquad \text{(Equation 4-18)}$$

$$T = \frac{2Z_1}{Z_1 + Z_2} \qquad \text{(Equation 4-19)}$$

Hence, if the two phases are acoustically matched ($Z_1 = Z_2$), the acoustic perturbation is fully propagated through the interface ($R = 0$). For many materials, in particular solids, the acoustic impedance is the product of density ρ and the speed of sound [247,252].

$$Z = \rho v_s \qquad \text{(Equation 4-20)}$$

As mentioned above, scattering is a major contributor to the overall attenuation of an acoustic signal. Scattering within a solid can be described macroscopically by the attenuation coefficient α, as shown above. However, due to its particular relevance to PEMWE systems, attenuation via resonant scattering from gas bubbles and bubble clouds will be discussed in more detail here. Resonant scattering occurs when sound propagates through a liquid medium with one or more bubbles in it, as the sound perturbation causes bubbles to oscillate and therefore absorb a part of the acoustic energy [247]. Depending on the size of the bubble or bubble cloud, a resonance frequency exists at which the bubble oscillations induced by the mechanical perturbation are maximal; hence, the attenuation due to energy transfer from the sound perturbation to bubble oscillation is maximised as well. Knowledge of this specific frequency allows to draw conclusions on the size of the gas bubbles or the gas volume fraction in the sample. The resonance frequency f_r of an individual bubble is a function of its radius r, the density of the surrounding liquid ρ_l, the ambient pressure p_∞, and the polytropic coefficient γ (ranges between 1.0 (isothermal) and 1.4 (adiabatic)) [193,253]:

$$f_r = \frac{1}{2\pi}\sqrt{\frac{3\gamma p_\infty}{\rho_l r^2}} \qquad \text{(Equation 4-21)}$$

However, most systems contain a multitude of gas bubbles in close proximity (e.g. the flow channels of a PEMWE). Depending on their size, each bubble exhibits an individual resonance frequency, contributing to the overall resonance frequency spectrum of the bubble cloud. The overall resonance frequency of a bubble cloud (radius r_c) is a function of the volume fraction of gas x in it [253].

$$f_r = \frac{1}{2\pi}\sqrt{\frac{3\gamma p_\infty}{x\rho_l r_c^2}} \qquad \text{(Equation 4-22)}$$

4.4.3 Acoustic Emission Testing

Acoustic emission (AE) is a diagnostic tool using a piezoelectric sensor to detect mechanical perturbations emitted by a sample (Figure 23 (a)). The sensor generates a continuous voltage signal, with its intensity and shape dependent on the sound detected from the sample. For ease of analysis, acoustic hits are extracted from the continuous voltage signal if a predefined noise threshold is exceeded. Choosing an adequate noise threshold ensures that random noise is excluded from the data analysis, while all relevant signal from the sample is detected. Selecting an appropriate value for the noise threshold often requires initial experiments and knowledge of the acoustic equipment used.

An acoustic hit begins when the signal exceeds the noise threshold and ends when the signal falls back below the threshold (Figure 23 (b)). The voltage-time profile between these start and end points forms the hit waveform. Besides the number of hits per unit time, a number of hit characteristics are used for data analysis and to draw conclusions on the underlying physical and chemical processes causing the mechanical perturbations detected by the AE sensor. These include the hit amplitude (peak intensity), the hit duration, the hit rise time (time between exceeding the noise threshold and reaching the peak intensity), the hit energy (the area below the hit profile in the waveform), the hit frequency, or the hit counts (number of individual peaks in the hit waveform). The use of other key metrics is possible and a range of methods have been deployed to extract conclusions from the vast amount of data generated by AE, e.g. principal component analysis [192,254] or machine learning [194].

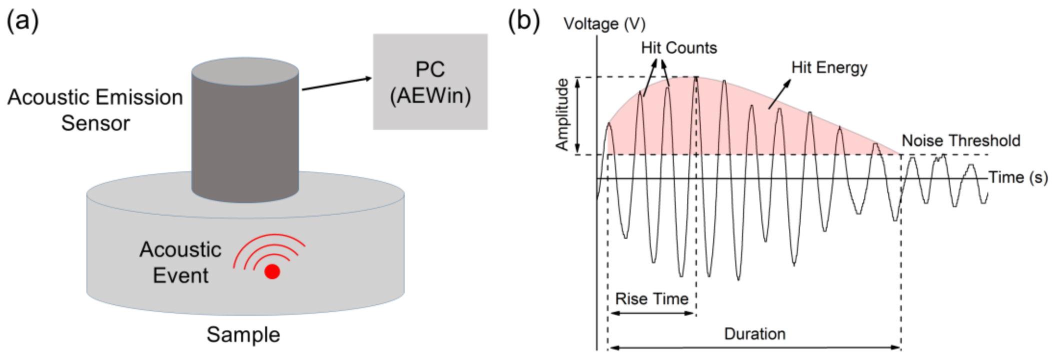

Figure 23: (a) The acoustic sensor is placed on the surface of the sample, providing a non-destructive, low-cost technique to detect acoustic events caused by physical or chemical processes. (b) Several characteristics, such as hit amplitude, duration, rise time, counts, or energy, can be extracted from the hit waveform for further analysis.

Throughout this work, an AE equipment set consisting of a S9208 sensor, a 26 dB pre-amplifier, a USB node, and the software AEWin was used (all Mistras NDT, USA). The USB node extracted acoustic hits from the sensor signal and data were recorded and analysed in AEWin.

4.4.4 Acoustic Time-of-Flight Testing

Acoustic time-of-flight (AToF) is an actively probing diagnostic technique based on probing a sample with an ultrasound pulse generated by a piezoelectric sensor (Figure 24 (a)). As outlined above, this acoustic signal is partly reflected and partly transmitted as it propagates through a sample. For AToF measurements, either the transmitted or reflected (or both) parts of the probing signal are detected and analysed. However, in this work, only pulse-reflection measurements were obtained. The resulting signal is a voltage-time profile (Figure 24 (c)), with its change over time, sample location, or experimental conditions being the main analysis technique. Either the change in the intensity [204] or the time-of-flight [200,205] of specific peaks can be analysed; however, as outlined for AE above, AToF measurements yield large amounts of data which can be analysed with a multitude of approaches (e.g. supervised machine learning [202]). An example of mapping the acoustic reflection intensity across the sensor width as a function of time is shown in Figure 24 (d). The AToF measurements in this work were taken with an acoustic array of 64 individual sensors (Figure 24 (b)), with every measurement being the average from a 'sensor unit' (16 adjacent sensors). Every sensor generated an input pulse frequency with a maximum repetition frequency of 20 kHz and measured the reflected signal (pulse-echo mode). The acoustic array was controlled and data recorded with an Olympus FOCUS PX system (Olympus Scientific Solutions, USA). A thin layer of acoustic gel (D12 Couplant Gel, Olympus Scientific Solutions, USA) was applied to the surface of the acoustic array before experiments to maximise the transmission of the probing signal into the PEMWE. The FocusPC software (Olympus Scientific Solutions, USA) was used for real-time data visualisation and export.

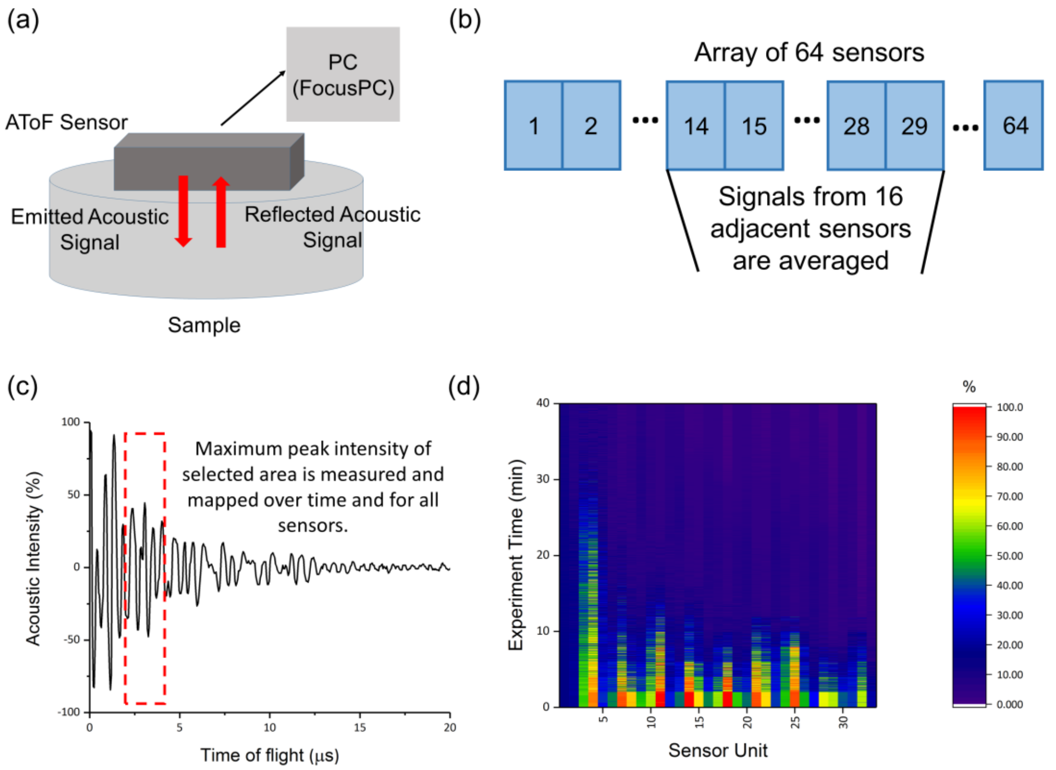

Figure 24: (a) The AToF sensor array consisting of 64 individual sensors is placed on the sample surface. It emits an acoustic pulse into the sample and measures the reflected signal. (b) For each measurement, the measured reflection signal from 16 adjacent sensors is averaged, resulting in (c) an acoustic waveform. A specific peak or time-of-flight interval is then selected and the maximum peak intensity in this interval is measured. (d) By mapping this maximum intensity across all units of 16 sensors (sensor unit) and another experimental variable (e.g. time), detailed information on processes in the sample can be obtained.

4.5 Fast Fourier Transform

Fourier transformation is a method of obtaining the frequency spectrum of a time series, e.g. a voltage-time profile. To analyse discretely sampled data the discrete Fourier transform is used, with the fast Fourier transform (FFT) being an especially efficient solution of the discrete Fourier transform [255,256]. The mathematical foundations of the FFT are beyond the scope of this thesis, but it was used to analyse data obtained with acoustic emission (AE) and acoustic time-of-flight (AToF) imaging. The frequency of individual AE hits was determined in AEWin, while the frequency of pulse-echo AToF waveforms was measured using the FocusPC software.

4.6 Conclusions

This work employs imaging-based techniques to gain insight into the water-gas distribution in the LGDL and flow channels; however, due to cost and accessibility concerns afflicted to neutron imaging, acoustic diagnostic tools are introduced to investigate mass transport processes in PEMWEs. Hence, this section described the underpinnings of these techniques, enabling a thorough understanding of the experimental results presented later. The underlying mechanisms of X-ray and neutron production for imaging, the interactions of photons and neutrons with matter, and the acquisition and detection of photons and neutrons were outlined. A brief description of tomographic reconstruction of two-dimensional data sets into a three-dimensional sample representation was given.

Lastly, the fundamentals of wave theory were described, followed by a discussion of the interaction of sound with matter, and piezoelectric materials, which are crucial for acoustic diagnostic methods.

5 *The Influence of Liquid-Gas Diffusion Layer Microstructure on the Water-Gas Distribution*

5.1 Overview

In this chapter, neutron radiography is deployed to measure the spatial distribution of water within three different LGDLs, while X-ray micro-computed tomography (XCT) is used to characterize the microstructure of the LGDL materials. The combination of these two techniques yields valuable insight into water transport within the LGDL and the influence of microstructure on the water-gas distribution. Significant local water heterogeneity is observed and results suggest a link between flow-field geometry/location and LGDL mass transport. It is further shown that the pore volume in these LGDLs is significantly under-utilized, pointing the way towards design optimisation of LGDL materials and architectures. The work in this chapter has been published in *Journal of Power Sources* [90].

5.2 Introduction

The ability of neutrons to penetrate many materials with a high molecular mass, while being strongly attenuated by specific light materials, such as hydrogen and lithium, makes neutron imaging a powerful tool for visualizing water distribution in PEMWEs. By combining neutron imaging with X-ray micro-computed tomography (XCT) the water-gas distribution in the LGDL can be related to its microstructure.

This chapter uses operando through-plane neutron radiography of PEMWEs at current densities of up to 1.5 A cm^{-2} to examine mass transport of water within LGDLs under rib (land) locations. As outlined in Section 5.3.1, the PEMWE cell used in these experiments used aluminium components to maximise neutron transmission, however, this led to reduced electrochemical performance. Hence, to avoid excessive voltages, the PEMWE cell was only operated up to 1.5 A cm^{-2}. Three different LGDL materials, one sintered powder, and two fibrous materials, are investigated and XCT is employed to link the microstructure of the LGDL to its mass transport and the water saturation in the LGDL pores.

5.3 Experimental

More details on the experimental procedure can be found in Section 4.1; however, all information necessary for the understanding of the experiments outlined in this section can be found below for the reader's convenience.

5.3.1 PEMWE Cell

The PEMWE cell used for these experiments (Figure 25), consisted of two aluminium end plates (thickness: 20 mm), gold coated, aluminium parallel channel flow-field plates (thickness: 3 mm) on both anode and cathode sides, a titanium LGDL on the anode side, Toray carbon paper (thickness: ~100 µm) as gas diffusion layer (GDL) on the cathode side, and a catalyst coated membrane (CCM, thickness: ~150 µm) with a square active area of 25 cm^2. An aluminium holder was used at each end of the cell to ensure an even pressure distribution over the active area. The PEMWE cell was held together with four inner M3 screws (tightened to 1.7 Nm) and four outer M5 screws (tightened to 2.3 Nm). Kapton tape was applied to the end-plates and the bolts to avoid electrical shorts between end-plates and flow-fields. The flow-fields consisted of 15 parallel, vertical channels with a length of 5 cm, a depth of 3 mm, evenly distributed over the active area, which is similar to flow-field geometries previously employed [40,72,83]. The CCM was based on Nafion 115, with 0.6 mg cm^{-2} of platinum on carbon on the cathode side and 3.0 mg cm^{-2} of iridium/ruthenium oxide on the anode side (ITM Power, UK). The different types of LGDL are shown in Table 2.

The parallel flow-fields were designed with diagonally opposing inlet and outlet, as described by Majasan et al. [73] and discussed in Section 3.2.3. In these Z-type flow-fields, a non-uniform distribution of water flow velocity and pressure is observed. Due to the pressure field enforced by the flow-field geometry, flow through the channels near the outlet is favoured. It was found that the flow velocity in the channels closest to the outlet is significantly higher than in the remainder of the channels (up to a factor of 5) [72,75,76].

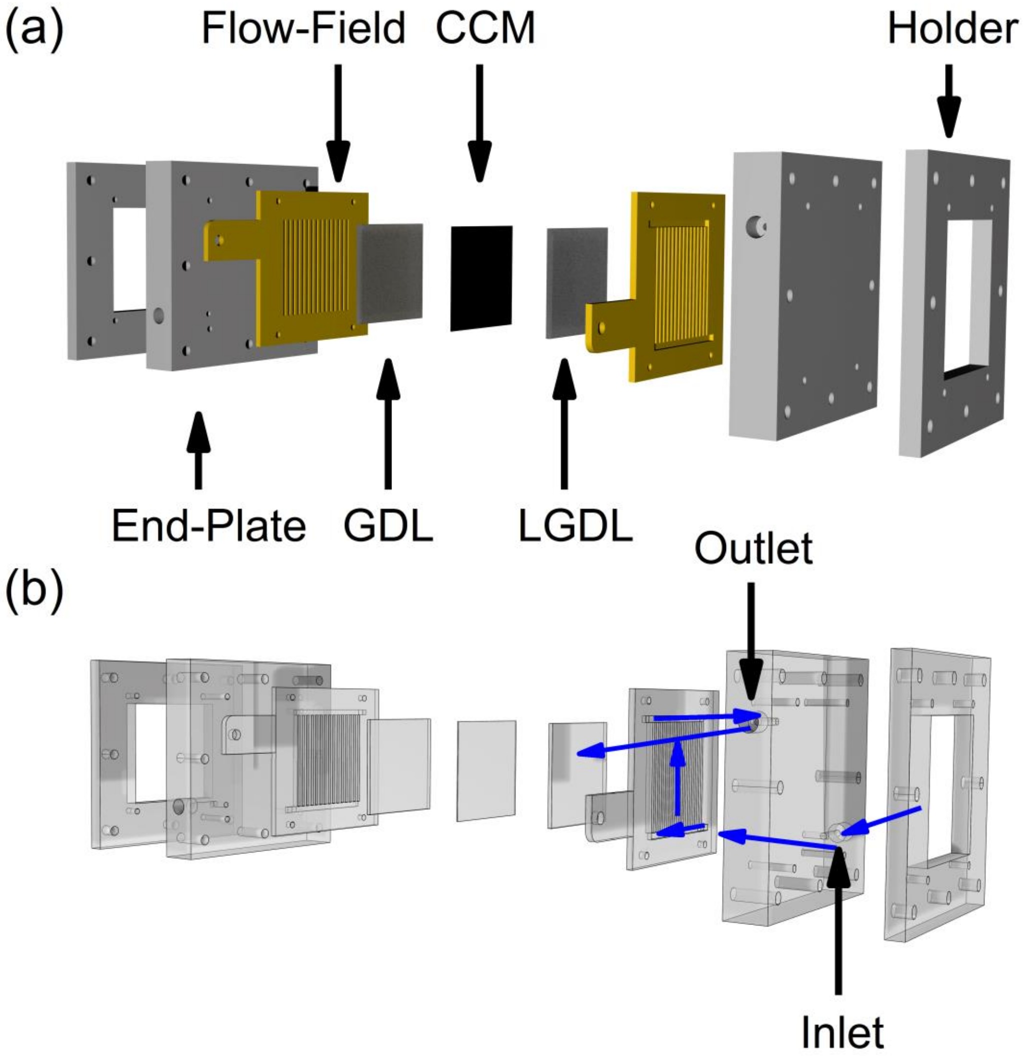

Figure 25: PEMWE cell used for all experiments in this work. (a) The cell consists of two aluminium holders and end-plates, two gold-coated, aluminium, parallel channel flow-field plates, a titanium liquid-gas diffusion layer (LGDL) on the anode side, a carbon paper gas diffusion layer on the cathode side, and a catalyst coated membrane (CCM). (b) The water inlet is placed at the bottom of the flow-field, with the outlet being placed diagonally opposite at the top of the flow-field. Blue arrows indicate the path of water flow for one of the electrodes.

Electrochemical testing was performed between 0 A cm^{-2} and 1.5 A cm^{-2} with an IviumStat potentiostat connected to an IviumBoost10012 (100 A, Ivium Technologies, Netherlands). Deionized water was circulated through the anode side of the PEMWE with an inflow temperature of 50 °C and a constant water flow rate of 100 ml min^{-1}, which equals a water ratio [40] of 47.6 at 1.5 A cm^{-2}. This high rate of water circulation was chosen to ensure effective gas removal in all channels such that the mass transport effects within the LGDL could be highlighted. The cathode side was run dry without water inflow.

Table 2: Description, thickness, and supplier of the three LGDLs used in this chapter. The ID will be used in the text to refer to a specific LGDL.

ID	Description	Thickness (mm)	Supplier
Sinter	Sintered titanium particles	2.0	Merelex (USA)
Thick Felt	Sintered titanium fibres	1.0	NIKKO Techno (Japan)
Thin Felt	Sintered titanium fibres	0.1	NIKKO Techno (Japan)

5.3.2 Neutron Imaging and Imaging Analysis

Neutron radiography was carried out at the Cold Neutron Tomography and Radiography beamline V7 (CONRAD) at Helmholtz-Zentrum Berlin, Germany. For every set of conditions, 30 through-plane images were taken with an exposure time of 5 s. For the detector system [242] a pixel size of 23.9 µm with a corresponding total field-of-view of 49 x 49 mm was set. Before starting an experiment with a specific LGDL, images without neutron beam (dark-field) and of the PEMWE cell before water was pumped through it (dry image) were taken (30 images each, 5 s exposure).

All images were then analysed using ImageJ (Fiji, Version 1.52p). Outliers were removed from all images (Radius: 2 pixels, Threshold: 50). Then each set of 30 images (PEMWE cell, dark-field, dry images) was median averaged and the dark-field was subtracted. These images were then normalized by dividing by the dry image. This accounts for dead pixels on the detector, the locally varying intensity of the neutron beam and also removes the contributions from PEMWE components which remain unchanged during operation (end plates, flow-fields, and titanium in the LGDL). The greyscale value was converted to a water thickness using the Beer-Lambert law [154,238]. The distance between PEMWE cell and detector was 10 cm, which reduced the effect of neutron scattering and therefore improved the accuracy of the quantification of water thickness. For this distance between cell and detector, the attenuation coefficient of neutrons in water was 5.2 cm^{-1}, as provided by the beamline. Details on the image analysis can be found in Section 4.3.2.4 and Figure 20.

The purpose of this study is to examine the water/gas composition within the LGDL. To do this, the land locations are focused on as the open flow channels are dominated by relatively unstable two-phase flow with time-varying bubble dynamics, which precludes accurate analysis of the effective water thickness in the LGDL. Indeed, flow dynamics within channels have been extensively studied using optical cells [43,44,73,218], but it is the particular ability of neutron imaging to examine water under lands and within porous structures that is exploited here [87,88].

A potential limitation of the through-plane measurement technique is that the results for the water thickness are a summation of water through the anode, cathode and membrane components. This is another reason the water thickness is only quantified for the rib (‘land’) areas. However, as the CCM was fully hydrated before the experiments and remains so throughout these experiments, and the CCM and carbon paper are relatively thin, water in the LGDL of the anode side will dominate the neutron absorption response.

5.3.3 X-ray Micro-Computed tomography

X-ray computed tomograms were acquired for all LGDL materials used in this chapter. The Zeiss Xradia Versa 520 (Carl Zeiss X-ray Microscopy Inc., Pleasanton, CA) lab-based X-ray system was used to acquire the XCT datasets. The acquisition parameters are summarized in Table 3. Radiographic images were reconstructed into tomograms with the Zeiss Scout-and-Scan Control System Reconstructor software. Volume renderings were generated and analysed using Avizo (Thermo Fisher Scientific, US), which is a well-established tool for the segmentation and analysis of XCT datasets of porous media [257–259]. The greyscale tomograms were then segmented using a manual threshold method according to the greyscale value. The porosity of the sample was calculated from this segmentation. Avizo was then used to create a pore network model (and the related pore size distribution), from which the flux of water at 50 °C through the LGDL with an input pressure of 1.3 bar and an output pressure at 1.0 bar was calculated in the software. Tortuosity values were calculated using TauFactor, which has been extensively validated against other methods of tortuosity calculation [234].

Table 3: Voltage, power, exposure time per projection, number of projections, voxel size, and sample diameter chosen for acquisition over 360° of XCT datasets.

ID	Tube Voltage [kV]	Power [W]	Exposure Time [s]	Number of Projections	Voxel Size [µm]	Sample Diameter [mm]
Sinter	80	7	7	1601	1.85	3
Thick Felt	80	7	7	2401	1.52	3
Thin Felt	60	5	10	2401	1.52	3

5.3.4 Water Saturation and Residence Time

Information on the water saturation (fraction of pores filled with water) and the water residence time in the LGDL can be obtained by combining neutron imaging and XCT data. As mentioned in Section 5.3.2, the water thickness can only be reliably calculated for the rib areas. Hence, the analysis of water saturation and residence time is limited to these areas. The water saturation S is obtained by dividing the volume of water in the LGDL by the total pore volume. The water volume is the product of the averaged water thickness W and the active area A. As the total pore volume of the LGDL is the product of its thickness d the porosity ε and the active area, one obtains:

$$S = \frac{W}{\varepsilon d} \qquad \text{(Equation 5-1)}$$

This value indicates the fraction of pore volume that is filled with water, which equates to the pore utilization of the LGDL. Similarly, the average water residence time in the LGDL τ is obtained by dividing the amount of water in the LGDL by the total amount of water transported through it per unit time M which is comprised of the water consumption due to the oxygen evolution reaction (determined using Faraday’s law and average current density) and electro-osmotic drag through the CCM. This assumes that all water entering the LGDL is either electrochemically reacted or carried across the membrane.

$$\tau = \frac{\rho W A}{M} \qquad \text{(Equation 5-2)}$$

Details on the calculation of these mass flows were described by Ito et al. [40,41] and can be found in Section 3.2.2. M is typically a gravimetric value, hence the density of water ρ is used to convert τ into a volumetric value.

5.4 Results and Discussion

5.4.1 Structural Characterisation of LGDLs using X-ray CT

Tomograms of all three LGDL materials, as well as the pore size distribution (PSD), are shown in Figure 26. As outlined in Section 5.3.3, voxel sizes of below 2 µm were obtained for all three LGDLs. As minimum pore sizes of around 20 µm are observed in the samples, XCT is a suitable tool to address and analyse the microstructure of the LGDLs used in this work, but it should be noted that pores smaller than the resolution of the XCT data sets cannot be investigated with the given methodology. Values for the porosity (with and without disconnected pores), pore volume (product of LGDL volume and porosity), and the through-plane tortuosity are given in Table 4.

Table 4: Porosity, porosity without disconnected pores, pore volume, and through-plane tortuosity for the three LGDLs, obtained from X-ray CT.

ID	Porosity [%]	Porosity without disconnected pores [%]	Pore Volume [mm^3]	Tortuosity
Sinter	29.5	28.7	1476.4	3.3
Thick Felt	47.1	42.3	1177.3	2.2
Thin Felt	76.9	60.5	192.2	1.4

The sinter (Figure 26 (a)) exhibits a coarse structure of large particles with relatively few large pores. Porosity is found to be around 30 %, which is close to values previously found for sinter materials [114]. The vast majority of pore radii varied between 75 µm and 400 µm. A tortuosity of 3.3 was calculated for the sinter.

The thick felt (Figure 26 (b)) consists of densely packed titanium fibres, with fibres and pore space very evenly distributed. Porosity is around 47 %, significantly higher than for the sinter. The pore size distribution ranges from 20 µm to 140 µm, which is considerably smaller than for the sinter. The thick felt has a tortuosity of 2.2, which is 33 % lower than for the sinter.

The titanium fibres in the thin felt (Figure 26 (c)) are less densely packed than for the thick felt. Therefore, the space between the fibres is highly interconnected, resulting in very large pores. Hence, a major portion of the pore volume is attributed to these pores with an equivalent radius between 200 µm and 300 µm. Besides these large pores, there are a number of smaller pores with a PSD ranging from 20 µm to 160 µm. A porosity of around 77 % is measured for the thin felt. As a consequence of the high porosity, the thin felt also exhibits a low tortuosity of 1.4.

As the thick felt is much more porous than the sinter, but only half as thick, these two LGDLs exhibit a similar pore volume of ≥ 1000 mm^3. The thin felt is much more porous than the sinter and thick felt, but due to its low thickness has a pore volume of only around 200 mm^3. Hence it is expected that a much higher percentage of the thin felt is filled with water than for the other two LGDLs.

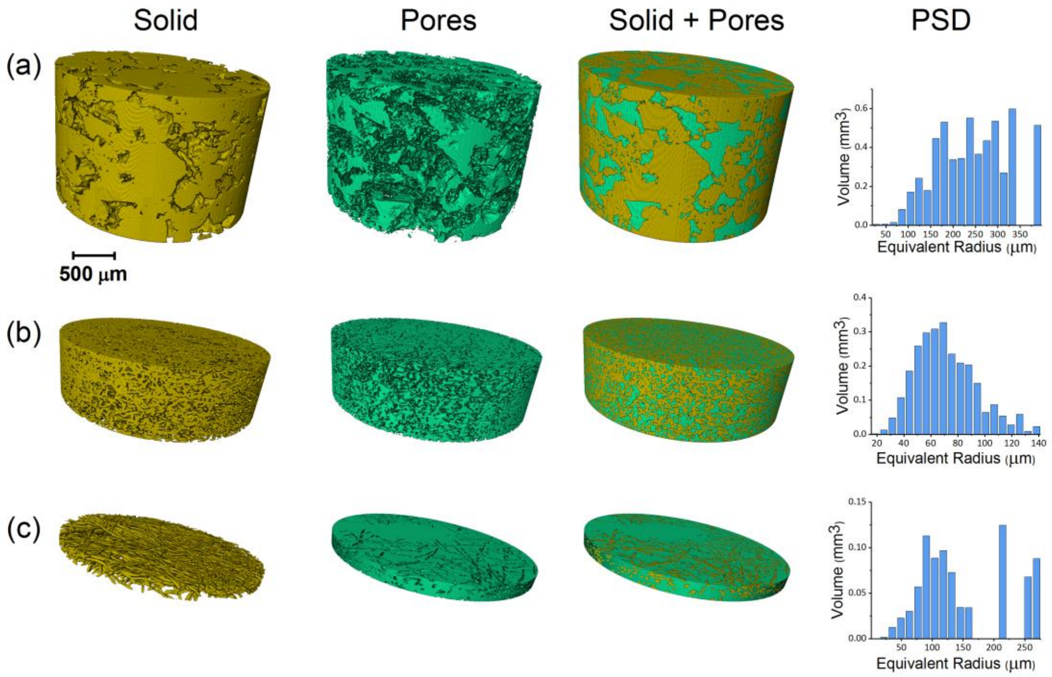

Figure 26: X-ray micro computed tomograms of (a) sinter, (b) thick felt, and (c) thin felt. The solid material, pore space, conjunction of solid and pores, and the pore size distribution (PSD) are shown.

The differences in pore size and distribution are further illustrated in Figure 27, which shows the pore network model for the sinter and the thick felt. Due to the low thickness of the thin felt, no reliable pore network model could be created for this LGDL. The pore network model (Figure 27 (a) and (e)) consists of pores (spheres, Figure 27 (b) and (f)) and throats (cylinders, Figure 27 (c) and (g)). After calculating the flux of water through the pore network model (Section 5.3.3), the flow through each throat can be visualised (Figure 27 (c) and (g)). The same throat network is also displayed with the throats being scaled and colored by their radius (Figure 27 (d) and (h)). The comparison between the size-dependent and the flow-dependent scaling of the throats reveals that specific pathways for water flow through the LGDL are clearly favoured. The idea of preferential pathways through the LGDL of a PEMWE has been proposed and visualized for oxygen gas bubbles [83] and for water transport [160,161] and is further supported by the negligible water flow through the majority of throats in the pore network model of sinter and thick felt. This indicates that a majority of flow occurs through a small fraction of available pathways, even though these pathways do not necessarily have wider throats.

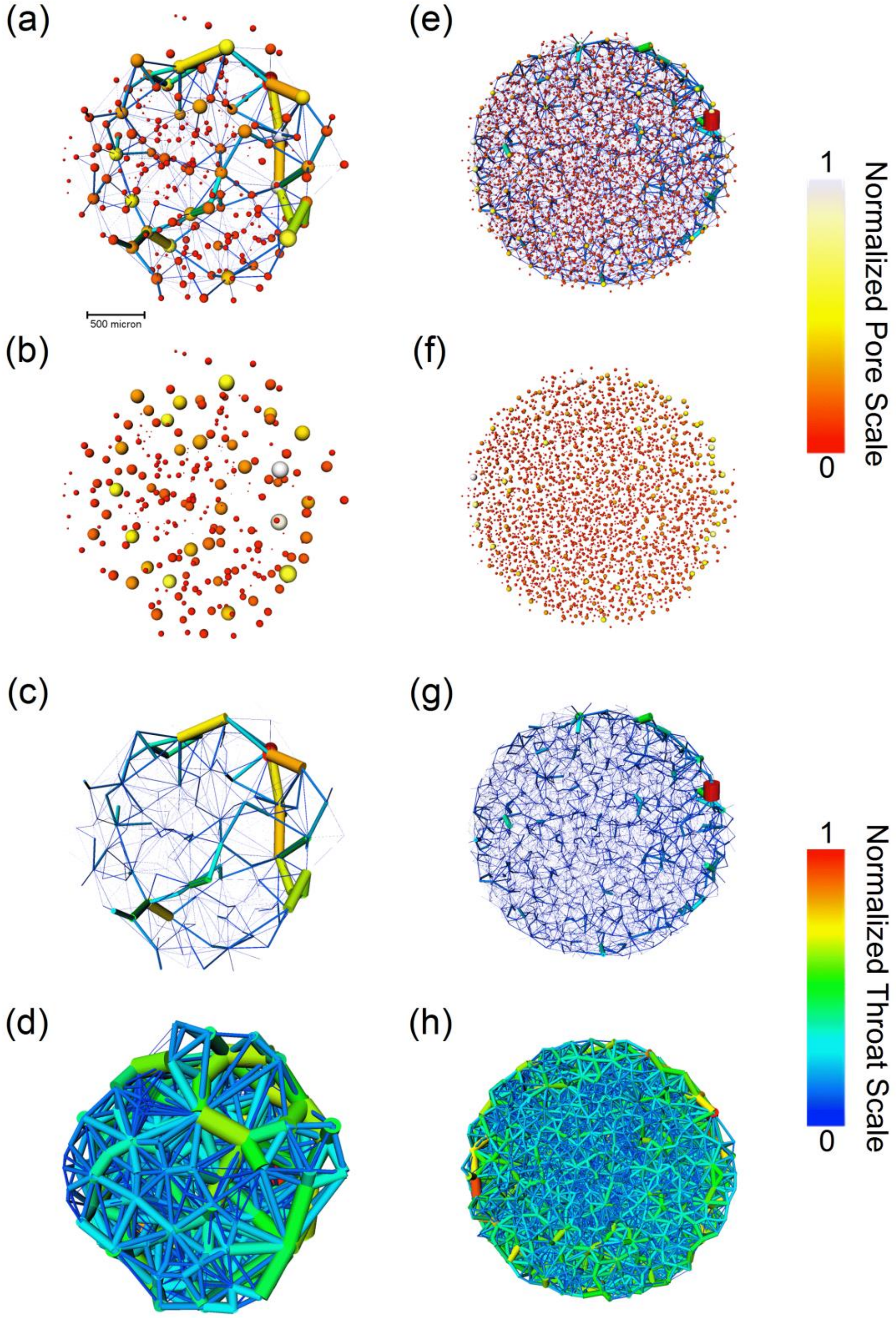

Figure 27: Pore network model for the sinter ((a) – (d)) and the thick felt ((e) – (h)). The whole network ((a) and (e)) consists of pores (spheres) and throats (cylinders). Pores ((b) and (f)) are scaled according to their radius and colored according to their volume. Throats are scaled and colored by water flow through the respective throat ((c) and (g)), or according to their radius ((d) and (h)). The color maps are all normalized to the maximum value in the specific LGDL.

5.4.2 Water Distribution using Neutron Imaging

Images of the active area of the PEMWE with LGDL and flow channels are shown as a function of current density for all three LGDLs in Figure 28, with the water thickness being displayed as a color map. For the LGDLs, a water thickness between 0.0 mm (white) and 0.5 mm (pink) is observed, while a water thickness between 0.6 mm (red) and 3.0 mm (black) is found in the flow channels. As current density is increased, the water thickness would be expected to decrease in the LGDL and the flow channels due to the higher water consumption rate (gas production rate). For the sinter, a clear trend of increasing amounts of oxygen (indicated by a reduction in water thickness) can be observed with increasing current density. However, the decrease of water thickness is relatively modest over this range.

The same trend, albeit more pronounced, can be seen for both fibrous materials. The thin felt is already mostly filled with gas at a current density of 0.25 A cm^{-2} and exhibits a water thickness close to 0 mm for higher current densities across the whole active area. This illustrates the widely different gas and water transport properties of different materials due to their varying thicknesses and porosities. Further, the porous structure of the sintered material with relatively larger pores can be clearly discerned, revealing its courser microstructure, as shown in Section 5.4.1. The felts, on the other hand, display a more homogenous distribution of gas, consistent with the smaller pore sizes found from the XCT analysis.

Further, the water-gas distribution in different flow channels can be observed and higher amounts of gas (lower water thickness) can be seen in the top-right corner of the flow-field. The cause of this gas accumulation is unclear, but it can be caused by non-uniform distribution of water flow across the flow channels (see Section 3.2.3) [72,75,76]. This highlights the possibility to investigate non-uniform water-gas distribution in PEMWE flow channels using neutron radiography and emphasizes its potential to examine different flow-field geometries and engineering approaches for PEMWE optimisation.

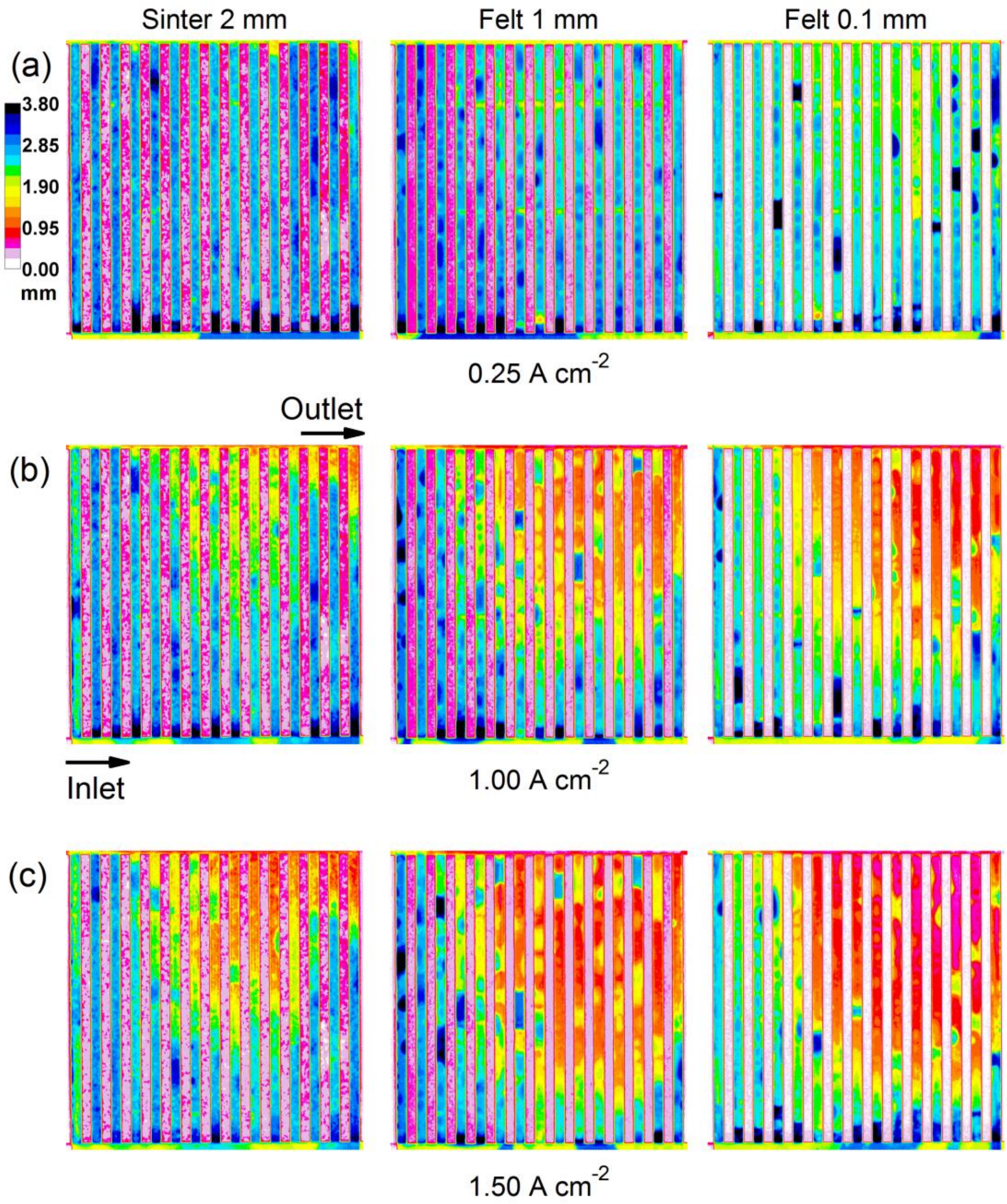

Figure 28: Neutron radiographs at a current density of (a) 0.25 A cm^{-2}, (b) 1 A cm^{-2}, and (c) 1.5 A cm^{-2} for all three LGDLs. The water thickness is displayed as a color map. The locations of the water inlet and outlet of the flow-field are indicated in (b) for the sinter. For further analysis flow-field ribs are counted from left to right.

To quantify the water-gas transport characteristics of the LGDL materials, the water thickness over the rib (land) areas is examined in more detail (Figure 29). A mask is used, extracting only the pixel values of the individual rib areas as described in Section 5.3.2. By analysing the average value over all 14 ribs (Figure 29 (a)), it is clear that all materials contain a decreasing amount of water with increasing current density. This is due to the increased water consumption, and the fact that water is increasingly displaced as more gas is produced at higher current densities. The thin felt retains much less water than the other two LGDLs due to its reduced thickness. On the other hand, the thick felt and the sinter contain almost identical amounts of water. As shown in Section 5.4.1, the thick felt is significantly more porous than the sinter, which facilitates a much higher water holdup for the thick felt, even with only half the thickness of the sinter.

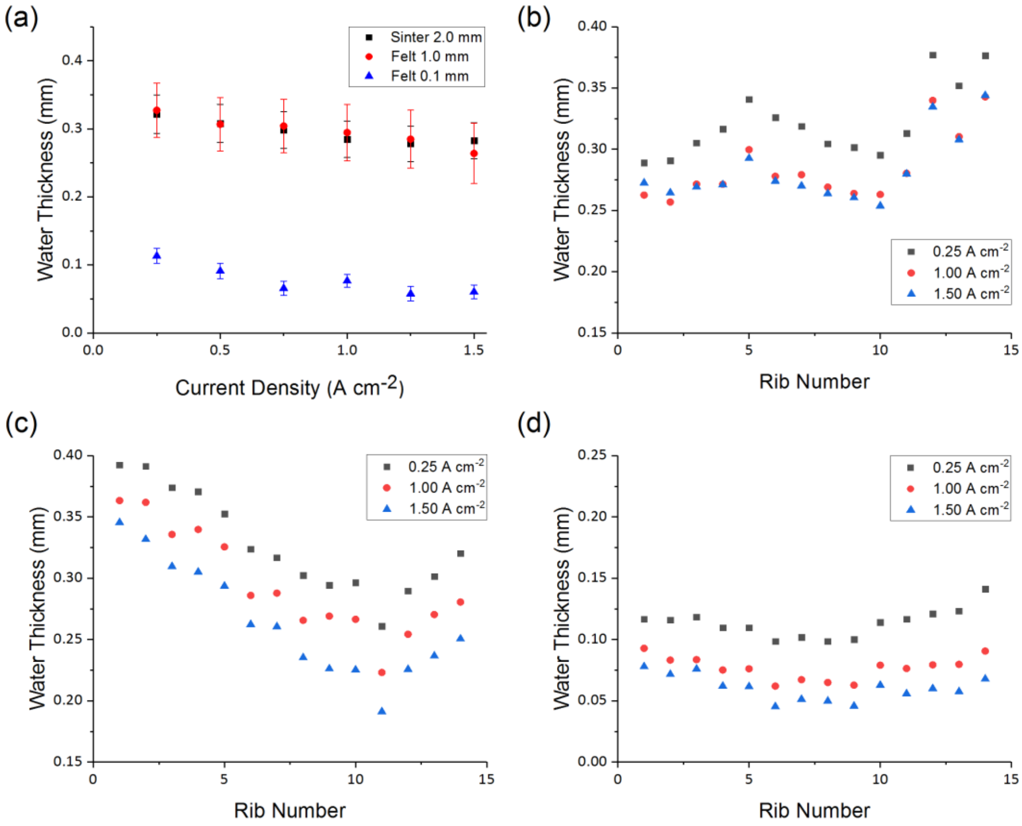

Figure 29: (a) Water thickness in all three LGDLs as a function of current density. Spatially resolved water thickness over the rib area for the (b) sinter, (c) thick felt, and (d) thin felt at a current density of 0.25 A cm^{-2}, 1 A cm^{-2}, and 1.5 A cm^{-2}. Error bars indicate the standard deviation over the active area.

At low current densities, the water thickness in the thin felt exceeds its physical thickness (0.1 mm), which is likely to be due to the contribution from the water content inside the carbon paper. In this case, the thicknesses of the CCM (127 µm) and carbon paper (130 µm) are comparable in magnitude to that of the thin felt and the water content of these introduces a significant measurement error. In contrast, the thicknesses of the sinter and the thick felt far exceed that of CCM and carbon paper, and hence only a small relative uncertainty is introduced into the measurement for these two LGDLs. Further, the overall trend of water thickness (spatially and with current density) is unaffected by this limitation of the measurement technique.

The water thickness in both the sinter and the thin felt reaches a plateau between 1 A cm^{-2} and 1.25 A cm^{-2} and does not decrease further, which indicates that an equilibrium between water and gas transport has been reached. Initially, when the current density is increased, new pathways through the LGDL are formed, which reduces the average water thickness of the LGDL. The formation of new gas pathways and detachment sites from the surface of the LGDL have been observed by Hoeh et al. [83]. As the current density increases above a critical point, new pathways for gas removal can no longer be created, as all accessible pores are used either for gas removal or water transport. In this case, the mass transport rate through the LGDL can only be increased by accelerating the gas and water transport through existing pathways. This leads to an increase in gas bubble detachment frequency on the surface of the LGDL [83,84]. As no new pathways are formed, the ratio between water and gas transport pores remains constant, which causes the externally observable water thickness in the LGDL to remain constant (Figure 29 (a)).

When examining the difference in water thickness between individual ribs for the three LGDLs (Figure 29 (b)-(d)), clear differences are visible. All three materials show a decrease in water thickness with increasing current density across all ribs. The sinter (Figure 29 (b)) shows little local variance over the first 10 ribs, but a continuous increase in water thickness for the last four ribs. The thick felt (Figure 29 (c)) exhibits a clear gradient in water thickness, but also an increase in water thickness for the last four ribs.

This can potentially be explained by the uneven water flow velocity distribution in the parallel flow-field. As mentioned earlier (Section 5.3.1) the flow-field in this work is of the Z-flow pattern, which favors flow through the channels on the far right side (closer to the outlet) [72,75,76]. The water velocity in the final channel is up to five times higher than in the middle channels and this coincides with an increase of water thickness for the sinter and the thick felt in the same area. This implies that the heterogeneity in water flow distribution affects the LGDL and leads to higher measured water thickness. Therefore, the results indicate a close link between the water velocity in the flow channels and the water content and mass transport in the LGDL under the land.

Interestingly, the thin felt (Figure 29 (d)) shows almost no local gradient in water thickness. This indicates that the thin felt has a very limited capacity for water and gas, likely due to its small thickness, high porosity, and low tortuosity. Hence the constant flow of water over the surface of the thin felt exposed to the flow channels is sufficient to enforce a very uniform water-gas distribution.

5.4.2.1 LGDL Water Saturation and Residence Time

Water content (saturation) and residence time as a function of current density, averaged over the entire active area, were calculated according to Section 5.3.4 and are displayed for the sinter and the thick felt in Figure 30. Due to the comparable thickness with the water-saturated CCM, the calculated values for the thin felt exhibited a large standard deviation and are omitted from the analysis.

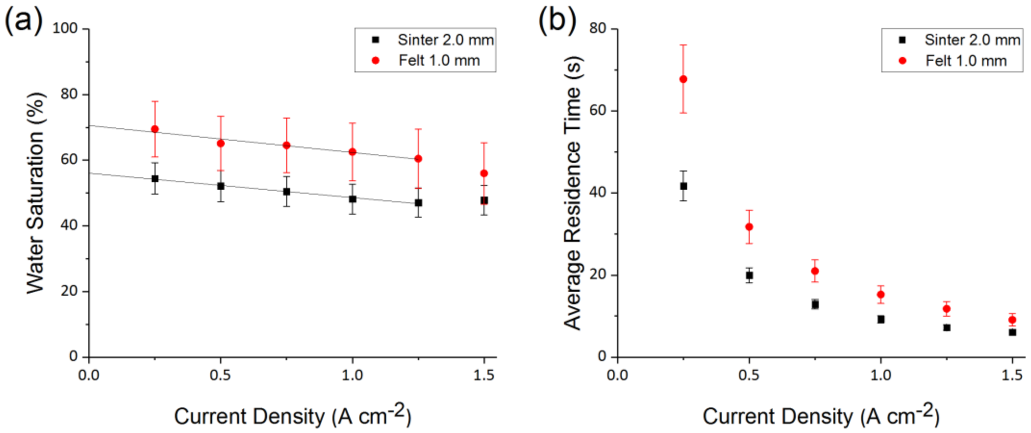

Figure 30: (a) Water saturation and (b) average water residence time in the LGDL for the sinter and thick felt between 0 A cm^{-2} and 1.5 A cm^{-2} at a constant water flow rate of 100 ml min^{-1}. Error bars indicate the standard deviation over the active area.

For the sinter, average water saturation (Figure 30 (a)) ranges from 54 % at 0.25 A cm^{-2} to 47 % at 1.5 A cm^{-2}. Similar values are found for the thick felt; however, the water saturation is slightly higher than for the sinter due to the lower pore volume of the thick felt. Around half of the pore volume of the LGDLs is not used for water transport within the range of current density in this work. The water residence time (Figure 30 (b)) varies between 42 s and 6 s for the sinter, and between 68 s and 8 s for the thick felt.

The linear extrapolation in Figure 30 (a) indicates the water saturation at 0 A cm^{-2}, which is

56.0 % and 70.6 % for the sinter and felt, respectively. This illustrates that a significant fraction of the LGDL is not filled with water, even without gas being produced due to electrochemical activity. The XCT analysis in Section 5.4.1 showed that a fraction of the LGDL pores are disconnected and can therefore not contribute to the transport of gas and water. However, for the sinter and thick felt there was only a moderate amount of disconnected porosity, which is not significant enough to explain the low values of water saturation obtained even at 0 A cm^{-2}. This leads to the conclusion that a number of pores, which are connected to the rest of the pore network, are not, or insufficiently, reached by water flow (stranded pores). This effect has been computationally predicted for fibrous materials used in redox flow batteries and is affiliated with small variations in local porosity [260].

Based on this characterization, it is likely that the performance of a PEMWE could be further improved by tailoring the LGDL to avoid disconnected or stranded ('dead') pore space. This could be achieved by reducing pore volume, which increases electrical and thermal conductivity but does not affect the mass transport properties of the LGDL. Another potential approach is to create materials in which the formation of new water pathways is favored, so that sufficient mass transport can be guaranteed even at elevated current density. The approach of combining neutron radiography and XCT is a promising technique for the evaluation of new materials and LDGL architectures.

5.5 Conclusion

This work combines X-ray micro-computed tomography and neutron radiography to investigate the link between LGDL microstructure and mass transport properties. Three different LGDLs were examined (one sintered and two fibrous materials); the sinter was found to have a porosity of ~30 %, while the thick and thin felt have porosities of 47 % and 77 %, respectively. Pore network models were created from the XCT datasets and used to calculate the flux of water through individual throats of the LGDL. It was found that the flow occurs predominantly through a small fraction of throats, supporting the idea of preferential pathways through the LGDL.

Neutron radiography was employed for *operando* imaging of a PEMWE, varying the LGDL material. Various differences between the three LGDLs were observed during the operation of the PEMWE, with water thickness being clearly influenced by the thickness and porosity of the LGDL. The imaging also revealed the structure of oxygen bubbles in the flow channels, and locations with an increased gas fraction.

To further investigate the differences between LGDL materials, the water thickness under the rib areas of the flow-fields was analysed. This offers the potential to observe the spatially-resolved water content in the LGDL only.

The main findings from this analysis are:

- Neutron radiography is a powerful tool to visualize the water-gas distribution in PEMWE flow channels *operando*, enabling analysis of the link between flow-field geometry and flow phenomena, facilitating the analysis and optimisation of PEMWE architecture.
- A decrease in water thickness with increasing current density was revealed for all LGDLs, which is caused by the increased rate of gas production.
- Significant inhomogeneity in water thickness was observed for the sinter and the thick felt across the active area. This highlights the need for novel LGDL structures or materials to avoid poor performance due to local mass transport limitations at high current density.
- Increased water thickness was found in areas that are likely to exhibit increased

flow velocity in the flow channels. This indicates a link between flow-field geometry and mass transport in the LGDL which has not been previously reported in literature.

By combining water thickness data obtained by neutron radiography and microstructural information gained from XCT, water saturation and water residence time in the pores of the LGDLs were calculated. It was revealed that around half of the pore volume is not utilized for water transport and that this value varies only slightly with increasing current density. Further, the water residence time in the LGDL was measured to range between 6 s and 68 s. Extrapolation to 0 A cm^{-2} shows that a significant fraction of pores remain dry, even in the absence of electrochemical activity. This cannot be explained from the amount of disconnected pores found in the XCT analysis and therefore implies the existence of stranded pores. These pores are connected to the overall pore network, but no water flow through them occurs due to small scale variations in porosity in the vicinity of these pores. This indicates that further improvements on LGDL structure and materials need to be made to increase pore utilization. The reduction of unused pore volume can potentially lead to improved usage of active area and hence to an improvement in the efficiency of PEMWEs.

The above findings illustrate the excellent capabilities of neutron imaging as a diagnostic tool for PEMWEs. The combination of neutron radiography and XCT yields deep insight into the mass transport characteristics of LGDLs, which would not be possible by either of these techniques alone. The findings give an indication of the shortcomings of the materials most frequently used as LGDLs in PEMWEs and suggest pathways to novel structures that could mitigate these issues.

However, methods such as neutron imaging and XCT are time-consuming and require expensive equipment with limited access. Therefore, the following sections are dedicated to establishing a set of new acoustic diagnostic tools, which in some cases can provide rapid and low-cost alternatives to the imaging methods used so far.

6 Two-Phase Flow Diagnosis in PEMWE Flow Channels with Acoustic Emission

6.1 Overview

In this chapter, acoustic emission analysis is used as a low-cost, non-destructive, *operando* diagnostic tool to provide information about the relative number and size of gas bubbles generated locally within a PEMWE, providing effective characterization of the local flow conditions. An optically transparent single-channel PEMWE is used to investigate the relationship between the acoustic signals obtained and the two-phase flow conditions inside the cell. The number of acoustic hits, their frequency, and average peak amplitude is reported for several flow rates and current densities. Using high-speed imaging, the average bubble number and size in the flow channels is compared to the acoustic signal. Results show good correlation between the number of acoustic 'hits' and the number of bubbles passing through the flow channel. The size of bubbles is also shown to affect the average frequency of the hits. Consequently, the transition between bubbly and slug flow regime can be identified by acoustic emission analysis, paving the way for a simple, low-cost, non-destructive means of mapping flow inside PEMWEs.

Building on these results, acoustic emission is applied to a PEMWE with a parallel flow-field, diagnosing a sudden drop in the number of acoustic hits, while hit duration, amplitude, and energy increase significantly as the current density is increased from 0.5 A cm^{-2} to 1 A cm^{-2}. It is found that the change in acoustic regime coincides with a significant extension of the stagnant bubble region in the flow channels of the PEMWE, observed with high-speed optical imaging. These results demonstrate that acoustic emission can be used effectively as an *operando* diagnostic tool to monitor bubble formation (two-phase flow conditions) in PEMWEs, facilitating rapid testing or prototyping, and contributing to operational safety. Further, this establishes acoustic emission as an alternative method of investigating processes in the flow channels to expensive and less accessible techniques such as neutron imaging.

The results in this chapter form part of publications by the author in *Journal of Power Sources* [218] and *Frontiers in Energy* [261].

6.2 Introduction

Understanding how various factors influence performance and durability of a PEMWE is key to optimising cell design, component materials, and operating conditions. Various diagnostic techniques have been applied to PEMWEs to gain greater insight into their operation. These techniques range from computational methods [55,100,262] to avoid costs of production and experimentation and low-cost, readily-available techniques which only require access to a potentiostat, such as electrochemical impedance spectroscopy to identify electrochemical losses in a system [43,118], to high-end experiments such as neutron imaging used to visualize water content in the liquid-gas diffusion layer [88,89], bubble dynamics, and flow regimes [85–87].

This chapter aims to deliver a simple low-cost diagnostic tool of two-phase flow in operational PEMWEs without the need for any cell modification. High-speed flow visualisation using a single-channel optical PEMWE is combined with local AE measurements to correlate acoustic signals with flow characteristics with a view to establishing a diagnostic tool for standard (unmodified) PEMWEs. AE is a low-cost, non-destructive, operando diagnostic tool, detecting mechanical perturbations in a sample with a sensor mounted to the external sample surface (Figure 31).

Two different PEMWE cell designs are used, each focused on investigating different flow processes. A single-channel cell is used to show the effects of varying current density and flow regimes on the AE signal, while the influence of stagnant gas bubbles in the flow channels was investigated in a PEMWE cell with a parallel flow-field.

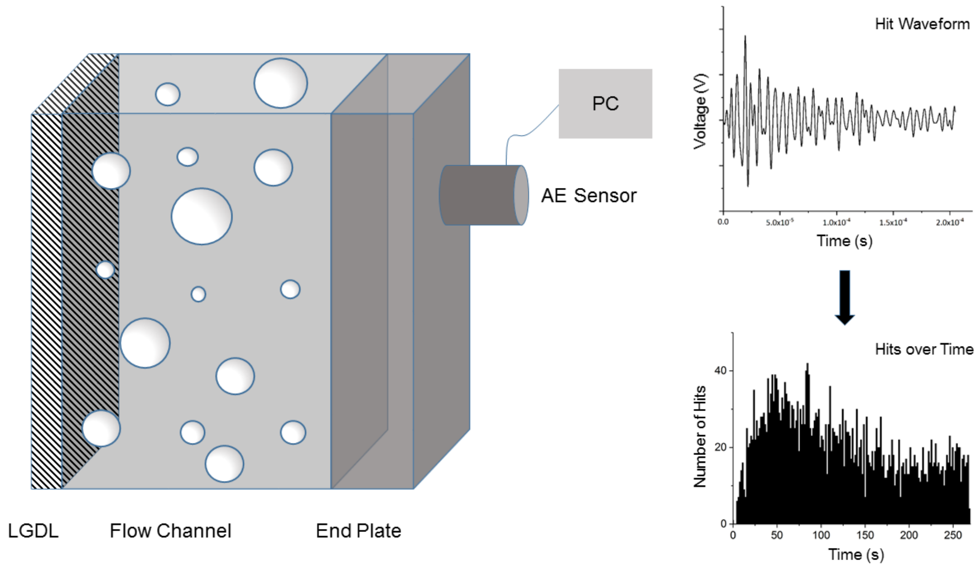

Figure 31: Application of acoustic emission to the flow channel of a PEMWE. The raw signal (waveform) of one acoustic hit and an example of how the number of hits changes over time are shown on the right.

6.3 Experimental

6.3.1 PEMWE Cells

To correlate the acoustic emission signature with local flow characteristics, optically transparent cells were constructed to allow for optical high-speed imaging of the two-phase flow in the flow channels. Any duplication with Section 4.1 is intended for the convenience of the reader.

6.3.1.1 Single-Channel Cell

A single-channel PEMWE was used to investigate the link between the flow regime and AE signals (Figure 32 (a)). The cell comprised a single flow channel, which mitigates the uneven distribution of flow in multi-channel systems (Nie et al. [72]) and ensures the influence of different flow rates and current densities can be examined precisely. A single-channel cell design was chosen to make sure the flow behaviour could be observed without obtaining signals from several flow channels at the same time, each with a different flow regime due to uneven water flow distribution. The single channel had a length of 9.0 cm, a width of 5.0 mm, and a depth of 2.0 mm. The channel dimensions were chosen to allow for adequate visual observation and make sure the flow regime can fully develop over the length of the flow channel. A CCM with a length of 9.0 cm and a width of 1.5 cm was used, yielding an active area of 13.5 cm^2. The CCM was based on Nafion 115, with 0.6 mg cm^{-2} platinum on the cathode and 3.0 mg cm^{-2} iridium/ruthenium oxide on the anode side (ITM Power, UK). Transparent Perspex was used as the material for the end-plates, allowing for optical inspection and operando high-speed imaging of bubble development and movement. The cell was held together with twelve tie bolts with a torque of 1.5 Nm applied to them to ensure good sealing and electrical contact. Sintered titanium powder was used as LGDL on both the anode and cathode side. The electrolyser was operated at ambient pressure and with a water inflow temperature of 50 °C, which is within the range of commonly applied temperatures in the literature [43,118]. Water flow rate ranged from 5 ml min^{-1} to 30 ml min^{-1}, which corresponds to a water ratio [134] between 4 and 24 at 2 A cm^{-2}.

6.3.1.2 Parallel Flow-Field Cell

The PEMWE used for the experiments on diagnosis of stagnant bubbles (Figure 32 (b)) had a 9 cm^2 active area and consisted of transparent Perspex end-plates, parallel titanium flow-fields, a titanium sinter LGDL at the anode, a Toray H-060 carbon paper as the GDL at the cathode, and a CCM, which was based on Nafion 115 with 0.6 mg cm^{-2} platinum on the cathode and 3.0 mg cm^{-2} iridium/ruthenium oxide on the anode (ITM Power, UK). The flow-field consisted of nine parallel channels, with a length of 3.0 cm and a land and channel width of 1.76 mm. The electrolyser was run at ambient pressure with a deionised water inflow temperature of 50 °C and a water inflow rate of 10 ml min^{-1} at the anode and cathode.

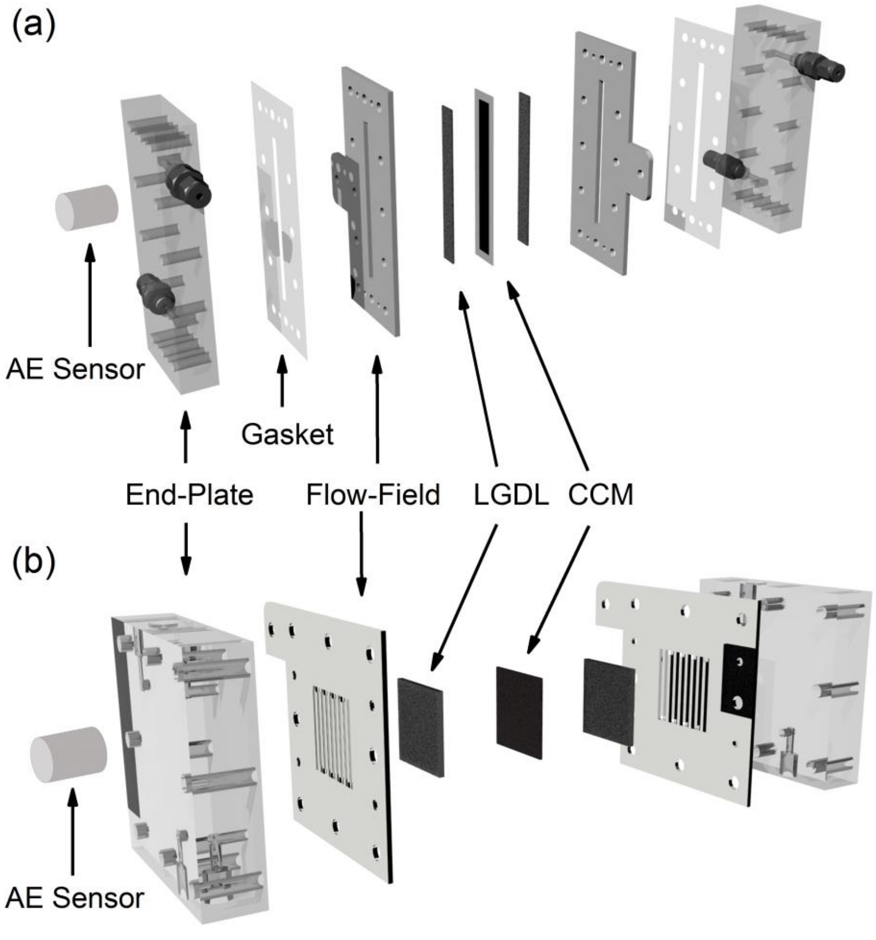

Figure 32: (a) Single-channel PEMWE cell with end-plate, flow-field, liquid-gas diffusion layer (LGDL), and catalyst coated membrane (CCM). (b) The second PEMWE cell had a parallel (exact flow-field geometry not displayed) flow-field with nine channels, but is otherwise functionally identical to (a). For both cells the AE sensor is mounted to the surface of the end-plate. Gaskets are only shown in (a), but were used for both cells to accommodate LGDL and CCM.

6.3.2 Electrochemical Testing

The electrochemical performance of the single-channel and the parallel flow-field cell can be seen in Figure 33, with both cells showing typical polarisation behaviour and the voltage within the range of typical values reported in the literature [31,43,59,120].

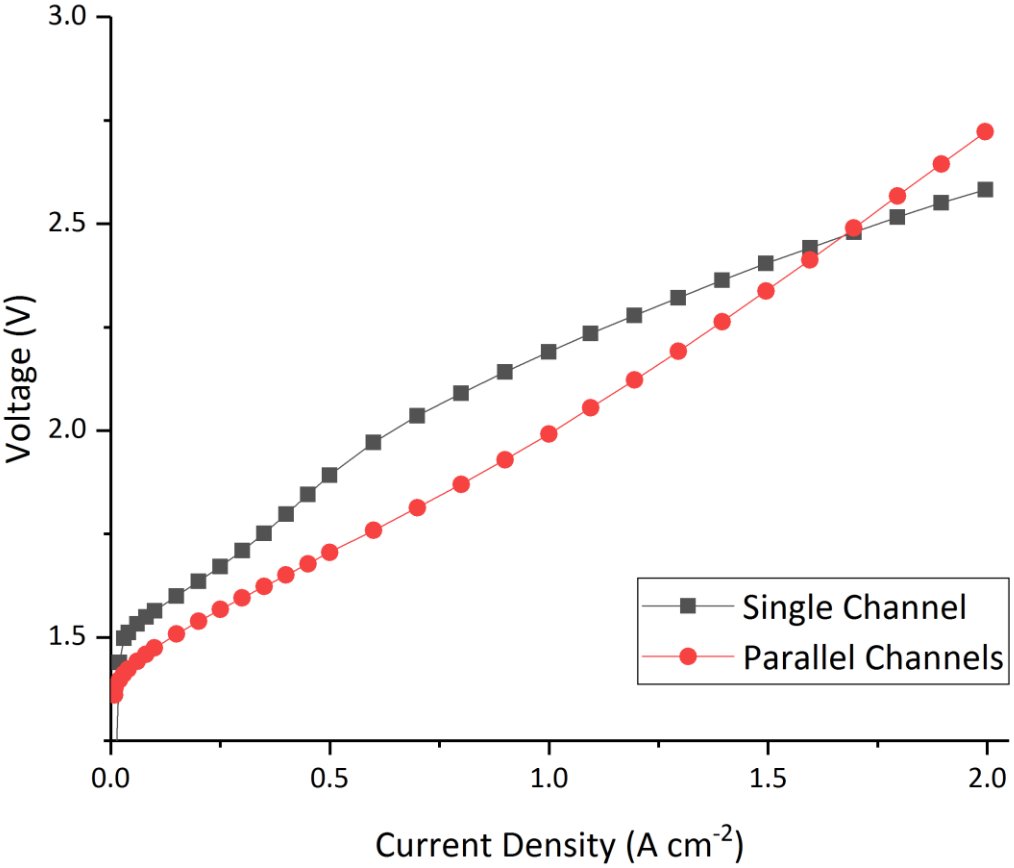

Figure 33: Electrochemical performance of (a) the single-channel, and (b) the parallel flow-field PEMWE between 0 A cm^{-2} and 2 A cm^{-2}.

A potentiostat (Gamry Reference 3000 Galvanostat/Potentiostat with a Gamry 30k Booster; Gamry Instruments, USA) was used for electrochemical testing with the current density ranging between 0 A cm^{-2} and 2 A cm^{-2}.

6.3.3 Acoustic Emission

The acoustic emission of the PEMWEs was monitored using a piezoelectric sensor (S9208; Mistras NDT, UK). The signal was filtered and pre-amplified by 26 dB and a digital node extracted an acoustic hit from the continuous signal whenever the noise threshold of 37 dB was exceeded. For each data point, acoustic data was recorded over the course of 1 minute during galvanostatic operation of the PEMWE cell. The AE sensor was mounted on the anode side, with two different locations investigated. Acoustic signals arising from the cathode are a potential source of error; however, it is unlikely that a significant magnitude of acoustic signal can pass through the various acoustic impedances from the cathode to the anode side. This is especially significant for the interface between anode LGDL and flow channel, which would need to be passed by any signal from the cathode side. As this is a solid/liquid interface, it is likely that up to 90 % of the signal is reflected [247].

6.3.3.1 Sensor Positioning

For the single-channel PEMWE, two separate points of interest (sensor locations) were chosen. The lower point of interest was located 1.5 cm from the start of the flow channel near the inlet; the upper location 1.5 cm from the top of the channel near the outlet. These two distinct locations were chosen so as to represent markedly different flow regimes as typically 400 % more gas has to pass through the upper location. For the parallel flow-field cell, the sensor was placed in the centre of the flow-field.

Due to the nature of sound transmission, no clear area can be defined within which acoustic data is collected. Whether a mechanical perturbation is detected by the sensor is contingent on the location and intensity of the perturbation, with the intensity necessary for detection increasing with the distance between acoustic source and sensor. Therefore, detection of bubbles is increasingly likely as they are located closer to the sensor.

6.3.4 Acoustic Emission Post-Processing

Data collection and analysis was performed using the commercial software AEWin (Physical Acoustics, USA). The number of acoustic hits per unit time (hit rate H), the corresponding average frequency of hits f, and their average amplitude A were recorded for the single-cell PEMWE. For the parallel flow-field PEMWE, the hit rate, the average hit amplitude, the averaged time from exceeding the threshold until falling back below it (average hit duration D) and the average hit energy E were analysed. An acoustic hit is registered whenever the amplitude of the acoustic signal exceeds a certain predefined threshold; it ends when the signal has permanently damped back below the threshold. When the signal associated with an acoustic hit is analysed by fast Fourier transform (FFT) or similar techniques, a characteristic peak frequency is obtained. By averaging the peak frequency of all hits occurring within one sampling period, the average peak frequency f is obtained. This is the frequency of the voltage-time profile of a specific AE hit averaged over all hits; it is not the frequency with which hits occur over time. Various studies have established that bubble oscillations cause pressure impulses at a frequency specific to bubble size, which can be picked up by AE [193,263–265]. The necessary equations to analyse the frequency information gained through FFT can be found in Section 4.4.2.1.

6.3.5 High-Speed Imaging

A high-speed camera (Photron FASTCAM SA1) was used for imaging of the flow channel(s). Images were taken at 2000 frames per second and a resolution of 1024×1024 pixels over the course of 5.46 s (maximum available acquisition time at this frame rate) for each set of experimental conditions. A temporal resolution of 2000 frames per second was chosen to ensure no feature of the flow was missed, and the evolution of flow regime along the channel could be observed with high temporal detail. This resulted in 10920 images for each set of conditions, which offers a large set of data for quantitative analysis. For the single-channel cell, quantitative analysis of the image sets was performed to calculate the number and size of captured bubbles (see Section 4.2.1).

The images of the single-channel cell used for quantitative analysis were high-resolution images of the region where the AE sensor was placed, taken with a Tokina MACRO 100 F2.8 D lens (spatial resolution 50 µm), whereas the whole length of the flow channel was captured with a Sigma 1:2.8 DG HSM lens (spatial resolution 300 µm). For the parallel flow-field cell, the Tokina MACRO 100 F2.8 D lens was used as well, but the obtained images were not analysed quantitatively.

6.3.6 Image Post-Processing

MATLAB (MathWorks) was used to perform all necessary post-processing steps. As outlined in Section 4.2.1, images were thresholded, filtered, circular structures in the images were identified, and finally, overlapping circles were removed (only retaining the largest overlapping circle. Size D and number N of bubbles were then averaged for all images within one set of conditions. The lower detection limit for this algorithm is a diameter of 5 pixels, equalling 125 µm. The process is limited to circular bubbles, which means that in the case of elliptic slug bubbles only the length of the minor axis of the bubble is registered. To reduce computation time, only every 10th image was used for data analysis. The resulting number of more than 1000 analysed images is sufficient for representative analysis. To make sure the algorithm produces trustworthy results, bubble size and number were also determined manually over the current density range for a water flow rate of 5 ml min^{-1}, by counting and measuring gas bubbles in seven randomly selected images for each current density. In the case of non-spherical gas bubbles, the size of the bubble was taken as the length of the minor axis.

6.4 Results

6.4.1 Flow Regime Diagnosis in a Single-Channel PEMWE

The typical characteristics of acoustic emission in the single-channel cell are shown in Figure 34 for different flow rates over a range of current density at both sensor locations. For the upper location, the number of hits (Figure 34 (a)) rapidly increases initially and reaches a maximum at around 0.5 A cm^{-2}. The number of hits then decreases and reaches a plateau at approximately 1.5 A cm^{-2}. For low current densities (< 0.5 A cm^{-2}), the water flow rate has a negligible influence, whereas above this value the number of hits is a clear function of flow rate, reaching values of 5 hits per second at 5 ml min^{-1} and 12 hits per second at 30 ml min^{-1}. This provides a correlation between flow processes in the PEMWE and its acoustic emission. In contrast, at the lower channel location the peak is less pronounced (Figure 34(d)), with the peak value at different current densities ranging from 0.5 A cm^{-2} to 0.8 A cm^{-2}, and a much less prominent decrease in the number of hits at higher current densities.

Figure 34 (b) and (e) illustrate the average peak frequency of AE hits as a function of current density. As discussed in Section 4.4.2.1, the frequency of bubble oscillation is linked to bubble size. Hence, the results from Figure 34 (b) and (e) imply a constant increase in bubble size at both the upper and lower locations, as the mass of oxygen produced increases with current density. However, the frequency decreases by 14.5 kHz (A cm^{-2})$^{-1}$ for the upper location, but only 9 kHz (A cm^{-2})$^{-1}$ for the lower location.

Again, this is in line with expectation as for the upper location approximately 400% more gas is passing through the flow channel and therefore relative changes in bubble size between low and high current density are expected to be more pronounced.

At the same time, it can be seen from Figure 34 (c) and (f) that the average amplitude of AE hits is relatively independent of current density for both locations, as the value of A is constant as a function of current density. If the number of bubbles is expected to change when varying current density, this would lead to a changing amplitude of the AE signal (see Section 4.4.2.1) if it is assumed that the acoustic hits are emitted as a consequence of simultaneous oscillations. Hence, the invariance of amplitude implies that the signal does not originate in the simultaneous oscillation of bubbles, but in discrete, separate events such as the collision of bubbles with the end plate or channel wall of the electrolyser.

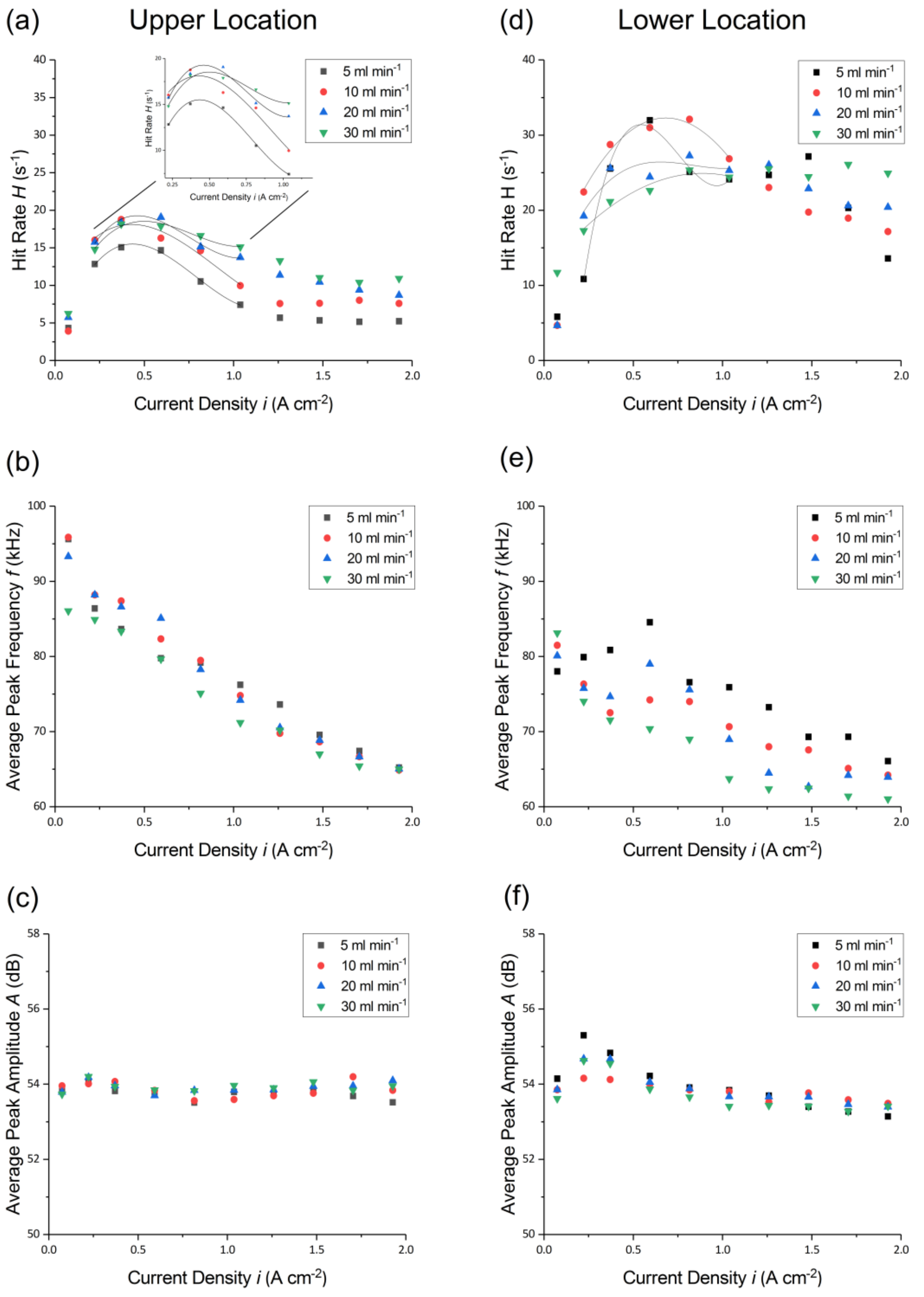

Figure 34: Hit rate (a, d), hit frequency (b, e) and hit amplitude (c, f) of acoustic emission at the upper (a-c) and lower (d-f) sensor location. The inset in (a) shows the region around the peak in more detail.

This leads us to propose a model of the origin of the acoustic emission signal in the observed system. Bubbles of different sizes move through the flow channels, which, depending on the depth of the flow channel relative to their size, float freely or impinge on the walls of the channel. The collision between bubble and wall leads to deformation of the bubble. Consequently, the bubble oscillates around its original shape with a frequency specific to its size. This causes an acoustic perturbation, which is transferred into the back plate and travels towards the other side of the plate where it is registered by the AE sensor.

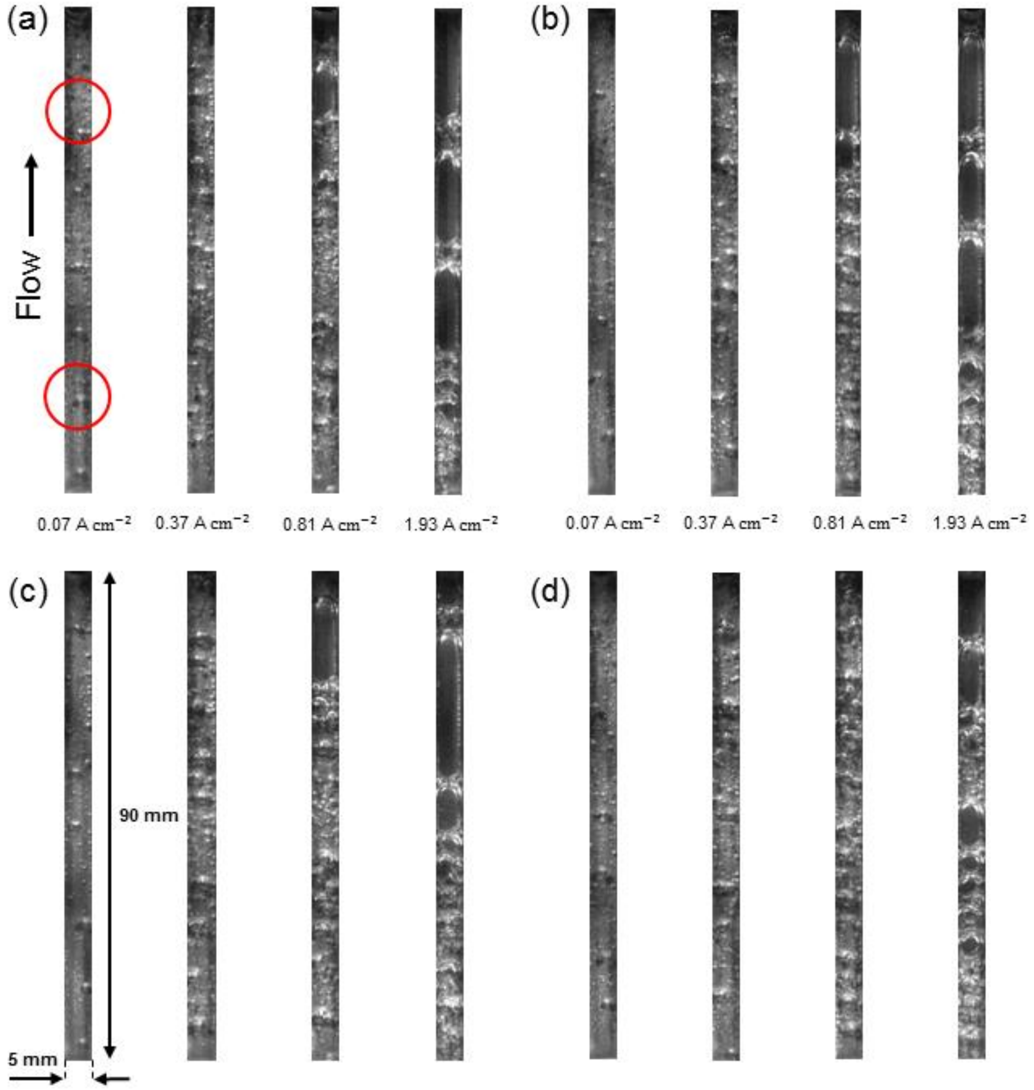

Figure 35: High-speed imaging of the single flow channel over a range of current densities at (a) 5 ml min^{-1}, (b) 10 ml min^{-1}, (c) 20 ml min^{-1}, and (d) 30 ml min^{-1}. Upper and lower sensor location are indicated by the red circles in (a).

To gain a better understanding of these processes, high-speed visual imaging of the flow channel was used. Figure 35 shows the entire length of the flow channel, with the upper and lower locations of the AE sensor indicated by red circles. Bubble size increases with current density; for 0.07 A cm^{-2} and 0.37 A cm^{-2} the bubbly flow regime is predominant at both locations. For 0.81 A cm^{-2} and 1.93 A cm^{-2} slug flow is the dominant flow regime at the upper sensor location. At the lower sensor location, the regime is in the transition from bubbly to slug flow at 1.93 A cm^{-2}. While images for the low current densities of 0.07 A cm^{-2} and 0.37 A cm^{-2} are similar for different flow rates, a general trend towards elongation of slugs with decreasing flow rate can be observed at high current densities. To quantify this effect, the algorithm described in Section 4.2.1 was used to calculate bubble sizes and numbers for the regions around the AE sensor, as shown in Figure 36.

For both locations, at the lowest current density at 0.07 A cm^{-2}, bubble numbers (Figure 36 (a) and (b)) are up to 140 % higher than for the other current densities. However, for all other current densities, especially at the upper location, the development of the number of bubbles over current density follows the same trend as the number of acoustic hits (Figure 36 (a)); a steep incline is followed by a decline for current densities higher than 0.5 A cm^{-2} which ends in a plateau for high current densities. This trend coincides with the expected behaviour of the transition between bubbly and slug flow. As current density increases the number of bubbles increases to accommodate the produced gas. As the channel is fully filled with bubbles (the maximum amount of bubbles), coalescence occurs and the flow regime transits to slug flow. This can be seen in Figure 35 for the upper location for current densities higher than 0.5 A cm^{-2}, but not for current densities lower than that. Although the trend is not as clear for the lower location, a correlation between AE (Figure 36 (d)) and high-speed imaging data can be observed. This indicates a qualitative correlation between the number of bubbles and acoustic hits and supports the conclusion made above that the acoustic emission observed originates from the collision of bubbles with the channel walls. The data from manual counting of bubbles shows that the algorithm overestimates the number of bubbles; however, the trend with current density is qualitatively very similar.

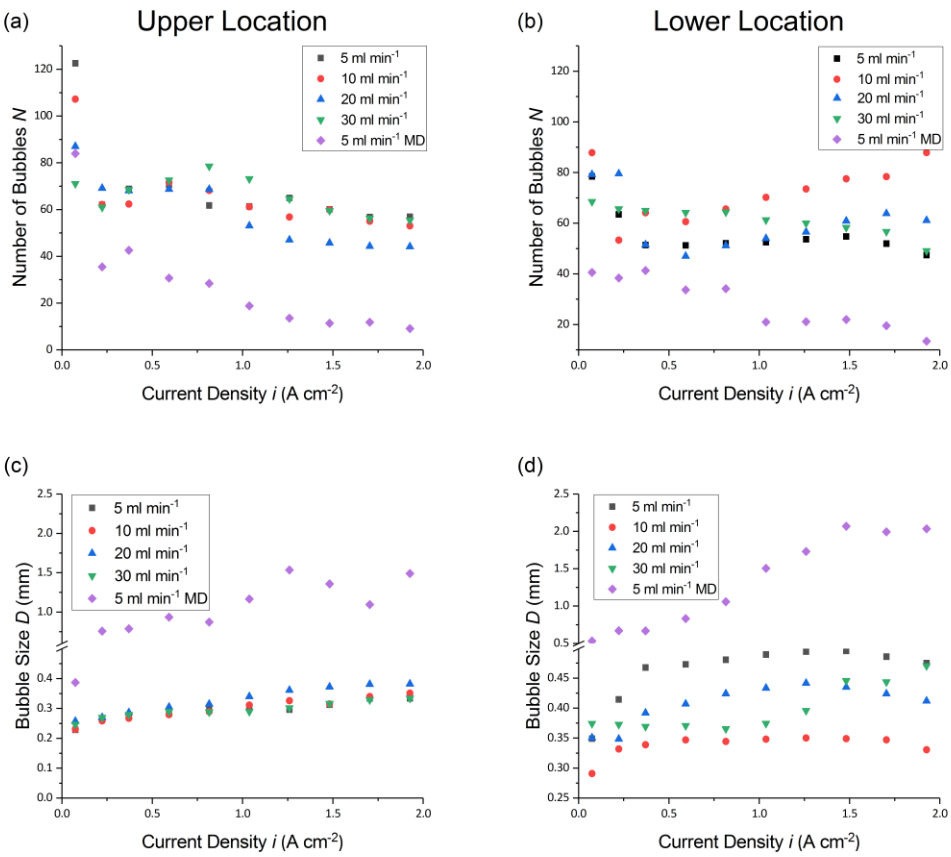

Figure 36: Number (a, b) and size (c, d) of bubbles extracted from high-speed imaging for the upper (a, c) and lower (b, d) sensor location. Manually determined (MD) values added for comparison.

The results from manual counting show the same deviation in bubble number for low current densities as that determined from high-speed imaging. Hence, from 0.07 A cm^{-2} to 0.22 A cm^{-2} a multitude of small bubbles are produced, which due to the low energy associated with their vibration are not able to produce an acoustic perturbation strong enough to be observed in the experimental setup.

The size of bubbles in the flow channel changes with current density (Figure 36 (c) and (d)). For the upper location, an increase in average bubble size between 30-50 % from lowest to highest current density is observed. Again, the trend for the lower location is less pronounced, although an overall increase in bubble size with current density is apparent. This supports the above findings, as the frequency of AE decreases with increasing current density (Figure 34 (b) and (e)). Hence, the notion that acoustic emission is a suitable technique to observe the evolution of bubble size in the flow channels is strengthened. As the change in the size of bubbles is caused by a change in current density, AE can potentially be used to monitor global or local current densities. Comparison with the manually obtained bubble size shows that the true size is not captured accurately by the algorithm. However, this work is concerned with detecting qualitative, not quantitative, changes and the increasing trend in bubble size is correctly identified by the algorithm. For future applications, the accuracy of the algorithm could potentially be improved by increasing the contrast between gas bubbles and the surrounding water, for example by injecting dark die into the PEMWE inlet water stream.

To investigate the relationship between flow regime and acoustic emission signal, a flow regime map was developed. This requires knowledge of water and gas flow in the PEMWE cell. The necessary equations and procedures for the flow map calculations are outlined in Section 3.2.2; necessary parameters are shown in Table 5.

Table 5: Values used for development of the flow map for the single-channel PEMWE.

Constant	Value
M_{O2} (kg mol^{-1})	32×10^{-3}
M_{H2O} (kg mol^{-1})	18×10^{-3}
ρ_{O2} (kg m^{-3})	1.33
ρ_{H2O} (kg m^{-3})	972
A (cm^2)	13.5
F (C mol^{-1})	9.65×10^4
n_{chan}	1
a (cm^2)	0.1

Cubaud et al. [67] have provided a flow regime map for air in water flowing through square microchannels with a width of several hundred micrometres. As this is much smaller than the channel size used in this work, it can be expected that the influence of surface tension over inertial forces in Cubaud's work was more dominant [266]. Although this configuration is not identical to that of the anode side of a PEMWE, the material parameters for air are similar to those of oxygen. Another limitation is that the flow channel in Cubaud's study was a horizontally oriented, single-serpentine channel, whereas this work uses a vertically oriented single channel. Lastly, Cubaud's work is based on the observation of two-phase flow through a channel with the gas being injected upstream of the site of observation, however, when observing two-phase flow in a PEMWE, gas is additionally flowing to the observation site from the LGDL surface. Nevertheless, by using this flow map to check the flow regime at different points of operation of the PEMWE used in this work, valuable insights into the relation between acoustic emission and flow regime can be obtained. To ensure that Cubaud's flow map is representative despite the mentioned limitations, the flow regime was determined from high-speed images for the upper location. For each point of operation, 10 randomly chosen images were visually examined. Images were classified as either bubbly regime or regimes with a higher gas flow rate. Good accordance with Cubaud's work was found (see Figure 37).

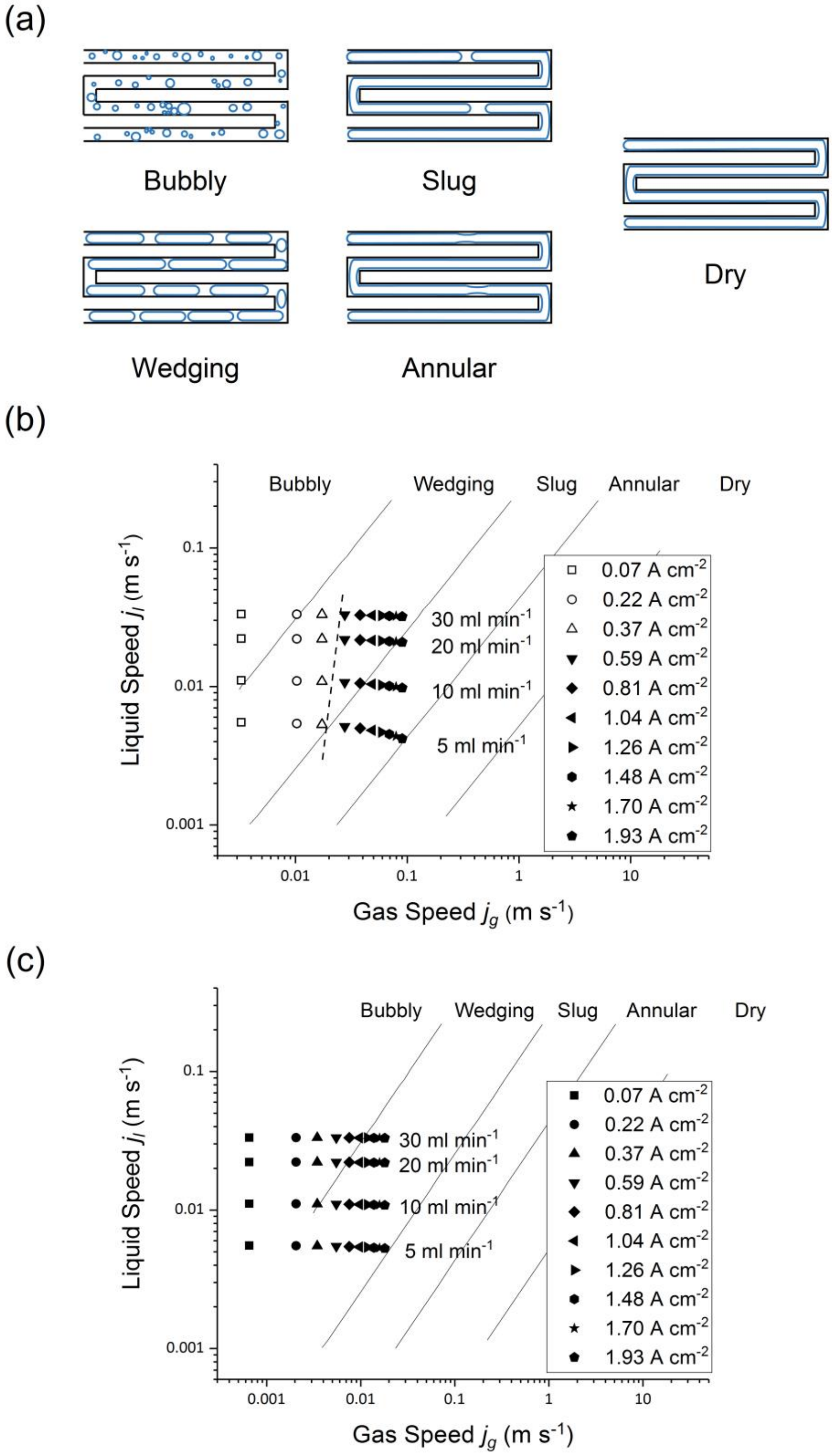

Figure 37: (a) Flow regimes as defined by Cubaud et al. [67]*. Flow regime maps for the upper (b) and lower (c) sensor locations. The dashed line in (b) marks the transition between bubbly and slug flow as indicated by acoustic emission. Hollow symbols in (b) mark points which were experimentally determined to be bubbly flow, while full symbols mark points of wedging regime or regimes with higher gas flow rates.*

The flow regime map for upper and lower sensor locations (Figure 37 (b) and (c)) at all points of operation examined in this work covers all flow regimes from bubbly to dry flow (Figure 37 (a)). The amount of gas produced increases with current density, which results in higher bubble speeds. Simultaneously, the water flow rate decreases with current density but is mainly dependent on the amount of water circulated. As the current density increases, the flow regime undergoes a series of transitions, initially from the bubbly regime via the wedging regime to the slug regime. When the slug bubbles have almost interconnected, the annular regime is reached, which then transitions into the dry regime. It is evident (Figure 37 (a)) that the wedging regime is a transitory regime between bubbly and slug flow and is specific to Cubaud's [67] work. Hence, it can be assumed that the transition between bubbly and slug flow in the system investigated in this work lies within the wedging regime. For the upper location, points of operation range from the bubbly flow regime up to the transition between slug and annular flow, while for the lower location the boundary between wedging and slug flow is only reached for the lowest water flow rate of 5 ml min^{-1}. This is in line with the fact that the range of flow regimes is much wider for the upper location (Figure 35).

As illustrated above, the number of acoustic hits is linked to the number of bubbles flowing through the flow channel of the PEMWE. With increasing current density, the bubble size initially increases to accommodate the surplus of gas produced by the reaction. At a certain point, the available space is almost completely filled with discrete gas bubbles and further gas production results in coalescence of bubbles. Therefore, the maximum number of gas bubbles is observed at the transition between bubbly and slug flow regime. This offers a possibility to use AE to detect the change from bubbly to slug flow. To illustrate this capability, Figure 38 shows the location of the peak on the current density axis of Figure 34 (a) against the flow rate of circulated water for the upper location. The peak locations were taken from the regression around the maxima of the curves in Figure 34 (a). A cubic regression was chosen to account for the asymmetrical peak shape. The maximum of the acoustic hits is shifted towards higher current densities with increasing water flow rate; an increase of 0.0027 (A cm^{-2}) (ml min^{-1})$^{-1}$ in the peak location is observed. The transition into slug flow is favoured by low water flow rates (Figure 35), as this reduces the water-to-gas ratio.

To further illustrate how acoustic emission can diagnose the regime within the flow channels of a PEMWE, the peak locations from Figure 38 were connected by a dashed line in Figure 37 (b). This line represents the transition between bubbly and slug flow for the upper sensor location, as determined from AE. For the range of water flow rates investigated in this work the predicted change to slug flow falls within the wedging regime, which is a transitory regime between bubbly and slug flow. Furthermore, the regime border as determined by AE corresponds to information gathered from high-speed imaging. The gradient of the regime boundary is different from that observed in Cubaud's flow map; however, this is not surprising as the examined systems are not identical. The way in which changes to the experimental system can affect the shape and location of regime boundaries can be seen by comparing flow regime maps of different authors for similar systems [65,67].

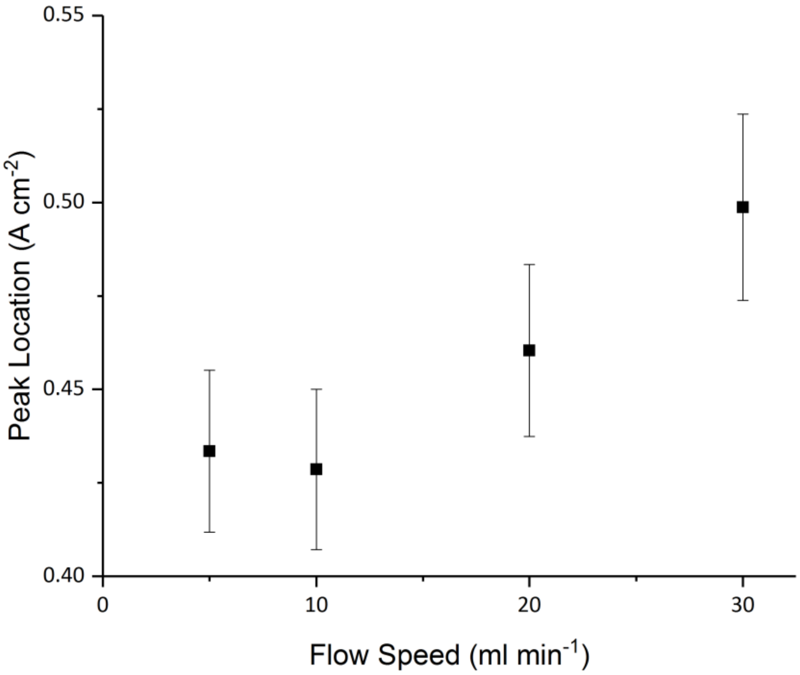

Figure 38: Current density at which the maximum number of acoustic hits was registered as a function of water flow rate, which indicates the transition from bubbly to slug flow.

6.4.2 Diagnosis of Stagnant Bubbles in a Parallel Flow-Field PEMWE

This chapter investigates the diagnosis of stagnant bubbles in the flow channels of a PEMWE cell using AE. In this work, stagnant bubbles are defined as remaining in a constant location with little to no movement, however, these bubbles can still be removed from their location occasionally. The bubble evolution as a function of the current density has been captured with high-speed imaging experiments; exemplary images are shown as a function of increasing current density in Figure 39. As the cross-sectional area of the flow channels is finite and as all bubbles have to leave the flow-field through the manifold at the top end of the flow channels, the ability of the PEMWE cell to remove product gas is limited. This leads to bubbles blocking the top end of the flow channels at high current densities. For a given flow rate, the length of channel that contains stagnant bubbles at the top end of the flow channel increases significantly with current density. Here, a stagnant bubble is defined as a bubble that does not change its location, and particularly a bubble at the top end of the channel not entering the combining manifold, but remaining at the top end of the flow channel. The location of the largest stagnant bubble in each image in Figure 39 is marked in red. The amount of oxygen produced at the anode increases as a function of current density (Faraday’s law, see Section 3.2.2); hence, growth in the length of stagnant bubbles is expected with increasing current density. At a current density of 0.3 A cm^{-2} (Figure 39 (a)) the top end of each channel is almost free of stagnant bubbles, while a clear growth of these bubbles can be observed at 0.6 A cm^{-2} (Figure 39 (b)). At 1 A cm^{-2} (Figure 39 (c)), bubble blockage covers more than a quarter of the channel length.

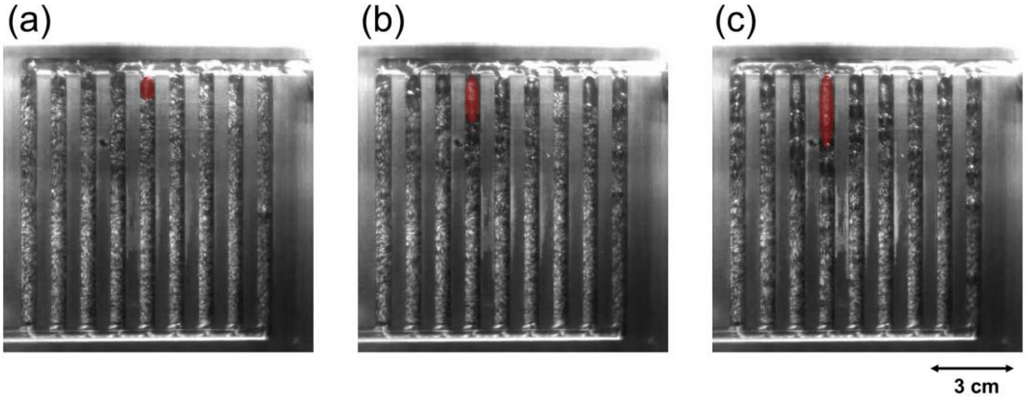

Figure 39: Exemplary results from high-speed imaging of the anode flow field of the PEMWE at (a) 0.3 A cm^{-2}, (b) 0.6 A cm^{-2}, and (c) 1 A cm^{-2} at a water inflow rate of 10 ml min^{-1}. The largest stagnant bubble at the top end of the flow channels is marked in red for each current density.

The acoustic emission parameters are strongly influenced by the current density (Figure 40). As illustrated above, current density leads to bubble blockage at the top end of the flow channels; hence, Figure 40 can be interpreted as the correlation between the acoustic emission signal and the formation of stagnant bubbles. The acoustic hit rate drops from 80.0 s^{-1} to the limit of detection for the acoustic emission system used in this work (1.0 s^{-1}) between 0.5 A cm^{-2} and 1 A cm^{-2} (Figure 40 (a)). The limit of detection is an artefact of the data acquisition, which cuts off any hit longer than 1.0 s, which means that from 1 A cm^{-2} onwards the AE signal continuously exceeds the noise threshold, with no individual acoustic hits discernible. This significant decrease of acoustic hits highlights a dramatic change of two-phase flow within the flow channels. The relationship between the number of acoustic hits and the number of bubbles passing through the flow channels has been established in Section 6.4.1, which found that the number of acoustic hits scales directly with the number of bubbles passing through the flow channels. Hence, a drop in the number of acoustic hits indicates a decrease in the number of bubbles generated and passing through the flow channels, which is likely due to the blocking of the flow channel by a stagnant bubble. This stagnant bubble stops smaller bubbles from traveling upwards through the flow channels; instead, the bubbles coalesce into the stagnant bubble. Hence, the drop in the number of acoustic hits between 0.5 A cm^{-2} and 1 A cm^{-2} is likely caused by the extension of stagnant bubbles into the sensor area.

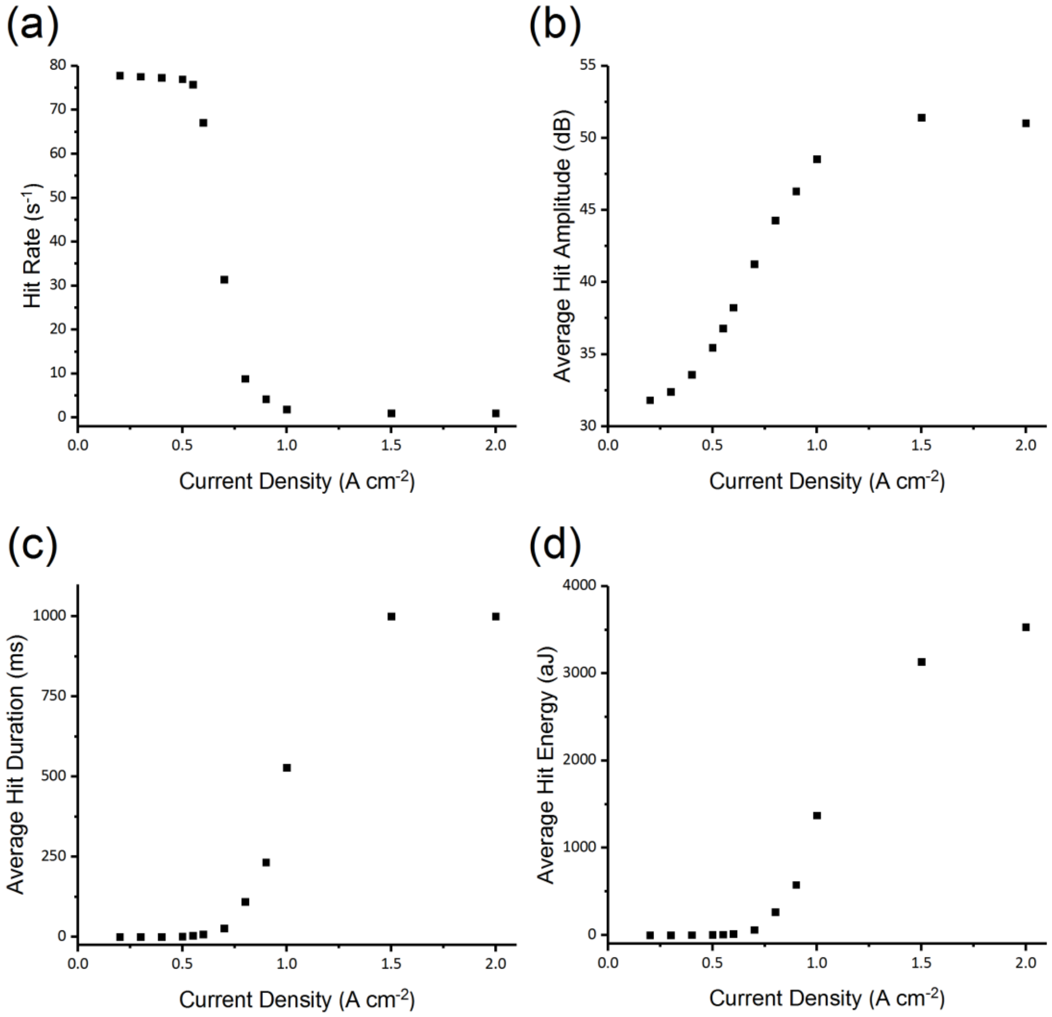

Figure 40: Acoustic emission parameters as a function of current density for a water inflow rate of 10 ml min^{-1}. Acoustic hit rate (a), average hit amplitude (b), average hit duration (c), and average hit energy (d) are shown.

Further, the average hit amplitude (Figure 40 (b)) increases steeply by around 50 % between 0.5 A cm^{-2} and 1 A cm^{-2}, the same range within which the hit rate drops. The average hit duration increases from less than 0.1 ms to the cut off value of 1.0 s mentioned above (Figure 40 (c)). For current densities above 1 A cm^{-2}, a constant signal is detected, indicating permanent contact between a bubble and the end-plate. Finally, an increase in hit duration and amplitude causes an increase in acoustic energy (Figure 40 (d)). All these changes occur in a step-like manner between 0.5 A cm^{-2} and 1 A cm^{-2}.

The decreasing number of hits, while hit amplitude and contact time between bubble and end-plate increase, all suggest that the signal change is caused by the extension of the stagnant bubble region towards the sensor location in the current density range between 0.5 A cm^{-2} and 1 A cm^{-2} (Figure 40). This is supported by the extension of the stagnant bubble region, observed via high-speed imaging (Figure 39), a major part of which occurs between 0.6 A cm^{-2} and 1 A cm^{-2}.

6.5 Conclusion

This chapter successfully demonstrated the potential of acoustic emission as a low-cost diagnostic tool for PEMWEs; in particular to study two-phase flow within the flow channels during gas formation. Two studies on different PEMWE cells showed the capability of AE to diagnose the flow regime and stagnant bubbles in the flow channels.

A close link between bubble size and number within the flow channel of a PEMWE and the AE measured on the surface of the end-plates has been established. Two locations along the single flow channel of a PEMWE have been investigated via AE measurements and high-speed imaging. For the upper location, AE measurements showed that the number of acoustic hits reaches a maximum around 0.5 A cm^{-2} and decreases to a plateau at higher current densities. The average frequency of these hits decreases with current density, which can be attributed to an increase in average bubble size. High-speed imaging at the upper location is consistent with the acoustic emission results. The number of bubbles detected follows the same trend as the number of acoustic hits with current density. This implies that AE can monitor relative changes in the number of bubbles flowing through an electrolyser and therefore can detect the change between bubbly and slug flow regime. Image analysis also showed a trend towards increasing bubble size at higher current densities, which supports the frequency data from acoustic emission; hence, AE can be used to detect changes in bubble size in a PEMWE. Similar trends were observed for the lower location; however, not as pronounced as for the upper location. This is consistent with smaller amounts of gas passing by the lower location, which causes the relative changes in bubble number and size to be less significant.

To further strengthen the link between acoustic emission and flow regime diagnosis, a flow map was invoked. The states of operation in the PEMWE for this study covered the range from bubbly flow to the onset of the annular regime. By analysing the current density at which the number of acoustic hits reaches its maximum, a regime boundary between bubbly and slug flow for the flow system used in this work was found. This regime boundary lies within the wedging regime, as defined by Cubaud et al. [67], which is a transitory regime between bubbly and slug flow. This supports the idea that the maximum of acoustic hits is found at the transition between the bubbly and the slug regime and hence implies that acoustic emission can be used to identify this regime change. As the number and size of bubbles in a PEMWE are consequences of local and global current density, AE can offer novel insight into the flow characteristics of the system and, potentially, local non-uniformity in the distribution of current density.

In a separate study, acoustic emission has been demonstrated as a useful technique for *operando* diagnosis of bubble blockage in a single-cell PEMWE. High-speed imaging of an optically-transparent PEMWE cell with a parallel flow-field was used to visualize the bubble movement in the flow channels. The length of the part of the flow channel containing stagnant bubbles was found to increase with current density, eventually reaching the location of the acoustic emission sensor. With increasing flow channel blockage, a dramatic change in acoustic activity was observed. The acoustic hit rate dropped from 80.0 s^{-1} to 1.0 s^{-1}, average hit amplitude increased from 32 dB to 50 dB, average hit duration from 0.1 ms to 1.0 s and average hit energy from 0.004 aJ to 3400 aJ. These changes occurred abruptly between 0.5 A cm^{-2} and 1 A cm^{-2}, which coincides with a significant extension of the stagnant bubble region in the flow channels. This leads us to conclude that the change in acoustic activity is caused by the flow regime in the channels changing from two-phase flow to stagnant bubbles. The accumulation of gas in the flow channels occurs when gas production exceeds the capacity of the system for gas removal, which can affect the water distribution in the PEMWE. Further, as the accumulation of gas in the flow channels is strongly affected by the flow-field geometry, the results in this work also demonstrate the potential of using AE to screen different flow-field geometries for gas blockage and draw conclusions on how to optimise flow-field designs.

The use of this *operando* diagnostic tool has successfully been applied to PEMWEs, but could be extended to other applications. The accumulation of gas within a system or plant can cause inefficiencies or pose a hazard in many areas of chemical production and transport. Moreover, it has been shown that the change of two-phase flow regime influences the pressure drop [67,267]. Hence, the technique presented in this chapter could be deployed to screen various flow-field configurations or monitor safe limits of operation, replacing less cost-effective or accessible diagnostic tools such as neutron or X-ray imaging [83,88,90].

However, due to the strong acoustic signal obtained from the flow channels, it was not possible to investigate LGDL mass transport processes using AE. Further, the use of an individual sensor requires the repetition of experiments with different sensor locations to obtain spatially resolved information. In response to these shortcomings, acoustic time-of-flight imaging will be introduced in the following section as a diagnostic tool providing spatially-resolved data on the water-gas distribution in the flow channels as well as the LGDL.

7 *Acoustic Time-of-Flight Imaging of PEMWEs to Probe Internal Structure and Flow Characteristics*

7.1 Overview

In this chapter, acoustic time-of-flight (AToF) imaging has been demonstrated as a low-cost, rapid, non-destructive, *operando* tool to characterize processes in the flow channels and LGDL of a PEMWE. An array of 64 piezoelectric sensors was used, with all sensors emitting input pulses and detecting the acoustic wave reflected by the sample (pulse-echo mode). The shape and intensity of this reflected waveform depends on the ratio of reflection and transmission at phase interfaces and is strongly affected by resonant scattering of acoustic waves by gas bubbles. This AToF imaging technique was deployed to produce reflection intensity maps of the anode flow-field and LGDL; by measuring the AToF response for current densities ranging from 0 A cm^{-2} to 2 A cm^{-2}, a close correlation was found between the acoustic attenuation in the flow-field and the production and removal of oxygen gas through the flow channels. Furthermore, a close link between the AToF response and water thickness in the LGDL was demonstrated, as supported by literature data. The application of AToF imaging has been established as a novel technique of investigating PEMWE operation and as an alternative to more complex imaging techniques such as neutron imaging. The work in this chapter has been published in *International Journal of Hydrogen Energy* [268].

7.2 Introduction

The widespread industrial use of PEMWEs for hydrogen production and grid stabilization will be accelerated through advances in the performance and cost of the technology. One of the most effective ways of improving such technology is through the establishment and use of a robust set of metrology tools to screen the effect of design modification, support optimization of operational parameters and facilitate low-cost maintenance and repair. Traditional electrochemical testing methods, including the interpretation of polarization curves and electrochemical impedance spectroscopy, are valuable diagnostic techniques, but do not offer the same level of spatially resolved information as modern imaging technologies. X-ray computed tomography [153,156,170,172], neutron imaging [85,88–90] or optical imaging [43,44,73,81] have been used to visualise internal operational processes such as the two-phase flow in the flow channels, the microstructure of the liquid-gas diffusion layer (LGDL), water-gas dynamics in the LGDL, or the particle structure of the catalyst layer. However, these techniques are often expensive and may require adaptations of the PEMWE cell to facilitate measurement.

Acoustic diagnostic techniques can overcome many of these disadvantages and promise low-cost, fast, and non-destructive *operando* analysis of PEMWEs and other electrochemical energy storage and conversion devices. AToF is an acoustic technique wherein samples are actively probed with ultrasound waves; the transmitted or reflected response signal is recorded as a function of time-of-flight (ToF) through the sample. The intensity of a reflection signal depends on how strongly the input signal has been attenuated by the sample. Acoustic attenuation occurs at an interface between two different phases due to reflection or resonant scattering, for example from a gas bubble or group of bubbles (Figure 41). At each interface, a portion of the incoming signal is reflected, while the remaining signal is transmitted into the next domain. When an acoustic signal interacts with a bubble interface, it is not only partially reflected, but can also be resonantly scattered if the signal frequency is close to the resonant frequency of the bubble. In this case, the signal is scattered in all directions, causing a very high acoustic attenuation of the input signal. A more detailed discussion of acoustic attenuation mechanisms is found in

Section 4.4.2.2.

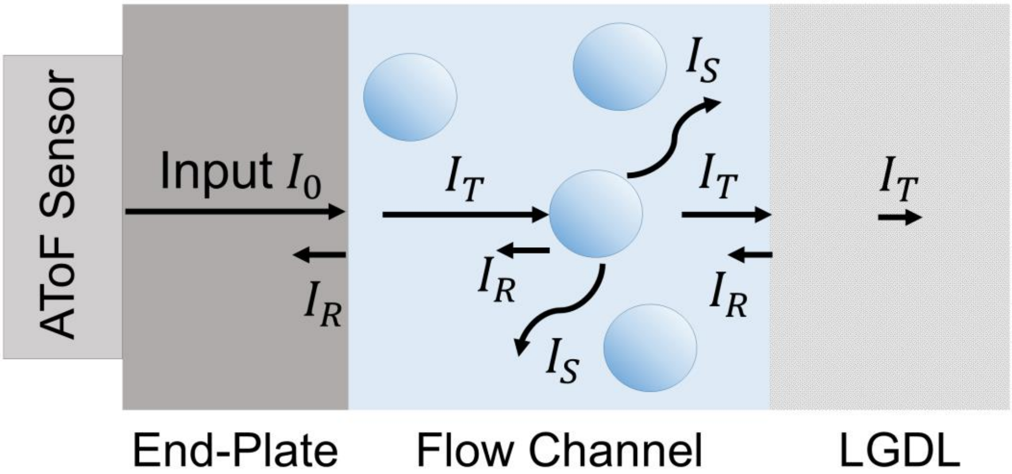

Figure 41: Schematic diagram of acoustic attenuation mechanisms in a PEMWE. The input signal (I_0) is emitted by the AToF sensor and penetrates the end-plate. At each phase interface, a portion of the signal is reflected (I_R), while the remaining signal is transmitted through the next domain (I_T). In the flow channels, the signal can be reflected at liquid/gas interfaces (I_R), but also attenuated by resonant scattering with gas bubbles (I_S). Arrow lengths indicate the relative intensity of an acoustic signal.

This chapter applies AToF for low-cost, non-destructive, and *operando* imaging of PEMWEs. Where previous work on AToF analysis of batteries has mostly relied on single sensors, an array of 64 sensors was deployed in this work. Reflection (pulse-echo) measurements were used to investigate gas/water (two-phase) processes occurring in the flow-field and LGDL as a function of current density. This provides insights into mass transport phenomena in PEMWEs, which would otherwise have required more expensive and time-consuming diagnostic approaches.

7.3 Experimental

Some of the details found in this section are also included in Section 4.1 to support the reader.

7.3.1 PEMWE Cell

The PEMWE used for experiments (Figure 42 (a) and (b)) had a square 9 cm^2 active area and consisted of acrylic end-plates, titanium flow-fields, a titanium LGDL on the anode side, a carbon paper gas diffusion layer (GDL) on the cathode side, and a catalyst coated membrane (CCM). The flow-fields consisted of nine parallel channels with a length of 3 cm, a width of 1.76 mm, and a depth of 2.00 mm. Sintered titanium powder (Merelex, USA) was used as LGDL and Toray H-060 carbon paper as GDL. The CCM was coated with 3.0 mg cm^{-2} iridium/ruthenium oxide on the anode side and 0.6 mg cm^{-2} platinum on carbon on the cathode side (ITM Power, UK). The cell was held together with eight M5 screws, each fastened to a torque of 2.5 Nm. Water was circulated through anode and cathode with an inlet temperature of 50 °C and a flow rate of 50 ml min^{-1} at each electrode.

A Gamry Reference 3000 Galvanostat/Potentiostat with a Gamry 30k Booster (Gamry Instruments, USA) was used for electrochemical testing between 0 A cm^{-2} and 2 A cm^{-2}. The *i-V* curve was obtained following the guidelines of the Horizon 2020 Fuel Cells and Hydrogen Joint Undertaking Programme [269]. Electrochemical impedance spectroscopy (EIS) data were recorded in the frequency range from 10 mHz to 10 kHz at specific DC current densities between 0 A cm^{-2} and 2 A cm^{-2} with an AC current modulation of 10 % of the applied DC current.

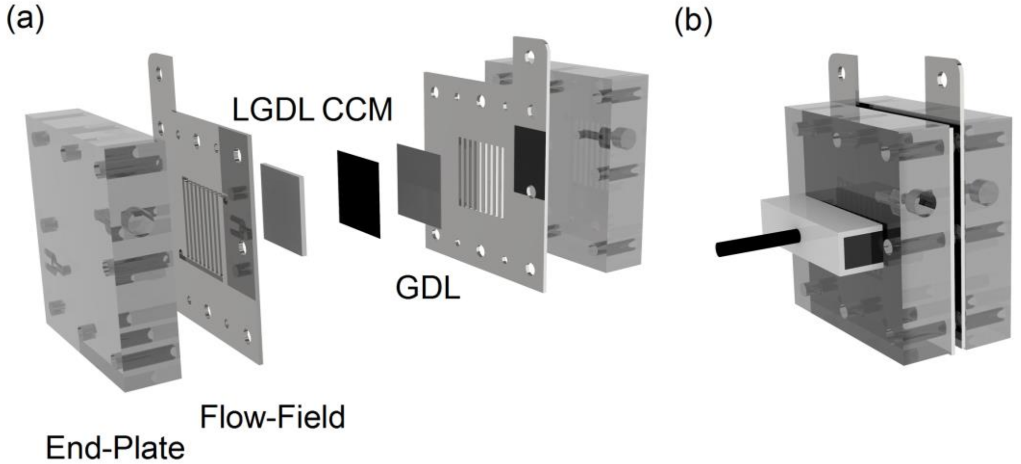

Figure 42: (a) The PEMWE setup consists of end-plates, parallel flow-fields, a titanium sintered liquid-gas diffusion layer (LGDL), the catalyst coated membrane (CCM), and the gas diffusion layer (GDL) on the cathode side. (b) The AToF sensor array is mounted on the outer surface of the anode end-plate.

7.3.2 AToF Measurements

All measurements were taken with an array of 64 acoustic sensors in pulse-echo mode on the anode side of the PEMWE. Each data point was averaged from the signals received from 16 neighbouring sensors (1-16, 2-17, 3-18, …., 49-64), which is called a 'sensor unit'. Each sensor unit recorded one measurement per second. The signal received was the reflected portion of the input signal, which was a pulse sequence with a maximum repetition frequency of 20 kHz. All data was amplified before recording. The amplitude of this amplification is called the acoustic gain. Sensors were controlled and read out with an Olympus FOCUS PX system (Olympus Scientific Solutions, USA). All AToF data in this work is given as a percentage of the sensor saturation value. Before each experiment, a layer of acoustic gel (D12 Couplant Gel, Olympus Scientific Solutions, USA) was applied to the outer surface of the PEMWE and the sensor. This provided good acoustic coupling between sensor and PEMWE surface and ensured a consistent signal across the surface. Two different types of AToF experiments were conducted: fixed position experiments and area scans. For fixed position experiments, the sensor was mounted to a specific location and data were recorded continuously while the current density was increased from 0 A cm^{-2} to 2 A cm^{-2} in 0.1 A cm^{-2} increments, each lasting 120 s. Three different locations along the length of the flow-field were defined, each covering the whole width of the flow-field. The lower location was 0.5 cm from the bottom end of the active area, the upper location 0.5 cm from its top end, and the middle location exactly 1.5 cm from either end of the flow-field. On the other hand, area scans were performed by moving the sensor array across the active area (10 mm s^{-1}) from the bottom to the top of the flow channels, while operating the PEMWE at a constant current density. The sensor array was mounted onto an additional Rexolite block (thickness: 2 cm) to avoid damaging the sensor surface while gliding it over the PEMWE surface.

To analyse the acoustic response from different components of the PEMWE, different time-of-flight intervals of the echo-response were analysed; as the LGDL was located after the flow-field, peaks at a higher ToF were attributed to the LGDL, lower ToF peaks were attributed to the flow-field. Experiments were conducted with different acoustic gains (signal amplification). A clear signal from the anode flow-field was obtained at a gain of 40 dB, however, this acoustic intensity was not strong enough to obtain a clear reflection signal from the LGDL. Therefore, experiments were also carried out at a gain of 60 dB, in which case the signal from the flow-field was saturated, but sufficient signal intensity for analysis was obtained from the LGDL.

For comparison to AToF measurements of the PEMWE during operation, measurements of the dry PEMWE cell (without water inflow) at all three different sensor locations were taken as well.

7.3.3 AToF Data Analysis

Data was visualised in real-time in the FocusPC software (Olympus Scientific Solutions, USA), which was also used for data export. The FocusPC interface was used to measure the maximum reflection intensity in time-of-flight intervals containing the reflection peaks related to specific components of the PEMWE, e.g. flow-fields or the LGDL. The waveform intervals correlated to components of the PEMWE were chosen manually based on a number of AToF scans with varying parameters. Subsequently, the peak intensity was recorded for each sensor unit and throughout the duration of the experiment. More details on AToF data analysis can be found in Section 4.4.4.

The resulting data points were mapped and analysed qualitatively and quantitatively. Each peak of the waveform (intensity value in an acoustic map) is caused by the reflection of the acoustic input signal at an interface. The intensity of a reflection peak relates to the fraction of signal which is reflected at a given interface (the acoustic reflection R), which is a function of the acoustic impedances of the adjacent phases (see Section 4.4.2.2).

Understanding the causes of reflection in a system enables an understanding of the nature of an interface from observing the intensity of the recorded reflection peaks. However, the pulse-echo signal is not only influenced by reflection at interfaces, but also by resonant scattering. This occurs when an acoustic wave travels through a medium containing gas bubbles (such as water in the flow channels of a PEMWE). If the frequency of the wave is at or near the resonance frequency of a gas bubble, a major fraction of the wave is scattered. However, during operation of a PEMWE, a multitude of gas bubbles are produced, covering a wide range of bubble sizes, hence, a wide range of frequencies exist within which resonant scattering between acoustic wave and bubbles can occur. The flow-channels of a PEMWE under operation therefore strongly attenuate the AToF signal and the degree of attenuation of the signal in the flow channels is a measure of the amount of gas being transported. Details on the scattering frequency of individual gas bubbles and bubble clouds are found in Section 4.4.2.2 and were used in the following for data interpretation.

To obtain frequency information from the pulse-echo response, fast Fourier transform (FFT) analysis of the AToF waveform was performed using the FocusPC software. The pulse-echo response across the entire time-of-flight was analysed, yielding an intensity spectrum as a function of frequency. The frequency at which the maximum intensity was found, will be referred to as peak frequency in the following. Comparison of the peak frequency with values obtained from the equations in Section 4.4.2.2 serves to indicate whether the obtained signal predominantly originated from resonant scattering.

7.4 Results and Discussion

7.4.1 Electrochemical Testing

The PEMWE cell showed typical polarization behaviour (Figure 43 (a)), consistent with previously reported data sets [31,43,59,120]. EIS was used to examine the influence of mass transport effects on the overall PEMWE performance (Figure 43 (b)): while the width of the left-hand arc (high-frequency) in the Nyquist plot determines the activation overpotential, the right-hand arc (low-frequency) quantifies the mass transport overpotential [78,120,270]. The width of the right-hand arc increased from low to high current density, by around 30 % from 0.25 A cm^{-2} to 2 A cm^{-2}. This indicates a significantly higher overpotential due to mass transport processes at higher current densities.

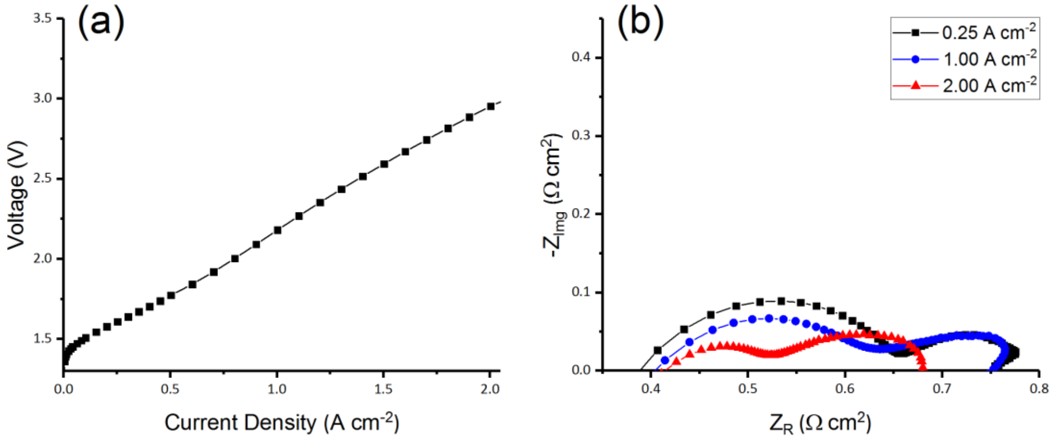

Figure 43: (a) Overall PEMWE cell performance, shown as voltage against current density ranging from 0.00 A cm^{-2} to 2.00 A cm^{-2}. (b) Electrochemical impedance spectra of the PEMWE, represented as negative imaginary impedance $-Z_{img}$ against the real impedance Z_r (Nyquist plot), for 0.25 A cm^{-2}, 1 A cm^{-2}, and 2 A cm^{-2}.

On the anode side of a PEMWE, as current density increases, an increasing flux of water has to be transported to the active catalyst sites, while increasing amounts of oxygen have to be removed from the system. The water transport capacity from the flow-field, through the porous LGDL, to the CCM and oxygen transport in the reverse direction is finite and consequently increasing mass transport inefficiencies occur with increasing current density and lead to an increase in PEMWE operational voltage. This rise is due to the mass transport overpotential, which is caused by the overall increase of mass transport in the

PEMWE system.

7.4.2 Structural Investigation with AToF

The ability of acoustic waves to penetrate through layers of material can be used for rapid inspection and diagnostics. AToF scanning of the entire active area (as described in Section 7.3.2) provided a spatially resolved 3D imaging technique, visualising the structure of different PEMWE components. Experiments at two different acoustic gains were used to investigate the structure and assembly of flow-field and LGDL in the PEMWE. Each AToF experiment offered depth-profiling of the same layers of the PEMWE, such as flow-field and LGDL, but investigation of different layers was carried out in separate experiments to obtain an optimal and clear signal from each component. The PEMWE was operated at 0.25 A cm^{-2} for both experiments, hence water and oxygen gas both exist in flow-field as well as the pore phase of the LGDL. Based on preliminary experiments, different time-of-flight intervals were chosen for each component, measuring the maximum reflection peak intensity in the respective interval.

The structure of the flow-field was visualized with AToF, showing details of the flow channels, the ribs and water inlet and outlet. A low reflective peak was observed in channel areas (blue areas in Figure 44 (a)), while the ribs were marked by high reflective peaks (yellow areas). Comparison between the actual geometry of the parallel flow-field (Figure 44 (b)) with the AToF image showed that all eight ribs and nine channels were detected. The ratio between rib length and width was 17.05 for the actual flow-field design, and was manually measured to be 18.70 from the AToF image. Based on the width of the active area (30 mm, 32 pixel) a spatial resolution of 0.94 mm was obtained. The fact that high reflection intensities were detected in the rib areas, while lower intensities were found in the channel areas, suggests that the acoustic impedance of the acrylic end-plate was more closely matched with the acoustic impedance of the water-filled channels than with the acoustic impedance of the titanium flow-field ribs. This might seem counter-intuitive, but can be derived from the material values (Section 4.4.2.2). Further, the very low reflection intensity in the flow channels is likely to be attributed to resonant scattering from oxygen bubbles. This will be further validated in Section 7.4.3.

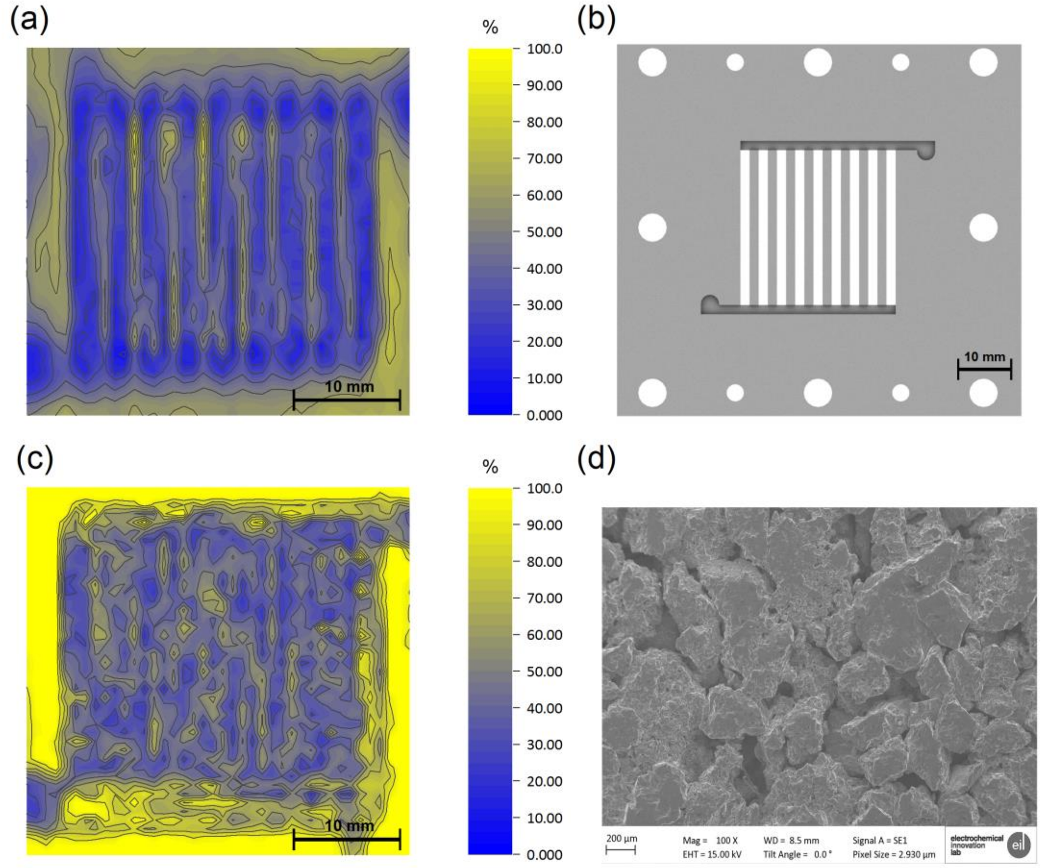

Figure 44: (a) AToF scan of the anode flow-field of the PEMWE, showing rib and channel areas, as well as water inlet and outlet. (b) The CAD design of the flow-field, shown for comparison. (c) AToF scan of the LGDL, illustrating a granular distribution of high and low reflection intensity. (d) SEM image of the LGDL microstructure given for comparison. Image was obtained on a Zeiss EVO MA10 (Carl Zeiss, USA) at an electron accelerating voltage of 15 kV and a magnification of 100x. Both AToF area scans were obtained during operation of the PEMWE at a constant current density of 0.25 A cm^{-2}. Hence, water was circulated through the flow-field, and LGDL and flow channels contained water as well as oxygen.

Investigating a different set of peaks at a higher acoustic time-of-flight (hence relating to a PEMWE component located behind the flow-field), an AToF image of the LGDL was obtained during operation of the PEMWE at 0.25 A cm^{-2} (Figure 44 (c)). The LGDL was a porous sintered titanium structure (Figure 44 (d)) with pores being filled with either water or gas. For the AToF response, a granular distribution of high and low reflective peaks, randomly distributed over the LGDL area, was observed. AToF is a depth-profiling technique, hence the reflection intensity from the LGDL was affected by acoustic processes in the flow-field and end-plate. As the reflection at an interface is a function of the acoustic impedance of both materials at this interface, the acoustic response from LGDL pores and particles was different in rib and land areas. This makes it difficult to clearly assign low or high reflection peaks to either pores or particles. Further, the granularity of the AToF response was much coarser than the microstructure of the LGDL. As observed above, the spatial resolution of the AToF measurement is 0.94 mm, while the size of pores and particles of the LGDL are significantly smaller (Figure 44 (d)). This suggests that with the given experimental equipment AToF cannot be used to distinguish individual pores or particles, but rather larger accumulations of gas or water in a network of adjacent pores. However, by observing the overall reflection intensity as a function of current density, conclusions can be drawn on the volume averaged macroscopic processes in the LGDL (Section 7.4.3.2).

The above results show that AToF scans are a powerful 3D imaging and depth-profiling tool for quick inspection and qualitative analysis. However, to obtain quantitative data as a function of current density, fixed position AToF measurements are also investigated below to reduce any error that may be introduced while moving the acoustic sensor.

7.4.3 AToF for Quantitative Assessment

By applying AToF across the whole width of the active area at a fixed location, while varying current density, statistically reliable data (probing of a constant state of operation for 120 s) on the acoustic response was obtained. Experiments were conducted at three different sensor locations (lower, middle, and upper as defined in Section 7.3.2) and two different acoustic time-of-flight intervals to access the flow-field and LGDL, respectively.

7.4.3.1 Flow-Field

Figure 45 (a) shows the AToF response from the flow-field at the middle location on a logarithmic scale between 0 A cm^{-2} and 2 A cm^{-2}, hence, illustrating the evolution of the reflection intensity in the middle segment of the flow-field across the entire active area (and all flow channels and ribs) as a function of current density. To visualize the large relative changes in intensity across the current density range, the use of a logarithmic scale was required. A general trend from high reflection intensity to low reflection intensity was observed as current density was increased. While the average intensity of the flow-field reflection peaks was around 55 % at 0 A cm^{-2}, it dropped to 5 % at 2 A cm^{-2}. At 0 A cm^{-2}, the AToF signal was reflected at the interface between the end-plate and flow channels/ribs. Due to the mismatch in physical properties, and hence acoustic impedance, the transition from end-plate to water in the flow channels produced a strong reflection peak. As current density increased, the flow channels were not only filled with water, but also with an increasing amount of oxygen bubbles. As outlined in Section 4.4.2.2, gas bubbles attenuate the AToF signal via resonant scattering. This explains why the averaged intensity decreased continuously with increasing current density. As more gas was produced, the acoustic input wave was scattered (anisotropically) more strongly, which reduced the intensity of the echo signal detected.

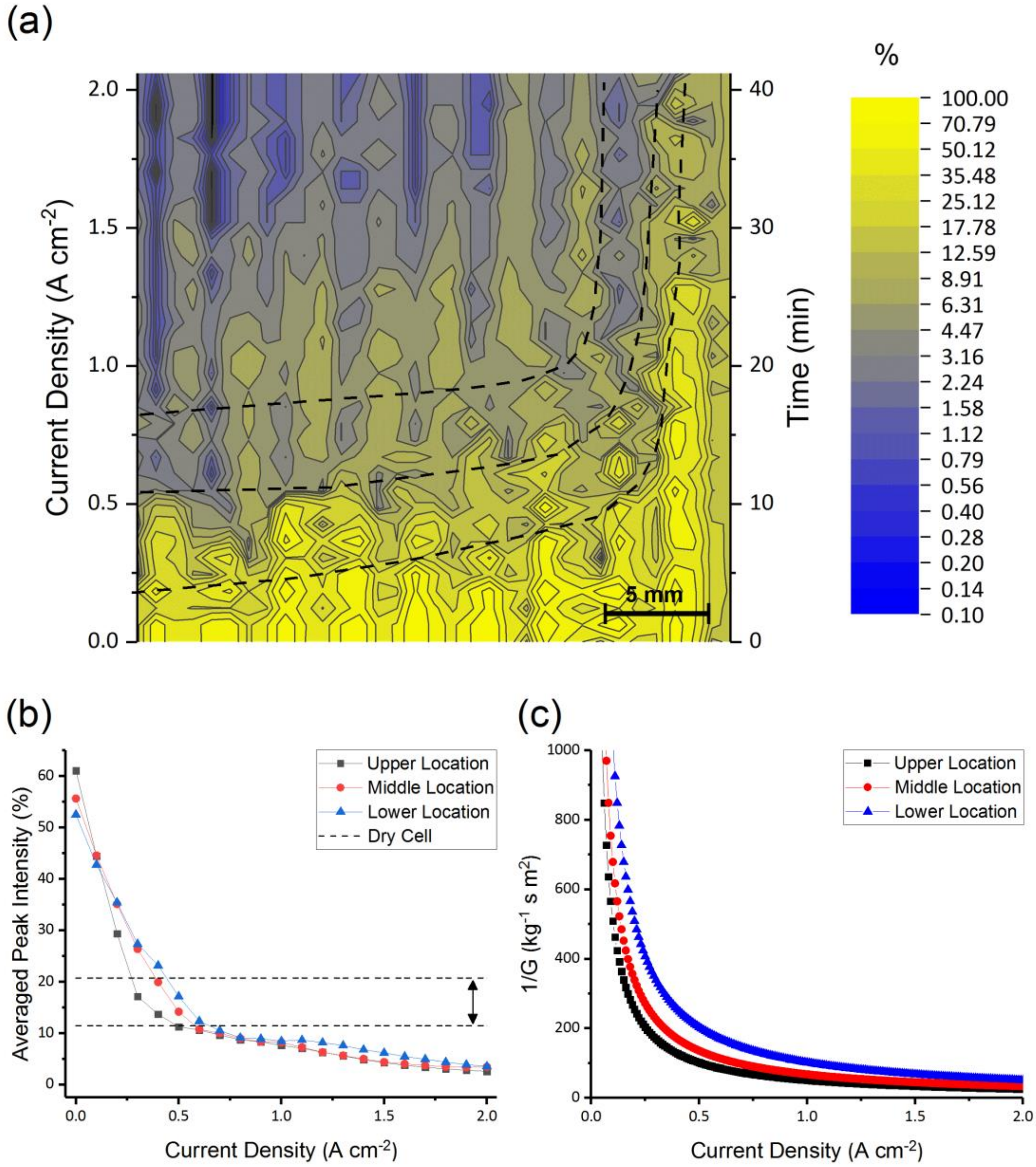

Figure 45: (a) AToF reflection map of the flow-field across all flow channels at the middle sensor location for current densities ranging from 0 A cm^{-2} to 2 A cm^{-2}. This illustrates the evolution of the reflection intensity in a segment across the width of the flow-field, roughly the same height as the AToF sensor, as a function of current density. The intensity of the reflection peaks is indicated using a logarithmic color map. Dashed black lines indicate parabolic lines of identical intensity. (b) The average intensity of reflection peaks across all flow channels for lower, middle, and upper sensor locations as a function of current density. The average intensity band measured in the dry cell is shown for comparison (dashed black lines). (c) For comparison, the inverse of the amount of oxygen per flow channel, G, is shown as a function of current density for all three sensor locations.

This also suggests that resonant scattering was the dominant attenuation mechanism in the flow channels. As current density increases, the amount of oxygen increases, and a number of flow regimes is typically observed in the flow channels. It is well-established that at low current densities the bubbly flow regime is observed, which then consecutively develops into slug and annular flow with increasing current density and location along any given flow channel [40]. Due to the large number of individual bubbles [218], the bubbly regime exhibits by far the highest amount of liquid/gas and gas/solid interfaces. If acoustic reflection at interfaces were to be the dominant attenuation mechanism, a maximum of reflection would be expected in the bubbly regime, with a decrease in reflection intensity for higher current densities due to the reduction in interfaces and the increasing amount of resonant scattering. However, as a continuous decrease in reflection intensity was observed experimentally, it appears likely that the dominant mechanism of acoustic attenuation in the flow channels was resonant scattering.

To establish the link between oxygen gas production and AToF signal, the pulse-echo response averaged across all channels (Figure 45 (b)) and the inverse (increasing gas flow reduces the reflection intensity) of the gravimetric gas flow per flow channel, *G*, (Figure 45 (c)) are displayed as a function of current density. The gas flow was calculated theoretically based on Faraday's law [40,218]. The different gas flows at the sensor locations was accounted for by adapting the active area used for the calculation, according to the location of the sensor along the flow channels. The pulse-echo response showed a continuous decrease with current density, which mirrors the behaviour of the inverse oxygen flow $1/_{G}$. An initial drop at low current densities was followed by a linear decrease from around 0.5 A cm^{-2} to 2 A cm^{-2}. The distance between the curves for different locations was not as pronounced for the pulse-echo response as for the calculated inverse gas flow. This implies that attenuation due to resonant scattering was the dominant mechanism. However, it was convoluted by other attenuation mechanisms, such as reflection from gas/liquid and liquid/solid interfaces.

This was further supported by comparing the average reflection intensity in the flow channels under operation and in the completely dry cell. The band of average reflection intensity (two standard deviations) ranged between 11.46 % and 20.75 % (dashed black lines in Figure 45 (b)) for AToF measurements of the cell completely filled with air and void of water. However, the dry reflection intensity was considerably higher than values obtained during PEMWE operation at current densities beyond 0.75 A cm^{-2}, where the flow channels contained a water-gas mixture. Hence, the signal attenuation in the flow channels could not be solely caused by the reflection at the gas interface. It is therefore implied that resonant scattering caused the unexpectedly low reflection intensity values.

Another feature of the AToF signal was that it exhibited an approximately parabolic profile across the flow channels. From left to right, the transition from a given acoustic intensity level to a lower one (e.g. yellow to blue in Figure 45 (a)) occurred at an increasingly high current density. Therefore, the lines of equal AToF intensity (black dashed lines in Figure 45 (a)) formed a parabolic profile roughly increasing from left to right. The effect of non-uniform flow distribution, following a parabolic profile, in a parallel flow-field is well documented [72,75,76] and has been observed with optical imaging of the PEMWE flow channels [73]. This is a consequence of the flow-field being designed in a Z-pattern, with water inlet and outlet being located at diagonally opposed ends of the parallel flow-field, which causes the water flow rate to be higher in the channels to the right (closer to the outlet) by a factor of up to five compared to the remainder of the channels [72]. This further established the ability of AToF to represent the physical processes in the flow-field.

To further confirm resonant scattering as a dominant force of acoustic attenuation in the flow channels, for the middle location, the calculated frequencies for resonant scattering were compared with the peak of the signal frequency spectrum obtained via FFT (Figure 46). The frequency of resonant scattering was calculated as a function of current density (as described in Section 4.4.2.2), using a mass balance and Faraday's law to determine the gas fraction [40,218]. For the middle location, the active area was assumed to be half of the entire active area, thus only accounting for the amount of gas that had accumulated in the flow channels at the middle sensor location. Assuming the bubble cloud diameter being equal to the width of a flow channel, the resonant frequency is trending towards infinite values for 0 A cm^{-2} and falls to around 0.50 MHz at 2 A cm^{-2}. Additionally, the frequency of peak intensity was determined from the AToF signal for each current density via FFT analysis of the waveform along the entire observed time-of-flight. This indicated the most common echo-signal frequency occurring in the PEMWE and was linked to the processes causing the echo-response. The peaks related to the flow channels were by far the most dominant signal; hence, it is assumed that the obtained frequency spectrum was representative of the flow channel processes. Peak frequencies were observed in the range from around 2.70 MHz to 0.95 MHz. The development of the observed peak frequency broadly followed the trend of the calculated bubble cloud frequency. This indicated that a major part of the received pulse-echo signal originated from the resonant scattering of bubbles and bubble clouds, respectively. Due to its anisotropy, this mechanism caused strong attenuation of the overall signal; however, the fraction of signal scattered towards the AToF sensor was still significant, as indicated by the measured and calculated frequency spectra.

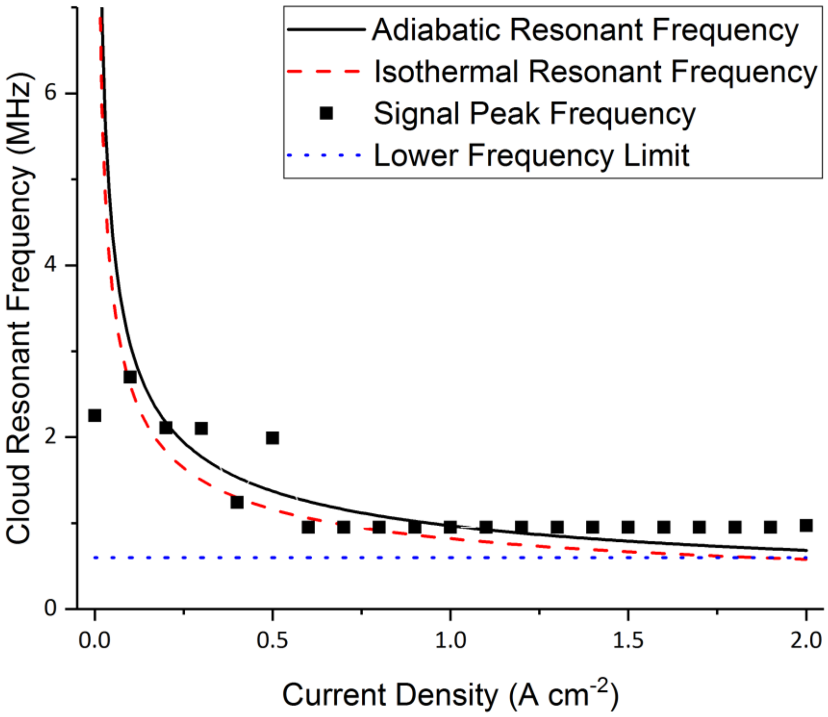

Figure 46: The resonant scattering frequency of a bubble cloud with the diameter of a flow channel for isothermal and adiabatic operation of the PEMWE as a function of current density. The peak frequency of the AToF signal (obtained via FFT analysis) is shown as single data points, which are consistent with the resonant scattering frequency. The lower frequency detection limit is given for reference (dashed blue line). All calculations and measurements refer to the middle sensor location.

7.4.3.2 LGDL

By increasing the acoustic gain and investigating a different time-of-flight interval, a detailed AToF investigation of the LGDL was made possible. The LGDL lacked clear macroscopic structures compared to the flow field (channels, ribs), but consisted of a high number of water or gas-filled pores and titanium particles. As for the flow-field, the LGDL was probed between 0 A cm^{-2} and 2 A cm^{-2} at upper, middle, and lower sensor locations. The resulting current (time) / location map is shown for the middle position in Figure 47(a). The x-axis shows the line scan across the middle section and the y-axis the varying average cell current density as it increases with time.

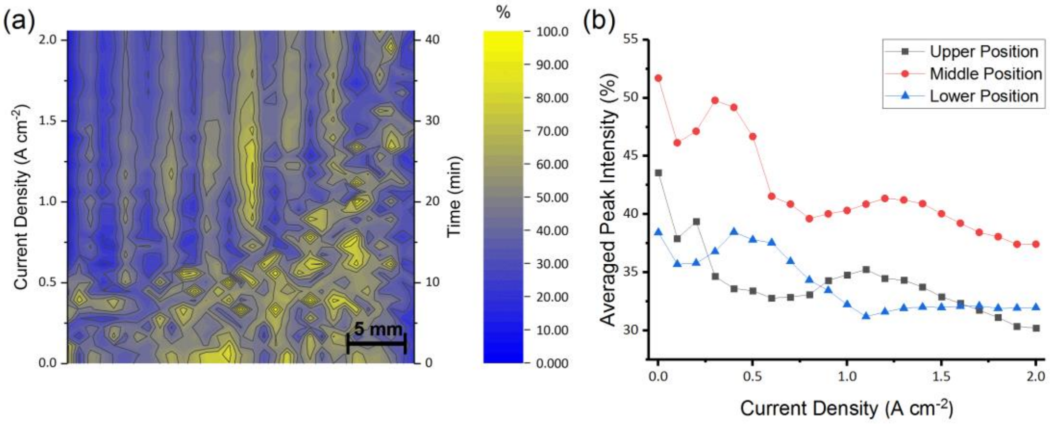

Figure 47: (a) AToF reflection map across the LGDL width at the middle sensor location for current densities ranging from 0 A cm^{-2} to 2 A cm^{-2}. The intensity of the reflection peaks is indicated using a linear color map. (b) Average intensity of reflection peaks across the LGDL width for lower, middle, and upper sensor locations as a function of current density.

For low current densities below 0.5 A cm^{-2}, randomly distributed reflection maxima and minima were observed, which is similar to Figure 44 (c). Above 0.5 A cm^{-2}, this random distribution disappeared and a structure of clearly localized maxima and minima developed, which mirrored the rib/channel structure of the flow-field. It is well established through neutron imaging studies that the LGDL carries more oxygen gas and less water under the rib areas than under the channel areas of the flow-field in an operating PEMWE [87–89]. This trend was confirmed by AToF imaging, providing further confidence in this technique and establishing the possibility to examine the water-gas distribution in the LGDL in more detail via AToF. However, it has to be noted that the measurement of LGDL processes through AToF is affected by the flow-field. As the acoustic signal has to travel through the flow-field before reaching the LGDL, and the signal reflected by the LGDL has again to cross through the flow-field before being detected, processes in the flow-field can potentially lead to deviations in the signal associated with the LGDL, e.g. the existence of rib/channel features in the AToF response from the LGDL can potentially be an artefact caused by the input signal being transmitted through the flow-field before penetrating the LGDL.

The overall intensity of reflection peaks attributed to the LGDL decreased with increasing current density (Figure 47 (b)). The variance between individual locations is likely caused by differences in local porosity of the LGDL and the formation of gas and water pathways in specific areas. A decrease from around 52 % acoustic intensity at 0 A cm^{-2} to around 38 % at 2 A cm^{-2} was observed for the middle position. However, the typical decrease in reflection peaks with current density was considerably smaller in the LGDL than in the flow channels. Other than in the flow-field, where almost the entire channel was filled with gas at high current density, in the LGDL only certain parts of the porosity of the LGDL contained gas at any given time. The remainder consisted of solid titanium and water pathways, which change little with current density.

The development of reflection intensity with current density observed here is consistent with through-plane water thickness measurements performed using neutron imaging [90], which will be presented in Section 5. Neutron imaging can reliably measure the absolute water thickness in a sample due to the strong interactions of neutrons with hydrogen atoms and therefore data on the water thickness in the LGDL obtained via neutron imaging can be used for validation and calibration of AToF data. As shown in Section 5, a decrease in water thickness by 12 % between 0.25 A cm^{-2} and 1.5 A cm^{-2} was found averaged across all rib areas using the same LGDL material as this work. This compares to a decrease of 13 % in reflection intensity across the active area found in this work between 0.2 A cm^{-2} and 1.5 A cm^{-2}. The close correlation in neutron imaging data and AToF response emphasized the possibility of applying AToF imaging to LGDL processes and validated the chosen methodology.

7.5 Conclusion

This work establishes AToF imaging as a promising diagnostic tool for PEMWEs, however, the resolution limitations outlined in Section 7.4.2 have to be considered carefully when applying AToF imaging. It is demonstrated that the internal structure and assembly of flow-field and LGDL can be visualized using AToF scans across the PEMWE active area. This can be used for rapid, non-destructive inspection and diagnosis of PEMWE systems and offers a much lower cost and easily deployable *operando* imaging capability than established methods, such as X-ray or neutron imaging. By measuring the pulse-echo response of a PEMWE operated between 0 A cm^{-2} and 2 A cm^{-2} a range of effects typical for PEMWEs have been observed, which corroborates the effectiveness of AToF imaging. These effects were related to the flow-field as well as the LGDL.

Acoustic investigation of the flow-field showed a general decrease in reflection intensity with increasing current density. This indicates an increasing acoustic attenuation, which is caused by the increasing amount of oxygen gas produced and removed through the flow channels. It is shown by calculating the amount of oxygen produced due to electrochemical activity that the AToF signal scales closely with the inverse of the amount of gas in the flow channels. By determining the peak frequency of the AToF signal as a function of current density using FFT analysis, and comparing these data with theoretical expectations for the frequency of resonant scattering of bubbles, the link between gas bubbles in the flow channels and acoustic attenuation was confirmed. Further, AToF imaging yielded a parabolic profile of intensity across the flow channels, an effect well established in the literature, which corroborates the validity of the data obtained in this work.

AToF imaging of the LGDL showed a granular distribution of reflection maxima and minima. However, the spatial resolution of the AToF equipment was not sufficient to resolve the LGDL microstructure of gas/water pathways and titanium particles. Just as for the flow-field, a general trend of decreasing reflection intensity with increasing current density was observed between 0 A cm^{-2} and 2 A cm^{-2}. However, the trend was less pronounced than for the flow-field. It was demonstrated that the AToF response scales closely to data on the water thickness in the identical LGDL material, obtained via neutron imaging. Further, AToF imaging showed a distinct difference between areas of the LGDL under rib and land areas of the flow-field, respectively. This can potentially be attributed to the accumulation of gas and water under rib and channels of the flow-field, respectively. This effect has been well documented by neutron imaging. Overall, this confirms the ability of AToF imaging to investigate macroscopic processes in the LGDL.

In conclusion, it was demonstrated that AToF imaging is well suited to investigate mass transport processes in flow-field as well as the LGDL of PEMWEs. It offers a low-cost, rapid, non-destructive, *operando* imaging tool. In a research context, it can potentially replace more time-consuming, expensive and specialized investigation techniques such as neutron and X-ray imaging. Commercial applications could include rapid inspection of single cells and PEMWE stacks or the diagnosis of non-uniform distribution of reactants across the active area, which could indicate faulty cell assembly or issues related to the CCM.

8 Future Work

8.1 Overview

This section will outline a number of experimental plans, which naturally follow from the ideas and results outlined in this work. In some cases, preliminary results are shown to demonstrate the feasibility or value of these projects, which would form a good starting point for postdoctoral research or a PhD project.

8.2 Novel Engineering Approaches

One of the key conclusions from this work is that the established designs and materials used for PEMWEs come with a number of disadvantages and are not optimized for mass transport under high current density. This calls for novel approaches to the design of LGDL and flow-fields, using well-defined structures instead of naturally available materials (e.g. sintered powder), and tailoring geometries to optimize mass transport.

8.2.1 Additive Manufacturing of LGDLs

In recent years, additive manufacturing (‘3D printing’) has become one of the most promising approaches for manufacturing of novel structures for energy-related structures, such as battery or supercapacitor electrodes, electronic circuits, or flexible lighting [271]. Additive manufacturing usually refers to extrusion-type 3D printing; however, it also encompasses selective laser sintering (SLS), selective laser melting (SLM), and electron beam melting (EBM), which are used to 3D print metal structures from a bed of metal powder. These processes have successfully been used to 3D print PEMWE components, such as titanium LGDLs [272], stainless steel flow-plates [62,273], and stainless steel plates integrating flow-field and LGDL in one component [51].

The versatility of 3D printing can also be used to create LGDL structures with tailored pore shapes and hydrophilicity. Additive manufacturing offers the capability of creating LGDLs with conical pores, hence manipulating the contact angle between pore wall and water. This results in tuneable hydrophilicity of the pore and allows to distribute pores with modified water contact angle across the active area, therefore allowing for a targeted distribution of water to achieve optimized water ingress and equilibration of non-uniform distribution of reactants or current density across the active area.

8.2.1.1 Preliminary Results

To gain a first impression of the influence of the pore shape on mass transport in a PEMWE, three titanium LGDL (Thickness: 1 mm) were designed and manufactured (Protolabs, UK): one with straight, cylindrical pores (Figure 48 (b)), one with conical pores opening towards the CCM (Figure 48 (c)), and one with conical pores opening towards the flow channels

(Figure 48 (d)). It is expected that the three different pore shapes result in different water contact angles on the pore walls and therefore in varying hydrophilicity for the three LGDLs. Due to limitations in the spatial resolution of the 3D printing process, all pores were designed with an average diameter of 1.2 mm; hence, conical pores had a smaller opening of 0.8 mm and a larger opening of 1.6 mm. This resulted in a pore angle against the vertical of 21.8 °, which is, depending on the geometrical orientation of the LGDL pores, either added or subtracted from the water contact angle on titanium. Assuming a contact angle of water on titanium of around 60 ° [52,274,275], a water droplet contact angle in the LGDL pores opening towards the flow-field of around 38.2 °, and for the pores opening towards the catalyst layer of 81.8° is obtained. This illustrates the significant effect of pore orientation on its hydrophilicity.

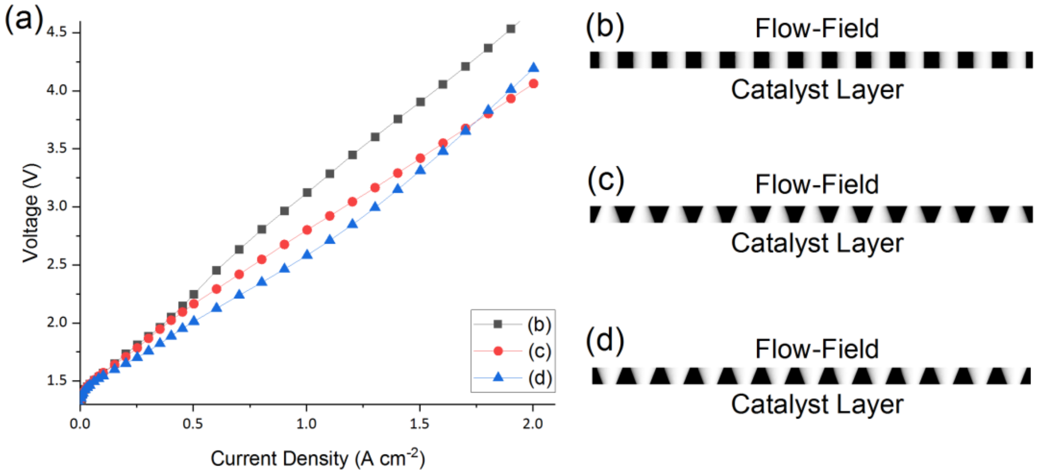

Figure 48: (a) Performance, shown as i-V curves, between 0 A cm^{-2} and 2 A cm^{-2} of the LGDLs with (b) cylindrical pores, (c) conical pores opening towards the CCM, and (d) conical pores opening towards the flow channels.

Electrochemical testing demonstrated clear differences in PEMWE performance for the LGDLs (Figure 48 (a)). While the LGDLs with straight and pores opening towards the CCM exhibited a linear increase in voltage between 0 A cm^{-2} and 2 A cm^{-2}, the LGDL with conical pores opening towards the flow channels showed a non-linear increase in voltage at high current densities. This suggested an increase in concentration overpotential, potentially due to insufficient supply of water to the CCM, and demonstrated that PEMWE performance can be affected by tailoring the LGDL pore shape. To demonstrate and quantify the effect of pore shape (hydrophilicity) on the concentration overpotential and

PEMWE performance, a systematic study, examining a wide range of 3D printed LGDLs with different pore shapes and sizes, would be required to ensure that the performance effect observed above is due to a change in mass transport, and not the variation of other parameters such as the available triple-phase boundary.

The electrochemical performance of the LGDLs tested here is poor, with voltages exceeding 4 V at 2 A cm^{-2}. However, due to the limitations on the minimum achievable feature size of the additive manufacturing process, the LGDL pores were large compared to the pore sizes of commonly deployed materials (e.g. 20 µm to 140 µm for a typical titanium felt, see Section 5.4.1). Therefore, the high operational voltage observed here is likely due to a lack of triple-phase boundary, but can be improved upon by creating LGDL structures with smaller pores. As additive manufacturing technology is constantly evolving [276], it is likely that such structures can be manufactured in the future.

8.3 Combination of Acoustic Techniques with Neutron Imaging

The capabilities of acoustic techniques (AE, AToF) to detect changes in the two-phase flow in the flow channels have been demonstrated in this work. Further, a link between flow-field geometry and the water distribution in the LGDL has been found (Section 5.4.2). By deploying neutron imaging and acoustic techniques simultaneously, a more detailed understanding of the link between two-phase flow and LGDL water-gas distribution can be obtained and the suitability of acoustic techniques as a low-cost alternative to radiation-based imaging can be confirmed.

Particularly AToF is well suited to be used in conjunction with neutron imaging due to its capability to measure the water-gas distribution in the LGDL as well as in the flow-fields. These experiments could confirm the correlation between the LGDL water thickness and the acoustic attenuation, but would also allow to observe the evolution of two-phase flow and water-gas distribution in the LGDL simultaneously and cross-validated by two different experimental techniques. The results could subsequently be used to create a calibration between AToF signal and water-gas distribution, which would pave the way to use AToF as an *operando* performance tool for PEMWE stacks and commercial plants. Pham et al. [277] demonstrated the combined use of AToF measurements and synchrotron X-ray imaging to validate the AToF capabilities to detect gas evolution and delamination in Li-ion batteries, which shows the feasibility and promise of combining AToF with advanced imaging methods.

8.4 Investigation of the Influence of Flow-Field Geometry on the Water-Gas Distribution in the Liquid-Gas Diffusion Layer

Results in Section 5 indicate a link between flow-field geometry and the water-gas distribution in the LGDL underneath the flow-field. This correlation can be further investigated by a systematic study using neutron imaging to compare the water thickness distribution in x- and y-direction in the LGDL when using different flow-field geometries (parallel, single-serpentine, triple-serpentine).

It is expected that areas of the flow channels with a high gas fraction, such as the upper regions in a parallel flow-field, also exhibit increased gas fractions (decreased through-plane water thickness) in the areas of the LGDL underneath those areas.

By comparing the water-gas distribution with the flow velocity and distribution of water and gas in the flow channels adjacent to specific areas in the LGDL, the extent and nature of the influence of flow-field processes on mass transport in the LGDL can be established. This would introduce the mass transport characteristics of a flow-field as a novel parameter to consider in optimizing cell assembly, besides established factors such as pressure drop and contact resistance with the LGDL.

8.5 Investigation of the Link between Flow Regime and PEMWE Performance

As outlined in Section 3.2.4, uncertainty remains on whether the flow regime in the flow channels has an influence on PEMWE performance and the nature of this influence. While there is experimental evidence suggesting that flow regimes with a low water-to-gas ratio, such as plug or slug flow, cause a decrease in performance [40–42], it has also been argued that PEMWE performance might improve in slug flow [43,44].

However, to the author’s knowledge, no systematic study comparing PEMWE performance under a wide range of water and gas flows has been performed yet. By injecting oxygen upstream of the PEMWE anode, the amount of gas in the flow channels can be controlled and specific flow regimes achieved (see Figure 49). Varying the amount of injected gas, as well as the amount of circulated water, PEMWE performance and EIS spectra could be acquired in a very wide range, covering all relevant flow regimes.

Further, AE sensors can be used to detect and quantify the flow regime in different locations across the PEMWE active area while varying water flow and gas injection. This would allow to reliably quantify the two-phase flow and obtain a clear link between performance and flow regime.

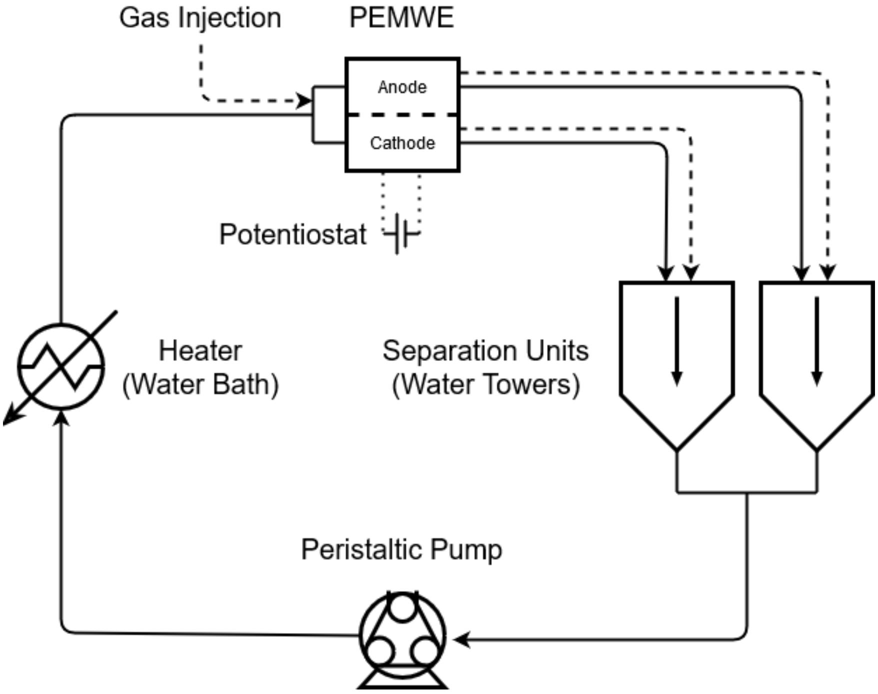

Figure 49: P&ID of the balance-of-plant used for PEMWE testing with anode gas injection to investigate the influence of the flow regime on electrochemical performance. Solid lines denote liquid flows, while dashed lines indicate gas flows. The potentiostat is connected to anode and cathode simultaneously.

8.6 Conclusion

The rise of renewable energy sources as widespread alternative to conventional energy production methods and an established part in the energy mix of industrial nations brings the need for electricity grid stabilization and balancing. Excess energy requires storage, which can be subsequently released in case of insufficient energy production. A multitude of mechanical and electrochemical technologies offer this capability, with pumped hydroelectric systems being by far the most commercially developed system. Due to its limitation to specific geographic conditions, the use of other energy storage systems is inevitable.

Among candidate technologies, hydrogen-based solutions are promising and large-scale projects have been realised. Excess energy is used to produce hydrogen via water electrolysis, which can subsequently be stored, injected into the gas grid or converted back into energy using fuel cells. For electrolysis and fuel cells, PEM technology has gained notable traction due to its advantages over alkaline systems. PEMWEs offer high attainable current density of 2 A cm^{-2} and beyond, a more compact build than alkaline water electrolysis, and low gas crossover.

As PEMWEs grow more mature, the operational current density is further increasing, which requires increasing amounts of reactants being transported to, from and within a PEMWE cell. This calls for the adequate design of PEMWE cells so as to ensure sufficient supply with water and removal of oxygen on the anode side. Inhomogeneity of reactant transport has to be avoided to prevent local membrane dry-out or hotspot formation. Historically, there has been little scientific interest for mass transport processes in PEMWEs compared to electrocatalyst and membrane development, with a lack of understanding of processes in key components such as flow-fields and LGDL, and few low-cost, *operando*, and non-destructive diagnostic tools available.

Therefore, the goal of this thesis was to develop a more thorough understanding of the mass transport processes in LGDL and flow-fields and develop a suite of diagnostic tools, facilitating rapid and low-cost investigation of these processes. Due to the very high attenuation of neutrons in water, neutron imaging was selected to gain insight into the water-gas distribution in the LGDL. Acoustic methods were, to the author's knowledge, applied for the first time to PEMWEs in a quest to develop more cost-effective and readily available diagnostic tools for mass transport processes in PEMWEs, offering an alternative to established methods like radiation-based imaging.

After outlining the necessary theoretical background, reviewing the available literature focussed on mass transport processes, and outlining the experimental methodology employed in this work (Sections 2 to 4), a number of results obtained over the course of this work are presented. In Section 5, results on the water-gas distribution in the LGDL, obtained with neutron imaging, are presented. In a first step, measurements of the through-plane water thickness are correlated to an in-depth study of the LGDL microstructure using X-ray computed tomography. A clear link between microstructure and water saturation is shown, and the results indicate a link between flow-field geometry and LGDL water content. To establish a suite of low-cost diagnostic tools as an alternative to less cost-effective and accessible techniques, such as neutron imaging or X-ray tomography, a number of results on the investigation of mass transport processes in PEMWEs with acoustic diagnostic methods are presented. Section 6 shows how acoustic emission can be used to qualitatively diagnose the number and size of gas bubbles in the flow channel of a PEMWE or detect gas blockage, which potentially can be developed into an *operando* tool for the measurement of local changes in current density and to rapidly evaluate changes in PEMWE design or operational conditions. Another acoustic method, acoustic time-of-flight imaging, is used in Section 7 to gain insight into the water-gas distribution in the flow channels as well as the LGDL. The results show a clear correlation with physical expectations, results reported in the literature, and results obtained with neutron imaging.

It has to be noted that this work has focussed on mass transport and its diagnosis in single-cell electrolysers, not PEMWE stacks. Due to the multiple sources of acoustic signal and the increased material thickness that is required to be penetrated by any acoustic or radiation signal, applying the techniques and conclusions from this work to stacks is non-trivial. However, these issues can be addressed by a multitude of potential approaches, for example the integration of acoustic sensors into bipolar plates, thus allowing to capture acoustic signal only from individual cells in a stack. This approach could be even further optimised by incorporating thin air gaps into the designs of bipolar plates, serving as acoustic barriers, allowing to minimise acoustic interaction between individual cells of a stack. Besides integrating sensors into bipolar plates of individual stacks, AToF imaging of PEMWE stacks could also be facilitated by using probes with a higher acoustic gain, penetrating several cells of a stack.

In summary, this work has significantly contributed to the understanding of the water-gas distribution in the LGDL of PEMWEs, challenged the existing approach to PEMWE component design, and introduced two novel low-cost diagnostic tools to the suite of methods available to researchers investigating mass transport processes in PEMWEs.

Dissemination

First-Author Publications

1. Maier M, Meyer Q, Majasan J, Tan C, Dedigama I, Robinson J, et al. Operando flow regime diagnosis using acoustic emission in a polymer electrolyte membrane water electrolyser. J. Power Sources 2019;424:138–49. doi:10.1016/j.jpowsour.2019.03.061.
2. Maier M, Dodwell J, Ziesche R, Tan C, Heenan T, Majasan J, et al. Mass transport in polymer electrolyte membrane water electrolyser liquid-gas diffusion layers: A combined neutron imaging and X-ray computed tomography study. J. Power Sources 2020;455. doi:10.1016/j.jpowsour.2020.227968.
3. Maier M, Meyer Q, Majasan J, Owen RE, Robinson JB, Dodwell J, et al. Diagnosing Stagnant Gas Bubbles in a Polymer Electrolyte Membrane Water Electrolyser Using Acoustic Emission. Front Energy Res 2020;8. doi:10.3389/fenrg.2020.582919.
4. Maier M, Owen RE, Pham MTM, Dodwell J, Majasan J, Robinson JB, et al. Acoustic time-of-flight imaging of polymer electrolyte membrane water electrolysers to probe internal structure and flow characteristics. Int J Hydrogen Energy 2021;46:11523–35. doi:10.1016/j.ijhydene.2021.01.077.
5. Maier M, Smith K, Dodwell J, Hinds G, Shearing P, Brett DJL, Mass Transport in PEM Water Electrolysers: A Review. *Submitted to Int J Hydrogen*

Other Publications

1. Tan C, M Heenan TM, Ziesche RF, Daemi SR, Hack J, Maier M, et al. Four-Dimensional Studies of Morphology Evolution in Lithium−Sulfur Batteries. ACS Appl Energy Mater 2018;1:5090–100. doi:10.1021/acsaem.8b01148.
2. Robinson JB, Maier M, Alster G, Compton T, Brett DJL, Shearing PR. Spatially resolved ultrasound diagnostics of Li-ion battery electrodes. Phys Chem Chem Phys 2019. doi:10.1039/C8CP07098A.
3. Majasan JO, Cho JIS, Maier M, Dedigama I, Shearing PR, Brett DJL. Effect of Anode Flow Channel Depth on the Performance of Polymer Electrolyte Membrane

Water Electrolyser. ECS Trans 2018;85:1593–603. doi:10.1149/08513.1593ecst.

4. Majasan JO, Iacoviello F, Cho JIS, Maier M, Lu X, Neville TP, et al. Correlative study of microstructure and performance for porous transport layers in polymer electrolyte membrane water electrolysers by X-ray computed tomography and electrochemical characterization. Int J Hydrogen Energy 2019;44:19519–32. doi:10.1016/j.ijhydene.2019.05.222.
5. Wu Y, Cho JIS, Whiteley M, Rasha L, Neville TP, Ziesche R, et al. Characterization of water management in metal foam flow-field based polymer electrolyte fuel cells using in-operando neutron radiography. Int J Hydrogen Energy 2019;5:2195–205. doi:10.1016/j.ijhydene.2019.11.069.
6. Bethapudi VS, Maier M, Hinds G, Shearing PR, Brett DJL, Coppens MO. Acoustic emission as a function of polarisation: Diagnosis of polymer electrolyte fuel cell hydration state. Electrochem Commun 2019;109:106582. doi:10.1016/j.elecom.2019.106582.
7. Robinson JB, Owen RE, Kok M, Maier M, Majasan J, Braglia M, et al. Identifying Defects in Li-Ion Cells Using Ultrasound Acoustic Measurements. J Electrochem Soc 2020. doi:10.1149/1945-7111/abb174.
8. Heenan T, Nabavi SA, Erans M, Robinson J, Kok M, Maier M, et al. The Role of Bi-Polar Plate Design and the Start-Up Protocol in the Spatiotemporal Dynamics during Solid Oxide Fuel Cell Anode Reduction. Energies 2020;13:3552. doi:10.3390/en13143552.
9. Majasan JO, Robinson JB, Owen RE, Maier M, Radhakrishnan ANP, Pham M, et al. Recent advances in acoustic diagnostics for electrochemical power systems. JPhys Energy 2021;3. doi:10.1088/2515-7655/abfb4a.
10. Dodwell J, Maier M, Majasan J, Jervis R, Castanheira L, Shearing P, et al. Open-circuit dissolution of platinum from the cathode in polymer electrolyte membrane water electrolysers. J Power Sources 2021;498:229937. doi:10.1016/j.jpowsour.2021.229937.
11. Majasan JO, Cho JIS, Maier M, Shearing PR, Brett DJL. Optimisation of Mass Transport Parameters in a Polymer Electrolyte Membrane Electrolyser Using

Factorial Design-of-Experiment. Front Energy Res 2021;9:1–9. doi:10.3389/fenrg.2021.643587.

Conferences

1. H2FC Conference, Poster Presentation, Application of Advanced Diagnostic Techniques to Study Mass Transfer Mechanisms in Polymer Electrolyte Membrane Electrolysers, St. Andrews, UK, 2017.
2. 22nd World Hydrogen Economic Conference (WHEC), Oral Presentation, In-situ Acoustic Emission Analysis of a Polymer Electrolyte Membrane Water Electrolyser, Rio de Janeiro, Brazil, 2018.
3. 235th ECS Meeting, Oral Presentation, Application of Acoustic Emission to Study Electrochemical Energy Storage Devices, Dallas, USA, 2019.

References

[1] Bryngelsson D, Wirsenius S, Hedenus F, Sonesson U. How can the EU climate targets be met? A combined analysis of technological and demand-side changes in food and agriculture. Food Policy 2016;59:152–64. doi:10.1016/j.foodpol.2015.12.012.

[2] South D, Vangala S, Hung K. The Biden Administration's Approach to Addressing Climate Change. Clim Energy 2021;37:8–18. doi:10.1002/gas.22222.

[3] Friedlingstein P, Andrew RM, Rogelj J, Peters GP, Canadell JG, Knutti R, et al. Persistent growth of CO2 emissions and implications for reaching climate targets. Nat Geosci 2014;7:709–15. doi:10.1038/NGEO2248.

[4] Mallouk TE. Divide and conquer. Nat Chem 2013;5:362–3. doi:10.1038/nchem.1634.

[5] Dunn B, Kamath H, Tarascon JM. Electrical energy storage for the grid: A battery of choices. Science (80-) 2011;334:928–35. doi:10.1126/science.1212741.

[6] Staffell I, Scamman D, Velazquez Abad A, Balcombe P, Dodds PE, Ekins P, et al. The role of hydrogen and fuel cells in the global energy system. Energy Environ Sci 2019;12:463–91. doi:10.1039/c8ee01157e.

[7] Bockris JOM. The hydrogen economy: Its history. Int J Hydrogen Energy 2013;38:2579–88. doi:10.1016/j.ijhydene.2012.12.026.

[8] Marbán G, Valdés-Solís T. Towards the hydrogen economy? Int J Hydrogen Energy 2007;32:1625–37. doi:10.1016/j.ijhydene.2006.12.017.

[9] Sharma S, Ghoshal SK. Hydrogen the future transportation fuel: From production to applications. Renew Sustain Energy Rev 2015;43:1151–8. doi:10.1016/j.rser.2014.11.093.

[10] Crabtree GW, Dresselhaus MS, Buchanan M V. The Hydrogen Economy. Phys Today 2004:39–45. doi:10.1063/1.1878333.

[11] Buttler A, Spliethoff H. Current status of water electrolysis for energy storage, grid balancing and sector coupling via power-to-gas and power-to-liquids: A review. Renew Sustain Energy Rev 2018;82:2440–54. doi:10.1016/j.rser.2017.09.003.

[12] Allidières L, Brisse A, Millet P, Valentin S, Zeller M. On the ability of pem water electrolysers to provide power grid services. Int J Hydrogen Energy 2019;44:9690–

700. doi:10.1016/j.ijhydene.2018.11.186.

[13] Holladay JD, Hu J, King DL, Wang Y. An overview of hydrogen production technologies. Catal Today 2009;139:244–60. doi:10.1016/j.cattod.2008.08.039.

[14] da Silva Veras T, Mozer TS, da Costa Rubim Messeder dos Santos D, da Silva César A. Hydrogen: Trends, production and characterization of the main process worldwide. Int J Hydrogen Energy 2017;42:2018–33. doi:10.1016/j.ijhydene.2016.08.219.

[15] Bhandari R, Trudewind CA, Zapp P. Life cycle assessment of hydrogen production via electrolysis - A review. J Clean Prod 2014;85:151–63. doi:10.1016/j.jclepro.2013.07.048.

[16] Dincer I, Acar C. Review and evaluation of hydrogen production methods for better sustainability. Int J Hydrogen Energy 2014;40:11094–111. doi:10.1016/j.ijhydene.2014.12.035.

[17] Turner J, Sverdrup G, Mann MK, Maness P-C, Kroposki B, Ghirardi M, et al. Renewable hydrogen production. Int J Energy Res 2008;32:379–407. doi:10.1002/er.

[18] Carmo M, Fritz DL, Mergel J, Stolten D. A comprehensive review on PEM water electrolysis. Int J Hydrogen Energy 2013;38:4901–34. doi:10.1016/j.ijhydene.2013.01.151.

[19] Villagra A, Millet P. An analysis of PEM water electrolysis cells operating at elevated current densities. Int J Hydrogen Energy 2019;44:9708–17. doi:10.1016/j.ijhydene.2018.11.179.

[20] Kopp M, Coleman D, Stiller C, Scheffer K, Aichinger J, Scheppat B. Energiepark Mainz: Technical and economic analysis of the worldwide largest Power-to-Gas plant with PEM electrolysis. Int J Hydrogen Energy 2017;42:13311–20. doi:10.1016/j.ijhydene.2016.12.145.

[21] Aßmann P, Gago AS, Gazdzicki P, Friedrich KA, Wark M. Toward developing accelerated stress tests for proton exchange membrane electrolyzers. Curr Opin Electrochem 2020;21:225–33. doi:10.1016/j.coelec.2020.02.024.

[22] Saba SM, Müller M, Robinius M, Stolten D. The investment costs of electrolysis –

A comparison of cost studies from the past 30 years. Int J Hydrogen Energy 2018;43:1209–23. doi:10.1016/j.ijhydene.2017.11.115.

[23] Based on IEA data from the IEA (2014), Electricity production from renewable sources, excluding hydroelectric, includes geothermal, solar, tides, wind, biomass, and biofuels. www.iea.org/statistics. All rights reserved; as modified by Maximilian Maier n.d.

[24] Bertuccioli L, Chan A, Hart D, Lehner F, Madden B, Standen E. Study on development of water electrolysis in the EU. 2014.

[25] Russell J, Nuttal L, Fickett A. Hydrogen Generation by Solid Polymer Electrolyte Water Electrolysis. Am Chem Soc Div Fuel Chem Prepr 1973;18:24–40.

[26] Medina P, Santarelli M. Analysis of water transport in a high pressure PEM electrolyzer. Int J Hydrogen Energy 2010;35:5173–86. doi:10.1016/j.ijhydene.2010.02.130.

[27] Schalenbach M, Carmo M, Fritz DL. Pressurized PEM water electrolysis: Efficiency and gas crossover. Int J Hydrogen Energy 2013;38:14921–33. doi:10.1016/j.ijhydene.2013.09.013.

[28] Grigoriev SA, Kalinnikov AA, Millet P, Porembsky VI, Fateev VN. Mathematical modeling of high-pressure PEM water electrolysis. J Appl Electrochem 2010;40:921–32. doi:10.1007/s10800-009-0031-z.

[29] Bensmann B, Hanke-Rauschenbach R, Peña Arias IK, Sundmacher K. Energetic evaluation of high pressure PEM electrolyzer systems for intermediate storage of renewable energies. Electrochim Acta 2013;110:570–80. doi:10.1016/j.electacta.2013.05.102.

[30] Sartory M, Wallnöfer-Ogris E, Salman P, Fellinger T, Justl M, Trattner A, et al. Theoretical and experimental analysis of an asymmetric high pressure PEM water electrolyser up to 155 bar. Int J Hydrogen Energy 2017;42:30493–508. doi:10.1016/j.ijhydene.2017.10.112.

[31] Chisholm G, Kitson PJ, Kirkaldy ND, Bloor LG, Cronin L. 3D printed flow plates for the electrolysis of water: an economic and adaptable approach to device manufacture. Energy Environ Sci 2014;7:3026–32. doi:10.1039/C4EE01426J.

[32] Hudkins JR, Wheeler DG, Peña B, Berlinguette CP. Rapid prototyping of electrolyzer flow field plates. Energy Environ Sci 2016;9:3417–23. doi:10.1039/C6EE01997H.

[33] Kang Z, Yang G, Mo J, Li Y, Yu S, Cullen DA, et al. Novel thin/tunable gas diffusion electrodes with ultra-low catalyst loading for hydrogen evolution reactions in proton exchange membrane electrolyzer cells. Nano Energy 2018;47:434–41. doi:10.1016/j.nanoen.2018.03.015.

[34] Bernt M, Siebel A, Gasteiger HA. Analysis of Voltage Losses in PEM Water Electrolyzers with Low Platinum Group Metal Loadings. J Electrochem Soc 2018;165:F305–14. doi:10.1149/2.0641805jes.

[35] Li A, Sun Y, Yao T, Han H. Earth-Abundant Transition-Metal-Based Electrocatalysts for Water Electrolysis to Produce Renewable Hydrogen. Chem - A Eur J 2018;24:18334–55. doi:10.1002/chem.201803749.

[36] Klose C, Saatkamp T, Münchinger A, Bohn L, Titvinidze G, Breitwieser M, et al. All-Hydrocarbon MEA for PEM Water Electrolysis Combining Low Hydrogen Crossover and High Efficiency. Adv Energy Mater 2020;1903995:1–9. doi:10.1002/aenm.201903995.

[37] Marangio F, Santarelli M, Calì M. Theoretical model and experimental analysis of a high pressure PEM water electrolyser for hydrogen production. Int J Hydrogen Energy 2009;34:1143–58. doi:10.1016/j.ijhydene.2008.11.083.

[38] Abdin Z, Webb CJ, Gray EM. Modelling and simulation of a proton exchange membrane (PEM) electrolyser cell. Int J Hydrogen Energy 2015;40:13243–57. doi:10.1016/j.ijhydene.2015.07.129.

[39] Toghyani S, Fakhradini S, Afshari E, Baniasadi E, Abdollahzadeh Jamalabadi MY, Safdari Shadloo M. Optimization of operating parameters of a polymer exchange membrane electrolyzer. Int J Hydrogen Energy 2019;44:6403–14. doi:10.1016/j.ijhydene.2019.01.186.

[40] Ito H, Maeda T, Nakano A, Hasegawa Y, Yokoi N, Hwang CM, et al. Effect of flow regime of circulating water on a proton exchange membrane electrolyzer. Int J Hydrogen Energy 2010;35:9550–60. doi:10.1016/j.ijhydene.2010.06.103.

[41] Ito H, Maeda T, Nakano A, Hwang CM, Ishida M, Kato A, et al. Experimental study on porous current collectors of PEM electrolyzers. Int J Hydrogen Energy 2012;37:7418–28. doi:10.1016/j.ijhydene.2012.01.095.

[42] Sun S, Xiao Y, Liang D, Shao Z, Yu H, Hou M, et al. Behaviors of a proton exchange membrane electrolyzer under water starvation. RSC Adv 2015;5:14506–13. doi:10.1039/C4RA14104K.

[43] Dedigama I, Angeli P, Ayers K, Robinson JB, Shearing PR, Tsaoulidis D, et al. In situ diagnostic techniques for characterisation of polymer electrolyte membrane water electrolysers - Flow visualisation and electrochemical impedance spectroscopy. Int J Hydrogen Energy 2014;39:4468–82. doi:10.1016/j.ijhydene.2014.01.026.

[44] Dedigama I, Angeli P, Van Dijk N, Millichamp J, Tsaoulidis D, Shearing PR, et al. Current density mapping and optical flow visualisation of a polymer electrolyte membrane water electrolyser. J Power Sources 2014;265:97–103. doi:10.1016/j.jpowsour.2014.04.120.

[45] Garcia-Navarro J, Schulze M, Friedrich KA. Understanding the Role of Water Flow and the Porous Transport Layer on the Performance of Proton Exchange Membrane Water Electrolyzers. ACS Sustain Chem Eng 2019;7:1600–10. doi:10.1021/acssuschemeng.8b05369.

[46] Crowther TG, Wade AP, Wentzell PD, Gopal R. Characterization of acoustic emission from an electrolysis cell. Anal Chim Acta 1991;254:223–34. doi:10.1016/0003-2670(91)90030-9.

[47] Bühler M, Holzapfel P, McLaughlin D, Thiele S. From catalyst coated membranes to porous transport electrode based configurations in PEM water electrolyzers. J Electrochem Soc 2019;166:F1070–8. doi:10.1149/2.0581914jes.

[48] Bühler M, Hegge F, Holzapfel P, Bierling M, Suermann M, Vierrath S, et al. Optimization of anodic porous transport electrodes for proton exchange membrane water electrolyzers. J Mater Chem A 2019;7:26984–95. doi:10.1039/c9ta08396k.

[49] Selamet ÖF, Becerikli F, Mat MD, Kaplan Y. Development and testing of a highly efficient proton exchange membrane (PEM) electrolyzer stack. Int J Hydrogen

Energy 2011;36:11480–7. doi:10.1016/j.ijhydene.2011.01.129.

[50] Ayers K. The potential of proton exchange membrane–based electrolysis technology. Curr Opin Electrochem 2019;18:9–15. doi:10.1016/j.coelec.2019.08.008.

[51] Yang G, Mo J, Kang Z, Dohrmann Y, List FA, Green JB, et al. Fully printed and integrated electrolyzer cells with additive manufacturing for high-efficiency water splitting. Appl Energy 2018;215:202–10. doi:10.1016/j.apenergy.2018.02.001.

[52] Han B, Mo J, Kang Z, Yang G, Barnhill W, Zhang FY. Modeling of two-phase transport in proton exchange membrane electrolyzer cells for hydrogen energy. Int J Hydrogen Energy 2017;42:4478–89. doi:10.1016/j.ijhydene.2016.12.103.

[53] Aouali FZ, Becherif M, Ramadan HS, Emziane M, Khellaf A, Mohammedi K. Analytical modelling and experimental validation of proton exchange membrane electrolyser for hydrogen production. Int J Hydrogen Energy 2017;42:1366–74. doi:10.1016/j.ijhydene.2016.03.101.

[54] Awasthi A, Scott K, Basu S. Dynamic modeling and simulation of a proton exchange membrane electrolyzer for hydrogen production. Int J Hydrogen Energy 2011;36:14779–86. doi:10.1016/j.ijhydene.2011.03.045.

[55] Kim H, Park M, Lee KS. One-dimensional dynamic modeling of a high-pressure water electrolysis system for hydrogen production. Int J Hydrogen Energy 2013;38:2596–609. doi:10.1016/j.ijhydene.2012.12.006.

[56] Toghyani S, Afshari E, Baniasadi E, Atyabi SA. Thermal and electrochemical analysis of different flow field patterns in a PEM electrolyzer. Electrochim Acta 2018;267:234–45. doi:10.1016/j.electacta.2018.02.078.

[57] Dickinson EJF, Wain AJ. The Butler-Volmer equation in electrochemical theory: Origins, value, and practical application. J Electroanal Chem 2020;872:114145. doi:10.1016/j.jelechem.2020.114145.

[58] García-Valverde R, Espinosa N, Urbina A. Simple PEM water electrolyser model and experimental validation. Int J Hydrogen Energy 2012;37:1927–38. doi:10.1016/j.ijhydene.2011.09.027.

[59] Schuler T, Schmidt TJ, Büchi FN. Polymer Electrolyte Water Electrolysis:

Correlating Performance and Porous Transport Layer Structure: Part II. Electrochemical Performance Analysis. J Electrochem Soc 2019;166:F555–65. doi:10.1149/2.1241908jes.

[60] Han B, Steen SM, Mo J, Zhang FY. Electrochemical performance modeling of a proton exchange membrane electrolyzer cell for hydrogen energy. Int J Hydrogen Energy 2015;40:7006–16. doi:10.1016/j.ijhydene.2015.03.164.

[61] Han B, Mo J, Kang Z, Zhang FY. Effects of membrane electrode assembly properties on two-phase transport and performance in proton exchange membrane electrolyzer cells. Electrochim Acta 2016;188:317–26. doi:10.1016/j.electacta.2015.11.139.

[62] Yang G, Yu S, Mo J, Kang Z, Dohrmann Y, List FA, et al. Bipolar plate development with additive manufacturing and protective coating for durable and high-efficiency hydrogen production. J Power Sources 2018;396:590–8. doi:10.1016/j.jpowsour.2018.06.078.

[63] Reier T, Nong HN, Teschner D, Schlögl R, Strasser P. Electrocatalytic Oxygen Evolution Reaction in Acidic Environments – Reaction Mechanisms and Catalysts. Adv Energy Mater 2017;7:1601275. doi:10.1002/aenm.201601275.

[64] Mauritz KA, Moore RB. State of understanding of Nafion. Chem Rev 2004;104:4535–85. doi:10.1021/cr0207123.

[65] Mishima K, Hibiki T. Some characteristics of air-water two-phase flow in small diameter vertical tubes. Int J Multiph Flow 1996;22:703–12. doi:10.1016/0301-9322(96)00010-9.

[66] Onda K, Murakami T, Hikosaka T, Kobayashi M, Notu R, Ito K. Performance Analysis of Polymer-Electrolyte Water Electrolysis Cell at a Small-Unit Test Cell and Performance Prediction of Large Stacked Cell. J Electrochem Soc 2002;149:A1069. doi:10.1149/1.1492287.

[67] Cubaud T, Ho CM. Transport of bubbles in square microchannels. Phys Fluids 2004;16:4575–85. doi:10.1063/1.1813871.

[68] Olesen AC, Frensch SH, Kær SK. Towards uniformly distributed heat, mass and charge: A flow field design study for high pressure and high current density

operation of PEM electrolysis cells. Electrochim Acta 2019;293:476–95. doi:10.1016/j.electacta.2018.10.008.

[69] Christian A, Rømer C, Knudsen S. A numerical study of the gas-liquid , two-phase flow maldistribution in the anode of a high pressure PEM water electrolysis cell. Int J Hydrogen Energy 2015;41:52–68. doi:10.1016/j.ijhydene.2015.09.140.

[70] Lafmejani SS, Olesen AC, Kær SK. VOF modelling of gas–liquid flow in PEM water electrolysis cell micro-channels. Int J Hydrogen Energy 2017;42:16333–44. doi:10.1016/j.ijhydene.2017.05.079.

[71] Minnaar C, De Beer F, Bessarabov D. Current Density Distribution of Electrolyzer Flow Fields: In Situ Current Mapping and Neutron Radiography. Energy and Fuels 2020;34:1014–23. doi:10.1021/acs.energyfuels.9b03814.

[72] Nie J, Chen Y, Cohen S, Carter BD, Boehm RF. Numerical and experimental study of three-dimensional fluid flow in the bipolar plate of a PEM electrolysis cell. Int J Therm Sci 2009;48:1914–22. doi:10.1016/j.ijthermalsci.2009.02.017.

[73] Majasan JO, Cho JIS, Dedigama I, Tsaoulidis D, Shearing P, Brett DJL. Two-phase flow behaviour and performance of polymer electrolyte membrane electrolysers: Electrochemical and optical characterisation. Int J Hydrogen Energy 2018;43:15659–72. doi:10.1016/j.ijhydene.2018.07.003.

[74] Li H, Nakajima H, Inada A, Ito K. Effect of flow-field pattern and flow configuration on the performance of a polymer-electrolyte-membrane water electrolyzer at high temperature. Int J Hydrogen Energy 2018;43:8600–10. doi:10.1016/j.ijhydene.2018.02.171.

[75] Wang J, Wang H. Discrete approach for flow field designs of parallel channel configurations in fuel cells. Int J Hydrogen Energy 2012;37:10881–97. doi:10.1016/j.ijhydene.2012.04.034.

[76] Wang J, Wang H. Flow-field designs of bipolar plates in PEM fuel cells: Theory and applications. Fuel Cells 2012;12:989–1003. doi:10.1002/fuce.201200074.

[77] Majasan JO, Cho JIS, Maier M, Dedigama I, Shearing PR, Brett DJL. Effect of Anode Flow Channel Depth on the Performance of Polymer Electrolyte Membrane Water Electrolyser. ECS Trans 2018;85:1593–603. doi:10.1149/08513.1593ecst.

[78] Kang Z, Mo J, Yang G, Retterer ST, Cullen DA, Toops TJ, et al. Investigation of thin/well-tunable liquid/gas diffusion layers exhibiting superior multifunctional performance in low-temperature electrolytic water splitting. Energy Environ Sci 2017;10:166–75. doi:10.1039/C6EE02368A.

[79] Kang Z, Yang G, Mo J, Yu S, Cullen DA, Retterer ST, et al. Developing titanium micro/nano porous layers on planar thin/tunable LGDLs for high-efficiency hydrogen production. Int J Hydrogen Energy 2018;43:14618–28. doi:10.1016/j.ijhydene.2018.05.139.

[80] Mo J, Kang Z, Retterer ST, Cullen DA, Toops TJ, Green JB, et al. Discovery of true electrochemical reactions for ultrahigh catalyst mass activity in water splitting. Sci Adv 2016;2:e1600690–e1600690. doi:10.1126/sciadv.1600690.

[81] Mo J, Kang Z, Yang G, Li Y, Retterer ST, Cullen DA, et al. In situ investigation on ultrafast oxygen evolution reactions of water splitting in proton exchange membrane electrolyzer cells. J Mater Chem A 2017;5:18469–75. doi:10.1039/c7ta05681h.

[82] Mo J, Kang Z, Yang G, Talley D. Visualization on Rapid and Micro-Scale Dynamics of Oxygen Bubble Evolution in PEMECs. Proc. 12th IEEE Int. Conf. Nano/Micro Eng. Mol. Syst., Los Angeles: 2017, p. 101–5.

[83] Hoeh MA, Arlt T, Manke I, Banhart J, Fritz DL, Maier W, et al. In operando synchrotron X-ray radiography studies of polymer electrolyte membrane water electrolyzers. Electrochem Commun 2015;55:55–9. doi:10.1016/j.elecom.2015.03.009.

[84] Leonard E, Shum AD, Normile S, Sabarirajan DC, Yared DG, Xiao X, et al. Operando X-ray tomography and sub-second radiography for characterizing transport in polymer electrolyte membrane electrolyzer. Electrochim Acta 2018;276:424–33. doi:10.1016/j.electacta.2018.04.144.

[85] Selamet OF, Pasaogullari U, Spernjak D, Hussey DS, Jacobson DL, Mat MD. Two-phase flow in a proton exchange membrane electrolyzer visualized in situ by simultaneous neutron radiography and optical imaging. Int J Hydrogen Energy 2013;38:5823–35. doi:10.1016/j.ijhydene.2013.02.087.

[86] Selamet OF, Pasaogullari U, Spernjak D, Hussey DS, Jacobsen DL, Mat MD. In-

situ two-phase flow investigation of Proton Exchange Membrane (PEM) electrolyzer by simultaneous optical and neutron imaging. ECS Trans 2011;41:349–62.

[87] Hoeh MA, Arlt T, Kardjilov N, Manke I, Banhart J, Fritz DL, et al. In-operando Neutron Radiography Studies of Polymer Electrolyte Membrane Water Electrolyzers. ECS Trans 2015;69:1135–40.

[88] Panchenko O, Borgardt E, Zwaygardt W, Hackemüller FJ, Bram M, Kardjilov N, et al. In-situ two-phase flow investigation of different porous transport layer for a polymer electrolyte membrane (PEM) electrolyzer with neutron spectroscopy. J Power Sources 2018;390:108–15. doi:10.1016/j.jpowsour.2018.04.044.

[89] Seweryn J, Biesdorf J, Schmidt TJ, Boillat P. Communication—Neutron Radiography of the Water/Gas Distribution in the Porous Layers of an Operating Electrolyser. J Electrochem Soc 2016;163:F3009–11. doi:10.1149/2.0641607jes.

[90] Maier M, Dodwell J, Ziesche R, Tan C, Heenan T, Majasan J, et al. Mass transport in polymer electrolyte membrane water electrolyser liquid-gas diffusion layers: A combined neutron imaging and X-ray computed tomography study. J Power Sources 2020;455. doi:10.1016/j.jpowsour.2020.227968.

[91] Kardjilov N, Manke I, Woracek R, Hilger A, Banhart J. Advances in neutron imaging. Mater Today 2018;21:652–72. doi:10.1016/j.mattod.2018.03.001.

[92] Ito H, Maeda T, Nakano A, Kato A, Yoshida T. Influence of pore structural properties of current collectors on the performance of proton exchange membrane electrolyzer. Electrochim Acta 2013;100:242–8. doi:10.1016/j.electacta.2012.05.068.

[93] Immerz C, Schweins M, Trinke P, Bensmann B, Paidar M, Bystroň T, et al. Experimental characterization of inhomogeneity in current density and temperature distribution along a single-channel PEM water electrolysis cell. Electrochim Acta 2018;260:582–8. doi:10.1016/j.electacta.2017.12.087.

[94] Immerz C, Bensmann B, Trinke P, Suermann M, Hanke-Rauschenbach R. Local current density and electrochemical impedance measurements within 50 cm single-channel PEM electrolysis cell. J Electrochem Soc 2018;165:F1292–9. doi:10.1149/2.0411816jes.

[95] Lafmejani SS, Olesen AC, Shakhshir SA, Kaer SK. Analysing Gas-Liquid Flow in PEM Electrolyser Micro-Channels using a Micro-Porous Ceramic as Gas Permeable wall. ECS Trans 2017;80:1107–15.

[96] Ojong ET, Kwan JTH, Nouri-Khorasani A, Bonakdarpour A, Wilkinson DP, Smolinka T. Development of an experimentally validated semi-empirical fully-coupled performance model of a PEM electrolysis cell with a 3-D structured porous transport layer. Int J Hydrogen Energy 2017;42:25831–47. doi:10.1016/j.ijhydene.2017.08.183.

[97] Zhang Z, Xing X. Simulation and experiment of heat and mass transfer in a proton exchange membrane electrolysis cell. Int J Hydrogen Energy 2020;45:20184–93. doi:10.1016/j.ijhydene.2020.02.102.

[98] Arbabi F, Montazeri H, Abouatallah R, Wang R, Bazylak A. Three-dimensional computational fluid dynamics modelling of oxygen bubble transport in polymer electrolyte membrane electrolyzer porous transport layers. J Electrochem Soc 2016;163:F3062–9. doi:10.1149/2.0091611jes.

[99] Upadhyay M, Lee S, Jung S, Choi Y, Moon S, Lim H. Systematic assessment of the anode flow field hydrodynamics in a new circular PEM water electrolyser. Int J Hydrogen Energy 2020;45:20765–75. doi:10.1016/j.ijhydene.2020.05.164.

[100] Toghyani S, Afshari E, Baniasadi E. Metal foams as flow distributors in comparison with serpentine and parallel flow fields in proton exchange membrane electrolyzer cells. Electrochim Acta 2018;290:506–19. doi:10.1016/j.electacta.2018.09.106.

[101] Toghyani S, Afshari E, Baniasadi E. Three-dimensional computational fluid dynamics modeling of proton exchange membrane electrolyzer with new flow field pattern. J Therm Anal Calorim 2019;135:1911–9. doi:10.1007/s10973-018-7236-5.

[102] Civan F. Porous Media Transport Phenomena. Wiley; 2011. doi:10.1029/2003WR002800.Aziz.

[103] Zinser A, Papakonstantinou G, Sundmacher K. Analysis of mass transport processes in the anodic porous transport layer in PEM water electrolysers. Int J Hydrogen Energy 2019;44:28077–87. doi:10.1016/j.ijhydene.2019.09.081.

[104] Schmidt G, Suermann M, Bensmann B, Hanke-Rauschenbach R, Neuweiler I.

Modeling Overpotentials Related to Mass Transport Through Porous Transport Layers of PEM Water Electrolysis Cells. J Electrochem Soc 2020;167:114511. doi:10.1149/1945-7111/aba5d4.

[105] Becker H, Castanheira L, Hinds G. Local measurement of current collector potential in a polymer electrolyte membrane water electrolyser. J Power Sources 2020;448:227563. doi:10.1016/j.jpowsour.2019.227563.

[106] Kang Z, Mo J, Yang G, Zhang F-Y, Reterer ST, Cullen DA. Micro/Nano Manufacturing of Novel Multifunctional Layers for Hydrogen Production from Water Splitting. Proc. 12th IEEE Int. Conf. Nano/Micro Eng. Mol. Syst., Los Angeles: 2017, p. 126–30.

[107] Lopata J, Kang Z, Young J, Bender G, Weidner JW, Shimpalee S. Effects of the Transport/Catalyst Layer Interface and Catalyst Loading on Mass and Charge Transport Phenomena in Polymer Electrolyte Membrane Water Electrolysis Devices. J Electrochem Soc 2020;167:064507. doi:10.1149/1945-7111/ab7f87.

[108] Babic U, Schmidt TJ, Gubler L. Communication—Contribution of Catalyst Layer Proton Transport Resistance to Voltage Loss in Polymer Electrolyte Water Electrolyzers. J Electrochem Soc 2018;165:J3016–8. doi:10.1149/2.0031815jes.

[109] Lee JK, Bazylak A. Optimizing Porous Transport Layer Design Parameters via Stochastic Pore Network Modelling : Reactant Transport and Interfacial Contact Considerations Optimizing Porous Transport Layer Design Parameters via Stochastic Pore Network Modelling : Reactant Tran. J Electrochem Soc 2020;167:013541. doi:10.1149/1945-7111/ab6557.

[110] Millet P, Dragoe D, Grigoriev S, Fateev V, Etievant C. GenHyPEM: A research program on PEM water electrolysis supported by the European Commission. Int J Hydrogen Energy 2009;34:4974–82. doi:10.1016/j.ijhydene.2008.11.114.

[111] Millet P, Ngameni R, Grigoriev SA, Mbemba N, Brisset F, Ranjbari A, et al. PEM water electrolyzers: From electrocatalysis to stack development. Int J Hydrogen Energy 2010;35:5043–52. doi:10.1016/j.ijhydene.2009.09.015.

[112] Millet P, Ngameni R, Grigoriev SA, Fateev VN. Scientific and engineering issues related to PEM technology: Water electrolysers, fuel cells and unitized regenerative

systems. Int J Hydrogen Energy 2011;36:4156–63. doi:10.1016/j.ijhydene.2010.06.106.

[113] Millet P, Mbemba N, Grigoriev SA, Fateev VN, Aukauloo A, Etiévant C. Electrochemical performances of PEM water electrolysis cells and perspectives. Int J Hydrogen Energy 2011;36:4134–42. doi:10.1016/j.ijhydene.2010.06.105.

[114] Grigoriev SA, Millet P, Volobuev SA, Fateev VN. Optimization of porous current collectors for PEM water electrolysers. Int J Hydrogen Energy 2009;34:4968–73. doi:10.1016/j.ijhydene.2008.11.056.

[115] Parra-Restrepo J, Bligny R, Dillet J, Didierjean S, Stemmelen D, Moyne C, et al. Influence of the porous transport layer properties on the mass and charge transfer in a segmented PEM electrolyzer. Int J Hydrogen Energy 2020;45:8094–106. doi:10.1016/j.ijhydene.2020.01.100.

[116] Mo J, Steen III SM, Retterer S, Cullen DA, Terekhov A, Zhang F-Y. Mask-Patterned Wet Etching of Thin Titanium Liquid/Gas Diffusion Layers for a PEMEC. ECS Trans 2015;66:3–10. doi:10.1149/06624.0003ecst.

[117] Mo J, Kang Z, Yang G, Retterer ST, Cullen DA, Toops TJ, et al. Thin liquid/gas diffusion layers for high-efficiency hydrogen production from water splitting. Appl Energy 2016;177:817–22. doi:10.1016/j.apenergy.2016.05.154.

[118] Kang Z, Mo J, Yang G, Li Y, Talley DA, Retterer ST, et al. Thin film surface modifications of thin/tunable liquid/gas diffusion layers for high-efficiency proton exchange membrane electrolyzer cells. Appl Energy 2017;206:983–90. doi:10.1016/j.apenergy.2017.09.004.

[119] Li H, Fujigaya T, Nakajima H, Inada A, Ito K. Optimum structural properties for an anode current collector used in a polymer electrolyte membrane water electrolyzer operated at the boiling point of water. J Power Sources 2016;332:16–23. doi:10.1016/j.jpowsour.2016.09.086.

[120] Steen SM, Mo J, Kang Z, Yang G, Zhang FY. Investigation of titanium liquid/gas diffusion layers in proton exchange membrane electrolyzer cells. Int J Green Energy 2017;14:162–70. doi:10.1080/15435075.2016.1253582.

[121] Baumann N, Cremers C, Pinkwart K, Tübke J. Membrane Electrode Assemblies for

Water Electrolysis using WO3-Supported IrxRu1-xO2Catalysts. Energy Technol 2016;4:212–20. doi:10.1002/ente.201500258.

[122] Wittstadt U, Wagner E, Jungmann T. Membrane electrode assemblies for unitised regenerative polymer electrolyte fuel cells. J Power Sources 2005;145:555–62. doi:10.1016/j.jpowsour.2005.02.068.

[123] Arisetty S, Prasad AK, Advani SG. Metal foams as flow field and gas diffusion layer in direct methanol fuel cells. J Power Sources 2007;165:49–57. doi:10.1016/j.jpowsour.2006.12.008.

[124] Baroutaji A, Carton JG, Stokes J, Olabi AG. Application of Open Pore Cellular Foam for air breathing PEM fuel cell. Int J Hydrogen Energy 2017;42:25630–8. doi:10.1016/j.ijhydene.2017.05.114.

[125] Deevanhxay P, Sasabe T, Tsushima S, Hirai S. Effect of liquid water distribution in gas diffusion media with and without microporous layer on PEM fuel cell performance. Electrochem Commun 2013;34:239–41. doi:10.1016/j.elecom.2013.07.001.

[126] Ismail MS, Damjanovic T, Ingham DB, Ma L, Pourkashanian M. Effect of polytetrafluoroethylene-treatment and microporous layer-coating on the in-plane permeability of gas diffusion layers used in proton exchange membrane fuel cells. J Power Sources 2010;195:6619–28. doi:10.1016/j.jpowsour.2010.04.036.

[127] Tseng CJ, Lo SK. Effects of microstructure characteristics of gas diffusion layer and microporous layer on the performance of PEMFC. Energy Convers Manag 2010;51:677–84. doi:10.1016/j.enconman.2009.11.011.

[128] Gostick JT, Ioannidis MA, Fowler MW, Pritzker MD. On the role of the microporous layer in PEMFC operation. Electrochem Commun 2009;11:576–9. doi:10.1016/j.elecom.2008.12.053.

[129] Pasaogullari U, Wang CY. Two-phase transport and the role of micro-porous layer in polymer electrolyte fuel cells. Electrochim Acta 2004;49:4359–69. doi:10.1016/j.electacta.2004.04.027.

[130] Lettenmeier P, Kolb S, Burggraf F, Gago AS, Friedrich KA. Towards developing a backing layer for proton exchange membrane electrolyzers. J Power Sources

2016;311:153–8. doi:10.1016/j.jpowsour.2016.01.100.

[131] Sung CC, Liu CY. A novel micro protective layer applied on a simplified PEM water electrolyser. Int J Hydrogen Energy 2013;38:10063–7. doi:10.1016/j.ijhydene.2013.06.034.

[132] Liu CY, Hu LH, Sung CC. Micro-protective layer for lifetime extension of solid polymer electrolyte water electrolysis. J Power Sources 2012;207:81–5. doi:10.1016/j.jpowsour.2012.01.045.

[133] Schuler T, Ciccone JM, Krentscher B, Marone F, Peter C, Schmidt TJ, et al. Hierarchically Structured Porous Transport Layers for Polymer Electrolyte Water Electrolysis. Adv Energy Mater 2020;10:1–12. doi:10.1002/aenm.201903216.

[134] Ito H, Maeda T, Nakano A, Hwang CM, Ishida M, Yokoi N, et al. Influence of Different Gas Diffusion Layers on the Water Management of Polymer Electrolyte Unitized Reversible Fuel Cell. ECS Trans 2010;33:945–54. doi:10.1149/1.3484588.

[135] Hwang CM, Ishida M, Ito H, Maeda T, Nakano A, Hasegawa Y, et al. Influence of properties of gas diffusion layers on the performance of polymer electrolyte-based unitized reversible fuel cells. Int J Hydrogen Energy 2011;36:1740–53. doi:10.1016/j.ijhydene.2010.10.091.

[136] Hwang CM, Ishida M, Ito H, Maeda T, Nakano A, Kato A, et al. Effect of titanium powder loading in gas diffusion layer of a polymer electrolyte unitized reversible fuel cell. J Power Sources 2012;202:108–13. doi:10.1016/j.jpowsour.2011.11.041.

[137] Zhan Z, Xiao J, Li D, Pan M, Yuan R. Effects of porosity distribution variation on the liquid water flux through gas diffusion layers of PEM fuel cells. J Power Sources 2006;160:1041–8. doi:10.1016/j.jpowsour.2006.02.060.

[138] Zhan Z, Xiao J, Zhang Y, Pan M, Yuan R. Gas diffusion through differently structured gas diffusion layers of PEM fuel cells. Int J Hydrogen Energy 2007;32:4443–51. doi:10.1016/j.ijhydene.2007.03.041.

[139] Zhang Y, Verma A, Pitchumani R. Optimum design of polymer electrolyte membrane fuel cell with graded porosity gas diffusion layer. Int J Hydrogen Energy 2016;41:8412–26. doi:10.1016/j.ijhydene.2016.02.077.

[140] Lettenmeier P, Kolb S, Sata N, Fallisch A, Zielke L, Thiele S, et al. Comprehensive

investigation of novel pore-graded gas diffusion layers for high-performance and cost-effective proton exchange membrane electrolyzers. Energy Environ Sci 2017;10:2521–33. doi:10.1039/C7EE01240C.

[141] Kang Z, Yu S, Yang G, Li Y, Bender G, Pivovar BS, et al. Performance improvement of proton exchange membrane electrolyzer cells by introducing in-plane transport enhancement layers. Electrochim Acta 2019;316:43–51. doi:10.1016/j.electacta.2019.05.096.

[142] Forner-Cuenca A, Biesdorf J, Gubler L, Kristiansen PM, Schmidt TJ, Boillat P. Engineered Water Highways in Fuel Cells: Radiation Grafting of Gas Diffusion Layers. Adv Mater 2015;27:6317–22. doi:10.1002/adma.201503557.

[143] Forner-Cuenca A, Manzi-Orezzoli V, Biesdorf J, Kazzi M El, Streich D, Gubler L, et al. Advanced Water Management in PEFCs: Diffusion Layers with Patterned Wettability: I. Synthetic Routes, Wettability Tuning and Thermal Stability. J Electrochem Soc 2016;163:F788–801. doi:10.1149/2.0271608jes.

[144] Forner-Cuenca A, Biesdorf J, Manzi-Orezzoli V, Gubler L, Schmidt TJ, Boillat P. Advanced Water Management in PEFCs: Diffusion Layers with Patterned Wettability:II. Measurement of Capillary Pressure Characteristic with Neutron and Synchrotron Imaging. J Electrochem Soc 2016;163:F1389–98. doi:10.1149/2.0891613jes.

[145] Forner-Cuenca A, Biesdorf J, Manzi-Orezzoli V, Gubler L, Schmidt TJ, Boillat P. Advanced Water Management in PEFCs: Diffusion Layers with Patterned Wettability: III. Operando Characterization with Neutron Imaging. J Electrochem Soc 2016;163:F1389–98. doi:10.1149/2.0891613jes.

[146] Nouri-Khorasani A, Tabu Ojong E, Smolinka T, Wilkinson DP. Model of oxygen bubbles and performance impact in the porous transport layer of PEM water electrolysis cells. Int J Hydrogen Energy 2017;42:28665–80. doi:10.1016/j.ijhydene.2017.09.167.

[147] Li Y, Kang Z, Deng X, Yang G, Yu S, Mo J, et al. Wettability effects of thin titanium liquid/gas diffusion layers in proton exchange membrane electrolyzer cells. Electrochim Acta 2019;298:704–8. doi:10.1016/j.electacta.2018.12.162.

[148] Bystron T, Vesely M, Paidar M, Papakonstantinou G, Sundmacher K, Bensmann B, et al. Enhancing PEM water electrolysis efficiency by reducing the extent of Ti gas diffusion layer passivation. J Appl Electrochem 2018;48:713–23. doi:10.1007/s10800-018-1174-6.

[149] Kang Z, Alia SM, Young JL, Bender G. Effects of various parameters of different porous transport layers in proton exchange membrane water electrolysis. Electrochim Acta 2020;354:136641. doi:10.1016/j.electacta.2020.136641.

[150] Suermann M, Gimpel T, Bühre L V., Schade W, Bensmann B, Hanke-Rauschenbach R. Femtosecond laser-induced surface structuring of the porous transport layers in proton exchange membrane water electrolysis. J Mater Chem A 2020;8:4898–910. doi:10.1039/c9ta12127g.

[151] Kalikmanov VI. Nucleation Theory. 2013.

[152] Li Y, Kang Z, Mo J, Yang G, Yu S, Talley DA, et al. In-situ investigation of bubble dynamics and two-phase flow in proton exchange membrane electrolyzer cells. Int J Hydrogen Energy 2018;43:11223–33. doi:10.1016/j.ijhydene.2018.05.006.

[153] Majasan JO, Iacoviello F, Cho JIS, Maier M, Lu X, Neville TP, et al. Correlative study of microstructure and performance for porous transport layers in polymer electrolyte membrane water electrolysers by X-ray computed tomography and electrochemical characterization. Int J Hydrogen Energy 2019;44:19519–32. doi:10.1016/j.ijhydene.2019.05.222.

[154] Panchenko O, Giesenberg L, Borgardt E, Zwaygardt W, Kardjilov N, Markötter H, et al. Influence of Stoichiometry on the Two-Phase Flow Behavior of Proton Exchange Membrane Electrolyzers. Energies 2019;12:350. doi:10.3390/en12030350.

[155] Lee CH, Lee JK, George MG, Fahy KF, LaManna JM, Baltic E, et al. Reconciling temperature-dependent factors affecting mass transport losses in polymer electrolyte membrane electrolyzers. Energy Convers Manag 2020;213:112797. doi:10.1016/j.enconman.2020.112797.

[156] Zielke L, Fallisch A, Paust N, Zengerle R, Thiele S. Tomography based screening of flow field / current collector combinations for PEM water electrolysis. RSC Adv

2014;4:58888–94. doi:10.1039/C4RA12402B.

[157] Leonard E, Shum AD, Danilovic N, Capuano C, Ayers KE, Pant LM, et al. Interfacial analysis of a PEM electrolyzer using X-ray computed tomography. Sustain Energy Fuels 2020;4:921–31. doi:10.1039/c9se00364a.

[158] Lee C, Lee JK, Zhao B, Fahy KF, Bazylak A. Transient Gas Distribution in Porous Transport Layers of Polymer Electrolyte Membrane Electrolyzers. J Electrochem Soc 2020;167:024508. doi:10.1149/1945-7111/ab68c8.

[159] Panchenko U, Arlt T, Manke I, Müller M, Stolten D, Lehnert W. Synchrotron Radiography for a Proton Exchange Membrane (PEM) Electrolyzer. Fuel Cells 2020:1–7. doi:10.1002/fuce.201900055.

[160] Arbabi F, Kalantarian A, Abouatallah R, Wang R, Wallace JS, Bazylak A. Feasibility study of using microfluidic platforms for visualizing bubble flows in electrolyzer gas diffusion layers. J Power Sources 2014;258:142–9. doi:10.1016/j.jpowsour.2014.02.042.

[161] Lee CH, Hinebaugh J, Banerjee R, Chevalier S, Abouatallah R, Wang R, et al. Influence of limiting throat and flow regime on oxygen bubble saturation of polymer electrolyte membrane electrolyzer porous transport layers. Int J Hydrogen Energy 2017;42:2724–35. doi:10.1016/j.ijhydene.2016.09.114.

[162] Garcia-Navarro JC, Schulze M, Friedrich KA. Measuring and modeling mass transport losses in proton exchange membrane water electrolyzers using electrochemical impedance spectroscopy. J Power Sources 2019;431:189–204. doi:10.1016/j.jpowsour.2019.05.027.

[163] Lettenmeier P, Wang R, Abouatallah R, Helmly S, Morawietz T, Hiesgen R, et al. Durable Membrane Electrode Assemblies for Proton Exchange Membrane Electrolyzer Systems Operating at High Current Densities. Electrochim Acta 2016;210:502–11. doi:10.1016/j.electacta.2016.04.164.

[164] Rozain C, Millet P. Electrochemical characterization of Polymer Electrolyte Membrane Water Electrolysis Cells. Electrochim Acta 2014;131:160–7. doi:10.1016/j.electacta.2014.01.099.

[165] Siracusano S, Trocino S, Briguglio N, Baglio V, Aricò AS. Electrochemical

impedance spectroscopy as a diagnostic tool in polymer electrolyte membrane electrolysis. Materials (Basel) 2018;11. doi:10.3390/ma11081368.

[166] Ivers-Tiffee E, Weber A. Evaluation of electrochemical impedance spectra by the distribution of relaxation times. J Ceram Soc Japan 2017;125:193–201. doi:10.2109/jcersj2.16267.

[167] Illig J, Ender M, Chrobak T, Schmidt JP, Klotz D, Ivers-Tiffée E. Separation of charge transfer and contact resistance in LiFePO 4-Cathodes by impedance Modeling. J Electrochem Soc 2012;159:952–60. doi:10.1149/2.030207jes.

[168] Schichlein H, Müller AC, Voigts M, Krügel A, Ivers-Tiffée E. Deconvolution of electrochemical impedance spectra for the identification of electrode reaction mechanisms in solid oxide fuel cells. J Appl Electrochem 2002;32:875–82. doi:10.1023/A:1020599525160.

[169] Yuan X-Z, Song C, Wang H, Zhang J. Electrochemical Impedance Spectroscopy in PEM Fuel Cells: Fundamentals and Applications. London: Springer Verlag; 2010. doi:10.1007/978-1-84882-846-9.

[170] Majasan JO, Iacoviello F, Shearing PR, Brett DJ. Effect of Microstructure of Porous Transport Layer on Performance in Polymer Electrolyte Membrane Water Electrolyser. Energy Procedia 2018;151:111–9. doi:10.1016/j.egypro.2018.09.035.

[171] Weiß A, Siebel A, Bernt M, Shen T-H, Tileli V, Gasteiger HA. Impact of Intermittent Operation on Lifetime and Performance of a PEM Water Electrolyzer. J Electrochem Soc 2019;166:F487–97. doi:10.1149/2.0421908jes.

[172] Suermann M, Takanohashi K, Lamibrac A, Schmidt TJ, Büchi FN. Influence of Operating Conditions and Material Properties on the Mass Transport Losses of Polymer Electrolyte Water Electrolysis. J Electrochem Soc 2017;164:F973–80. doi:10.1149/2.13517109jes.

[173] Schuler T, De Bruycker R, Schmidt TJ, Büchi FN. Polymer Electrolyte Water Electrolysis: Correlating Porous Transport Layer Structural Properties and Performance: Part I. Tomographic Analysis of Morphology and Topology. J Electrochem Soc 2019;166:F270–81. doi:10.1149/2.0561904jes.

[174] Li Y, Yang G, Yu S, Kang Z, Talley DA, Zhang FY. Direct thermal visualization of

micro-scale hydrogen evolution reactions in proton exchange membrane electrolyzer cells. Energy Convers Manag 2019;199:111935. doi:10.1016/j.enconman.2019.111935.

[175] Kang Z, Mo J, Yang G, Li Y, Talley DA, Han B, et al. Performance Modeling and Current Mapping of Proton Exchange Membrane Electrolyzer Cells with Novel Thin/Tunable Liquid/Gas Diffusion Layers. Electrochim Acta 2017;255:405–16. doi:10.1016/j.electacta.2017.09.170.

[176] Lafmejani SS, Müller M, Olesen AC, Kær SK. Experimental and numerical study of flow in expanded metal plate for water electrolysis applications. J Power Sources 2018;397:334–42. doi:10.1016/j.jpowsour.2018.07.032.

[177] Lafmejani SS, Olesen AC, Kaer SK. Analysing Gas-Liquid Flow in PEM Electrolyser Micro-Channels. ECS Trans 2016;75:1121–7.

[178] Altaf H, Vorhauer N, Tsotsas E, Vidaković-Koch T. Steady-State Water Drainage by Oxygen in Anodic Porous Transport Layer of Electrolyzers: A 2D Pore Network Study. Processes 2020;8:362. doi:10.3390/pr8030362.

[179] Roberts TM, Talebzadeh M. Acoustic emission monitoring of fatigue crack propagation. J Constr Steel Res 2003;59:695–712. doi:10.1016/S0143-974X(02)00064-0.

[180] Nair A, Cai CS. Acoustic emission monitoring of bridges: Review and case studies. Eng Struct 2010;32:1704–14. doi:10.1016/j.engstruct.2010.02.020.

[181] Bellenger F, Mazille H, Idrissi H. Use of acoustic emission technique for the early detection of aluminum alloys exfoliation corrosion. NDT E Int 2002;35:385–92. doi:10.1016/S0963-8695(02)00011-7.

[182] Jomdecha C, Prateepasen A, Kaewtrakulpong P. Study on source location using an acoustic emission system for various corrosion types. NDT E Int 2007;40:584–93. doi:10.1016/j.ndteint.2007.05.003.

[183] Ohzuku T, Tomura H, Sawai K. Monitoring of Particle Fracture by Acoustic Emission during Charge and Discharge of Li/MnO2 Cells. J Electrochem Soc 1997;144:3496–500. doi:10.1149/1.1838039.

[184] Rhodes K, Dudney N, Lara-Curzio E, Daniel C. Understanding the Degradation of

Silicon Electrodes for Lithium-Ion Batteries Using Acoustic Emission. J Electrochem Soc 2010;157:A1354–60. doi:10.1149/1.3489374.

[185] Kalnaus S, Rhodes K, Daniel C. A study of lithium ion intercalation induced fracture of silicon particles used as anode material in Li-ion battery. J Power Sources 2011;196:8116–24. doi:10.1016/j.jpowsour.2011.05.049.

[186] Villevieille C, Boinet M, Monconduit L. Direct evidence of morphological changes in conversion type electrodes in Li-ion battery by acoustic emission. Electrochem Commun 2010;12:1336–9. doi:10.1016/j.elecom.2010.07.014.

[187] Kircheva N, Genies S, Brun-Buisson D, Thivel PX. Study of Solid Electrolyte Interface Formation and Lithium Intercalation in Li-Ion Batteries by Acoustic Emission. J Electrochem Soc 2012;159:A18–25. doi:Doi 10.1149/2.045201jes.

[188] Dev B, Walter ME, Arkenberg GB, Swartz SL. Mechanical and thermal characterization of a ceramic/glass composite seal for solid oxide fuel cells. J Power Sources 2014;245:958–66. doi:10.1016/j.jpowsour.2013.07.054.

[189] Dev B, Walter ME. Comparative study of the leak characteristics of two ceramic/glass composite seals for solid oxide fuel cells. Fuel Cells 2015;15:115–30. doi:10.1002/fuce.201400095.

[190] Legros B, Thivel P-X, Bultel Y, Boinet M, Nogueira RP. Electrochemical Impedance and Acoustic Emission Survey of Water Desorption in Nafion Membranes. Electrochem Solid-State Lett 2009;12:B116–8. doi:10.1149/1.3131728.

[191] Legros B, Thivel PX, Druart F, Bultel Y, Nogueira R. Diagnosis and Modelling of Proton- Exchange-Membrane Fuel Cell via and Acoustic-Emission Measurements. Electromotion, Lille: 2009, p. 1–6. doi:10.1109/ELECTROMOTION.2009.5259133.

[192] Legros B, Thivel PX, Bultel Y, Boinet M, Nogueira RP. Acoustic emission: Towards a real-time diagnosis technique for Proton exchange membrane fuel cell operation. J Power Sources 2010;195:8124–33. doi:10.1016/j.jpowsour.2010.07.045.

[193] Pandit AB, Varley J, Thorpe RB, Davidson JF. Measurement of bubble size distribution: an acoustic technique. Chem Eng Sci 1992;47:1079–89. doi:10.1016/0009-2509(92)80233-3.

[194] Yen GG, Lu H. Acoustic emission data assisted process monitoring. ISA Trans

2002;41:273–82. doi:10.1016/S0019-0578(07)60087-1.

[195] Jingdai W, Congjing R, Yongrong Y. Characterization of Flow Regime Transition and Particle Motion Using Acoustic Emission Measurement in a Gas-Solid Fluidized Bed. AIChE J 2010;56:1173–83. doi:10.1002/aic.

[196] Fang L, Liang Y, Lu Q, Li X, Liu R, Wang X. Flow noise characterization of gas-liquid two-phase flow based on acoustic emission. Measurement 2013;46:3887–97. doi:10.1016/j.measurement.2013.07.032.

[197] Al-lababidi S, Addali A, Yeung H, Mba D, Khan F. Gas Void Fraction Measurement in Two-Phase Gas/Liquid Slug Flow Using Acoustic Emission Technology. J Vib Acoust 2009;131:1–7. doi:10.1115/1.4000463.

[198] Husin S, Addali A, Mba D. Feasibility study on the use of the Acoustic Emission technology for monitoring flow patterns in two phase flow. Flow Meas Instrum 2013;33:251–6. doi:10.1016/j.flowmeasinst.2013.07.011.

[199] Sood B, Osterman M, Pecht M. Health monitoring of lithium-ion batteries. Proc - 10th Annu IEEE Symp Prod Compliance Eng ISPCE 2013 2013:3–8. doi:10.1109/ISPCE.2013.6664165.

[200] Hsieh AG, Bhadra S, Hertzberg BJ, Gjeltema PJ, Goy A, Fleischer JW, et al. Electrochemical-acoustic time of flight: in operando correlation of physical dynamics with battery charge and health. Energy Environ Sci 2015;8:1569–77. doi:10.1039/C5EE00111K.

[201] Bhadra S, Hsieh AG, Wang MJ, Hertzberg BJ, Steingart DA. Anode Characterization in Zinc-Manganese Dioxide AA Alkaline Batteries Using Electrochemical-Acoustic Time-of-Flight Analysis. J Electrochem Soc 2016;163:A1050–6. doi:10.1149/2.1201606jes.

[202] Davies G, Knehr KW, Van Tassell B, Hodson T, Biswas S, Hsieh AG, et al. State of Charge and State of Health Estimation Using Electrochemical Acoustic Time of Flight Analysis. J Electrochem Soc 2017;164:A2746–55. doi:10.1149/2.1411712jes.

[203] Bommier C, Lu Y, Williams M, Bommier C, Chang W, Lu Y, et al. In Operando Acoustic Detection of Lithium Metal Plating in Commercial LiCoO 2 / Graphite

Pouch Cells In Operando Acoustic Detection of Lithium Metal Plating in Commercial LiCoO 2 / Graphite Pouch Cells. Cell Reports Phys Sci n.d.:100035. doi:10.1016/j.xcrp.2020.100035.

[204] Robinson JB, Maier M, Alster G, Compton T, Brett DJL, Shearing PR. Spatially resolved ultrasound diagnostics of Li-ion battery electrodes. Phys Chem Chem Phys 2019. doi:10.1039/C8CP07098A.

[205] Robinson JB, Pham M, Kok MDR, Heenan TMM, Brett DJL, Shearing PR. Examining the Cycling Behaviour of Li-Ion Batteries Using Ultrasonic Time-of-Flight Measurements. J Power Sources 2019;444:227318. doi:10.1016/j.jpowsour.2019.227318.

[206] Ladpli P, Kopsaftopoulos F, Chang FK. Estimating state of charge and health of lithium-ion batteries with guided waves using built-in piezoelectric sensors/actuators. J Power Sources 2018;384:342–54. doi:10.1016/j.jpowsour.2018.02.056.

[207] Ladpli P, Kopsaftopoulos F, Nardari R, Chang F-K. Battery charge and health state monitoring via ultrasonic guided-wave-based methods using built-in piezoelectric transducers. Smart Mater Nondestruct Eval Energy Syst 2017 2017;10171:1017108. doi:10.1117/12.2260107.

[208] Ladpli P, Nardari R, Kopsaftopoulos F, Wang Y, Chang FK. Design of multifunctional structural batteries with health monitoring capabilities. 8th Eur Work Struct Heal Monit EWSHM 2016 2016;1:23–35.

[209] Chang W, Mohr R, Kim A, Raj A, Davies G, Denner K, et al. Measuring effective stiffness of Li-ion batteries: Via acoustic signal processing. J Mater Chem A 2020;8:16624–35. doi:10.1039/d0ta05552b.

[210] Fazalul Rahiman MH, Abdul Rahim R, Fazalul Rahiman MH, Tajjudin M. Ultrasonic transmission-mode tomography imaging for liquid/gas two-phase flow. IEEE Sens J 2006;6:1706–14. doi:10.1109/JSEN.2006.884549.

[211] Rahiman MHF, Rahim RA, Rahim HA, Mohamad EJ, Zakaria Z, Muji SZM. An investigation on chemical bubble column using ultrasonic tomography for imaging of gas profiles. Sensors Actuators, B Chem 2014;202:46–52.

doi:10.1016/j.snb.2014.05.043.

[212] Roy RA, Carey W, Nicholas M, Schindall J, Crum LA. Low-frequency scattering from submerged bubble clouds. J Acoust Soc Am 1992;92:2993–6. doi:10.1121/1.404368.

[213] Brightman E, Dodwell J, Dijk N Van, Hinds G. In situ characterisation of PEM water electrolysers using a novel reference electrode. Electrochem Commun 2015;52:1–4. doi:10.1016/j.elecom.2015.01.005.

[214] Dodwell J, Maier M, Majasan J, Jervis R, Castanheira L, Shearing P, et al. Open-circuit dissolution of platinum from the cathode in polymer electrolyte membrane water electrolysers. J Power Sources 2021;498:229937. doi:10.1016/j.jpowsour.2021.229937.

[215] Gago AS, Ansar SA, Saruhan B, Schulz U, Lettenmeier P, Cañas NA, et al. Protective coatings on stainless steel bipolar plates for proton exchange membrane (PEM) electrolysers. J Power Sources 2016;307:815–25. doi:10.1016/j.jpowsour.2015.12.071.

[216] Beverskog B, Puigdomenech I. Pourbaix diagrams for the ternary system of iron-chromium-nickel. Corrosion 1999;55:1077–87. doi:10.5006/1.3283945.

[217] Pourbaix M. Atlas of electrochemical equilibria in aqueous solutions. 1974. doi:10.1016/0022-0728(67)80059-7.

[218] Maier M, Meyer Q, Majasan J, Tan C, Dedigama I, Robinson J, et al. Operando flow regime diagnosis using acoustic emission in a polymer electrolyte membrane water electrolyser. J Power Sources 2019;424:138–49. doi:10.1016/j.jpowsour.2019.03.061.

[219] Otsu N. A Threshold Selection Method from Gray-Level Histograms. IEEE Trans Syst Man Cybern 1979;SMC-9:62–6. doi:10.1109/TSMC.1979.4310076.

[220] Mukhopadhyay P, Chaudhuri BB. A survey of Hough Transform. Pattern Recognit 2015;48:993–1010. doi:10.1016/j.patcog.2014.08.027.

[221] Liu D, Yu J. Otsu method and K-means. Proc - 2009 9th Int Conf Hybrid Intell Syst HIS 2009 2009;1:344–9. doi:10.1109/HIS.2009.74.

[222] Jun Z, Jinglu H. Image segmentation based on 2D Otsu method with histogram

analysis. Proc - Int Conf Comput Sci Softw Eng CSSE 2008 2008;6:105–8. doi:10.1109/CSSE.2008.206.

[223] Huang M, Yu W, Zhu D. An improved image segmentation algorithm based on the Otsu method. Proc - 13th ACIS Int Conf Softw Eng Artif Intell Networking, Parallel/Distributed Comput SNPD 2012 2012:135–9. doi:10.1109/SNPD.2012.26.

[224] Cherabit N, Zohra Chelali F, Djeradi A. Circular Hough Transform for Iris localization. Sci Technol 2012;2:114–21. doi:10.5923/j.scit.20120205.02.

[225] Just S, Pedersen K. Circular Hough Transform. Encycl Biometrics 2009:181–181. doi:10.1007/978-0-387-73003-5_1059.

[226] Rizon M, Yazid H, Saad P, Md Shakaff AY, Saad AR, Sugisaka M, et al. Object Detection using Circular Hough Transform. Am J Appl Sci 2005;2:1606–9. doi:10.3844/ajassp.2005.1606.1609.

[227] Banhart J. Advanced Tomographic Methods in Materials Research and Engineering. Oxford: Oxford University Press; 2008.

[228] Evans RD. The atomic nucleus. New York: 1955. doi:10.3103/S0027134912010092.

[229] Hubbell JH. Photon mass attenuation and energy-absorption coefficients. Int J Appl Radiat Isot 1982;33:1269–90. doi:10.1016/0020-708X(82)90248-4.

[230] Salvo L, Suéry M, Marmottant A, Limodin N, Bernard D. 3D imaging in material science: Application of X-ray tomography. Comptes Rendus Phys 2010;11:641–9. doi:10.1016/j.crhy.2010.12.003.

[231] Zhao Z, Gang GJ, Siewerdsen JH. Noise, sampling, and the number of projections in cone-beam CT with a flat-panel detector. Med Phys 2014;41:1–10. doi:10.1118/1.4875688.

[232] Tan C. Development of X-ray Tomography Tools for Characterisation of Lithium-Sulfur Batteries. University College London, 2019.

[233] Gruner SM, Tate MW, Eikenberry EF. Charge-coupled device area x-ray detectors. Rev Sci Instrum 2002;73:2815. doi:10.1063/1.1488674.

[234] Cooper SJ, Bertei A, Shearing PR, Kilner JA, Brandon NP. TauFactor: An open-source application for calculating tortuosity factors from tomographic data.

SoftwareX 2016;5:203–10. doi:10.1016/j.softx.2016.09.002.

[235] Avizo Software User’s Guide 2018.

[236] ZEISS Xradia 520 Versa Submicron X-ray Imaging: Extending the Limits of Your Exploration n.d.

[237] Doster W. The new Munich neutron source FRM II: Overview and uses for biological studies. AIP Conf Proc 2007;958:16–9. doi:10.1063/1.2825773.

[238] Bellows RJ, Lin MY, Arif M, Thompson AK, Jacobson D. Neutron Imaging Technique for In Situ Measurement of Water Transport Gradients within Nafion in Polymer Electrolyte Fuel Cells. J Electrochem Soc 1999;146:1099–103.

[239] Satija R, Jacobson DL, Arif M, Werner SA. In situ neutron imaging technique for evaluation of water management systems in operating PEM fuel cells. J Power Sources 2004;129:238–45. doi:10.1016/j.jpowsour.2003.11.068.

[240] Ziesche RF, Arlt T, Finegan DP, Heenan TMM, Tengattini A, Baum D, et al. 4D imaging of lithium-batteries using correlative neutron and X-ray tomography with a virtual unrolling technique. Nat Commun 2020;11:1–11. doi:10.1038/s41467-019-13943-3.

[241] Kardjilov N, Fiori F, Giunta G, Hilger A, Rustichelli F, Strobl M, et al. Neutron tomography for archaeological investigations. J Neutron Res 2006;14:29–36. doi:10.1080/10238160600673201.

[242] Williams SH, Hilger A, Kardjilov N, Manke I, Strobl M, Douissard PA, et al. Detection system for microimaging with neutrons. J Instrum 2012;7. doi:10.1088/1748-0221/7/02/P02014.

[243] Kardjilov N, Hilger A, Manke I. CONRAD-2: Cold Neutron Tomography and Radiography at BER II (V7). J Large-Scale Res Facil JLSRF 2016;2:2–7. doi:10.17815/jlsrf-2-108.

[244] Kardjilov N, Hilger A, Manke I, Woracek R, Banhart J. CONRAD-2: The new neutron imaging instrument at the Helmholtz-Zentrum Berlin. J Appl Crystallogr 2016;49:195–202. doi:10.1107/S1600576715023353.

[245] Majasan JO, Cho JIS, Maier M, Shearing PR, Brett DJL. Optimisation of Mass Transport Parameters in a Polymer Electrolyte Membrane Electrolyser Using

Factorial Design-of-Experiment. Front Energy Res 2021;9:1–9. doi:10.3389/fenrg.2021.643587.

[246] Filippi P, Habault D, Lefebvre J-P, Bergassoli A. Acoustics: Basic Physics, Theory and Methods. London: Academic Press; 1999.

[247] McClements DJ. Ultrasonic Characterisation of Emulsions and Suspensions. Adv Colloid Interface Sci 1991;37:33–72.

[248] Uchino K. Advanced Piezoelectric Materials - Science and Technology. Elsevier; 2017.

[249] Bhalla S, Moharana S, Talakokula V, Kaur N. Piezoelectric Materials - Applications in SHM, Energy Harvesting and Bio-Mechanics. John Wiley & Sons; 2017.

[250] Kircheva N, Thivel P-X, Genies S, Brun-Buisson D, Bultel Y. Study of SEI formation in Li-ion batteries by acoustic emission technique. ECS Trans 2011;35:19–26. doi:10.1149/1.3644900.

[251] Plesset MS, Prosperetti A. Bubble Dynamics and Cavitation. Ann Rev Fluid Mech 1977;9:145–85.

[252] Lynnworth LC. Ultrasonic Impedance Matching from Solids to Gases. IEEE Trans Sonics Ultrason 1965;12:37–48. doi:10.1109/T-SU.1965.29359.

[253] Hwang PA, Teague WJ. Low-frequency resonant scattering of bubble clouds. J Atmos Ocean Technol 2000;17:847–53. doi:10.1175/1520-0426(2000)017<0847:LFRSOB>2.0.CO;2.

[254] Tranchot A, Etiemble A, Thivel PX, Idrissi H, Roué L. In-situ acoustic emission study of Si-based electrodes for Li-ion batteries. J Power Sources 2015;279:259–66. doi:10.1016/j.jpowsour.2014.12.126.

[255] Brigham EO, Morrow RE. The fast Fourier transform. IEEE Spectr 1967;4:63–70. doi:10.1109/MSPEC.1967.5217220.

[256] Bergland GD. A guided tour of the fast Fourier Transform. IEEE Spectr 1969;6:41–52. doi:10.1109/MSPEC.1969.5213896.

[257] Li Y, Xia XL, Sun C, Ai Q, Liu B, Tan HP. Tomography-based analysis of apparent directional spectral emissivity of high-porosity nickel foams. Int J Heat Mass Transf 2018;118:402–15. doi:10.1016/j.ijheatmasstransfer.2017.11.005.

[258] Wang G, Shen J, Liu S, Jiang C, Qin X. Three-dimensional modeling and analysis of macro-pore structure of coal using combined X-ray CT imaging and fractal theory. Int J Rock Mech Min Sci 2019;123:104082. doi:10.1016/j.ijrmms.2019.104082.

[259] Bird MB, Butler SL, Hawkes CD, Kotzer T. Numerical modeling of fluid and electrical currents through geometries based on synchrotron X-ray tomographic images of reservoir rocks using Avizo and COMSOL. Comput Geosci 2014;73:6–16. doi:10.1016/j.cageo.2014.08.009.

[260] Kok MDR, Jervis R, Brett D, Shearing PR, Gostick JT. Insights into the Effect of Structural Heterogeneity in Carbonized Electrospun Fibrous Mats for Flow Battery Electrodes by X-Ray Tomography. Small 2018;14:1–15. doi:10.1002/smll.201703616.

[261] Maier M, Meyer Q, Majasan J, Owen RE, Robinson JB, Dodwell J, et al. Diagnosing Stagnant Gas Bubbles in a Polymer Electrolyte Membrane Water Electrolyser Using Acoustic Emission. Front Energy Res 2020;8. doi:10.3389/fenrg.2020.582919.

[262] Chandesris M, Médeau V, Guillet N, Chelghoum S, Thoby D, Fouda-Onana F. Membrane degradation in PEM water electrolyzer: Numerical modeling and experimental evidence of the influence of temperature and current density. Int J Hydrogen Energy 2015;40:1353–66. doi:10.1016/j.ijhydene.2014.11.111.

[263] Strasberg M. Gas Bubbles as Sources of Sound in Liquids. J Acoust Soc Am 1956;28:20–6. doi:10.1121/1.1908212.

[264] Hsi R, Tay M, Bukur D, Tatterson G, Morrison G. Sound spectra of gas dispersion in an agitated tank. Chem Eng J 1985;31:153–61. doi:10.1016/0300-9467(85)80056-3.

[265] Manasseh R, LaFontaine RF, Davy J, Shepherd I, Zhu YG. Passive acoustic bubble sizing in sparged systems. Exp Fluids 2001;30:672–82. doi:10.1007/s003480000245.

[266] Shao N, Gavriilidis A, Angeli P. Flow regimes for adiabatic gas-liquid flow in microchannels. Chem Eng Sci 2009;64:2749–61. doi:10.1016/j.ces.2009.01.067.

[267] Choi CW, Yu DI, Kim MH. Adiabatic two-phase flow in rectangular microchannels with different aspect ratios: Part i - Flow pattern, pressure drop and void fraction. Int

J Heat Mass Transf 2011;54:616–24. doi:10.1016/j.ijheatmasstransfer.2010.07.067.

[268] Maier M, Owen RE, Pham MTM, Dodwell J, Majasan J, Robinson JB, et al. Acoustic time-of-flight imaging of polymer electrolyte membrane water electrolysers to probe internal structure and flow characteristics. Int J Hydrogen Energy 2021;46:11523–35. doi:10.1016/j.ijhydene.2021.01.077.

[269] Aricò AS, Siracusano S, Briguglio N, Baglio V, Dijk N Van, Yildirim H, et al. EUROPEAN COMMISSION HORIZON 2020 PROGRAMME FUEL CELLS AND HYDROGEN JOINT UNDERTAKING (FCH 2 JU). 2016.

[270] Springer TE. Characterization of Polymer Electrolyte Fuel Cells Using AC Impedance Spectroscopy. J Electrochem Soc 1996;143:587. doi:10.1149/1.1836485.

[271] Fu K, Yao Y, Dai J, Hu L. Progress in 3D Printing of Carbon Materials for Energy-Related Applications. Adv Mater 2017;29. doi:10.1002/adma.201603486.

[272] Mo J, Dehoff RR, Peter WH, Toops TJ, Green JB, Zhang FY. Additive manufacturing of liquid/gas diffusion layers for low-cost and high-efficiency hydrogen production. Int J Hydrogen Energy 2016;41:3128–35. doi:10.1016/j.ijhydene.2015.12.111.

[273] Yang G, Mo J, Kang Z, List FA, Green JB, Babu SS, et al. Additive manufactured bipolar plate for high-efficiency hydrogen production in proton exchange membrane electrolyzer cells. Int J Hydrogen Energy 2017;42:14734–40. doi:10.1016/j.ijhydene.2017.04.100.

[274] Strnad G, Chirila N, Petrovan C, Russu O. Contact Angle Measurement on Medical Implant Titanium Based Biomaterials. Procedia Technol 2016;22:946–53. doi:10.1016/j.protcy.2016.01.094.

[275] Lim YJ, Oshida Y. Initial contact angle measurements on variously treated dental/medical titanium materials. Biomed Mater Eng 2001;11:325–41.

[276] Ambrosi A, Pumera M. 3D-printing technologies for electrochemical applications. Chem Soc Rev 2016;45:2740–55. doi:10.1039/C5CS00714C.

[277] Pham MTM, Darst JJ, Finegan DP, Robinson JB, Heenan TMM, Kok MDR, et al.

Correlative acoustic time-of-flight spectroscopy and X-ray imaging to investigate gas-induced delamination in lithium-ion pouch cells during thermal runaway. J Power Sources 2020;470:228039. doi:10.1016/j.jpowsour.2020.228039.